This is to certify that the
dissertation entitled

MAGNETIC GLYCO-NANOPARTICLES: A NEW TOOL
TO DETECT BACTERIA, CANCER AND ATHEROSCLEROSIS

presented by

Kheireddine El-Boubbou

has been accepted towards fulfillment
of the requirements for the

Ph. D. degree in Chemistry

Major Professor's Signature

7/12/2010

Date

MAGNETIC GLYCO-NANOPARTICLES: A NEW TOOL TO DETECT BACTERIA, CANCER AND ATHEROSCLEROSIS

By

Kheireddine El-Boubbou

A DISSERTATION

Submitted to
Michigan State University
in partial fulfillment of the requirements
for the degree of

DOCTOR OF PHILOSOPHY

Chemistry

2010

ABSTRACT

MAGNETIC GLYCO-NANOPARTICLES: A NEW TOOL TO DETECT BACTERIA, CANCER AND ATHEROSCLEROSIS

By

Kheireddine El-Boubbou

Rapid and sensitive detection of pathogenic bacteria, cancer, and atherosclerotic plaques is critical for the prevention of such diseases and bioterrorism. To address these issues, we developed a magnetic iron oxide glyco-nanoparticle (MGNP)-based system as novel "*detecting and imaging*" vehicle with unique properties. In fact, there is an urgent need for an effective method for microbial decontamination and rapid pathogen detection without time consuming cell culturing. We proved that MGNPs can be utilized not only for fast pathogen detection, but also for strain differentiation and efficient pathogen decontamination. Using MGNPs, we were able to detect the presence of the bacterium *Escherichia coli* (*E. coli*) within five minutes as well as remove up to 88% of the microbe. Moreover, three different *E. coli* strains were easily identified using two MGNPs highlighting its potentials in bio-sensing. These results gave us great confidence to apply MGNPs for cancer detection. The development of simple and effective techniques to identify reliable detection methods and to delineate the fine characteristics of cancer cells can have great potential impacts on cancer diagnosis and treatment. We demonstrated the utilization of MGNP nanocomposites not only to detect and differentiate cancer cells but also to quantitatively profile their carbohydrate bindings by magnetic

resonance imaging (MRI). Using an array of MGNPs, a range of cells including closely related isogenic tumor cells, cells with different metastatic potential and malignant *vs* normal cells were readily distinguished based on their respective "MRI signatures". As the interactions between glyco-conjugates and endogenous lectins present on cancer cell surface are crucial for cancer development and metastasis, the ability to characterize and unlock the glyco-code of individual cell lines can facilitate both the understanding of the roles of carbohydrates as well as the expansion of diagnostic and therapeutic tools for cancer. Building on the success of bacterium and cancer detection, we moved on to examine the utility of MGNPs for *in vivo* atherosclerotic detection. Despite the significant progress in cardiology, there remain large unmet needs to detect atherosclerotic plaques. One of the major causes of such dramatic event is "inflammation" which occurs during early onset of the disease leading to over-expression of cell-adhesion receptors. Our proposed work is based on the knowledge that hyaluronic acid (HA) is upregulated in atherosclerotic lesions and its principal cell-adhesion receptor, CD44 is involved in several atherogenic processes. Thus, we engineered hyaluronic-coated magnetic nanoparticles (HA-MGNPs) to non-invasively image atherosclerotic plaques *via* MRI. Today's nanotechnologies are enabling better detection and diagnosis systems with great therapeutic potentials. Tomorrow is likely to bring a full understanding of the "cell-NP bio-conversation" where major problems relating to detection will be solved translating insights from the "nano-world" into clinical practice.

DEDICATION

I would like to dedicate this thesis to my father, Hassan Wafic El-Boubou for his endless support, to my mother, Bochra Saad El-Masri for her prayers, love and faith in me and to my lovely girl, Najwa Aown, who stood by me through difficult times. They all taught me how to believe in myself, keep my dreams alive and achieve success which requires belief, vision, hard work, determination, and dedication.

ACKNOWLEDGEMENTS

Lots of people, professors, students, and family contributed to my achievements and set me up to be able to reach my future goals. Without them, I could not accomplish so much today.

First of all, I would like to express deep gratitude, passionate appreciation and many thanks to my advisor, Prof. Xuefei Huang. He was that "person in life" that left a big impact on me and gave me reasons to fill my life with specific purposes. He taught me the "real" meaning of science. His patience, inspiration and wisdom impressed me. He changed me to a more mature, independent and planned person. The time I spent with him was more than a journey to Ph.D. It's a journey into exploring new horizons in life, seeing things in a different perspective, thinking more into the details and asking to learn more to be able to give more. It was a unique experience that is well appreciated and greatly admired. Indeed, the people we admire tend to be those who "we would most like to be like". And when you admire someone, you can borrow a little bit of their life blueprint to help formulate your own. So thanks Dr. Huang for shaping my life.

I would also like to express my sincere gratitude to Prof. Cyndee Gruden in the Department of Civil Engineering at the University of Toledo. Thanks for her help, support and encouragement. I am grateful for her willingness to discuss various research efforts with me at any time and providing invaluable advice. She did not only open her lab for me, but also motivated me and taught me a lot about *E. coli* bacteria, culturing and microbial sensing.

Special thanks to Prof. David Zhu in the Department of Radiology and Psychology at MSU for the support, encouragement, fruitful arguments and instructive ideas. Thanks for your confidence in me and so many valuable discussions on our experiments. He taught me all the details about MRI and helped me understand its concepts. Working with him was a pleasant experience. Without him we will not be able to perform *in vitro* and *in vivo* studies using MRI. Thanks for helping and reserving the time slots for the scanner. It's greatly appreciated.

Special thanks to our former postdoc, Dr. Lijun Huang, for his help and excellent hands in the lab. He endured my enthusiasm in chemistry and motivates me. One can learn a lot by just watching him. Thanks also for Dr. Balasubramanian Srinivasan (Bala) for the sound arguments we had and great help. I would also like to thank Dr. Zhen Wang (Jason) for teaching me the basics of sugar chemistry and special synthetic techniques when I first joined the lab.

Thanks to Dr. Chrysoula Vassilio for her help in cancer cells. She was always there at any time whenever we asked for assistance. She taught me the cell culture techniques and valuable knowledge on molecular biology.

Thanks for Prof. Xudong Fan and Prof. Terry Biogini for teaching me how to operate Transmission Electron Microscope (TEM).

Thanks for Mr. Guang for helping me in growing and counting *E. coli* bacteria, and Mr. Vivek for his excellent hands in the preparation of sugar building blocks.

Moreover, I would like to acknowledge the many outstanding people I met during my graduate studies, and all former and present lab members who provided encouragement and help in one way or another. In no particular order those people are: Dr. Mohamad El-Dakdouki, Dr. Medha Kamat, Dr. Adeline Miermont, Dr. Bin Sun, Dr. Gopinath Tiruchinapally, Dr. Youlin Zeng, Bo Yang, Gilbert Wasonga, Luyuan Zhou, Nardos Teumelsan, Xiaowei Lu, Yuqing Jing, Philip Bentley, Steven DuLaney, and Hovig Kouyoumdjian. Although we all face certain anxieties and pressures, good moments and notable times always outweigh and persist. I have learnt a lot from discussions with them either on group meetings or at casual time. Thanks guys.

Thanks for Dr. Steven Sucheck for his assistance and guidance in the courses I took with him.

Thanks for Dr. Viranga Tillekeratne, Dr. Richard Hudson, and Dr. James Slama for their inspiring discussions on synthetic organic mechanisms in "Organic Journal Clubs" we had every Thursday. It was an outstanding experience that makes your mechanistic way of thinking much stronger.

Special Thanks for my committee members: Dr. Gregory Baker, Dr. Gary Blanchard and Dr. John McCracken.

Last but not least, I would like to thank the people who will never forget you no matter what happened. The only people that do not understand any chemistry but are, chemically, the most connected to you. Thanks for their never-ending love, care, and support (financially and spiritually) at any time. Many and deep thanks to mom, dad, sisters and brothers.

TABLE OF CONTENTS

LIST OF FIGURES

Images in this dissertation are presented in color

LIST OF ABBREVIATIONS

Magnetic glyco-nanoparticles (MGNPs)

Escherichia coli (E. coli)

Magnetic resonance imaging (MRI)

Hyaluronan or hyaluronic acid (HA)

Hyaluronan-coated magnetic nanoparticles (HA-MGNPs)

Nanoparticles (NPs)

Enzyme-linked immunosorbent assay (ELISA)

Polymerase chain reaction (PCR)

Quartz crystal microbalance (QCM)

Surface plasmon resonance (SPR)

Dynamic light scattering (DLS)

Magnetic iron oxide nanoparticles (MNPs)

Polyethylene glycol (PEG)

Polyvinylpyrrolidone (PVP)

Polyglutamic acid (PGA)

Polyvinyl alcohol (PVA)

Van der Waals (vdW)

Transmission Electron Microscopy (TEM)

Thermogravimetric Analysis (TGA)

Fourier Transform Infrared (FT-IR)

High-Resolution Magic Angle Spinning (HR-MAS)

Nuclear magnetic resonance (NMR)

Photochemically activated phosphate perfluorophenylazides (PFPAs)

Colony-forming unit (cfu)

Hyaluronic-dopamine (HA-DN)

Polyvinylbenzyl- *O*-β-D-galactose-D-gluconamide (PVLA)

Superparamagnetic iron oxide nanoparticles (SPIONs)

sialyl Lewis^X (sLe^x)

Gold nanoparticles (AuNPs)

Auric acid ($HAuCl_4$)

Cetyltrimethyl ammonium bromide (CTAB)

Gold nanosphere (GNS)

Gold nanorod (GNR)

Tetraoctylammonium bromide (TOAB)

Ethylene-diamine tetraacetic acid (EDTA)

Self-assembled monolayers (SAMs)

Atomic force microscopy (AFM)

Isothermal titration calorimetry (ITC)

Mannose (Man)

Glucose (Glc)

Galactose (Gal)

Lactose (Lacto)

Maltose (Malto)

N-acetylglucosamine (GlcNAc)

Galactosamine (GalN)

Sialic acid (Sia)

Fucose (Fuc)

Cellobiose (Cel)

Concanavalin A (Con A)

Wheat Germ Agglutinin (WGA)

Bandeiraea Simplicifolia isolectin (BS-I)

Tetragonolobus Purpureas Agglutinin (TPA)

Fluorescein isothiocyanate (FITC)

Macromolecular aggregation factor (MAF)

Shiga toxins (Sts)

Cholera toxin (CT)

Dextran (Dex)

Reversible addition-fragmentation chain transfer (RAFT)

Quantum dots (QDs)

Lymphatic vessel endothelial receptor 1 (LYVE-1)

Lymphatic endothelial cells (LEC)

Single-walled carbon nanotube (SWNT)

poly(lactide-co-glycolide) (PLGA)

Ehrlich ascites tumor (EAT)

Intravenous (IV)

Chitosan (CS)

Human corneal epithelial (HCE)

Mitomycin C (MMC)

Doxorubicin (DOX)

Tetraethoxysilane (TEOS)

Aminopropyltriethoxysilane (APTES)

Alkyne-siloxane (AS)

Double deionized water (DDW)

1-[3-(Dimethylamino)-propyl]-3-ethylcarbodiimide hydrochloride (EDC)

Benzotriazole-1-yl-oxy-tris-(dimethylamino)-phosphonium hexafluorophosphate (BOP)

2-(1H-benzotriazole-1-yl)-1,1,3,3-tetra-methyluronium hexafluorophosphate (HBTU)

1-Hydroxybenzotriazole (HOBT)

Diisopropylethylamine (DIPEA)

Dimethylformamide (DMF)

Dichloromethane (DCM)

Computed tomography (CT)

Optical coherence tomography (OCT)

Ultrasound (US)

Positron emission tomography (PET)

3-(4,5-Dimethylthiazol-2-yl)-2,5-diphenyltetrazolium bromide (MTT)

Time of echo (TE)

Region of interest (ROI)

Extracellular matrices (ECM)

Smooth muscle cells (SMCs)

HA-binding domain (HABD)

CHAPTER 1

Glyco-Nanoparticles: Translating Insights from the "*Sugar-Code*" into Diagnostics and Therapeutics

1.1. Introduction

Rapid and sensitive detection of infectious pathogenic agents, cancer, and atherosclerosis is critical for the prevention of such diseases and bioterrorism. Although biosensor technology have been extensively studied[1] and carefully translated to "point of care" devices at the clinical level, nano-biosensors[2, 3] are actually in the early stages of development and their major potentials remain to be exploited. As the understanding of nano-fabrication, the control of nano-synthesis and the "cell-nanoparticle bio-conversation" become more advanced, major problems relating to biological detection will be solved.

Glyco-nanotechnolgy is gaining more eminence as the next great frontier of modern science.[4, 5] Recently, nano-based glyco-sensors have attracted a great deal of attention owing to their carbohydrate functionality, small sizes, polyvalency, biocompatibility, simplicity, as well as beneficial optical, electronic and magnetic properties. Knowing that the surfaces' of cells, microorganisms, pathogens, and viruses have either carbohydrates or carbohydrate receptors, it is of tremendous importance to use this natural phenomenon for sensing, detection and identification purposes. Thus, glycoscience is a very instructive example of how one common topic of interest stimulates both chemistry and biology to collectively open novel scientific frontiers.[6-8] In spite of this great potential, nano-based glyco-sensing, diagnosis and therapeutics are yet to be fully explored.

In fact, there is a tremendous need for developing biosensors for selective detection of biomolecules which can be more sensitive, less time- and labor-consuming. Herein, a novel magnetic carbohydrate-based nano-sensing system for the detection of pathogens, cancer and atherosclerotic plaques was developed and evaluated. Our system incorporates the use of sugar-coated magnetic iron oxide nanocomposites as innovative "*detecting and imaging*" agents with unique properties. This work will be divided into three parts, which will be discussed in three separate chapters. Briefly, we explored the following:

1) *pathogen detection:* synthesis of magnetic glyco-nanoparticles (MGNPs) not only for fast *Escherichia coli (E. coli)* detection and enumeration, but also for strain differentiation and efficient pathogen decontamination.

2) *cancer detection:* fabrication of monosaccharide-functionalized MGNP array for sensitive detection and differentiation of nine types of cancer cells using magnetic resonance imaging (MRI).

3) *atherosclerotic detection:* engineering of highly colloidal, monodispersed and superparamagnetic hyaluronan-coated magnetic nanoparticles (HA-MGNPs) as targeted MRI contrast agents for the detection and imaging of atherosclerotic plaque *in vivo*.

1.2. The "Glyco" Perspective

Signal transduction and appropriate communication between two cells are chief factors for proper cell growth. Indeed, the "bio-conversation" between two cells involves a messenger from the sender (called a ligand) and a site on the cell surface (called a receptor) receiving the signal. When the signal is received, it is passed along within the cell. Carbohydrates are one of the most common cell-surface ligands that direct the initiation of many medicinally important physiological processes where they intervene in a wide variety of events, including inflammatory and immunological responses, tumor metastasis, cell-cell signaling, apoptosis, adhesion, bacterial and viral recognition, and anticoagulation.[9-12]

Glyco-recognition is generally a multivalent process. Carbohydrates bind lectins (carbohydrate-binding proteins) in a cooperative manner improving the typically weak affinity of monomeric sugar ligands to their lectins.[13] Accordingly, the recognition of glycosyl residues on the cell surface requires the clustering of surface receptors, a phenomenon referred to as the "cluster-glycoside effect".[14] Indeed, this cluster or polyvalency effect is proved to be responsible for enhancing the binding affinities by several orders of magnitude.

All these characteristics are particularly attractive as they offer an alternative non-routine identification of biological targets. Routine discrimination of bio-analytes is primarily performed using antibodies. However, antibody based-sensors are commonly prone to protein denaturation. Moreover, antibodies are specific for one particular target and are of the "key-lock" identity, possessing minimal cross-reactivity for other biomarkers.[15] Moreover, extensive

prior knowledge on specific target is required, which can be very time-consuming. Carbohydrates do not denature nor lose activity. They are smaller than antibodies which allow higher ligand-immobilized densities, better uniformity and conjugation on the nano-surfaces. In response to all these observations, extensive work has been conducted for conjugating of multivalent carbohydrates to the scaffolds of polymers,[16] liposomes,[17] dendrimers,[18] beads,[19] and recently nanomaterials.[20] The ability to architect different sugars on nano-surfaces in a controlled polyvalent fashion can lead to better understanding of the carbohydrate-recognition events that promises to have diagnostic and therapeutic potentials and may uncover the important "sugar code" in cellular interactions.

1.3. The "Nano" Perspective

Nanomaterials are promising platforms for carbohydrate display and have recently attracted much attention where extensive efforts have been devoted to methodological studies toward their synthesis and their surface modifications.[21-24] In fact, advances in nanoresearch have led to the development of novel nanoparticles where size, geometry and surface functionality can be controlled at the nanoscale.[25-27] Diverse metal and semiconductor core materials have been used to construct nanoparticles (NPs) with important physical and electronic properties ranging from high optical extinctions (gold),[28] stable photoemission (quantum dots),[29] superparamagnetism (iron oxide),[30] and surface-enhanced Raman effect (silver and gold).[31, 32] The constructed NPs, because of their small nanometer sizes, possess novel electronic, optical and structural properties

rendering them excellent vehicles for biological applications at the cellular and molecular level. When coupled to affinity ligands, such NPs can function as biological mediators. However, to be suited for biomedical applications, several features should be fine-tuned including synthesis, magnetic, electronic properties, stability, characterization and targeting specificity (which will be discussed in details in the upcoming sections).

With all the advances in this field, NPs still present a challenging research area since little is known about their behavior and interaction with microorganisms, particularly at the cellular and molecular level. The question that remains to be answered is: How do microbial and mammalian cells respond in the presence of surface-modified nanoparticles? It will be ~ 10 years from now to fully understand the exact mechanisms of how NPs network with the cells and biological entities *in vitro* as well as *in vivo*. Size, shape and surface charge are among the most prominent factors that can influence this special "bio-conversation". Other features, such as surface modification (hydrophilicity and hydrophobicity), density, molecular weight, and crystallinity direct their targeting, sensing and electronic properties, which significantly affects the interactions with biological environments.

1.4. Glyco-nanotechnology

Extensive work has been done using carbohydrate-functionalized polymers to detect lectins,[33] virus,[34] and bacteria.[16] Moreover, carbohydrate-microarrays have been employed to study carbohydrate-carbohydrate interactions, investigate the carbohydrate-binding specificities of bacteria, detect

pathogens, and screen anti-adhesive therapeutics.[10, 35-39] Seeberger et al. reported the use of carbohydrate microarray to detect strain-specific differences in binding bacteria in complex biological systems.[36] Glyco-nanotechnology have emerged as promising machinery to prepare, study and evaluate saccharide-coated nanoparticles to better investigate carbohydrate-binding recognition events at both the cellular and molecular level.[40, 41] Glyco-nanoparticles combine the properties of nanometer-scale objects with the unique architecture of the polyvalent-carbohydrate display, greatly enhancing the weak affinities of individual ligands to their binding partners. Although numerous reports of nanoparticles functionalized with carbohydrates as stabilizing agents have been reported,[42-47] few reviews have focused on NPs immobilized with biologically-relevant carbohydrates that have shown to play key role in the recognition processes affecting the fate of the nanoparticles and its specificity to certain receptors. Critical to the performance of glyco-nanomaterials is the proper display of carbohydrate ligands, taking into consideration the coupling chemistry, the type and length of the spacer linkage, and the ligand density.

1.5. Nano-biosensors

Important progress has been reported using various nano-biosensors to detect DNA,[48] proteins,[49, 50] viruses,[51] pathogens,[52-55] cancer cells,[56-59] and atherosclerotic plaques.[60, 61] Of the various substances employed for biosensing applications, glyco-sensors[62] have become a major target because of the significant molecular characteristics of carbohydrates in living systems.

Generally, biosensors used for detection employ a substrate comprising a ligand that binds to a receptor producing a detectable signal. In nanosensors, the substrate is usually a nanocomposite made of any of iron oxide (magnetic), gold and silver (optical), silica, carbon nanotubes, or quantum dots.[63] The most common ligands employed are antibodies,[64] proteins or peptides,[65] oligonucleotides,[49] or carbohydrates[66] to name few. The functionalized-nanocomposites, thereafter, may be used for the recognition of specific targeted receptor, e.g., to detect specific enzymes, tumor cells, signaling molecules, infected sites and proteins. Current available methods for detection of pathogenic bacteria and disease biomarkers include optical, colorimetric and fluorescent assays, enzyme-linked immunosorbent assay (ELISA), polymerase chain reaction (PCR) approaches, quartz crystal microbalance (QCM) analyses, surface plasmon resonance (SPR), dynamic light scattering (DLS), and electrochemical methods.[1, 67] Despite these wide choices of platforms, important challenges still remain in minimizing sensor size, reducing detection time, eliminating target-labeling and developing simple and inexpensive fabrication protocols. The urgent necessity of biological detection will expectantly lead to more economic, simple to use, and versatile sensors that will have a great impact on biomedical applications.[68] Recently, on the diagnostic front, biocompatible magnetic iron oxide nanoparticles (MNPs) attracted much attention as they can be used not only as carriers in immunoassay,[49] biosensing,[69] and bioseparation[70] but also as drug delivery vehicles[59] and MRI contrast agents[56]. Moreover, MGNPs were also shown to be ideally suited for these purposes where their

biological applications highlight the important roles they play in glycoscience and biomedicine.[5]

To extend the scope of biomedical research on carbohydrate-mediated molecular recognition and anti-infection responses, the studies of carbohydrate-based nano-systems will be reviewed. The use of magnetic glyco-nanomaterials in bio-separation, bacterium detection, cell interactions, diagnosis, imaging and *in vivo* applications will be discussed. A special section on the preparation, synthetic insights, and functionalization of iron oxide NPs will be thoroughly discussed as those were the nanocomposites used in our study. Iron oxide NPs offer grand advantages due to their ability to respond to magnetic fields making them suitable for molecular imaging, biological and medical applications.

1.6. Magnetic Iron Oxide Nanoparticles (MNPs)

MNPs have the potential to revolutionize chemical sectors, biotechnology industries, and the medical fields. Of the various magnetic nanocrystals studied, magnetite (Fe_3O_4) and maghemite (γ-Fe_2O_3) nanomaterials protected with a polymeric coating, proved to be superb nanoprobes for both *in vitro*[71-74] and *in vivo*[59, 64, 65, 75, 76] applications. Due to their intrinsic magnetic properties, iron oxide NPs have been the subject of intense investigation as diagnostic and therapeutic agents. Some of the chief properties of iron oxide nanoparticles are: a) biocompatibility; b) superparamagnetism; c) imagebility (*via* MRI); d) uniformity (control over size and shape); e) functionality (surface modification), and f) colloidal stability. To better understand the behavior of iron oxide nanoparticles, it is of immense significance to understand their properties in more details.

MNPs consist mainly of two central parts: a) a magnetic core having one or more magnetic Fe_3O_4/Fe_2O_3 crystals, and b) a polymer coating associated with the core. The crystalline structures of magnetite have the general formula $Fe_2^{(3+)}O_3.Fe^{(2+)}O$. Each iron oxide crystal is made of magnetic domains and has inverse spinel structure with oxygen ions forming a close-packed face-centered cubic lattice and Fe cations occupying interstitial tetrahedral and octahedral sites **(Figure 1-1)**. In magnetite, magnetization arises from electron hopping between ferrous (Fe^{2+}) and ferric (Fe^{3+}) ions that coexist at the octahedral sites.

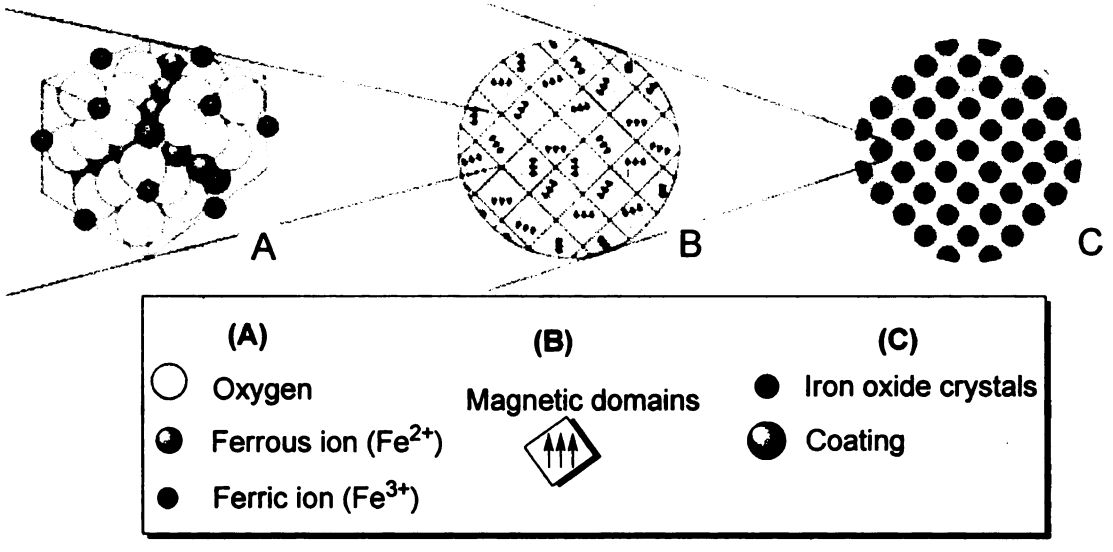

Figure 1-1. Magnetic iron oxide nanocrystal with corresponding magnetic domains and spinel crystal structure.[77]

The "polymer coating" is a natural or synthetic polymer that functions to keep the metal oxides dispersed and colloidal. If they are used for *in vitro* applications, good chemical stability is necessary and adequate. For *in vivo* applications, besides having the proper constituents, good control over size, stability, biocompatibility, and biodegradability are required. Thus, a brief discussion of some of the basic concepts of magnetism and synthetic pathways

is needed to better support the use of MNPs and understand their function in driving certain processes.

1.6.a. Magnetic Properties

Iron oxide nanoparticles have unique magnetic properties that allow them to move in high magnetic field gradient making them useful in areas of bio-separation, detection, imaging and hence medicine.

In fact, all materials are magnetic to a certain extent, with their response depending on their atomic structure and temperature. Most materials display small magnetism, even in the presence of an applied magnetic field (H). These are classified as either diamagnetic or paramagnetic **(Figure 1-2)**. However, some materials exhibit ordered magnetic states and are magnetic even without a field applied, and these are classified as ferromagnetic, ferrimagnetic, and antiferromagnetic (depending on the nature of the coupling interaction between the spins within the material). The classification of a material's magnetic properties is based on its magnetic susceptibility (χ), which is defined by the ratio of induced magnetization (M) / (H).

In diamagnetic materials, the magnetic moment is anti-parallel to H resulting in very small and negative susceptibilities. Diamagnetic materials do not retain magnetic properties when the external field is removed. Paramagnetic materials, on the other hand, have their magnetic moments aligned parallel to H and higher susceptibilities. While in ferri- and ferromagnetic materials, magnetic moments also align parallel to H, coupling interactions between the electrons of the material result in ordered magnetic domains and large spontaneous

magnetization. Superparamagnetism is exhibited by small ferromagnetic or ferrimagnetic nanoparticles.

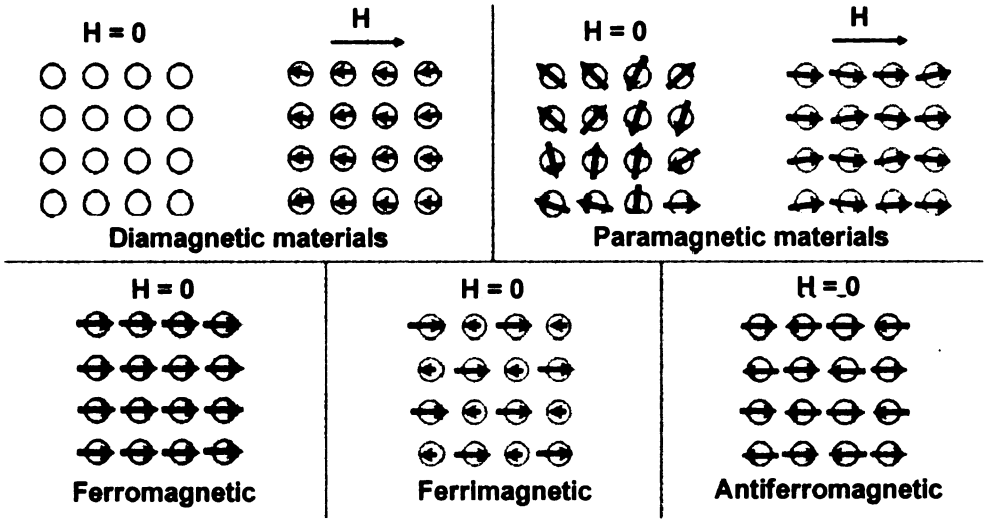

Figure 1-2. Different types of magnetic materials and their spin responses in the presence or absence of an external magnetic field (H).[78]

When the size of the NPs is below a critical value (~15 nm), the individual nanoparticles behave as a single magnetic domain exhibiting superparamagnetic behavior. Multiple domains in one particle, therefore, maintain one large magnetic moment. At low temperature, nanoparticles self-organize in solution where all magnetic spins align. At adequately high temperatures (i.e. block temperature T_B), thermal energy is sufficient to induce free rotation of the particles resulting in a loss of net magnetization in the absence of an external magnetic field. Application of a magnetic field can cause the magnetic dipoles to reorient. Thus, superparamagnetic nanoparticles respond rapidly to an applied magnetic field, but exhibit negligible residual magnetism away from the magnetic field. Superparamagnetism is essential for the synthesis of stable colloidal nanoparticles, as the non-alignment of spin limits the inter-particle attraction that

would otherwise occur. These features make superparamagnetic nanoparticles attractive for a broad range in medicine.

In brief, the main advantages of using small iron oxide nanoparticles (~15 nm) are their superparamagnetism, higher effective surface areas (more surface, more area for reactions), lower sedimentation rates (high stability) and improved cellular and tissue diffusion. The small particle size, however, has some consequences. As particle sizes decrease, surface area/volume ratios increase which can dramatically changes the magnetic properties. Typically, the saturation magnetization (M_s) values of nanoparticles (corresponding to the complete alignment of all individual moments), decrease with NP size due to disordered crystal structure resulting from high surface curvature. The magnetic spins of atoms close to the surface are less organized than for those in the bulk near the core, a phenomenon known as "spin canting" **(Figure 1-3)**.

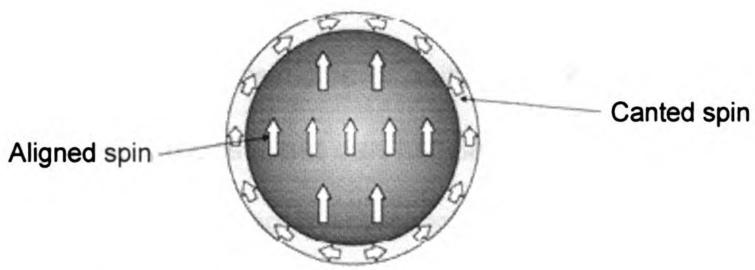

Figure 1-3. Disorganization of spin close to the surface of a nanoparticle due to lack of crystallinity organization, a phenomenon known as spin canting.[79]

All the above discussed phenomena arise from finite size and surface effects that dominate the magnetic behavior of iron oxide NPs. Thus, detailed insights into the most-widely used synthetic methods for NPs along with factors

affecting their size, stability, surface charge and shape are extremely important and will be discussed.

1.6.b. Synthesis of MNPs

Particular attention should be paid to the synthetic methods of iron oxide nanoparticles as they can significantly affect the size, shape, magnetic properties and hence the fate of nanocomposites in practical applications. Numerous chemical methods can be used to synthesize such particles: co-precipitation, thermal decomposition, microemulsions, sol-gel syntheses, hydrothermal reactions, and spray pyrolysis to name few. All those techniques were excellently reviewed.[21, 23] The following central features dictate the success of any of these methods to be commercialized. The synthesis of monodispersed (i.e. uniform-size variation <5%) nanocomposites is the first main chemical challenge where the properties of NPs depend strongly on their dimensions. The second key factor consists of defining experimental conditions, leading to stable and colloidal suspensions of magnetic nanoparticles of suitable size. The third critical point is to select a reproducible process that can be industrialized. Most commonly, iron oxide nanoparticles are prepared by co-precipitation of ferrous and ferric salts solution in a basic media stabilized using biocompatible surfactant.[24, 80, 81] Target biomolecules can then be attached by covalent or electrostatic coupling to the protected nanoparticle. Alternatively, high-temperature thermal decomposition (> 200°C) of organo-metallic precursors in the presence of surfactants has been successfully employed to produce iron nanocrystals with marked improvements in size and shape control, size distribution and crystallinity.[27, 82-84] Herein, I will

focus on those two most extensively studied methods that were successfully used in clinical applications and were explored in our lab.

1) Co-precipitation Method

The co-precipitation technique is probably the simplest, easily scalable and most efficient chemical pathway to obtain magnetic nanoparticles with a good control in size, shape and uniformity. Iron oxides, either Fe_3O_4 or γ-Fe_2O_3 are usually prepared *via* the Massart method[85] by aging appropriate stoichiometric ratios of Fe^{2+} and Fe^{3+} salts in an aqueous basic media (usually NH_4OH or NaOH). Usually hydrolysis of ferric ion (solvated cations) will occur with the formation of oxo-ligands.

$$Fe^{2+} + 2Fe^{3+} + 8OH^- \longrightarrow Fe_3O_4 + 4H_2O$$

The magnetic nanoparticles thus produced are spherical, homogenous in size and shape, hydrophilic and negatively charged in an alkaline medium. Their yield, size, stability and polydispersity depend on many factors: the addition of the base, pH value, nature and concentration of the counterions, and Fe^{3+}/Fe^{2+} ratio. According to the thermodynamics of this reaction, complete precipitation of Fe_3O_4 in the presence of a base should be expected at a pH (~10-14), with a stoichiometric ratio of (Fe^{3+}/Fe^{2+} 2:1) under nitrogen. It was observed that purging nitrogen not only protects against oxidation of the magnetite to maghemite but also reduces the particle size. An increase of the mixing rate also tends to *decr*ease the particle size. Synthesis under vigorous stirring results in the *formation* of small particles by reducing their tendency to agglomerate. In the

same way, a decrease of the size and polydispersity is noted when the base is added to the salt mixture as compared to the opposite process. Moreover, the size is strongly dependent upon the acidity and the ionic strength of the precipitation medium. The higher the pH and ionic strength, the smaller the particle size and size distribution will be. These parameters determine the chemical composition of the crystal surface and consequently the electrostatic surface charge of the particles. The shape variation is also related to the variation of the electrostatic surface density of the nanoparticles.

In an alkaline medium of pH>8, polarizing or highly charged cations or anions, such as ammonium or alkaline may give rise to flocculation (the process by which NPs clump together). The addition of chelating organic anions (i.e. carboxylate ions such as acrylic or oleic acid) or surface complexing polymers (e.g. dextran, polyethylene glycol (PEG), polyvinylpyrrolidone (PVP), polyglutamic acid (PGA), or polyvinyl alcohol (PVA)) during the formation of magnetite can help control the distribution, size and stability of the nanoparticles.[86] According to the molar ratio between the organic ion and the iron salts, the chelation of these organic ions on the iron oxide surface can either prevent nucleation and then lead to larger particles or inhibit the growth of the crystal nuclei, leading to small nanoparticles. Ideally, the coating does not only protect and stabilize the core but also makes the nanoparticles biocompatible and make this method especially appropriate for *in vivo* applications.[30, 87]

Magnetite nanoparticles can also be stabilized with silica, especially aminosilanes, to form well-dispersed magnetic silica nanospheres.[88-91] An

advantage of silica coating is the established surface chemistry for silica surface modification. The surface hydroxyl groups can be chemically modified to afford different bio-conjugation groups, such as amines and carboxylates.[92] The size of the particles can be controlled by changing the silica/iron oxide ratio.[88] Surface functionalization of MNPs is extremely important not only for stability purposes, but also to increase the targeting-proficiency. Finding means to control the size while maintaining stable suspensions is the subject of intense study.

2) Thermal Decomposition Method

Several researchers report the use of elevated reaction temperatures and suggest its significance in optimal crystal formation and hence higher magnetization. Different studies show that enhanced uniformity with better size distributions occur at high temperatures. The investigations support the theory of nucleation and growth of the particles that will be discussed in the upcoming section.

Among the many available methods, thermal decomposition of organometallic compounds (iron-oleate complex) in high-boiling-point nonpolar organic solvents (benzyl ether) has proven to be an attractive route for the synthesis of highly monodispersed nanocrystals with high yield, uniformity, good crystallinity and reproducibility. Hyeon et al. first synthesized superparamagnetic maghemite γ-Fe_2O_3 nanocrystals *via* a high-temperature aging of iron-oleic metal complex using iron pentacarbonyl ($Fe(CO)_5$) in the presence of oleic acid at 100 °C (cited by more than 530 publications).[83] In 2004, instead of using the toxic and expensive $Fe(CO)_5$, they reported the elegant ultra-large-scale synthesis of

monodispersed nanocrystals *via* thermal decomposition of metal-oleate precursors in high boiling solvent **(Figure 1-4)**.[93]

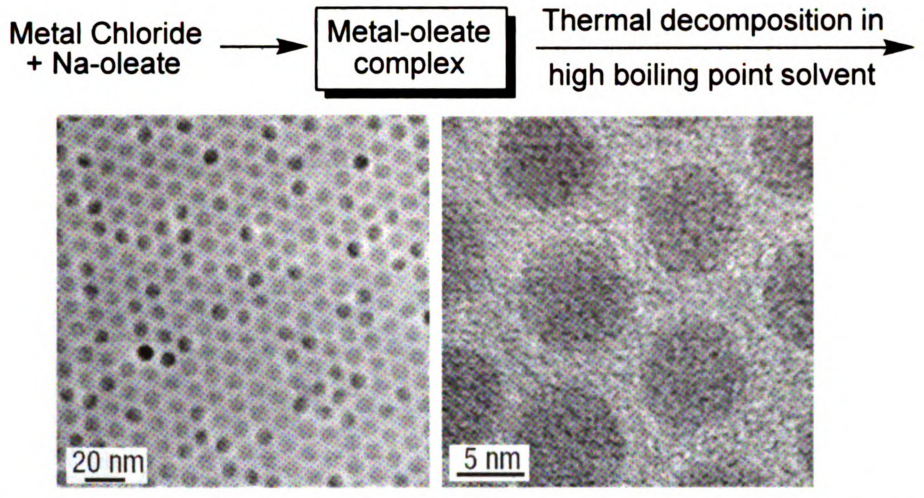

Figure 1-4. Synthesis of highly crystalline monodispersed nanocrystals *via* thermal decomposition of metal-oleate complex; TEM images of 9 nm iron oxide nanocrystals.[93]

Later, Sun et al. reported the synthesis of highly monodispersed magnetite Fe_3O_4 nanoparticles (cited by more than 450 publications) from a high-temperature (200-300 °C) 1,2-hexadecanediol solution of iron(III) acetylacetonate ($Fe(acac)_3$) in the presence of oleic acid and oleylamine **(Figure 1-5)**.[27] Metal ferrites (MFe_2O_4, where M=Co, Fe, Mn, etc.) were also synthesized in the form of monodisperse cubic and spherical nanoparticles by the seed-mediated growth process using $Fe(acac)_3$ and $M(acac)_2$ as reactants.[82]

3) Ligand Exchange

Despite its success, high-temperature thermolysis typically produces nanocrystals with hydrophobic surfaces and hence only dispersible in nonpolar organic solvents. The resulting insolubility in water greatly limits their biological

applications. It is therefore of great importance to find an effective approach to tune their solubility and make them fully dispersed in aqueous media. One of the most popular methods is "ligand-exchange",[94] where the hydrophobic chains on the particle surface are replaced by molecules containing polar groups.

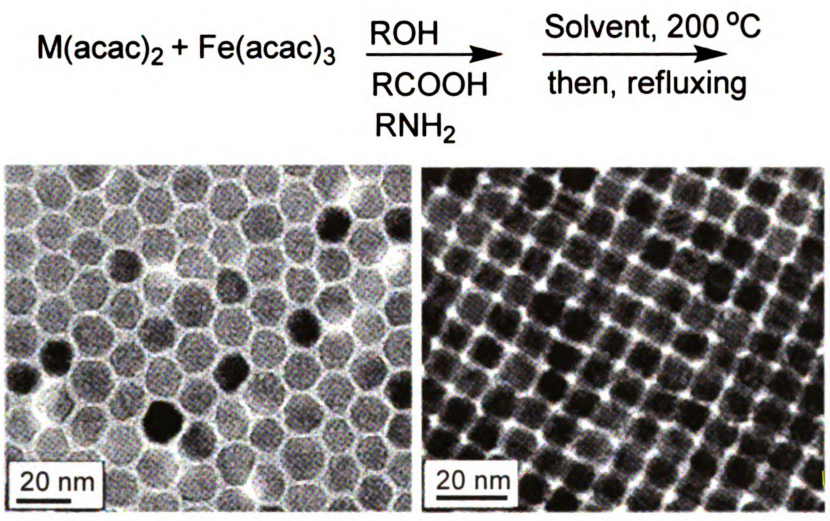

Figure1-5. Synthesis of highly crystalline monodispersed nanocrystals *via* thermal decomposition of $Fe(acac)_3$ in benzyl ether; TEM images of 10-12 nm Fe_3O_4 nanoparticles.[82]

At room temperature, the exchange ratio is typically low, leading to irreversible desorption of the new surfactants from the particle surface destabilizing the system and resulting in subsequent aggregation. Moreover, the efficacy of exchange is usually not that high (hydrophobic surface ligands are not fully exchanged). As a result the nanoparticles will not be fully dispersed in water and precipitation might occur. Indeed, surface modification by ligand-exchange is usually more complicated due to the dynamic nature of the outer layer coating and the different stabilization factors that will be discussed later. That's why researchers tend to use amphiphilic[65] or tri-block polymers[29] or further stabilize the polymer layer through cross-linking,[95] making it well-suited for subsequent

chemical modification. Here, it is worth mentioning that we explored a robust ligand-exchange method that will be discussed in Chapter 4.

1.6.c. Mechanistic Insights

Although there are numerous reports on the synthesis of iron nanocomposites, little on the understanding of the synthesis mechanism and control of uniformity are present.

Crystal growth typically follows an initial stage of either homogeneous (without the influence of foreign particles) or heterogeneous (with the influence of foreign particles) surface-catalyzed nucleation. The creation of a nucleus implies the formation of an interface at the boundaries of a new phase. In a homogeneous nucleation, a short single burst occurs when the concentration of constituent species reaches critical supersaturation. Then, the nuclei are allowed to grow uniformly by diffusion of solutes from the solution to their surface until the final size is attained. To achieve monodispersity, these two stages must be separated and nucleation should be avoided during the period of growth. For heterogeneous nucleation, the seeded-growth technique is effective in providing good size-controlled nanocrystals. Here, the uniformity of the initial nanocrystal seeds determines the monodispersity and uniformity of the final product. Indeed, mechanistic studies indicate that both heterogeneous and homogeneous nucleation followed by growth can lead to the formation of monodispersed nanocrystals.

As mentioned earlier, thermolysis in a high boiling-point solvent can result in the controlled synthesis of monodisperse nanocrystals. This involves a burst of

homogeneous nucleation followed by a diffusion controlled growth process. Recently, a detailed study of the shape control and formation mechanism of monodisperse magnetic ferrite (MFe_2O_4) produced by thermolysis has been investigated.[96] Researchers were able to reproducibly control the shape and the size of the nanocrystals by varying three conditions: a) concentration of precursors, b) heating rate and c) aging time. In brief, for reaction temperatures ~ 250-320 °C, the nucleation and growth dynamics dictate the size and shape evolution of the nanocrystals. Prenucleation of MFe_2O_4 occurs at ~ 250-300 °C but without any growth of nanocrystals. Heating between 300-320 °C, results in homogeneous nucleation. Moreover, the shape of MFe_2O_4 nanocrystals can be reproducibly controlled by prolonging the aging time at 320 °C. Practically, mixing can be done in 2 means: Rapid addition of reactants into a preheated hot solvent (high degree of supersaturation), or heating the reactants premixed with the solvent gradually (careful control of the heating rate). Both ways can help control the degree of supersaturation. The point is to accomplish a homogeneous nucleation separated from the growth process.

1.6.d. Colloidal Stability

"Dispersion or Colloidal Stability" is one of the most important factors that dictate the fate of nanoparticles in aqueous and physiological conditions. "Bare" iron oxide nanoparticles are not stable in water at neutral pH or in physiological fluids, tending to aggregate and precipitate quickly. Nanoparticles are likely to agglomerate in order to reduce their surface energy by strong magnetic dipole-dipole attractions between particles. Thus, either steric or electrostatic

stabilization is required to ensure stable aqueous dispersions which are usually achieved by different range of functionalities. Hence, colloidal stability is directly correlated to polymer or surfactant coating grafted on the iron oxide core. Indeed, stability has been a major topic of study, and there is still much to be understood concerning the origin and nature of interparticle and intraparticle forces and how they affect coagulation in dilute dispersions.

At the nanoscale dimensions, nanoparticles exhibit different properties from their bulk where forces of a different nature become significant: attractive long-range van der Waals (vdW) interactions, repulsive short-range interactions (steric stabilization) and electrostatic forces. The overall effect of the three forces buffers the particles against irreversible aggregation or adsorption to surfaces.

To produce stable nanoparticle dispersions, surfactants which provide control over the forces, miscibility and steric repulsion must be employed. This repulsion is largely entropic in nature, countering for long-range vdW attractions, and highly dependent on the chain and its mobility. Unfortunately, metal nanoparticles typically have facets which encourage surfactants to assemble into closed-packed domains, resulting in low chain mobility where short-range steric repulsion is overwhelmed by vdW attractive forces. This leads to poor control over dispersion stability and particle aggregation. Entropic steric repulsion can be greatly increased by modulating the nature and density of the surfactant or polymer. Two dispersant qualities for an ideal choice of a polymer are: a) polyvalent hydrophilic groups for adsorption to nanoparticle surface; b) hydrophobic linkers intercepted by hydrophilic cationic or anionic groups to

ensure high degree of configurational freedom, which translates into effective entropic steric repulsion in addition to adequate electrostatic repulsion regardless of the molecular packing density on the nanoparticle surface.

The role of polymers on stability is more complicated than electrostatic or steric stability due to many other factors such as solvent effects and polyelectrolytes present. In brief, there is a combination of electrostatic effects as well as effects that arise from the polymeric nature of the additive; this combined effect is referred to as electrostatic stabilization. Moreover, as mentioned earlier there is steric stabilization since the polymer molecules are adsorbed or anchored on the particle surfaces. As a rule of thumb, the higher the potential at the surface of a particle, the larger the repulsion between the particles, the more stable the colloid is.

1.6.e. Characterization of MNPs

An important challenge in the area of nanomaterials is the ability to characterize the structure of the capping agents on the surface of NPs. Identifying the size, shape, charge density, surface functionalities and getting deeper insights into the structural properties and hence the behavior of iron oxide nanoparticles would not have been possible without the following powerful characterization techniques. The following techniques are used to study the structure and organization of different organic/inorganic materials on the surface of NPs.

1) Transmission Electron Microscopy (TEM)

TEM is the most common technique used to examine the size of the crystalline core, the morphology and shape of nanoparticles. TEM is used because of the limited image resolution in light microscopes imposed by the wavelength of visible light. Electrons have wave-like characteristics, with a wavelength substantially less than visible light. TEM visualize objects using thin beam of rapidly moving electrons that encounter a specimen where the accelerated emitted electrons can be absorbed, scattered or transmitted. Because different regions of sample are variously transparent to electrons, different amount of electrons with changed energies pass through these region. This difference is responsible for the contrast. Since electrons are smaller than atoms, TEMs are capable of resolving atomic level detail.

2) Thermogravimetric Analysis (TGA)

TGA registers the loss or gain in weight of immobilized ligands or polymers (organic constituents) of a nanocomposite during heating. The variation in weight as a function of temperature is recorded showing how much of the organic substance is lost from the composite material. The change in weight of an untreated nanoparticle would be compared to that of a coated nanoparticle, which can then be used to calculate the average number of functionalized molecules on the surface of the metal core.

3) Fourier Transform Infrared (FT-IR)

In infrared spectroscopy, radiation energy is absorbed by organic molecules and converted into energy of molecular vibration. There are 2 types of molecular vibrations, stretching and bending. Only those vibrations which result in a change in the dipole moment of the molecule are observed in IR. Although IR is useful to characterize organic molecules functionalized on nanoparticles and gives qualitative information about the functional groups, however it remains difficult to fully identify the structural information of the functionalized ligand. Thus, other spectroscopic methods are necessary for accurate characterization.

4) High-Resolution Magic Angle Spinning (HR-MAS) NMR

A major hurdle in magnetic nanoparticle biofunctionalization is the ability to elucidate the chemical structure of the anchored organic ligands on the surface of the particles. Nuclear magnetic resonance (NMR) is a powerful tool if properly utilized to obtain detailed structural analysis of surface ligands on nanomaterials. However, study of ligands on magnetic materials by ^{1}H-NMR is difficult due to large broadening effects caused by the paramagnetic particles that produce field inhomogeneity. However, relatively sharp NMR resonances are possible by the use of high-resolution magic angle spinning NMR. HR-MAS NMR enables the fine-structure-resolved characterization of complex organic molecules bound to magnetic nanocomposites by strongly decreasing the effects of paramagnetic disturbances.[97] Compared to conventional probes, in HR-MAS it is possible to work with considerably higher concentrations, thus avoiding the loss of structural information.

5) Dynamic Light Scattering (DLS)

DLS also known as quasi-elastic light scattering, is a technique used widely for particle size and size distribution studies. DLS measures the *overall hydrodynamic size* (diameter of core spheres with their adsorbed and solvated coating materials) of the nanoparticles in suspension or aqueous media. This is different from TEM that measures only *the core size* (diameter of the core in its dried form). DLS is based on the Brownian motion of spherical particles which causes a Doppler shift of incident laser light. The average solution particle sizes are calculated by monitoring the diffusion characteristics of the nanoparticles in solution. Moreover, DLS can tell us about the dispersity and size distribution of the particles. Measurements of the nanoparticle may be taken in growth media or serum and tell more about the behavior of the particles in various salt concentrations. It is worth mentioning that nanoparticles can agglomerate in saline environments due to the reduction of the protective surface charge known as the electric double layer that surrounds the surface.

6) Zeta Potential

Zeta potential (ξ) is the electric potential difference between the outer dispersion medium and the fixed layer attached to the dispersed particle. Each particle dispersed in a solution is surrounded by oppositely charged ions that are strongly bound (fixed layer), and an outer diffuse cloud-like area (diffuse double layer) with varying compositions of ions of opposite polarities. When a voltage is applied to the solution, particles are attracted to the electrode of the opposite polarity, accompanied by the fixed layer and part of the diffuse double layer, or

their internal side of what is known as the "sliding surface". Zeta potential is considered to be the potential of this inner area. The magnitude of the zeta potential gives an indication of the potential stability of a colloidal system. If the particles have relatively large negative or positive zeta potentials ($\xi \approx$ -30 mV or +30 mV), they will repel each other and create dispersion stability. If the particles have low zeta potential values ($\xi \sim 0$ mV), there is no force to prevent the particles from agglomerating, which can lead to dispersion instability. It is worth mentioning that among the most important factors that affect zeta potential are pH and salt concentrations. A zeta potential value without a quoted pH or a specified media is a meaningless number.

1.6.f. Applications of MNPs

Biomedical applications of magnetic nanoparticles can be classified according to their application inside (*in vivo*) or outside (*in vitro*) the body. *In vivo* applications includes diagnosis (detection and imaging) and therapeutics (hyperthermia, gene and drug-delivery), while the main use of *in vitro* applications is in diagnosis (detection and bio-separation).

Potential *in vitro* applications employ magnetic nanoparticles with appropriate surface-functionalization by selectively binding the particles to species of interest and placing them under a magnetic field thus separating them from other species. The advantage of using magnetic nanoparticles over magnetic microparticles for such applications is that magnetic nano-suspensions are stable against sedimentation in absence of an applied magnetic field and are removable when magnetic field is applied. Moreover, unlike larger microbeads,

the small dimensions of NPs present minimal steric hindrance to reactants in solution for accessing the active sites of the bio-target. Thus, magnetic nanocrystals can have great impacts in bioseperation, sensing and biomedical applications.

Areas of *in vivo* applications include, but are not limited to, drug and gene delivery,[98] imaging *via* MRI,[99] and hyperthermia.[100] Several reports have been published on the use of MNPs as nano-carriers for such applications.[78, 101] Iron oxide nanoparticles can serve as efficient contrast agents because they have high magnetic moments and can therefore be used at very low concentrations. When coated with hydrophilic polymers, magnetite can be coupled to targeted molecules like antibodies, polypeptides, and carbohydrates that offer the promise of targeting specific organs within the body. Iron oxide nanoparticles hold great promise as nano-vehicles for targeting, imaging and delivering drug in one package, thus revolutionizing medicine.[102-104] In fact, several groups demonstrated the promising biological applications of MNPs. For example, Weissleder et al. showed that MNPs can be used for monitoring specific enzymes and detecting biomolecules such as viruses.[73, 74, 105-107] Cheon et al. reported the use of multifunctional magnetic nanocrystals to detect cancer *in vivo*.[108] Willner et al. demonstrated that magnetic nanoparticles can act as a magnetoswitch to induce selective bio-electrocatalysis, detect cancer, and amplify DNA detection.[68] The above studies and other explorations verify the potential of magnetic nanoparticles in life science, as summarized in several authoritative reviews[2, 86] mentioned earlier.

As shown from the above examples and discussions, the ability to control the size, shape, chemical composition, linker chemistry, and surface properties of the nanocrystals is critically important because it determines the performance of the nanomaterials in biological applications. Specifically, Sailor et al. have demonstrated that factors such as targeting ligand density, targeted-receptor nature, and nanoparticle shape evidently affect the extent of tumor-targeting efficacy.[103] It was found that the *in vivo* tumor-targeting ability in xenograft models of human tumors of elongated nanoworm is superior to that of the nanosphere (shape effect). Moreover, the smaller, neutral targeting ligand is more effective in tumor-targeting and has longer blood half-life than the larger, positively charged molecule (chemical composition), and that incorporation of a 5-kDa PEG linker improves targeting to tumor types relative to a short linker (linker chemistry). It is also well known and proved that uptake of nanoparticles into a wide variety of cells *in vivo* and *in vitro* is largely dictated by the size of the particles.[109-111] Moreover, surface modifications (positively or negatively charged) with polymers, peptides, proteins or carbohydrates enhance this uptake. Positively charged NPs bind to the negatively charged cell membranes *via* electrostatic interactions and are then internalized, while negatively charged NPs are uptaken by either receptor-mediated endocytosis or diffusion.[112]

1.7. Glyco-nanoparticles for *in vitro* and *in vivo* Detection

Despite the clinical success of iron oxide dextran-coated nanoparticles as MRI contrast agents for enhancing the T2 relaxation times, glyco-nanoparticles where the functionalized-carbohydrate plays a key role in recognition event rather than in stabilizing phenomenon have not been extensively studied in many biological and medical applications. Here, a number of important examples of sugar-coated NPs used for *in vitro* or *in vivo* applications will be discussed.

1.7.a. Magnetic Iron Oxide Glyco-nanoparticles

1) *In vitro* Detection:

Syková et al. showed that mannose-modified iron oxide NPs are efficient probes for labeling living cells particularly stem cells.[113] They showed that mannose modified-NPs crossed the cell membranes and were internalized well by rat bone marrow stromal cells. Yan et al. used mannose-functionalized iron oxide NPs prepared *via* photochemically activated phosphate perfluorophenylazides (PFPAs) coupling chemistry and showed by TEM that when the NPs were treated with *E. coli* strain ORN178, they selectively bound to the FimH lectin on the bacteria.[114] We observed similar phenomenon where we explored the utilization of MGNPs not only to detect *E. coli* bacteria but also calculate the capture efficiencies (~ 88% bacteria was removed). Here, it is worth mentioning that Iyer et al. immobilized biotinylated mannose conjugates on magnetic beads to capture and detect *E. coli* and compared them to antibody-coated beads.[19] They observed that the glyco-beads were better than their antibody-counterparts in both sensitivity and selectivity. Capture efficiencies of

~ 20-35% were observed with glyco-beads compared to only ~ 5-15% with antibodies, depending on the *E. coli* concentration (10^5-10^7 colony-forming unit (cfu)/mL) respectively. This is likely due to the smaller size of the glycoconjugate, which can result in better packing density on *E. coli* and thus binding. This fact was clearly demonstrated in our experiments where the exceptionally small sizes of MGNPs enhanced both sensitivity and selectivity of biosensing to yield capture efficiencies as high as ~ 88% (discussed in details in Chapter 2).

Moreover, Pieters et al. detected a gram-positive pathogenic *Streptococcus suis* bacteria known to bind to galabiose (Galα1,4Gal) using biotinylated sugars coated on 250 nm magnetic streptavidin-particles.[115] Using a luminescence assay that quantifies the bacterial ATP, monovalent and tetravalent galabioside-functionalized particles yielded strong signals (mono >> tetra) with a detection limit in the order of 10^4 bacteria/mL, whereas GlcNAc-coated particles yielded no signals indicating the galabiose recognition specificity. Importantly, experiments with larger magnetic particles (diameter ~10 mm) did not enable successful bacterial detection which pinpoints the importance of the much larger surface area of glycoparticles in detection.

Park et al. reported the fabrication of highly colloidal HA-DN (hyaluronic-dopamine)-coated superparamagnetic iron oxide nanocrystals as target-specific MR imaging vehicle and showed that the cellular uptake of HCT116 overexpressing CD44 was greatly enhanced compared to the low expressing NIH3T3 by measuring relative relaxation rates.[116] Mohapatra et al. reported the synthesis of HA-Fe_2O_3 hybrid nanocomposites *via* electrostatic interactions of oil-

in-water HA nanoemulsion and Fe_2O_3 nanoparticles and showed their effectiveness in delivering encapsulated atrial natriuretic peptides to the nuclei of A549 and HEK293 cells overexpressing CD44.[117]

2) *In vivo* Detection:

Cho et al. reported the synthesis of polyvinylbenzyl- *O*-β-D-galactose-D-gluconamide (PVLA)-functionalized superparamagnetic iron oxide nanoparticles (SPIONs) and demonstrated their utility to be targeted specifically into liver *via* the ASGP-R receptor, a galactosyl binding asialoglycoprotein, expressed predominantly on hepatocytes.[118] Galactose and galactosamine are known to accumulate selectively in the liver *via* ASGP-R receptor leading to hepatocyte necrosis.[119] In fact, *in vitro* studies showed time-dependent uptake of PVLA-SPIONs into the cytosol and cell membrane of hepatocytes, suggesting a receptor-mediated endocytosis.[118] *In vivo* MR images of rat liver indicated that the PVLA-SPIONs accumulated predominately in the liver compared with control nontargted pyrrolidone-SPIONs (T2 signal drop 75 % *vs* 36 %), which suggests their potential utility as liver-targeting MRI contrast agent (**Figure 1-6**).

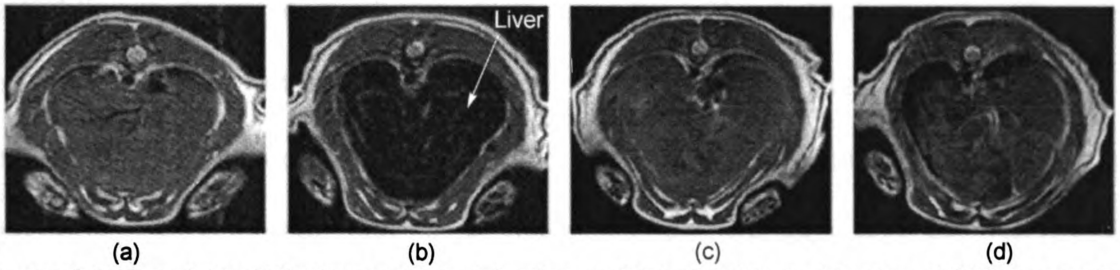

Figure 1-6. T2-weighted MR image (a) preinjection and (b) after 1-hour injection of PVLA-coated SPIONs; (c) pre- and (d) post-injection of pyrroridone-coated SPIONs. Significant signal drop (darkening) of liver compared to control pyrroridone-coated SPIONs.[118]

Davis et al. demonstrated the use of glycan sialyl Lewis^X (sLe^x) functionalized iron oxide coated-nanoparticles (NP-sLe^x) to specifically target

CD62 protein.[66] The carbohydrate-binding transmembrane proteins CD62E (E-selectin) and CD62P (P-selectin) are important in recruiting leukocytes to sites of inflammation and are up-regulated on the activated brain endothelium in response to injury. Specific visualization of the early-activated cerebral endothelium using magnetic NPs, thus, provides a unique tool for the pre-symptomatic diagnosis of brain disease and evaluation of new therapies. To this end, selectin expression on activated endothelium in the brain was induced by microinjection of interleukin-1β (IL-1β) followed by the systematic injection of NP-sLe^x (4 mg Fe/kg) in a rat model. Direct targeted detection of endothelial markers E/P selectin (CD62E/CD62P) in acute inflammation was observed *via* MRI. The resulting sensitivity and binding selectivity of GNPs, displaying multiple copies of the natural complex glycan ligand of selectins sLe^x, allowed acute detection of the disease in mammals with beneficial implications for treatment of neurological disease.

1.7.b. Gold Glyco-nanoparticles

Gold nanoparticles (AuNPs) exhibit several significant features: straightforward simple synthesis, high reproducibility, exceptional stability, and excellent optical and surface plasmon enhanced properties. Such properties make them well suited for applications in imaging, sensing, biology and medicine and thus hold potential promise in diagnosis, therapeutics and targeting.[31] As mentioned earlier, the optical properties of metallic nanoparticles depend on their size, shape, composition, structure, and morphology. Due to the novel properties at the surface of gold nanomaterials, absorption and scattering of

electromagnetic radiation by such nanocomposites are strongly enhanced.[120] Gold nanocomposites, including nanospheres, nanorods, and nanoshells (size ~ 10 to 100 nm) have large light absorption and scattering cross section in the SPR wavelength regions.[31] The magnitude of light scattering and emission by such nano-gold materials can be orders of magnitude higher than that from strongly fluorescing dyes.[121] Basically, the light that is absorbed and emitted by metallic nanoparticles depends on the nanoparticle diameter and its aspect ratio. The aspect ratio is defined as the ratio of length divided by the width of a nanocomposites (spheres have an aspect ratio of 1). Moreover, the shape and crystallographic facets are the major factors in determining the optical and surface properties of such particles. By changing the structure of the gold nanocomposites from a sphere to a core-shell (silica-gold)[122] to a hollow cage[123] to a rod,[121] the optical extinction wavelength shifts from the visible to near-infrared region (NIR) (650–900 nm). Such structural and compositional tuning is quite useful in potential *in vivo* applications where tissue absorption in NIR window is minimal. All these important properties lead to the design of gold nanoagents for optical detection, molecular and cell imaging, and photothermal therapy and *in vivo* targeting.[32, 124] For potential clinical trials, it is necessary to understand their potential risks to human health. Although the noncytotoxicity of gold nanoparticles in human cells has been studied in details,[125-127] it is difficult to predict how toxic nano-golds will be at certain doses for clinical endpoints.

Although the synthesis of gold nanospheres is dated back to 1857 by Faraday[128] and their use as contrast agents for biological electron microscopy

since the 1970s,[129] deeper insights into the fabrication of colloidal gold nanomaterials with controlled sizes, shapes and properties emerged only recently. Generally, reduction of metal salts, i.e. auric acid ($HAuCl_4$), in aqueous media by reducing agents causes Au^{3+} to be reduced to neutral Au atoms that gradually starts to precipitate to form nm spherical particles upon vigorous stirring. Surfactants, such as citrate, have been utilized as surface stabilizers and/or templates to control the synthesis. When bound to the nanoparticle surface, such molecules can not only decrease the surface energy and control the growth and shape of the particles, but also act as a stabilizer against aggregation. In general, two types of AuNPs, a negatively charge citrate-stabilized gold nanosphere (GNS) and a surface positive charge cetyltrimethyl ammonium bromide (CTAB)-protected gold nanorod (GNR) are commonly synthesized.[130]

Here, the most common, successful and known techniques for the fabrication of gold nanoparticles will be discussed. Of the simplest and most used methods to synthesize GNSs is the one pioneered by Turkevich[131, 132] in 1951 and refined by Frens[133, 134] in 1973. Briefly, it involves the reduction of $HAuCl_4$ by citrate to produce a broad size range spheres (diameters ~ 10 to 150 nm) with low monodispersity (especially for > 30 nm particles). Another widely known approach developed in 1994 is the Brust's method[135] and its variations that yield ~ 2-5 nm gold nanoparticles. Simply, Au ions are transferred to an organic phase mediated by a phase transfer catalyst tetraoctylammonium bromide (TOAB), followed by reduction with strong reducing agent, $NaBH_4$. To prevent aggregation, a stronger binding agent, usually a thiol ligand, is added that

strongly binds gold due to the soft character of both Au and S extensively studied by the Whitesides[136] group. In 1995, Gelbart et al.[137] synthesized gold particles with diameters ranging from 1.5 to 20 nm by varying the Au(III) ion to stabilizer thiol molar ratio. In 1996, Schmid et al.[138] employed a powerful methodology, known as seed-mediated growth (widely used to date), which gives better control over size and shape. Briefly, gold ions are reduced by strong reducing agents to form seeds, i.e. small particles that are then used in the next growth step.[139] In the second stage, the reducing agent is generally mild,[140] reducing only the precursor ions which are adsorbed onto the seed surface without creating any new nucleation center. Since then, extensive studies on the mechanistic insights and controlled-synthetic methodologies of nano-golds by Murhpy et al.[129, 141-145] and El-Sayed et al.[120, 121, 146-149] have been conducted. In 2009, Perrault and Chan[150] reported a well-controlled synthesis of monodispersed gold nanospheres (50-200 nm) with a narrow size and shape distribution using hydroquinone. In this method, hydroquinone is used to reduce $HAuCl_4$ in an aqueous solution that contains gold seeds produced using the citrate method.

GNRs, on the other hand, have unique and improved surface-enhanced Raman scattering properties and electronic properties compared to GNSs.[129] GNRs have the strongest surface plasmon band enhancement among all the different shapes of gold and with suitable aspect ratios can absorb and scatter strongly on the NIR region. Indeed, the use of GNRs for dual molecular imaging and selective photothermal therapy of cancer cells using a NIR low-energy laser have been reported.[124]

In general, rod-shaped metal nanoparticles can be synthesized in either hard templates[151] or in the presence of neutral or charged surfactants.[152] For colloidal GNR synthesis, two main approaches have been widely utilized and are well established: the electrochemical[153] and seed-mediated growth[141] method. Of the two, the seed-mediated growth method is the most popular route due to simplicity, high quality and yield, size and shape control, and flexibility for structural modifications.

Initially, GNRs were mainly prepared by the electrochemical method developed by Wang et al. in the 1990s.[154] Briefly, a gold metal plate anode and a platinum plate cathode are immersed in an electrolytic solution consisting of rod-inducing CTAB cationic surfactant as the major component and co-surfactant TOAB as the minor. The latter surfactant induces the cylindrical shape of the gold nanoparticle and the ratio of the two surfactants roughly determines the aspect ratio of the nanorod. It is worth mentioning that GNSs (~ 12 nm) can be synthesized using the above procedure either by removing the cosurfactant or by increasing the mole ratio of the surfactant/cosurfactant above 6.

Using the seed-mediated approach, Wokaun et al.[155] reported the formation of gold colloids by adding gold nuclei to $HAuCl_4$ growth solutions. The nuclei were formed by reduction of $HAuCl_4$ with phosphorus, and the growth of gold nanorods was initiated with the addition of H_2O_2. In 2001, Murphy et al. reported the most widely known procedure that involves, first, the preparation of small size spherical gold nanoparticles, and second, growth of the prepared spherical particles in a rod-like micellar environment (**Figure 1-7**).[141, 142, 144] In this method,

colloidal gold nanorods were prepared by the addition of citrate-capped gold nano-spheres to $HAuCl_2$ growth solution obtained by the reduction of $HAuCl_4$ with ascorbic acid in the presence of CTAB surfactant with or without silver nitrate ($AgNO_3$). Briefly, three steps are required: (1) **Seed:** synthesis of the seed solution by the reduction of a metal salt, i.e. $HAuCl_4$, with strong reducing agent such as sodium borohydride ($NaBH_4$) in the presence of citrate; (2) **Growth:** preparation of the growth solution using rod-like micellar template CTAB mixed with $HAuCl_4$ and ascorbic acid; and the final step (3) **Seed-Growth:** addition of the seed solution to the growth solution in the presence[143] or absence[141] of Ag ions. In the first step citrate is present as a capping agent to prevent particle growth where the gold spheres thus produced are 3±5 nm in diameter. The seeds then serve as nucleation sites for nanorod growth.

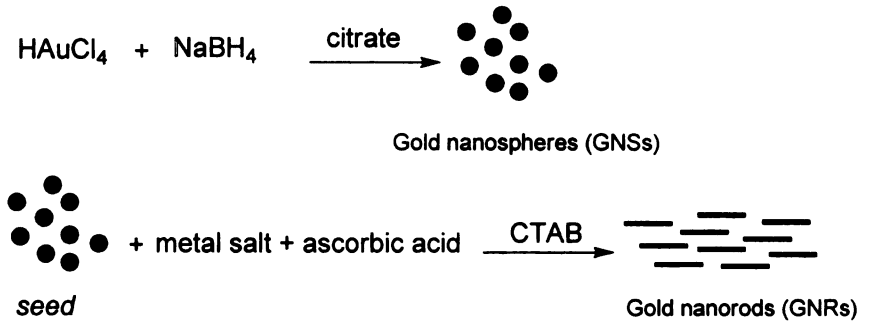

Figure 1-7. Seed-mediated growth of gold nanoparticles.

The aspect ratio is controlled by the ratio of metal seed to metal salt, thus restricting the size to nm regime. It was observed as the amount of seed was decreased, the aspect ratio increased, and the longer wavelength plasmon band gradually red-shifted and broadened. Moreover, with increasing amount of seeds, the overall rate of particle formation increases, and hence the growth rate. In the

absence of seed, particle formation rate is very slow. It is worth mentioning that ascorbic acid is a mild reducing agent and cannot reduce the gold salt in the presence of the micelle without the presence of seed. Consequently, minimal additional nucleation occurs during particle growth. Similar to iron oxide nanoparticle synthesis, in nano-gold fabrication it is also crucial to separate the continuous nucleation throughout the growth process in order to better control the shape and size of the nanocomposites. The disadvantages and limitations of this method, however, are mainly the formation of noncylindrical nanorods and a large amount of spherical particles. Moreover, in all cases, centrifugation and extraction are always performed to separate rods from any spheres that have been formed.

In 2003, modifications to this method have been applied for synthesizing nanorods with aspect ratios of 1.5 to 10 by El-Sayed.[147] For synthesis of pure gold nanorods (99%) with minimal nanospheres and aspect ratios up to 5, the following strategies were employed: (1) replacement of the citrate-capped seed with a stronger CTAB stabilizer in the seed formation step; (2) adjustment of Ag ions concentration of the growth solution to control the aspect ratio (increasing Ag ion concentration increases the aspect ratio); (3) addition of Ag ions to the growth solution before seed addition to facilitate rod formation and tune the aspect ratio. To grow NRs with aspect ratios ranging from 4.6 to 10, a binary surfactant mixture composed of benzyl-dimethylhexadecyl-ammonium chloride (BDAC) and CTAB was used. NRs are grown in this mixture either by aging or by addition of a growth solution suitable to shorter NRs. The yield, monodispersity,

size, aspect ratio and shape of gold nanorods can be controlled by many parameters, such as seed concentration, relative concentrations of gold precursors, ascorbic acid, salts and different surfactants, temperature, pH, purity of additives, solvent, and the aging time.

1) *In vitro* Detection:

a) Studying Carbohydrate-Carbohydrate and Carbohydrate-Protein Interactions

Gold glyco-nanoparticles have been extensively and successfully employed by several groups for studying carbohydrate-protein and carbohydrate-carbohydrate interactions which are the major mechanisms for cell adhesion and recognition. Jesús de la Fuente and Soledad Penadés did elegant work in this field where they prepared carbohydrate-functionalized gold, gold–iron, and semiconductor nanocrystals for studying carbohydrate interactions and investigating carbohydrate-mediated cell–cell adhesion processes. In an early report, Penadés et al. demonstrated the use of either disaccharide lactose (lacto-) or trisaccharide Lewis^X (Le^x-) AuNPs as multivalent ligand carriers for studying Ca^{2+}-mediated carbohydrate interactions.[156] Le^x antigen or lactose was derivatized with an alkylthiol, and AuNPs were prepared by reducing $HAuCl_4$ with $NaBH_4$ in presence of the glyco-thiols. Using TEM, it was revealed that only specific binding between Ca^{2+} and Le^x-AuNPs result in self-aggregation, while lacto-AuNPs did not show any clustering (**Figure 1-8**). Removal of the cations *via* ethylene-diamine tetraacetic acid (EDTA) addition reversed the assembly, proving the specific role of the sugar in inducing aggregation. This ability was

also confirmed by an atomic force microscopy (AFM) study of adhesion forces between Le^x antigens self-assembled on gold surfaces (2D).[157] Furthermore, they reported the quantification of the kinetics of Ca^{2+}-mediated carbohydrate-self interactions *via* SPR by using combination of self-assembled monolayers (SAMs) of alkanothiolates on gold with carbohydrates as the substrate and AuNPs as the analyte.[158] Furthermore, thermodynamic insights using isothermal titration calorimetry (ITC) were also investigated.[159] Their results showed that Ca^{2+}-mediated aggregation of Le^x-AuNPs is a slow process but highly exothermic, while the heat evolved in the case of lacto-AuNPs is very low and its thermal equilibrium is quickly achieved. Measurements in the presence of Mg^{2+} and Na^+ cations did not induce significant aggregation of Le^x-AuNPs confirming its selectivity for Ca^{2+}. All this work demonstrated the highly specific and chief role of carbohydrate-carbohydrate interactions in cell-cell adhesion processes.

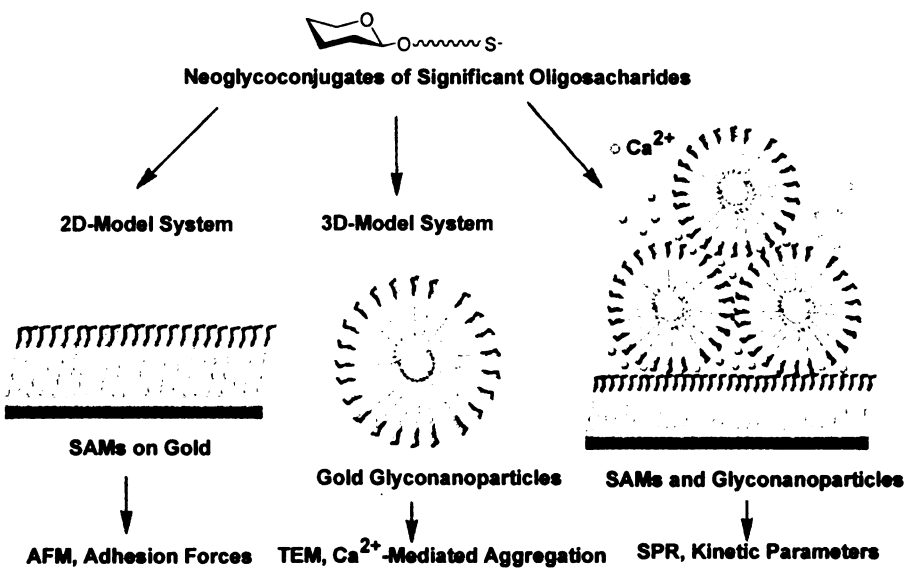

Figure 1-8. Various strategies for studying specific carbohydrate interactions that mimic sugar presentation on the cell surface, thus representing important roles in cell-cell adhesion and recognition.[20]

Lin et al. used SPR to quantitatively analyze the binding affinity of the polyvalent glyco-nanoparticles (mannose- (man), glucose- (glc), or galactose- (gal) AuNPs) with lectin, Concanavalin A (Con A).[160] The dissociation constant K_d of man-AuNPs with Con A was determined to be 2.3 nM, representing a binding affinity over 5 orders of magnitude higher than that of the monomeric mannose. This work quantitatively proves the high affinity and specificity of multivalent carbohydrate-protein interactions. Similar affinities were also observed by Wu et al. where they get K_d values in the nM range.[161] Moreover, Russell et al. demonstrated the utilization of functionalized glyco AuNPs to detect carbohydrate-binding lectins using colorimetric bioassays based on recognition-induced aggregation of the metal nanoparticles.[162]

For studying NP-cell interactions, Penadés et al. reported the preparation of gold and gold–iron nanoparticles[163] functionalized with maltose (malto), glucose and lactose and evaluate their biological effects.[164] Different cellular responses were obtained for each glyco-nanoparticle type depending on the sugar, demonstrating the importance of carbohydrate in cellular-recognition. Incubation with a human fibroblast cell line showed that lacto-MGNP are taken up by endocytosis without provoking apoptosis while malto-MGNP are endocyted and promoted cell death (80 % cytotoxicity). Surprisingly glc-MGNP had a completely different behavior where it was not endocytosed and did not have any effects on cell viability. This result encouraged them to test the possibility of using glc- or lacto- Au/Fe NPs to image an experimental C6 glioma in mice *in vivo* which will be discussed later.

Recently, the same group prepared a small library of multivalent gold nanoparticles functionalized with different structural mimics of the high mannose undecasaccharide of gp120 and evaluated their effect on the inhibition of HIV binding to DC-SIGN expressing cells *via* SPR (**Figure 1-9**).[165] A major mechanism of HIV infection implies the interaction of the virus envelop glycoprotein gp120 with DC-SIGN receptor expressed on dendritic cells. DC-SIGN selectively recognizes endogenous N-linked high-mannose-type oligosaccharide structures $Man_9(GlcNAc)_2$ of the HIV envelop glycoprotein gp120.[166] A highly significant inhibition (~ 20,000-fold more effective in inhibiting DC-SIGN/gp120 interaction) using Manα1-2Manα bearing GNPs (100% inhibition at 120 nM) than with the corresponding monovalent disaccharide (100% inhibition at 2.2 mM), was observed.[165] Moreover, inhibition of gp120-DC-SIGN binding was evaluated in a model using DC-SIGN-transfected Raji B cells.[167] GNPs bearing the Manα1-2Man disaccharide inhibited binding of HIV-1 to DC-SIGN by 85%, while free mannan inhibited binding only by 60%. Moreover, oligomannoside-functionalized AuNPs were able to inhibit the HIV DC-SIGN-mediated trans-infection of PM-1 T cells at nM concentrations. Manα1-2Man-AuNPs were able to inhibit *trans*-infection of PM-1 T cells by HIV-1 by 80%, compared to free mannan, which inhibited binding by 50%. In brief, they showed a successful carbohydrate-based multivalent system that can function as an anti-adhesive barrier at an early stage of HIV-1 infection, prevent viral attachment to DC-SIGN-expressing cells, and subsequently inhibit trans-infection of human T lymphocytes.

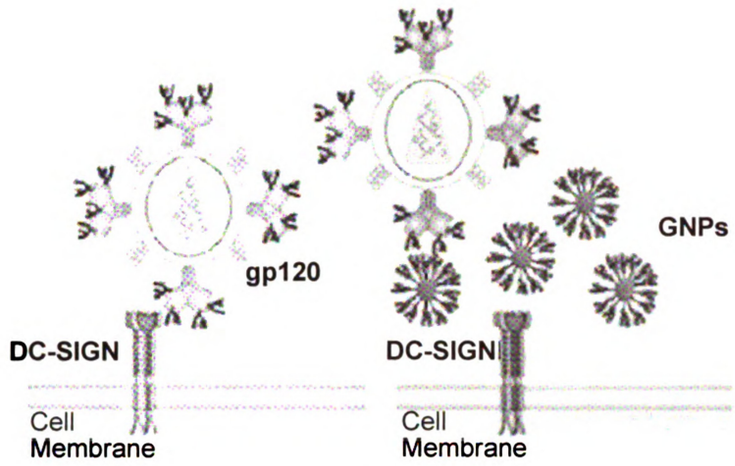

Figure 1-9. Inhibition of HIV binding to DC-SIGN using oligomannoside-GNPs.[165]

In another report, Kamerling et al. grafted sugars on AuNPs to explore carbohydrate-mediated self-recognition events in the marine sponge *Microciona prolifera* and studied their effects on cell-aggregation.[168] They demonstrated the chief role carbohydrates play in the proteoglycan-like macromolecular aggregation factor (MAF) self-aggregation, where they designed water-soluble AuGNPs coated with synthetic sulfated disaccharide fragments related to Glc*p*NAc3S(β1–3)Fuc*p* for mimicking the g-200 self-association. It is known that Ca^{2+}-dependent self-association of MAF occurs through highly repetitive epitopes (Glc*p*NAc3S(β1–3)Fuc*p*) on the g-200 glycan present on the N-glycosylated protein, MAFp3.[169] It was shown that the proteoglycan self-recognition is highly specific and any structural changes in the disaccharide completely disrupt the aggregation phenomenon. Examinations revealed that the stereochemistry, hydrophobic groups on the sugar moiety, the linker type and the presence of Ca^{2+} play an essential role in the specific organization of the sugar moieties. They found that the α-anomeric product, the sulfated disaccharide and the C6

methyl group of L-fucose to have an irreplaceable function in the self-recognition phenomenon.

b) Exploring Pathogen Detection

Pathogenicbacteria, viruses, and other microbes use cell-surface carbohydrates to invade host organisms and to deliver toxins (i.e. cholera toxin and shiga-like toxins). Protein-sugar interactions between the bacteria and the host cell are crucial first step in the infectious process. Multivalent protein-carbohydrate interactions generate adhesive forces where multiple copies of sugar usually provide potential means of strengthening those binding events. Thus instant and ultra-sensitive detection of bacteria using glyco-AuNPs, without time-consuming procedures, such as incubation or amplification by PCR, offers obvious clinical benefits.

At an early stages in this direction, Wu, Chen, Lin and coworkers confirmed the concept of multivalency where they showed the specific binding of mannose-encapsulated gold nanoparticles (man-AuNPs) to FimH adhesin of bacterial type 1 pili in *E. coli* by TEM.[170] That was one of the first examples to demonstrate that carbohydrate-functionalized AuNPs can be used as efficient labeling probe and multiligand carrier in a biological system (Figure 1-10).

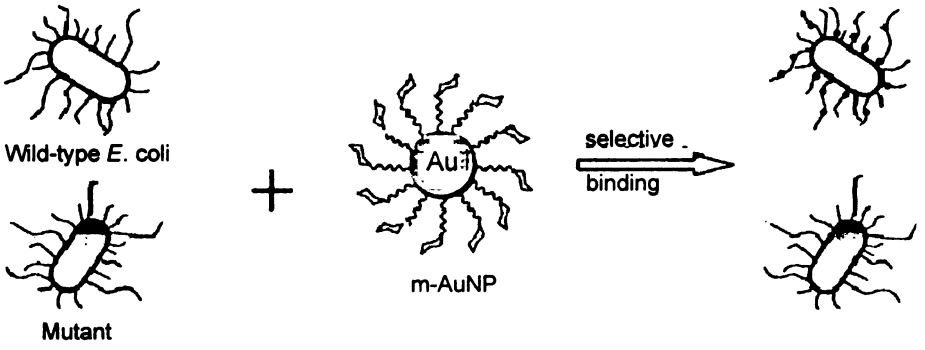

Figure 1-10. Selective binding of man-AuNPs to the wild-type *E. coli* strain ORN178. The mutant ORN208 showed no binding.[170]

Recently, Lin et al. designed AuNPs for Shiga-like toxin detection, separation and inhibition (**Figure 1-11**).[171] As *Escherichia coli* O157:H7 is a chief cause of foodborne illness, the development of a rapid and sensitive detection method of Shiga toxins (Sts), which are produced by the bacterium, is recommended. Sts are a family of AB_5 bacterial toxins which specifically recognizes cell surface glycosphingolipid Gb_3 (globotriaosylceramide) through multivalent binding of the symmetric B-subunit pentamer. The Gb3 glycolipid is known as the globotriose (P^k) blood group antigen or CD77, which contains the trisaccharide αGal(1-4)βGal(1-4)βGlc. Lin and coworkers engineered a globotriose-functionalized gold nanoparticles (P^k-AuNP) that specifically captured the recombinant Shiga-like toxin I (B-Slt) from bacterial cell lysate with > 95% purity while maintaining its activity.[171] They also demonstrated that a 20 nm water-soluble P^k-AuNP is an antagonist for B-Slt and shows >10^8-fold binding affinity enhancement over the monovalent P^k trisaccharide using SPR competition binding assay. Moreover, they developed a Pk-AuNP-based detection method for Slt-I by combining the technique with silver enhancement.

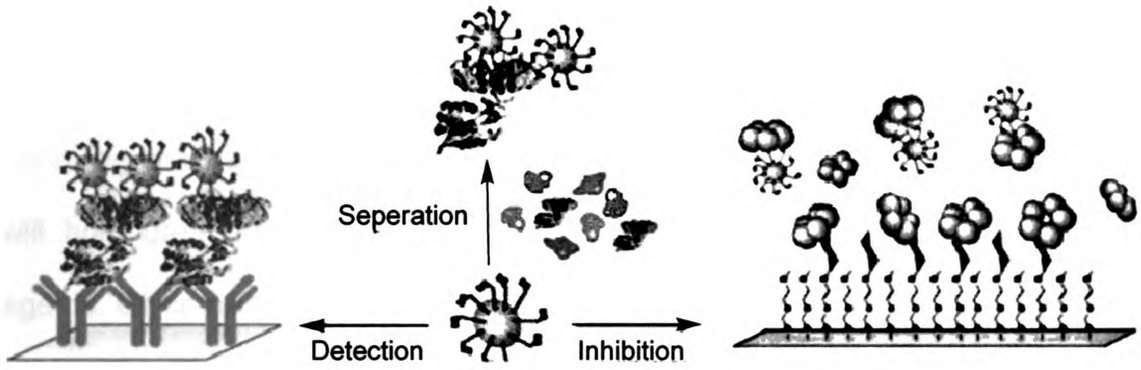

Figure 1-11. Schematic presentation of P^k-AuNPs for detection, separation and inhibition of Shiga-like toxin.[171]

Russell et al. developed a rapid colorimetric bioassay for the detection and quantification of cholera toxin (CT) within 10 minutes.[54] The bioassay is based on lactose-functionalized AuNPs that upon binding to the toxin induces aggregation and subsequent change in color upon surface plasmon absorption measurements. The selectivity of the bioassay stems from the thiolated lactose derivative that mimics the GM_1 (Galβ(1-3)GalNAc[Neu5Acα(2-3)]-β(1-4)Galβ(1-4)Glc-lipid) ganglioside, the receptor to which cholera toxin binds in the small intestine.

In another example, Perez described a quick and high-throughput nanoparticle-based antimicrobial susceptibility assay utilizing the differential changes in the surface plasmon band of dextran(Dex)-coated AuNP upon clustering.[172] Con A-induced clustering of Dex-AuNP yields sensitive and reproducible changes in the nanoparticles' absorption maximums, providing efficient means to sense the presence of available complex carbohydrates in bacterial suspension and hence giving the promise of identification of potential antimicrobial agents within 3 hrs.

c) Investigating DNA Interactions

The study and better understanding of the binding affinity of GNPs and DNA will hold great implications for their potential use as nonviral gene delivery agents. Glyco-nanoparticles are attractive probes for studying the less advanced carbohydrate-nucleic acid interactions and hence creation of DNA-binding systems. Their large surface area, multivalent interactions upon DNA-binding and their cationic ligands grafted onto the NP surface makes them ideal mimics for the naturally occurring protein-nucleic acid interactions. To this end, Penadès el al. reported the interaction of GNPs functionalized with Glc or Gal and amino ending ethylene glycol chains with a linear DNA.[173] TEM, AFM and gel electrophoresis examinations showed that mixed amino/α-Gal (1:1) nanoparticles are highly efficient DNA-binders and condense DNA into a compact globular shape, which is a desired property for gene transfection agents. AFM analysis revealed the presence of free DNA (and free nanoparticles) in the case of α-Gal, β-Glc, amino/β-Gal, and amino/β-Glc nanoparticles, pinpointing the specificity involved in carbohydrate-DNA interactions and calls for an urgent need to better understand the system.

Narain et al. proposed a cationic monodispersed and biocompatible glycopolymer-stabilized gold nanoparticles as an effective gene delivery vehicle that can enhance the cellular uptake by cell-mediated interactions, thus promoting higher transfection efficiencies.[174] The synthesis of cationic gold nanoparticles was achieved using the photoinitiator, Irgacure-2959, where cationic glycopolymers were first synthesized by the reversible addition-

fragmentation chain transfer (RAFT) process and the cationic glyconanoparticles were then produced in one step using UV radiation. It was found that cationic nanoparticles produced undergo receptor-mediated endocytosis due to the glycopolymer following their vesicular escape in Hela cells, due to the net cationic character of the nanoparticles.

2) <u>In vivo</u> Detection:

Penadès el al. reported the utilization of lacto-AuNPs as potent inhibitors of lung metastasis in C57/Bl6 mice and evaluated their potential as anti-adhesive tools against metastasis progression.[175] They showed that short *ex vivo* preincubation of tumoral B16F10 with lacto-AuNPs is enough to substantially inhibit lung metastasis (up to 70%) in a tumor metastasis model (**Figure 1-12**).

Moreover, the same group reported sugar-coated AuNPs combined with Gd(III) chelates as new paramagnetic probes for enhancing the relaxivity for MRI.[176] GNPs have small sizes (2-4 nm) and their carbohydrate-coating make them non-toxic to cells and mice. It was shown that sugar (glc, gal or lacto) stereochemistry and the relative position of the sugar with respect to the Gd ion seem to control the relaxivity values of these GNPs. Sugars may create specific interactions with water that bring water protons in the proximity of the metal ions favoring the water exchange with the bulk solvent.

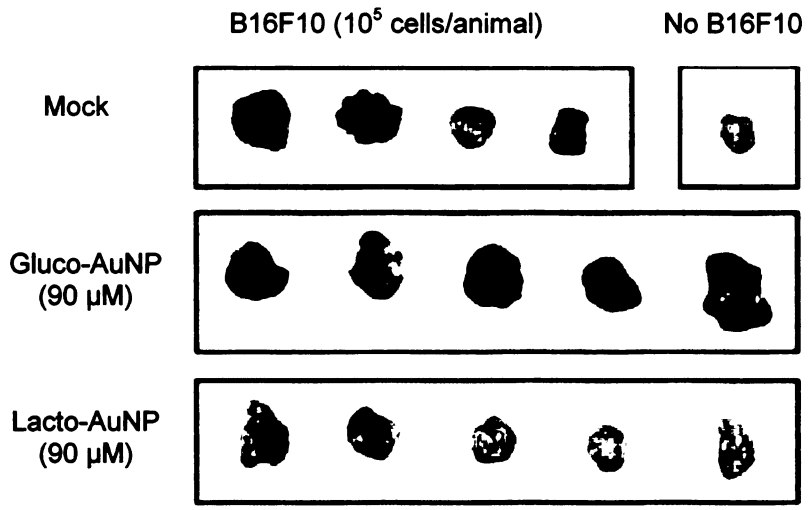

Figure 1-12. Specific effect of lacto-AuNPs on the metastatic potential of B16F10 to induce lung tumoral foci upon intravenous (i.v.) inoculation in C57/Bl6 mice. A positive control group was injected with a single dose of B16F10 melonoma cells (10^5 cells/animal). Other groups were treated with single doses of B16F10 melanoma cells (10^5 cells/animal), preincubated for 5 min at 37 °C with 90 μM of the control gluco-GNPs or with 90 μM of lacto-GNPs. After three weeks, the animals were sacrificed, and lungs were evaluated under a microscope for tumor foci analysis. Inspection of lungs inoculated with B16F10 cells pretreated with lacto-AuNPs showed a strong protective effect against lung metastasis (~ 70 % inhibition) in contrast to those obtained from animals primed with B16F10 cells or B16F10 cells pretreated with gluco-GNPs.[175]

In vivo imaging of glioma (generated with GL261 tumoral cells) in mice indicates that at the same Gd(III) concentration gal-GNPs were able to enhance the contrast in the tumoral zones better than lacto-GNPs or the clinically used contrast agent, magnevist proving the specificity of sugar targeting. Indeed, it is known that the asialoglycoprotein receptor which is expressed exclusively in hepatic parenchymal cells binds specifically to galactosyl-terminal glycoproteins, which might explain the difference in the enhanced relaxivity.

1.7. c. Glyco-Quantum Dots

1) *In vitro* Detection:

Less work has been done in the area of functionalizing quantum dots (QDs) especially when it comes to *in vivo* applications due to the potential toxicities of QDs. However, *glyco-quantum dots* present an advance that could help tap the much-heralded potential of QDs in the treatment of diseases. QDs are nanocrystals that glow when exposed to light. In comparison with organic dyes and fluorescent proteins, QDs have unique optical and electronic properties: size-tunable light emission, high quantum yield fluorescence, improved signal brightness, resistance against photobleaching, and simultaneous excitation of multiple fluorescence color.[29, 177] QDs protected with polysaccharides were reported in 2003 by Rosenzweig et al.[44] This group prepared CdSe-ZnS QDs protected with carboxymethyldextran and polylysine, and they proved the high affinity of dex-QDs toward the glucose binding protein, Con A. Along the same lines, Chaikof et al. reported the site-specific labeling of streptavidin-QDs with biotinylated end-terminated functionalized glycopolymers and demonstrated their potential in the specific carbohydrate-lectin binding phenomena using Con A and RCA_{120}, a gal-binding lectin.[178] Moreover, Surolia et al. prepared sugar-QDs for selective and sensitive detection of lectins.[179] Fang et al. have recently reported the labeling of mice, pigs and seaurchin live sperm with CdSe/ZnS core shells QDs functionalized with N-acetyl glucosamine or mannose.[180] GlcNAc-encapsulated QDs were concentrated at the sperm heads, while mannose-coated QDs tended to spread over the whole sperm body, due to the different distribution of the GlcNAc and mannose receptors on the sperm surface. Thus,

they proved that glyco-QDs are potential candidates that can be used as cell labels. Moreover, Kim et al. demonstrated an approach for the rapid and simple detection of protein glycosylation based on the energy transfer between lectin-conjugated AuNPs and sugar-conjugated QD.[181] They also showed the potential of their system in the high-throughput analysis of glycosylation degree, which is critical for the development of protein therapeutics.

2) *In vivo* Detection:

Kim et al. reported the fabrication of water-soluble, biocompatible and size-tunable hyaluronic acid-coated QDs (HA-QDs) where HA is coupled electrostatically to positively charged amines grafted on the surface of QDs.[182] They showed the specific labeling and uptake capability of HA-QDs to effectively target lymphatic vessel endothelial receptor 1 (LYVE-1) overexpressed on lymphatic endothelial cells (LEC) and HeLa cells with low cytotoxicity. Decreased cytotoxicity was significantly observed compared to unconjugated QD-treated cells. Moreover, *in vivo* fluorescent imaging was evaluated where they were able to selectively visualize the changes in lymphatic vessels (lymphangiogenesis) in real-time for days.[182]

Seeberger et al. reported the synthesis of carbohydrate (man, gal, galactosamine (GalN))-capped PEGylated QDs to study specific carbohydrate-protein interactions for *in vitro* applications and *in vivo* targeting.[183] *In vitro*, they showed that Gal- and GalN-capped QDs are selectively uptaken by hepatocellular carcinoma HepG2 cells *via* the ASGP-R receptor, a galactosyl binding asialoglycoprotein, expressed predominantly on hepatocytes. The uptake

was partially inhibited by preincubation with poly-L-lysine galactose polymer or by the knockdown of ASGP-R1 proving that the internalization is *via* receptor-mediated endocytosis. *In vivo*, they demonstrated in a mice study, that Man- and GalN-capped QDs accumulate selectively in the liver but not other parts of the body suggesting a mannose and ASGP-R receptors on Kupffer and hepatic cells respectively. These sugar-coated QDs became three times more concentrated in the mice livers than the regular PEG-QDs, demonstrating their targeting abilities. Furthermore, upon i.v. injection of GalN-capped QDs, a significant increase in serum transaminases (ALT) was observed indicating that liver injury was selectively mediated by GalN-QDs. It is worth mentioning that the same group recently presented an efficient synthesis of carbohydrate-functionalized QDs in micro flow reactors at 160 °C.[184]

In brief, giving QDs an icing-like cap of specific carbohydrates makes these nanoparticles accumulate in certain organs enhancing their effectiveness and decreasing their cytotoxicity. Such particles have the promise of selective targeting that could be used to deliver anti-cancer drugs to one organ, reducing the side-effects that occur with existing cancer drugs.

1.7. d. Glyco-Carbon Nanotubes

Sun et al. reported that single-walled carbon nanotube (SWNT) serves as an excellent scaffold for multivalent carbohydrate ligand display, with the Gal-SWNTs exhibiting strong cell adhesion resulting in efficient capturing of pathogenic *E. coli* in solution.[185] Moreover, they demonstrated that mannose or galactose-functionalized SWNTs represent a unique displaying scaffold for

multivalent monosaccharide ligands that bind effectively to *B. anthracis* spores in the presence of a divalent cation.[186] The binding results in substantial aggregation of the spores and corresponding colony forming units reduction which may potentially find valuable applications in the decontamination and anti-bioterrorism. Bertozzi and coworkers did some elegant work in functionalizing carbon nanotubes with glycopolymers to mimic cell surface proteins and hence study their interface with living cells.[187, 188]

1.7. e. Glyco-Micelles and Liposomes

Aoyama et al. reported that neutral micellar glycoviruses undergo saccharide-dependent self-aggregation and size-dependent cell endocytosis.[189] They prepared calix[4]resorcarene-based macrocyclic glyco-bundle amphiphiles having long alkyl (undecyl) chains and saccharide moieties ranging from cellobiose (Cel), lactose or maltose. Water-soluble glycocluster micellar amphiphilic nanoparticles (GNPs) grafted with the different saccharides were then constructed and combined with size-controlled plasmid pCMVluc DNA (7040 bp) resulting in glycoviral nanoparticles. It was shown that the obtained glycoviruses are small in size (~ 50 nm) with no net charge surface (ξ ~ 0 mV), and undergo saccharide-dependent (α-Glc > β-Gal >> β-Glc) self-aggregation, and transfect cell (Hela and HepG2) cultures via highly size-regulated pinocytic form of endocytosis. Alternation in stereochemistry of glycoside linkage (Mal vs Cel) or single OH group orientation (Cel vs Lac) resulted in drastic change in the adhesion properties of glycoclusters. It was also noted that glycovirus aggregates (>100 nm) are incorporated only slightly in the cells. It was shown that the size

effects in the glycoviral gene delivery allow only monomeric viruses to work effectively and that the activites of oligomeric and poorly active β-Gal-functionalized nanoparticles toward hepatic HepG2 cells are ~ 100 times higher than expected on the size basis, owing to the receptor-mediated specific pathway involving the asialoglycoprotein receptors on the hepatic cell surfaces. In general, they proved that neutral glyco-cluster nanoparticles are efficient in coating DNA where a specific uncharged and highly hydrophilic carbohydrate can prevent the glycoviruses from aggregation, rendering the system an effective gene delivery vehicle.[190]

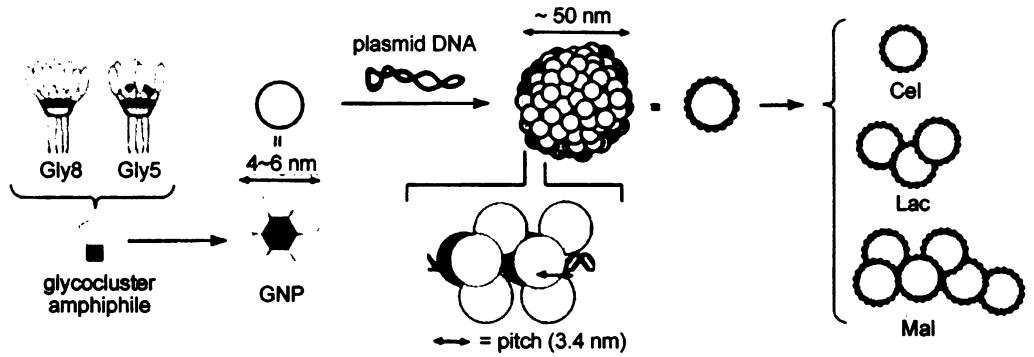

Figure 1-13. Construction of glycovirus. Growth of glycocluster amphiphile Gly8 or Gly5 through GNP to glycovirus and its aggregates.[189]

Later, the same group reported the synthesis of 15 nm ^{TOPO}QD conjugated with glyco calyx-[4]resorcarene based sugars and compared their uptake to the 50 nm sized GNP prepared earlier in an effort to better understand the size-effects on endocytosis.[191] It was shown that ^{TOPO}QD-conjugated sugar ball is taken up by Hela cells *via* endocytosis, but marks endosomes much more efficiently than the micellar homoaggregate of the amphiphile (GNP, 5 nm) and

much less than the virus-like DNA-GNP conjugate (50 nm), respectively. Knowing that all the above nanoparticles are functionalized with the same β-glucoside moiety not only strongly suggests that endocytosis is highly size-dependent (50 nm>> 15 nm>> 5 nm), but also pinpoints the utmost importance of viral-size control in designing artificial delivery vehicles.

Agrawal et al. synthesized HA-poly(ethylene glycol)-poly(lactide-co-glycolide) (HA-PEG-PLGA) polymeric nanoparticles encapsulated with Doxorubicin (DOX) and studied the *in vivo* release of the drug and the corresponding tissue distribution.[192] After intravenous (IV) injection in Ehrlich ascites tumor (EAT)-bearing mice, it was found compared to the control monomethoxy(polyethylene glycol) (MPEG)-PLGA nanoparticles, that HA-PEG-PLGA showed a higher concentration of DOX in the tumor (4-fold higher) with nonspecific uptake mainly in the liver. Moreover, HA-PEG-PLGAs were able to deliver higher amount of DOX in the inhibition studies, and were able to sustain the release for up to 15 days. The nontoxic HA-PEG-PLGAs not only were effective in targeting EAT tumor but also showed long tumor retention times with rapid clearance from normal tissues rendering them good targeted-drug delivery candidates.

Park et al. enclosed the synthesis of nano-sized and self-assembled HA-paclitaxel conjugate micelles and studied their promising potential as tumor-specific therapeutic agents for targeted delivery of paclitaxel to cells overexpressing HA receptors.[193] Apoptosis-inducing effect of HA-paclitaxel micelles on HCT-116 cells, overexpressing CD44, displayed apparent evidence

of cell death quantitatively assessed as increase in G2/M phase cell population (2-fold higher than Taxol and 4-fold higher than the control). In general, HA-paclitaxel nano-micelles exhibited greater cytotoxicity to CD44 overexpressing cells than for the HA receptor deficient cells, suggesting the proficiency of targeting using HA. Previously, the same group also demonstarted that HA nanogels encapsulating small interfering RNA (siRNA) could be delivered to HCT-116 cells in a HA receptor-mediated, target-specific manner.

Alonso et al. demonstrated that both chitosan (CS) nanoparticles and liposome-CS nanoparticle complexes interact with and penetrate the corneal and conjunctival epithelia.[194] The same group then reported an efficient novel ocular targeted gene delivery nano-vehicle composed of HA-CS nanoparticles prepared by ionotropic gelification, entrapped with pDNA (pEGFP or pβ-gal) and studied their transfection abilities in proliferating ocular cells.[195] It was shown that the HA-CS nanoparticles were nontoxic, were able to provide high transfection levels (up to 15% of cells transfected) in human corneal epithelial (HCE), and were proved to be internalized by hyaluronan CD44-receptor mediated endocytosis. Blocking of the receptor recognition sites of HA led to a decrease in the tumor-targeting selectivity. This gives evidence of the potential of HA-CS nanoparticles for targeting and intracellular delivery of genes to the cornea and conjunctiva.

Szoka et al. used HA-targeted liposomes (HALs) entrapped with DOX as tumor-targeting drug vehicles to treat CD44-expressing tumors.[17] They elegantly demonstrated the selective delivery of DOX drug to B16F10 melanoma cancerous cells, expressing high levels of CD44. B16F10 specifically bind and

internalize HALs rapidly in a temperature and concentration-dependent manner (uptake proportional to HA loading 0-3 mol % range), whereas cells expressing low levels of CD44 do not. HAL binding to B16F10 was inhibited by HA and by an anti-CD44 monoclonal antibody. Moreover, for periods up to 24 h, they observed a remarkable 8.2 and 4.4-fold increase in potency of the HAL-delivered DOX compared with free DOX in both transient and continuous exposure conditions, respectively. They also showed significantly enhanced cytotoxicity (almost 1-fold better) by HAL-DOX to CD44-overexpressing cells and much less toxicity to low-CD44 expressing cells compared to the free drug. All this proves the promise of targeting CD44 by HA-coated liposomes and the potential of using them as chemotherapeutic agents for drug delivery *in vivo*.

In 2004, Margalit et al. demonstrated the use of targeted-covalently linked-HA nano-liposomes (tHA-LIP) encapsulated with mitomycin C (MMC) as anticancer nanocarriers delivering drugs to tumor-bearing mice models *in vivo*.[196] *In vitro*, they observed 100-fold increase in potency of MMC encapsulated tHA-LIP in cells overexpressing but not in cells underexpressing, hyaluronan receptors. *In vivo*, in 3 mouse tumor models (C-26 solid tumors, B16F10.9 and D122 lung metastasis) tHA-LIP were long-circulating, 7-fold and 70-fold longer than drug-loaded nontargetd liposome (nt-LIP) and free MMC, respectively. When delivered in B16F10.9 tumor-bearing C57BL/6 mice *via* tHA-LIP, MMC accumulation in the tumor was 30-fold higher than the free drug, and 4-fold higher than nt-LIP proving selectively of targeting. tHA-LIP-mediated MMC accumulation in tumor-bearing lungs was 20% of injected dose, compared to 0.6%

and 4% with free drug and nt-LIP, respectively while tumor-free lungs showed low accumulation, irrespective of drug formulation. Moreover, to evaluate tHA-LIP effects on therapeutic responses, tumor response to treatment, tumor size, metastatic burden and survival were tested and found superior in animals receiving MMC-loaded tHA-LIP. Along the same lines, the same group demonstrated the use of DOX encapsulated tHA-LIP as tumor-targeted vehicles in both syngeneic and human xenograft mice.[197] Mediated by the long-circulating tHA-LIP, DOX accumulation in tumor-bearing lungs was 30-, 6.7-, and 3.5-fold higher than free DOX, nt-LIP, and liposomal doxorubicin (Doxil), respectively. In brief, DOX-encapsulating tHA-LIP generated significant improvements in pharmacokinetics, biodistribution, loading efficacy and cytotoxicity in four different mouse species, in tumors generated in different organs, and in tumors originating from different cell lines- all overexpressing HA receptors. All these successful and promising results shows that tHA-LIPs emerge as a valid targeted and specific cargo for tumor chemotherapy, with distinct advantages: cryoprotection, good drug encapsulation, sustained release, long circulation and high affinity binding to the tumor, allowing the liposomes to act as sustained-release drug vehicles.

Very recently, Paulson et al. developed CD22 sialic acid-decorated liposomal nanoparticles loaded with doxorubicin for *in vivo* targeting of B lymphoma cells.[198] A current clinical target for B cell lymphoma is CD22, a B cell specific member of the sialic acid binding Ig-like lectin (siglec) family that recognizes α2-6-linked sialylated glycans as ligands. In contrast to the approved

Doxil, which passively delivers DOX to solid tumors *via* leaky blood vessels, it was demonstrated that DOX-loaded sialic acid-decorated liposomal nanoparticles are actively targeted to and endocytosed by C22 on B cells, and significantly extend life in a murine xenograft model of human B cell lymphoma. Moreover, they bind and kill malignant B cells from peripheral blood samples obtained from patients with hairy cell leukemia, marginal zone lymphoma, and chronic lymphocytic leukemia. The results demonstrate the potential for using a carbohydrate recognition-based approach for efficiently targeting B cells *in vivo* that can offer improved treatment options for patients with B cell malignancies.

In conclusion, as shown above, carbohydrates displayed on nano-systems are useful in many areas of biomedical application such as pathogen detection, inhibition of metastatic diseases, gene and drug delivery and cellular imaging. Although recent advances have demonstrated the use of carbohydrate-functionalized nanoprobes for diagnosis, sensing, imaging and therapy, new methods and strategies to produce targeted probes based on the "sugar code" are certainly needed. To achieve these goals, the specificity of carbohydrate ligands needs to be improved and the characteristics and bio-functionalization of nanostructures should be better controlled to meet the demands of specific biological targets. Indeed, surface engineering of nanomaterials is critical to translate molecular recognition events into reliable biological readouts. A balance between specific receptor expression levels, proper ligand presentation, efficient ligand coupling, physiological barriers' consideration, and tumor distribution is crucial for a full successful biological system. Nonetheless, many obstacles for *in*

vivo intracellular targeting still exits: 1) successful application of targeted nanoparticles, 2) preserving the physiochemical properties of the nanoparticles 3) engineering of sizes comparable to target, 4) avoiding the reticulo-endothelial system 5) internalization into tumoral cells vs normal cells with high efficiency. New and better treatments are still to be explored, but there are substantial gains to be made by applying the nano-systems already developed. The main problems are lack of effective methods for non-surgical prevention or early detection and diagnosis. The next decade should explicit the accumulation of enormous amounts of data on nanotechnology and nano-biofunctionalization to make it to clinical practice. Nevertheless, functionalized nanoprobes are destined to play a major role in biomedical applications for many years to come. There is plenty of room at the bottom.

1.8. References

1. Borisov, S. M.; Wolfbeis, O. S., **Optical biosensors.** *Chem. Rev.* **2008,** *108*, 423-461.

2. Jain, K. K., **Nanotechnology in clinical laboratory diagnostics.** *Clin. Chim. Acta* **2005,** *358*, 37-54.

3. Yun, Y.-H.; Eteshola, E.; Bhattacharya, A.; Dong, Z.; Shim, J.-S.; Conforti, L.; Kim, D.; Schulz, M. J.; Ahn, C. H.; Watts, N., **Tiny medicine: Nanomaterial-based biosensors.** *Sensors* **2009,** *9*, 9275-9299.

4. Wang, X.; Ramstroem, O.; Yan, M., **Glyconanomaterials: Synthesis, characterization, and ligand presentation.** *Adv. Mater.* **2010,** *22*, 1946-1953.

5. de la Fuente, J. M.; Penades, S., **Glyconanoparticles: Types, synthesis and applications in glycoscience, biomedicine and material science.** *Biochim. Biophys. Acta* **2006,** *1760*, 636-651.

6. Gornik, O.; Dumic, J.; Flogel, M.; Lauc, G., **Glycoscience - a new frontier in rational drug design.** *Acta Pharm. (Zagreb, Croatia) FIELD Full Journal Title:Acta Pharmaceutica (Zagreb, Croatia)* **2006,** *56*, 19-30.

7. Oppenheimer, S. B.; Alvarez, M.; Nnoli, J., **Carbohydrate-based experimental therapeutics for cancer, HIV/AIDS and other diseases.** *Acta Histochem. FIELD Full Journal Title:Acta Histochemica* **2008,** *110*, 6-13.

8. Vliegenthart, J. F. G., **Carbohydrate based vaccines.** *FEBS Lett. FIELD Full Journal Title:FEBS Letters* **2006,** *580*, 2945-2950.

9. Raman, R.; Sasisekharan, V.; Sasisekharan, R., **Structural insights into biological roles of protein-glycosaminoglycan interactions.** *Chem. Biol.* **2005,** *12*, 267-277.

10. Seeberger, P. H.; Werz, D. B., **Synthesis and medical applications of oligosaccharides.** *Nature* **2007,** *446*, 1046-1051.

11. Stevens, R. L.; Colombo, M.; Gonzales, J. J.; Hollander, W.; Schmid, K., **The glycosaminoglycans of the human artery and their changes in atherosclerosis.** *J. Clin. Invest.* **1976,** *58*, 470–481.

12. Werz, D. B.; Seeberger, P. H., **Carbohydrates as the next frontier in pharmaceutical research.** *Chem. Eur. J.* **2005,** *11*, 3194-3206.

13. Kiessling, L. L.; Young, T.; Mortell, K. H., **Multivalency in protein-carbohydrate recognition.** *Glycoscience* **2001,** *2*, 1817-1861.

14. Lundquist, J. J.; Toone, E. J., **The cluster glycoside effect.** *Chem. Rev.* **2002,** *102*, 555-578.

15. Iqbal, S. S.; Mayo, M. W.; Bruno, J. G.; Bronk, B. V.; Batt, C. A.; Chambers, J. P., **A review of molecular recognition technologies for detection of biological threat agents.** *Biosens. Bioelectron.* **2000,** *15*, 549-578.

16. Disney, M. D.; Zheng, J.; Swager, T. M.; Seeberger, P. H., **Detection of bacteria with carbohydrate-functionalized fluorescent polymers.** *J. Am. Chem. Soc.* **2004,** *126*, 13343-13346.

17. Eliaz, R. E.; Szoka, F. C., Jr., **Liposome-encapsulated doxorubicin targeted to CD44: a strategy to kill CD44-overexpressing tumor cells.** *Cancer Res.* **2001,** *61*, 2592-2601.

18. Imberty, A.; Chabre, Y. M.; Roy, R., **Glycomimetics and glycodendrimers as high affinity microbial anti-adhesins.** *Chem. Eur. J.* **2008,** *14*, 7490-7499 and references therein.

19. Hatch, D. M.; Weiss, A. A.; Kale, R. R.; Iyer, S. S., **Biotinylated bi- and tetra-antennary glycoconjugates for Escherichia coli detection.** *ChemBioChem* **2008,** *9*, 2433-2442.

20. Barrientos, A. G.; de la Fuente, J. M.; Rojas, T. C.; Fernandez, A.; Penades, S., **Gold glyconanoparticles: Synthetic polyvalent ligands mimicking glycocalyx-like surfaces as tools for glycobiological studies.** *Chem. Eur. J.* **2003,** *9*, 1909-1921.

21. Laurent, S.; Forge, D.; Port, M.; Roch, A.; Robic, C.; Vander Elst, L.; Muller, R. N., **Magnetic iron oxide nanoparticles: Synthesis, stabilization, vectorization, physicochemical characterizations, and biological applications.** *Chem. Rev.* **2008,** *108*, 2064-2110.

22. Jun, Y.-w.; Lee, J.-H.; Cheon, J., **Chemical design of nanoparticle probes for high-performance magnetic resonance imaging.** *Angew. Chem. Int. Ed.* **2008,** *47*, 5122-5135.

23. Lu, A. H.; Salabas, E. L.; Schueth, F., **Magnetic nanoparticles: synthesis, protection, functionalization, and application.** *Angew. Chem., Int. Ed.* **2007,** *46*, 1222-1244.

24. Cheng, F. Y.; Su, C. H.; Yang, Y. S.; Yeh, C. S.; Tsai, C. Y.; Wu, C. L.; Wu, M. T.; Shieh, D. B., **Characterization of aqueous dispersions of Fe_3O_4 nanoparticles and their biomedical applications.** *Biomaterials* **2005,** *26*, 729-738.

25. Gupta, A. K.; Gupta, M., **Synthesis and surface engineering of iron oxide nanoparticles for biomedical applications.** *Biomaterials* **2005**, 3995-4021.

26. Isaac, K.; Wang, X.; Varughese, B.; Isaacs, L.; Ehrman, S. H.; English, D. S., **Magnetic iron oxide nanoparticles for biorecognition: Evaluation of surface coverage and activity.** *J. Phys. Chem. B* **2006,** *110*, 1553-1558.

27. Sun, S.; Zeng, H., **Size-controlled synthesis of magnetite nanoparticles.** *J. Am. Chem. Soc.* **2002,** *124*, 8204-8205.

28. Huang, X.; Neretina, S.; El-Sayed, M. A., **Gold nanorods: From synthesis and properties to biological and biomedical applications.** *Adv. Mater.* **2009,** *21*, 4880-4910 and references therein.

29. Gao, X.; Cui, Y.; Levenson, R. M.; Chung, L. W. K.; Nie, S., ***In vivo* cancer targeting and imaging with semiconductor quantum dots.** *Nat. Biotechnol.* **2004,** *22*, 969-976.

30. Qiao, R.; Yang, C.; Gao, M., **Superparamagnetic iron oxide nanoparticles: from preparations to *in vivo* MRI applications.** *J. Mater. Chem.* **2009,** *19*, 6274-6293.

31. Jain, P. K.; Huang, X.; El-Sayed, I. H.; El-Sayed, M. A., **Noble metals on the nanoscale: optical and photothermal properties and some applications in imaging, sensing, biology, and medicine.** *Acc. Chem. Res.* **2008,** *41*, 1578-1586.

32. Qian, X.; Peng, X.-H.; Ansari, D. O.; Yin-Goen, Q.; Chen, G. Z.; Shin, D. M.; Yang, L.; Young, A. N.; Wang, M. D.; Nie, S., ***In vivo* tumor targeting and spectroscopic detection with surface-enhanced Raman nanoparticle tags.** *Nat. Biotechnol.* **2008,** *26*, 83-90.

33. Xue, C.; Jog, S. P.; Murthy, P.; Liu, H., **Synthesis of highly water-soluble fluorescent conjugated glycopoly(*p*-phenylene)s for lectin and *Escherichia* coli.** *Biomacromolecules* **2006**.

34. Baek, M. G.; Stevens, R. C.; Charych, D. H., **Design and Synthesis of Novel glycopolythiophene assemblies for colorimetric detection of influenza Virus and *E. coli*.** *Bioconjugate Chem.* **2000,** *11*, 777-788.

35. de Paz, J. L.; Seeberger, P. H., **Recent advances in carbohydrayte microarrays.** *QSAR Comb. Sci.* **2006,** *25*, 1027-1032.

36. Disney, M. D.; Seeberger, P. H., **The use of carbohydrate microarrays to study carbohydrate-cell interactions and to detect pathogens.** *Chem. Biol.* **2004,** *11*, 1701-1707 and references cited therein.

37. Zhi, Z.-L.; Powell, A. K.; Turnbull, J. E., **Fabrication of carbohydrate microarrays on gold surfaces: Direct attachment of nonderivatized oligosaccharides to hydrazide-modified self-assembled monolayers.** *Anal. Chem.* **2006,** *78*, 4786-4793.

38. Disney, M. D.; Seeberger, P. H., **Catching bacteria with sugar.** *Chemistry & Biology* **2004,** *11*, 1602-1604.

39. Ngundi, M. M.; Taitt, C. R.; McMurry, S. A.; Kahne, D.; Ligler, F. S., **Detection of bacterial toxins with monosaccharide arrays.** *Biosens. Bioelectron.* **2006,** *21*, 1195-1201.

40. de la Fuente, J. M.; Penades, S., **Understanding carbohydrate-carbohydrate interactions by means of glyconanotechnology.** *Glycoconjugate J.* **2004,** *21*, 149-163.

41. Nagahori, N.; Nishimura, S.-I., **Glyconanotechnology.** *Nanotechnol. Carbohydr. Chem.* **2006**, 149-166.

42. Paul, K. G.; Frigo, T. B.; Groman, J. Y.; Groman, E. V., **Synthesis of ultrasmall superparamagnetic iron oxides using reduced polysaccharides.** *Bioconjugate Chem.* **2004,** *15*, 394-401.

43. Moore, A.; Marecos, E.; Bogdanov, A., Jr.; Weissleder, R., **Tumoral distribution of long-circulating dextran-coated iron oxide nanoparticles in a rodent model.** *Radiology* **2000,** *214*, 568-574.

44. Chen, Y.; Ji, T.; Rosenzweig, Z., **Synthesis of glyconanospheres containing luminescent CdSe-ZnS quantum dots.** *Nano Lett.* **2003,** *3*, 581-584.

45. Hu, Y.; Jiang, X.; Ding, Y.; Ge, H.; Yuan, Y.; Yang, C., **Synthesis and characterization of chitosan-poly(acrylic acid) nanoparticles.** *Biomaterials* **2002,** *23*, 3193-3201.

46. Ying, J. Y.; Jana, N. R.; Erathodiyil, N. **Functionalization of nanoparticles by glucosamine derivatives**. Patent 2008-SG160, 2008136773, **2008**.

47. Palmacci, S.; Josephson, L.; Groman, E. V. **Synthesis of polymer-covered superparamagnetic oxide colloids for magnetic resonance contrast agents or other applications**. Patent 93-US7682-9505669, **1995**.

48. Zhao, X.; Tapec-Dytioco, R.; Tan, W., **Ultrasensitive DNA detection using highly fluorescent bioconjugated nanoparticles.** *J. Am. Chem. Soc.* **2003,** *125*, 11474-11475.

49. Stoeva, S. I.; Lee, J.-S.; Smith, J. E.; Rosen, S. T.; Mirkin, C. A., **Multiplexed detection of protein cancer markers with biobarcoded nanoparticle probes.** *J. Am. Chem. Soc.* **2006,** *128*, 8378-8379.

50. Gu, H.; Xu, K.; Xu, C.; Xu, B., **Biofunctional magnetic nanoparticles for protein separation and pathogen detection.** *Chem. Commun.* **2006**, 941-949.

51. Amano, Y.; Cheng, Q., **Detection of influenza virus: Traditional approaches and development of biosensors.** *Anal. Bioanal. Chem.* **2005,** *381*, 156-164.

52. Gu, H.; Ho, P. L.; Tsang, K. W. T.; Wang, L.; Xu, B., **Using biofunctional magnetic nanoparticles to capture vancomycin-resistant Enterococci and other gram-positive bacteria at ultralow concentration.** *J. Am. Chem. Soc.* **2003,** *125*, 15702-15703.

53. Kim, B.-S.; Yang, W.-Y.; Ryu, J.-H.; Yoo, Y.-S.; Lee, M., **Carbohydrate-coated nanocapsules from Amphiphilic rod–coil molecule: Binding to bacterial type 1 pili.** *Chem. Commun.* **2005**, 2035-2037.

54. Schofield, C. L.; Field, R. A.; Russell, D. A., **Glyconanoparticles for the colorimetric detection of cholera toxin.** *Anal. Chem.* **2007,** *79*, 1356-1361 and references cited therein.

55. Gu, H.; Ho, P. L.; Tsang, K. W. T.; Yu, C. W.; Xu, B., **Using biofunctional magnetic nanoparticles to capture gram-negative bacteria at an ultra-low concentration.** *Chem. Commun.* **2003**, 1966-1967.

56. Jun, Y. W.; Huh, Y. M.; Choi, J. S.; Lee, J. H.; Song, H. T.; Kim, S.; Yoon, S.; Kim, K. S.; Shin, J. S.; Suh, J. S.; Cheon, J., **Nanoscale size effect of magnetic nanocrystals and their utilization for cancer diagnosis *via* magnetic resonance imaging.** *J. Am. Chem. Soc.* **2005,** *127*, 5732 -5733.

57. Peng, G.; Trock, E.; Haick, H., **Detecting simulated patterns of lung cancer biomarkers by random network of single-walled carbon nanotubes coated with nonpolymeric organic materials.** *Nano Lett.* **2008,** *8*, 3631-3635.

58. Sha, M. Y.; Xu, H.; Natan, M. J.; Cromer, R., **Surface-enhanced raman scattering tags for rapid and homogeneous detection of circulating tumor cells in the presence of human whole blood.** *J. Am. Chem. Soc.* **2008,** *130*, 17214-17215.

59. Yu, M. K.; Jeong, Y. Y.; Park, J.; Park, S.; Kim, J. W.; Min, J. J.; Kim, K.; Jon, S., **Drug-loaded superparamagnetic iron oxide nanoparticles for combined cancer imaging and therapy in vivo.** *Angew. Chem., Int. Ed.* **2008,** *47*, 5362-5365.

60. Kooi, M. E.; Cappendijk, V. C.; Cleutjens, K. B. J. M.; Kessels, A. G. H.; Kitslaar, P. J. E. H. M.; Borgers, M.; Frederik, P. M.; Daemen, M. J. A. P.; van Engelshoven, J. M. A., **Accumulation of ultrasmall superparamagnetic particles of iron oxide in human atherosclerotic plaques can be detected by in vivo magnetic resonance imaging.** *Circulation* **2003,** *107*, 2453-2458.

61. Ruehm, S. G.; Corot, C.; Vogt, P.; Kolb, S.; Debatin, J. F., **Magnetic resonance imaging of atherosclerotic plaque with ultrasmall superparamagnetic particles of iron oxide in hyperlipidemic rabbits.** *Circulation* **2001,** *103*, 415-422.

62. Jelinek, R.; Kolusheva, S., **Carbohydrate biosensors.** *Chem. Rev.* **2004,** *104*, 5987-6015.

63. Jianrong, C.; Yuqing, M.; Nongyue, H.; Xiaohua, W.; Sijiao, L., **Nanotechnology and biosensors.** *Biotechnol. Adv.* **2004,** *22*, 505-18.

64. Lee, J.-H.; Huh, Y.-M.; Jun, Y.-w.; Seo, J.-w.; Jang, J.-t.; Song, H.-T.; Kim, S.; Cho, E.-J.; Yoon, H.-G.; Suh, J.-S.; Cheon, J., **Artificially engineered magnetic particles for ultra-sensitive molecular imaging.** *Nat. Med.* **2006,** *13*, 95-99.

65. Yang, L.; Peng, X.-H.; Wang, Y. A.; Wang, X.; Cao, Z.; Ni, C.; Karna, P.; Zhang, X.; Wood, W. C.; Gao, X.; Nie, S.; Mao, H., **Receptor-targeted nanoparticles for *in vivo* imaging of breast cancer.** *Clin. Cancer Res.* **2009,** *15*, 4722-4732.

66. van Kasteren, S. I.; Campbell, S. J.; Serres, S.; Anthony, D. C.; Sibson, N. R.; Davis, B. G., **Glyconanoparticles allow pre-symptomatic *in vivo* imaging of brain disease.** *Proc. Natl. Acad. Sci.* **2009,** *106*, 18-23.

67. Lazcka, O.; Del Campo, F. J.; Munoz, F. X., **Pathogen detection: A perspective of traditional methods and biosensors.** *Biosens. Bioelectron.* **2007,** *22*, 1205-1217.

68. Katz, E.; Willner, I., **Integrated nanoparticle–biomolecule hybrid systems: Synthesis, properties, and applications.** *Angew. Chem. Int. Ed.* **2004,** *42*, 6042-6108.

69. Gao, B. J.; Li, L.; Ho, P. L.; Mak, G. C.; Gu, H.; Xu, B., **Combining fluorescent probes and biofunctional magnetic nanoparticles for rapid detection of bacteria in human blood.** *Adv. Mater.* **2006,** *18*, 3145-3148.

70. Shukoor, M. I.; Natalio, F.; Tahir, M. N.; Ksenofontov, V.; Therese, H. A.; Theato, P.; Schroeder, H. C.; Mueller, W. E. G.; Tremel, W., **Superparamagnetic gamma -Fe2O3 nanoparticles with tailored functionality for protein separation.** *Chem. Commun.* **2007**, 4677-4679.

71. Perez, J. M.; O'Loughin, T.; Simeone, F. J.; Weissleder, R.; Josephson, L., **DNA-based magnetic nanoparticle assembly acts as a magnetic relaxation nanoswitch allowing screening of DNA-cleaving agents.** *J. Am. Chem. Soc.* **2002,** *124*, 2856-2857.

72. Weissleder, R.; Kelly, K.; Sun, E. Y.; Shtatland, T.; Josephson, L., **Cell-specific targeting of nanoparticles by multivalent attachment of small molecules.** *Nat. Biotechnol.* **2005,** *23*, 1418-1423.

73. Perez, J. M.; Josephson, L.; Weissleder, R., **Use of magnetic nanoparticles as nanosensors to probe for molecular interactions.** *ChemBioChem* **2004,** *5*, 261-264.

74. Sun, E. Y.; Weissleder, R.; Josephson, L., **Continuous analyte sensing with magnetic nanoswitches.** *Small* **2006,** *2*, 1144-1147.

75. Park, J.-H.; von Maltzahn, G.; Zhang, L.; Schwartz, M. P.; Ruoslahti, E.; Bhatia, S. N.; Sailor, M. J., **Magnetic iron oxide nanoworms for tumor targeting and imaging.** *Adv. Mater.* **2008,** *20*, 1630-1635.

76. Lee, J.-H.; Huh, Y.-M.; Jun, Y.-w.; Seo, J.-w.; Jang, J.-t.; Song, H.-T.; Kim, S.; Cho, E.-J.; Yoon, H.-G.; Suh, J.-S.; Cheon, J., **Artificially engineered magnetic nanoparticles for ultra-sensitive molecular imaging.** *Nat. Med.* **2007,** *13*, 95-9.

77. Wang, Y. X.; Hussain, S. M.; Krestin, G. P., **Superparamagnetic iron oxide contrast agents: physicochemical characteristics and applications in MR imaging.** *Eur. Radiol.* **2001,** *11*, 2319-31.

78. Jeong, U.; Teng, X.; Wang, Y.; Yang, H.; Xia, Y., **Superparamagnetic colloids: controlled synthesis and niche applications.** *Adv. Mater.* **2007,** *19*, 33-60.

79. Boyer, C.; Whittaker, M. R.; Bulmus, V.; Liu, J.; Davis, T. P., **The design and utility of polymer-stabilized iron-oxide nanoparticles for nanomedicine applications.** *NPG Asia Mater.* **2010,** *2*, 23-30.

80. Ma, M.; Zhang, Y.; Yu, W.; Shen, H.-y.; Zhang, H.-q.; Gu, N., **Preparation and characterization of magnetite nanoparticles coated by amino silane.** *Colloids Surf. A* **2003,** *212*, 219-226.

81. Kang, Y. S.; Risbud, S.; Rabolt, J. F.; Stroeve, P., **Synthesis and characterization of nanometer-size Fe3O4 and Fe2O3 particles.** *Chem. Mater.* **1996,** *8*, 2209-2211.

82. Sun, S.; Zeng, H.; Robinson, D. B.; Raoux, S.; Rice, P. M.; Wang, S. X.; Li, G., **Monodisperse MFe_2O_4 (M = Fe, Co, Mn) nanoparticles.** *J. Am. Chem. Soc.* **2004,** *126*, 273-279.

83. Hyeon, T.; Lee, S. S.; Park, J.; Chung, Y.; Na, H. B., **Synthesis of highly crystalline and monodisperse maghemite nanocrystallites without a size-selection process.** *J. Am. Chem. Soc.* **2001,** *123*, 12798-12801.

84. Park, J.; Lee, E.; Hwang, N.-M.; Kang, M.; Kim Sung, C.; Hwang, Y.; Park, J.-G.; Noh, H.-J.; Kim, J.-Y.; Park, J.-H.; Hyeon, T., **One-nanometer-scale size-controlled synthesis of monodisperse magnetic iron oxide nanoparticles.** *Angew. Chem. Int. Ed.* **2005,** *44*, 2873-7.

85. Massart, R., **Preparation of aqueous magnetic liquids in alkaline and acidic media.** *IEEE Trans. Magn.* **1981,** *17*, 1247-8.

86. Gupta, A. K.; Gupta, M., **Synthesis and surface engineering of iron oxide nanoparticles for biomedical applications.** *Biomaterials* **2005,** *26*, 3995-4021.

87. Corot, C.; Robert, P.; Idee, J.-M.; Port, M., **Recent advances in iron oxide nanocrystal technology for medical imaging.** *Adv. Drug Delivery Rev.* **2006,** *58*, 1471-1504.

88. Bruce, I. J.; Sen, T., **Surface modification of magnetic nanoparticles with alkoxysilanes and their application in magnetic bioseparations.** *Langmuir* **2005,** *21*, 7029-7035.

89. Smith Emily, A.; Chen, W., **How to prevent the loss of surface functionality derived from aminosilanes.** *Langmuir* **2008,** *24*, 12405-9.

90. Yamaura, M.; Camilo, R. L.; Sampaio, L. C.; Macedo, M. A.; Nakamura, M.; Toma, H. E., **Preparation and characterization of (3-aminopropyl)triethoxysilane-coated magnetite nanoparticles.** *J. Magn. Magn. Mater.* **2004,** *279*, 210-217.

91. Klotz, M.; Ayral, A.; Guizard, C.; Menager, C.; Cabuil, V., **Silica coating on colloidal maghemite particles.** *J. Colloid Interface Sci.* **1999,** *220*, 357-361.

92. Koh, I.; Wang, X.; Varughese, B.; Isaacs, L.; Ehrman, S. H.; English, D. S., **Magnetic iron oxide nanoparticles for biorecognition: evaluation of surface coverage and activity.** *J. Phys. Chem. B* **2006,** *110*, 1553-1558.

93. Park, J.; An, K.; Hwang, Y.; Park, J.-G.; Noh, H.-J.; Kim, J.-Y.; Park, J.-H.; Hwang, N.-M.; Hyeon, T., **Ultra-large-scale syntheses of monodisperse nanocrystals.** *Nat. Mater.* **2004,** *3*, 891-895.

94. De Palma, R.; Peeters, S.; Van Bael, M. J.; Van den Rul, H.; Bonroy, K.; Laureyn, W.; Mullens, J.; Borghs, G.; Maes, G., **Silane ligand exchange to make hydrophobic superparamagnetic nanoparticles water-dispersible.** *Chem. Mater.* **2007,** *19*, 1821-1831.

95. Lee, H.; Yu, M. K.; Park, S.; Moon, S.; Min, J. J.; Jeong, Y. Y.; Kang, H.-W.; Jon, S., **Thermally cross-linked superparamagnetic iron oxide nanoparticles: synthesis and application as a dual imaging probe for cancer in vivo.** *J. Am. Chem. Soc.* **2007,** *129*, 12739-12745.

96. Bao, N.; Shen, L.; An, W.; Padhan, P.; Heath Turner, C.; Gupta, A., **Formation mechanism and shape control of monodisperse magnetic CoFe2O4 nanocrystals.** *Chem. Mater.* **2009,** *21*, 3458-3468.

97. Polito, L.; Colombo, M.; Monti, D.; Melato, S.; Caneva, E.; Prosperi, D., **Resolving the structure of ligands bound to the surface of superparamagnetic iron oxide nanoparticles by high-resolution magic-angle spinning NMR spectroscopy.** *J. Am. Chem. Soc.* **2008,** *130*, 12712-12724.

98. Namdeo, M.; Saxena, S.; Tankhiwale, R.; Bajpai, M.; Mohan, Y. M.; Bajpai, S. K., **Magnetic nanoparticles for drug delivery applications.** *J. Nanosci. Nanotechnol.* **2008,** *8*, 3247-3271.

99. Thorek Daniel, L. J.; Chen Antony, K.; Czupryna, J.; Tsourkas, A., **Superparamagnetic iron oxide nanoparticle probes for molecular imaging.** *Ann. Biomed. Eng.* **2006,** *34*, 23-38.

100. Jang, J.-t.; Nah, H.; Lee, J.-H.; Moon, S. H.; Kim, M. G.; Cheon, J., **Critical enhancements of MRI contrast and hyperthermic effects by dopant-controlled magnetic nanoparticles.** *Angew. Chem. Int. Ed.* **2009,** *48*, 1234-1238.

101. Jun, Y.-w.; Lee, J.-H.; Cheon, J., **Chemical design of nanoparticle probes for high-performance magnetic resonance imaging.** *Angew. Chem., Int. Ed.* **2008,** *47*, 5122-5135.

102. Park, J.-H.; von Maltzahn, G.; Xu, M. J.; Fogal, V.; Kotamraju, V. R.; Ruoslahti, E.; Bhatia, S. N.; Sailor, M. J., **Cooperative nanomaterial system to sensitize, target, and treat tumors.** *Proc. Natl. Acad. Sci.* **2009**, 1-6, 6 pp.

103. Park, J.-H.; von Maltzahn, G.; Zhang, L.; Derfus, A. M.; Simberg, D.; Harris, T. J.; Ruoslahti, E.; Bhatia, S. N.; Sailor, M. J., **Systematic surface engineering of magnetic nanoworms for in vivo tumor targeting.** *Small* **2009,** *5*, 694-700.

104. Lee, J.-H.; Lee, K.; Moon, S. H.; Lee, Y.; Park, T. G.; Cheon, J., **All-in-one target-cell-specific magnetic nanoparticles for simultaneous molecular imaging and siRNA delivery.** *Angew. Chem. Int. Ed.* **2009,** *48*, 4174-4179, S4174/1-S4174/5.

105. Perez, J. M.; Simeone, F. J.; Saeki, Y.; Josephson, L.; Weissleder, R., **Viral-induced self-assembly of magnetic nanoparticles allows the detection**

of viral particles in biological media. *J. Am. Chem. Soc.* **2003,** *125*, 10192-10193.

106. Koh, I.; Hong, R.; Weissleder, R.; Josephson, L., **Sensitive NMR sensors detect antibodies to influenza.** *Angew. Chem. Int. Ed.* **2008,** *47*, 4119-4121.

107. Grimm, J.; Perez, J. M.; Josephson, L.; Weissleder, R., **Novel Nanosensors for Rapid Analysis of Telomerase Activity.** *Cancer Res.* **2004,** *64*, 639-643.

108. Huh, Y.-M.; Jun, Y.-W.; Song, H.-T.; Kim, S.; Choi, J.-S.; Lee, J.-H.; Yoon, S.; Kim, K.-S.; Shin, J.-S.; Suh, J.-S.; Cheon, J., ***In vivo*** **magnetic resonance detection of cancer by using multifunctional magnetic nanocrystals.** *J. Am. Chem. Soc.* **2005,** *127*, 12387-12391.

109. Jun, Y.-w.; Seo, J.-w.; Cheon, J., **Nanoscaling laws of magnetic nanoparticles and their applicabilities in biomedical sciences.** *Acc. Chem. Res.* **2008,** *41*, 179-189.

110. Jun, Y.-w.; Huh, Y.-M.; Choi, J.-s.; Lee, J.-H.; Song, H.-T.; Kim, S.; Yoon, S.; Kim, K.-S.; Shin, J.-S.; Suh, J.-S.; Cheon, J., **Nanoscale size effect of magnetic nanocrystals and their utilization for cancer diagnosis via magnetic resonance imaging.** *J. Am. Chem. Soc.* **2005,** *127*, 5732-5733.

111. Thorek, D. L. J.; Tsourkas, A., **Size, charge and concentration dependent uptake of iron oxide particles by non-phagocytic cells.** *Biomaterials* **2008,** *29*, 3583-3590.

112. Peng, X.-H.; Qian, X.; Mao, H.; Wang, A. Y.; Chen, Z.; Nie, S.; Shin, D. M., **Targeted magnetic iron oxide nanoparticles for tumor imaging and therapy.** *Int. J. Nanomed.* **2008,** *3*, 311-321.

113. Horák, D.; Babič, M.; Jendelová, P.; Herynek, V.; Trchová, M.; Pientka, Z.; Pollert, E.; Hájek, M.; Syková, E., **D-Mannose-modified iron oxide nanoparticles for stem cell labeling.** *Bioconj. Chem.* **2007,** *18*, 635-644.

114. Liu, L.-H.; Dietsch, H.; Schurtenberger, P.; Yan, M., **Photoinitiated coupling of unmodified monosaccharides to iron oxide nanoparticles for sensing proteins and bacteria.** *Bioconjugate Chem.* **2009,** *20*, 1349-1355.

115. Pera, N. P.; Kouki, A.; Haataja, S.; Branderhorst, H. M.; Liskamp, R. M. J.; Visser, G. M.; Finne, J.; Pieters, R. J., **Detection of pathogenic Streptococcus suis bacteria using magnetic glycoparticles.** *Org. Biomol. Chem. 8*, 2425-2429.

116. Lee, Y.; Lee, H.; Kim, Y. B.; Kim, J.; Hyeon, T.; Park, H.; Messersmith, P. B.; Park, T. G., **Bioinspired surface immobilization of hyaluronic acid on**

monodisperse magnetite nanocrystals for targeted cancer imaging. *Adv. Mater.* **2008,** *20*, 4154-4157.

117. Kumar, A.; Sahoo, B.; Montpetit, A.; Behera, S.; Lockey, R. F.; Mohapatra, S. S., **Development of hyaluronic acid-Fe_2O_3 hybrid magnetic nanoparticles for targeted delivery of peptides.** *Nanomedicine* **2007,** *3*, 132-137.

118. Yoo, M. K.; Kim In, Y.; Kim Eun, M.; Jeong, H.-J.; Lee, C.-M.; Jeong Yong, Y.; Akaike, T.; Cho Chong, S., **Superparamagnetic iron oxide nanoparticles coated with galactose-carrying polymer for hepatocyte targeting.** *J. Biomed. Biotechnol.* **2007,** *2007*, 94740.

119. Han, C.; Li, G.; Lim, K.; DeFrances, M. C.; Gandhi, C. R.; Wu, T., **Transgenic expression of cyclooxygenase-2 in hepatocytes accelerates endotoxin-induced acute liver failure.** *J. Immunol.* **2008,** *181*, 8027-8035.

120. Eustis, S.; El-Sayed, M. A., **Why gold nanoparticles are more precious than pretty gold: Noble metal surface plasmon resonance and its enhancement of the radiative and nonradiative properties of nanocrystals of different shapes.** *Chem. Soc. Rev.* **2006,** *35*, 209-217.

121. Nikoobakht, B.; El-Sayed, M. A., **Surface-enhanced raman scattering studies on aggregated gold nanorods.** *J. Phys. Chem. A* **2003,** *107*, 3372-3378.

122. Westcott, S. L.; Oldenburg, S. J.; Lee, T. R.; Halas, N. J., **Formation and adsorption of clusters of gold nanoparticles onto functionalized silica nanoparticle surfaces.** *Langmuir* **1998,** *14*, 5396-5401.

123. Sun, Y.; Mayers, B. T.; Xia, Y., **Template-engaged replacement reaction: A one-step approach to the large-scale synthesis of metal nanostructures with hollow interiors.** *Nano Lett.* **2002,** *2*, 481-485.

124. Huang, X.; El-Sayed, I. H.; Qian, W.; El-Sayed, M. A., **Cancer cell imaging and photothermal therapy in the near-infrared region by using gold nanorods.** *J. Am. Chem. Soc.* **2006,** *128*, 2115-2120.

125. Colvin, V. L., **The potential environmental impact of engineered nanomaterials.** *Nat. Biotechnol.* **2003,** *21*, 1166-1170.

126. Shukla, R.; Bansal, V.; Chaudhary, M.; Basu, A.; Bhonde, R. R.; Sastry, M., **Biocompatibility of gold nanoparticles and their endocytotic fate inside the cellular compartment: A microscopic overview.** *Langmuir* **2005,** *21*, 10644-10654.

127. Connor, E. E.; Mwamuka, J.; Gole, A.; Murphy, C. J.; Wyatt, M. D., **Gold nanoparticles are taken up by human cells but do not cause acute cytotoxicity.** *Small* **2005,** *1*, 325-327.

128. Thompson, D., **Michael Faraday's recognition of ruby gold: the birth of modern nanotechnology.** *Gold Bull.* **2007,** *40*, 267-269.

129. Murphy, C. J.; Jana, N. R., **Controlling the aspect ratio of inorganic nanorods and nanowires.** *Adv. Mater.* **2002,** *14*, 80-82 and references therein.

130. Liu, X.; Dai, Q.; Austin, L.; Coutts, J.; Knowles, G.; Zou, J.; Chen, H.; Huo, Q., **A one-step homogeneous immunoassay for cancer biomarker detection using gold nanoparticle probes coupled with dynamic light scattering.** *J. Am. Chem. Soc.* **2008,** *130*, 2780-2782.

131. Turkevich, J.; Stevenson, P. C.; Hillier, J., **The nucleation and growth processes in the synthesis of colloidal gold.** *Discuss. Faraday Soc.* **1951,** *No. 11*, 55-75.

132. Turkevich, J.; Hubbell, H. H., **Low-angle x-ray diffraction of colloidal gold and carbon black.** *J. Am. Chem. Soc.* **1951,** *73*, 1-7.

133. Frens, G., **Particle size and sol stability in metal colloids.** *Colloid & Polymer Science* **1972,** *250*, 736-41.

134. Frens, G., **Controlled nucleation for the regulation of the particle size in monodisperse gold suspensions.** *Nature* **1973,** *241*, 20-2.

135. Brust, M.; Walker, M.; Bethell, D.; Schiffrin, D. J.; Whyman, R., **Synthesis of thiol-derivatized gold nanoparticles in a two-phase liquid-liquid system.** *Chem. Commun.* **1994**, 801-2.

136. Bain, C. D.; Troughton, E. B.; Tao, Y. T.; Evall, J.; Whitesides, G. M.; Nuzzo, R. G., **Formation of monolayer films by the spontaneous assembly of organic thiols from solution onto gold.** *J. Am. Chem. Soc.* **1989,** *111*, 321-35 and references therein.

137. Leff, D. V.; Ohara, P. C.; Heath, J. R.; Gelbart, W. M., **Thermodynamic control of gold nanocrystal size: experiment and theory.** *J. Phys. Chem.* **1995,** *99*, 7036-41.

138. Schmid, G.; West, H.; Malm, J.-O.; Bovin, J.-O.; Grenthe, C., **Catalytic properties of layered gold-palladium colloids.** *Chem. - A Eur. J.* **1996,** *2*, 1099-1103.

139. Brown, K. R.; Walter, D. G.; Natan, M. J., **Seeding of colloidal Au nanoparticle solutions. 2. Improved control of particle size and shape.** *Chem. Mater.* **2000,** *12*, 306-313.

140. Goia, D. V.; Matijevic, E., **Tailoring the particle size of monodispersed colloidal gold.** *Colloids Surf., A* **1999,** *146*, 139-152.

141. Jana, N. R.; Gearheart, L.; Murphy, C. J., **Wet chemical synthesis of high aspect ratio cylindrical gold nanorods.** *J. Phys. Chem. B* **2001,** *105*, 4065-4067.

142. Jana, N. R.; Gearheart, L.; Murphy, C. J., **Seeding growth for size control of 5-40 nm diameter gold nanoparticles.** *Langmuir* **2001,** *17*, 6782-6786.

143. Jana, N. R.; Gearheart, L.; Murphy, C. J., **Seed-mediated growth approach for shape-controlled synthesis of spheroidal and rod-like gold nanoparticles using a surfactant template.** *Adv. Mater.* **2001,** *13*, 1389-1393.

144. Jana, N. R.; Gearheart, L.; Murphy, C. J., **Evidence for seed-mediated nucleation in the chemical reduction of gold salts to gold nanoparticles.** *Chem. Mater.* **2001,** *13*, 2313-2322.

145. Jana, N. R.; Gearheart, L.; Obare, S. O.; Murphy, C. J., **Anisotropic chemical reactivity of gold spheroids and nanorods.** *Langmuir FIELD Full Journal Title:Langmuir* **2002,** *18*, 922-927.

146. Nikoobakht, B.; El-Sayed, M. A., **Evidence for bilayer assembly of cationic surfactants on the surface of gold nanorods.** *Langmuir* **2001,** *17*, 6368-6374.

147. Nikoobakht, B.; El-Sayed, M. A., **Preparation and growth mechanism of gold nanorods (NRs) using seed-mediated growth method.** *Chem. Mater.* **2003,** *15*, 1957-1962.

148. Varnavski, O. P.; Mohamed, M. B.; El-Sayed, M. A.; Goodson, T., III, **Relative enhancement of ultrafast emission in gold nanorods.** *J. Phys. Chem. B* **2003,** *107*, 3101-3104.

149. Link, S.; Hathcock, D. J.; Nikoobakht, B.; El-Sayed, M. A., **Medium effect on the electron cooling dynamics in gold nanorods and truncated tetrahedra.** *Adv. Mater.* **2003,** *15*, 393-396.

150. Perrault, S. D.; Chan, W. C. W., **Synthesis and surface modification of highly monodispersed, spherical gold nanoparticles of 50-200 nm.** *J. Am. Chem. Soc.* **2009,** *131*, 17042-17043.

151. Thurn-Albrecht, T.; Schotter, J.; Kastle, G. A.; Emley, N.; Shibauchi, T.; Krusin-Elbaum, L.; Guarini, K.; Black, C. T.; Tuominen, M. T.; Russell, T. P., **Ultrahigh-density nanowire arrays grown in self-assembled diblock copolymer templates.** *Science* **2000,** *290*, 2126-2129.

152. Brown, L. O.; Hutchison, J. E., **Controlled growth of gold nanoparticles during ligand exchange.** *J. Am. Chem. Soc.* **1999,** *121*, 882-883.

153. Yu, Y.-Y.; Chang, S.-S.; Lee, C.-L.; Wang, C. R. C., **Gold nanorods: electrochemical synthesis and optical properties.** *J. Phys. Chem. B* **1997,** *101*, 6661-6664.

154. Chang, S.-S.; Shih, C.-W.; Chen, C.-D.; Lai, W.-C.; Wang, C. R. C., **The shape transition of gold nanorods.** *Langmuir* **1999,** *15*, 701-709.

155. Wiesner, J.; Wokaun, A., **Anisometric gold colloids. Preparation, characterization, and optical properties.** *Chem. Phys. Lett.* **1989,** *157*, 569-75.

156. de la Fuente, J. M.; Barrientos, A. G.; Rojas, T. C.; Rojo, J.; Canada, J.; Fernandez, A.; Penades, S., **Gold glyconanoparticles as water-soluble polyvalent models to study carbohydrate interactions.** *Angew. Chem. Int. Ed.* **2001,** *40*, 2258-2261.

157. Tromas, C.; Rojo, J.; de la Fuente, J. M.; Barrientos, A. G.; Garcia, R.; Penades, S., **Adhesion forces between Lewis^x determinant antigens as measured by atomic force microscopy.** *Angew. Chem. Int. Ed.* **2001,** *40*, 3052-3055.

158. Hernaiz, M. J.; de la Fuente, J. M.; Barrientos, A. G.; Penades, S., **A model system mimicking glycosphingolipid clusters to quantify carbohydrate self-interactions by surface plasmon resonance.** *Angew. Chem. Int. Ed.* **2002,** *41*, 1554-1557.

159. de la Fuente, J. M.; Eaton, P.; Barrientos, A. G.; Menendez, M.; Penades, S., **Thermodynamic evidence for Ca^{2+}-mediated self-aggregation of lewis^x gold glyconanoparticles. A model for cell adhesion via carbohydrate-carbohydrate interaction.** *J. Am. Chem. Soc.* **2005,** *127*, 6192-6197.

160. Lin, C.-C.; Yeh, Y.-C.; Yang, C.-Y.; Chen, G.-F.; Chen, Y.-C.; Wu, Y.-C.; Chen, C.-C., **Quantitative analysis of multivalent interactions of carbohydrate-encapsulated gold nanoparticles with Concanavalin A.** *Chem. Commun.* **2003**, 2920-2921.

161. Liang, C.-H.; Wang, C.-C.; Lin, Y.-C.; Chen, C.-H.; Wong, C.-H.; Wu, C.-Y., **Iron oxide/gold core/shell nanoparticles for ultrasensitive detection of carbohydrate-protein interactions.** *Anal. Chem.* **2009,** *81*, 7750-7756.

162. Schofield, C. L.; Haines, A. H.; Field, R. A.; Russell, D. A., **Silver and gold glyconanoparticles for colorimetric bioassays.** *Langmuir* **2006,** *22*, 6707-6711.

163. de la Fuente, J. M.; Alcantara, D.; Eaton, P.; Crespo, P.; Rojas, T. C.; Fernandez, A.; Hernando, A.; Penades, S., **Gold and gold-iron oxide magnetic glyconanoparticles: synthesis, characterization and magnetic properties.** *J. Phys. Chem. B* **2006,** *110*, 13021-13028.

164. de la Fuente Jesus, M.; Alcantara, D.; Penades, S., **Cell response to magnetic glyconanoparticles: does the carbohydrate matter?** *IEEE Trans Nanobioscience* **2007,** *6*, 275-81.

165. Martinez-Avila, O.; Hijazi, K.; Marradi, M.; Clavel, C.; Campion, C.; Kelly, C.; Penades, S., **Gold manno-glyconanoparticles: Multivalent systems to block HIV-1 gp120 binding to the lectin DC-SIGN.** *Chem. Eur. J.* **2009,** *15*, 9874-9888, S9874/1-S9874/58.

166. Feinberg, H.; Mitchell, D. A.; Drickamer, K.; Weis, W. I., **Structural basis for selective recognition of oligosaccharides by DC-SIGN and DC-SIGNR.** *Science* **2001,** *294*, 2163-2166.

167. Martinez-Avila, O.; Bedoya, L. M.; Marradi, M.; Clavel, C.; Alcami, J.; Penades, S., **Multivalent manno-glyconanoparticles inhibit DC-SIGN-mediated HIV-1 trans-infection of human T cells.** *ChemBioChem* **2009,** *10*, 1806-1809.

168. Carvalho de Souza, A.; Halkes, K. M.; Meeldijk, J. D.; Verkleij, A. J.; Vliegenthart, J. F. G.; Kamerling, J. P., **Gold glyconanoparticles as probes to explore the carbohydrate-mediated self-recognition of marine sponge cells.** *ChemBioChem* **2005,** *6*, 828-831.

169. Spillmann, D.; Thomas-Oates, J. E.; van Kuik, J. A.; Vliegenthart, J. F. S.; Misevic, G.; Burger, M. M.; Finne, J., **Characterization of a novel sulfated carbohydrate unit implicated in the carbohydrate-carbohydrate-mediated cell aggregation of the marine sponge Microciona prolifera.** *J. Biol. Chem.* **1995,** *270*, 5089-97.

170. Lin, C. C.; Yeh, Y. C.; Yang, C. Y.; Chen, C. L.; Chen, G. F.; Chen, C. C.; Wu, Y. C., **Selective binding of mannose-encapsulated gold nanoparticles to type 1 pili in Escherichia coli.** *J. Am. Chem. Soc.* **2002,** *124*, 3508-3509.

171. Chien, Y.-Y.; Jan, M.-D.; Adak, A. K.; Tzeng, H.-C.; Lin, Y.-P.; Chen, Y.-J.; Wang, K.-T.; Chen, C.-T.; Chen, C.-C.; Lin, C.-C., **Globotriose-functionalized gold nanoparticles as multivalent probes for Shiga-like toxin.** *ChemBioChem* **2008,** *9*, 1100-1109.

172. Nath, S.; Kaittanis, C.; Tinkham, A.; Perez, J. M., **Dextran-Coated Gold Nanoparticles for the Assessment of Antimicrobial Susceptibility.** *Anal. Chem.* **2008,** *80*, 1033-1038.

173. Eaton, P.; Ragusa, A.; Clavel, C.; Rojas Cristina, T.; Graham, P.; Duran Raul, V.; Penades, S., **Glyconanoparticle-DNA interactions: an atomic force microscopy study.** *IEEE Trans Nanobioscience* **2007,** *6*, 309-18.

174. Ahmed, M.; Deng, Z.; Liu, S.; Lafrenie, R.; Kumar, A.; Narain, R., **Cationic glyconanoparticles: their complexation with DNA, cellular uptake, and transfection efficiencies.** *Bioconjugate Chem.* **2009,** *20*, 2169-2176.

175. Rojo, J.; Diaz, V.; De la Fuente, J. M.; Segura, I.; Barrientos, A. G.; Riese, H. H.; Bernad, A.; Penades, S., **Gold glyconanoparticles as new tools in antiadhesive therapy.** *ChemBioChem* **2004,** *5*, 291-297.

176. Marradi, M.; Alcantara, D.; de la Fuente, J. M.; Garcia-Martin, M. L.; Cerdan, S.; Penades, S., **Paramagnetic Gd-based gold glyconanoparticles as probes for MRI: tuning relaxivities with sugars.** *Chem. Commun.* **2009**, 3922-3924.

177. Chan, W. C. W.; Nile, S., **Quantum dot bioconjugates for ultrasensitive nonisotopic detection.** *Science* **1998,** *281*, 2016-2018.

178. Sun, X.-L.; Cui, W.; Haller, C.; Chaikof, E. L., **Site-specific multivalent carbohydrate labeling of quantum dots and magnetic beads.** *ChemBioChem* **2004,** *5*, 1593-1596.

179. Babu, P.; Sinha, S.; Surolia, A., **Sugar-quantum dot conjugates for a selective and sensitive detection of lectins.** *Bioconjugate Chem.* **2007,** *18*, 146-151.

180. Robinson, A.; Fang, J.-M.; Chou, P.-T.; Liao, K.-W.; Chu, R.-M.; Lee, S.-J., **Probing lectin and sperm with carbohydrate-modified quantum dots.** *ChemBioChem* **2005,** *6*, 1899-1905.

181. Oh, E.; Lee, D.; Kim, Y.-P.; Cha, S. Y.; Oh, D.-B.; Kang, H. A.; Kim, J.; Kim, H.-S., **Nanoparticle-based energy transfer for rapid and simple detection of protein glycosylation.** *Angew. Chem. Int. Ed.* **2006,** *45*, 7959-7963.

182. Bhang, S. H.; Won, N.; Lee, T.-J.; Jin, H.; Nam, J.; Park, J.; Chung, H.; Park, H.-S.; Sung, Y.-E.; Hahn, S. K.; Kim, B.-S.; Kim, S., **Hyaluronic acid-quantum dot conjugates for in vivo lymphatic vessel imaging.** *ACS Nano* **2009,** *3*, 1389-1398.

183. Kikkeri, R.; Lepenies, B.; Adibekian, A.; Laurino, P.; Seeberger, P. H., **In vitro imaging and in vivo liver targeting with carbohydrate capped quantum dots.** *J. Am. Chem. Soc.* **2009,** *131*, 2110-2112.

184. Kikkeri, R.; Laurino, P.; Odedra, A.; Seeberger, P. H., **Synthesis of carbohydrate-functionalized quantum dots in microreactors.** *Angew. Chem. Int. Ed. 49*, 2054-2057, S2054/1-S2054/7.

185. Gu, L.; Elkin, T.; Jiang, X.; Li, H.; Lin, Y.; Qu, L.; Tzeng, T. R. J.; Joseph, R.; Sun, Y. P., **Single-walled carbon nanotubes displaying multivalent ligands for capturing pathogens.** *Chem. Commun.* **2005**, 874-876.

186. Wang, H.; Gu, L.; Lin, Y.; Lu, F.; Meziani, M. J.; Luo, P. G.; Wang, W.; Cao, L.; Sun, Y. P., **Unique aggregation of Anthrax (*Bacillus anthracis*) spores by sugar-coated single-walled carbon nanotubes.** *J. Am. Chem. Soc.* **2006,** *128*, 13364-13365.

187. Chen, X.; Tam, U. C.; Czlapinski, J. L.; Lee, G. S.; Rabuka, D.; Zettl, A.; Bertozzi, C. R., **Interfacing carbon nanotubes with living cells.** *J. Am. Chem. Soc.* **2006,** *128*, 6292-6293.

188. Chen, X.; Lee, G. S.; Zettl, A.; Bertozzi, C. R., **Biomimetic synthesis: Biomimetic engineering of carbon nanotubes by using cell surface mucin mimics.** *Angew. Chem. Int. Ed.* **2004,** *43*, 6111-6116.

189. Nakai, T.; Kanamori, T.; Sando, S.; Aoyama, Y., **Remarkably size-regulated cell invasion by artificial viruses. Saccharide-dependent self-aggregation of glycoviruses and its consequences in glycoviral gene delivery.** *J. Am. Chem. Soc.* **2003,** *125*, 8465-75.

190. Aoyama, Y.; Kanamori, T.; Nakai, T.; Sasaki, T.; Horiuchi, S.; Sando, S.; Niidome, T., **Artificial viruses and their application to gene delivery. Size-controlled gene coating with glycocluster nanoparticles.** *J. Am. Chem. Soc.* **2003,** *125*, 3455-7.

191. Osaki, F.; Kanamori, T.; Sando, S.; Sera, T.; Aoyama, Y., **A quantum dot conjugated sugar ball and its cellular uptake. On the size effects of endocytosis in the subviral region.** *J. Am. Chem. Soc.* **2004,** *126*, 6520-6521.

192. Yadav, A. K.; Mishra, P.; Mishra, A. K.; Mishra, P.; Jain, S.; Agrawal, G. P., **Development and characterization of hyaluronic acid-anchored PLGA nanoparticulate carriers of doxorubicin.** *Nanomedicine* **2007,** *3*, 246-257.

193. Lee, H.; Lee, K.; Park, T. G., **Hyaluronic acid-paclitaxel conjugate micelles: synthesis, characterization, and antitumor activity.** *Bioconjugate Chem.* **2008,** *19*, 1319-1325.

194. Diebold, Y.; Jarrín, M.; Sáez, V.; Carvalho, E. L.; Orea, M.; Calonge, M.; Seijo, B.; Alonso, M. J., **Ocular drug delivery by liposome-chitosan nanoparticle complexes (LCS-NP).** *Biomaterials* **2007,** *28*, 1553-64.

195. de la Fuente, M.; Seijo, B.; Alonso Maria, J., **Novel hyaluronic acid-chitosan nanoparticles for ocular gene therapy.** *Invest. Ophthalmol. Vis. Sci.* **2008,** *49*, 2016-24.

196. Peer, D.; Margalit, R., **Loading mitomycin C inside long circulating hyaluronan targeted nano-liposomes increases its antitumor activity in three mice tumor models.** *Int. J. Cancer* **2004,** *108*, 780-9.

197. Peer, D.; Margalit, R., **Tumor-targeted hyaluronan nanoliposomes increase the antitumor activity of liposomal doxorubicin in syngeneic and human xenograft mouse tumor models.** *Neoplasia* **2004,** *6*, 343-353.

198. Chen, W. C.; Completo, G. C.; Sigal, D. S.; Crocker, P. R.; Saven, A.; Paulson, J. C., ***In vivo* targeting of B-cell lymphoma with glycan ligands of CD22.** *Blood, 2010.*

CHAPTER 2

Magnetic Glyco-Nanoparticles: A Unique Tool for Rapid Pathogen Detection, Decontamination and Strain Differentiation

2.1. Pathogen Detection

Pathogenic bacteria continue to present a significant threat to public health. Consequently, accurate detection and enumeration of bacteria, such as *E. coli,* can help quantify the risks of contamination and reduce potential infections.[1] Traditional methods that require amplification or enrichment of the target bacteria tend to be laborious and time-consuming. Moreover, antibodies or lectins functionalized on magnetic particles are not superlative for detection because of the challenges entailed in immobilizing biomacromolecules and the low-capture efficiencies attained, typically in the 10-30% range.[2] Commercial and synthesized magnetic beads have also been used, but these detection systems have reduced sensitivity, less capture efficiency and limited detection range due to a wide bead and magnetic domain size distribution.[3,4] Indeed, it is advantageous to use magnetic nanoparticles for detection. The large active surface area offered by such nanoparticles is necessary for effective sugar presentation. The high surface/volume ratio offers more contact surface area for attaching carbohydrates and hence for capturing pathogens.[5] The sizes of nanoparticles are typically about two orders of magnitude smaller than a bacterium, which allows the attachment of multiple NPs onto a bacterial cell rendering easy magnet-mediated separation.[5,6] Moreover, the small

nanoparticles have faster kinetics in solution as compared to their micrometer-sized counterparts, which can result in fast detection.

Herein, we demonstrate the potential of sugar-coated MGNPs for fast bacterial detection and removal, which provides an attractive avenue for diagnostic applications. In fact, the diversity and broad knowledge pertaining to the surface-displayed carbohydrates could aid the design of indicative tests for accurate detection of bacteria through interactions with multivalent carbohydrate ligands.[7] We hypothesized that, due to this polyvalency, MGNPs displaying monosaccharides can be attached to *E. coli*, thereby producing a notably enhanced recognition and improving the capture efficiency. Indeed, one challenging aspect of studying carbohydrate-protein interactions is the low affinity (~ mM range) of oligosaccharides to their receptors leading to weak signal responses. Enhancing these responses underscores the need to generate simple monosaccharide ligands in a multivalent decoration providing insight into relevant protein-carbohydrate binding events. The implementation of this concept is crucial for minimizing and eliminating potential infections.

2.2. Syntheses of MGNPs

Our strategy to construct the artificially engineered MGNPs features: 1) a triethoxy silane anchor that can bind to the metal oxide nanoparticles; 2) a linker with the desired functional group allowing biomolecular attachment; 3) simple and efficient methods for covalently attaching requisite oligosaccharides to the spacers. Our journey commenced with the preparation of silica-coated form of Fe_3O_4 nanoparticles (NP **1**) (**Figure 2-1a**). In an effort to control the devised

nanocomposites to better suit the biorecognition purposes, we used PVP as the surfactant and tetraethoxysilane (TEOS) as the stable coated silica shell.[8] Silica-coated magnetite NP **1** was then caged with alkyne-siloxane (AS) linker or aminopropyltriethoxysilane (APTES)[9, 10] to yield alkyne- or amine-terminated NPs respectively, onto which monosaccharides were subsequently affixed (**Figure 2-1a**). Siloxanes provide common intermediates for a wide range of chemical modifications, particularly for biological applications.[11]

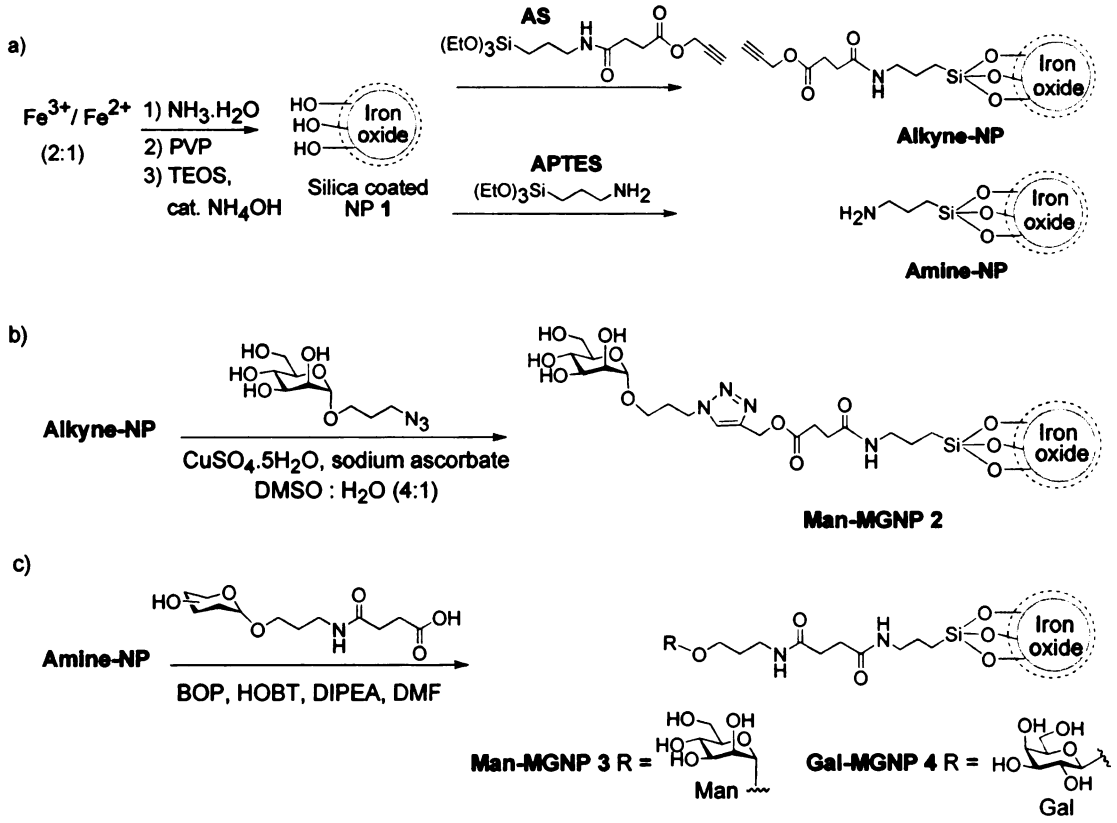

Figure 2-1. Syntheses of MGNPs.

Functionalization of the nanoparticles with D-mannose (Man) through either a triazole linker (MGNP **2**) formed by the [2+3] Huisgen reaction[12] (**Figure 2-1b**) or an amide linkage (MGNP **3**) (**Figure 2-1c**) was then attained. We also

synthesized galactose (Gal) functionalized MGNP **4** *via* amide coupling. The control of the shape, size, and dispersibility of MGNPs was accomplished by the choice of a suitable surfactant, a proper surface-coating and an efficient hydrophilic surface functionalization. With our covalent approach, all carbohydrates are uniformly oriented on the NP surface, which is crucial for high performances in cell-capturing studies.[13] All MGNPs were characterized by X-ray diffraction (XRD), TEM, TGA, FT-IR and HR-MAS NMR.

2.3. Characterization of MGNPs

2.3. a. Transmission Electron Microscopy (TEM)

TEM images of MGNP indicate that the diameters of the nanoparticle core are around ~ 6 - 15 nm (**Figure 2-2**). Samples were prepared by depositing 5 µl of the particle dispersion onto 200 mesh carbon-coated copper grids. The suspension was then allowed to settle for 1 to 2 minutes before excess liquid was removed with a paper wick.

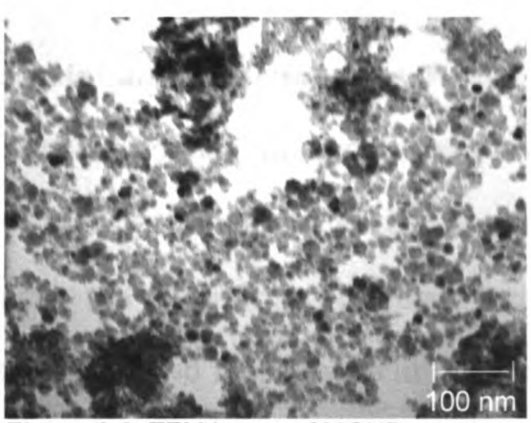

Figure 2-2. TEM image of MGNPs.

2.3. b. X-ray Diffraction (XRD)

XRD was carried out in a dry powder form to identify the nanocrystalline structure of the NPs. The observed diffraction peaks indicates that the NPs are indeed Fe_3O_4 magnetite[14-16] (**Figure 2-3**).

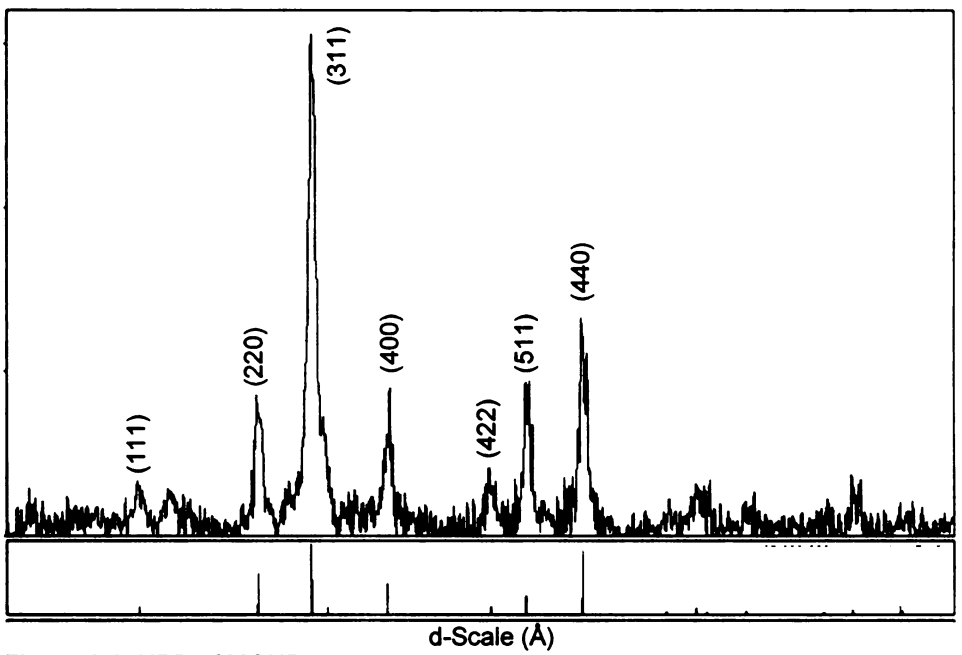

Figure 2-3. XRD of MGNPs.

2.3. c. Fourier Transform Infrared Spectroscopy (FT-IR)

FT-IR analysis was performed to characterize the surface nature of MGNPs, as depicted in **Figure 2-4**. The bare Fe_3O_4 NPs were coated with TEOS was proved by comparing the IR spectra of coated and uncoated NPs. The spectrum of the bare NP shows two main bands at 577 and 453 cm^{-1} related to Fe–O vibrations. Moreover, an intense and broad band appeared in the region 3200-3600 cm^{-1} region, corresponding to the O–H stretching vibration. Compared with the bare Fe_3O_4 NP, NP **1** mainly possess additional absorption bands in the

region 980-1220 cm^{-1} corresponding to stretching of Si-O-Si and Si-OH bonds.[17] The IR spectrum of Man-MGNP **2** has additional alkyl C-H stretching at ~ 2900 cm^{-1}.

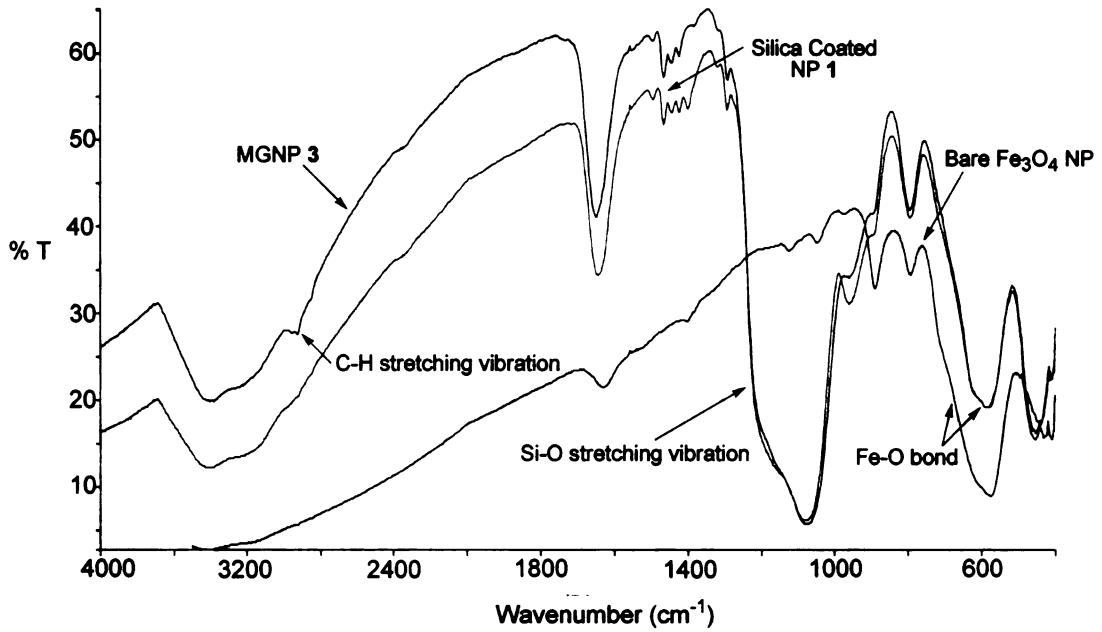

Figure 2- 4. FT-IR spectra of bare Fe_3O_4 NP (brown), NP **1** (blue) and MGNP **3** (black).

2.3. d. Thermogravimetric analysis (TGA)

For thermogravimetric analysis measurements, all nanoparticles were first heated to 100 °C (heating rate = 10 °C/min) and then cooled to 50 °C under dry nitrogen gas to remove all adsorbed water before any measurements were recorded. NP **1** exhibited a weight loss of 5.5 %, while Man-MGNP **3** and Gal-MGNP **4** have weight loss of 13 % and 11.5 % respectively (**Figure 2-5**), implying the presence of organic molecules on the surface of MGNPs. The number of mannose molecules on each MGNP **3** particle was estimated as follows: The lattice volume of magnetite is 592 $Å^3$ and Z=8 (8 Fe_3O_4

molecules/lattice). The average diameter of MGNP is ~10 nm. Assuming the MGNP is a sphere, the number of lattice in one MGNP particle is 884 and the number of Fe_3O_4 (MW=232) molecules in each MGNP particle is 7072. From TGA, the weight of Fe_3O_4 accounts for 88% of the MGNP and 6% of the MGNP is due to the carbohydrates attached. Therefore, on average, there are 220 mannose molecules (Man + APTES, MW ~ 500) on each MGNP.

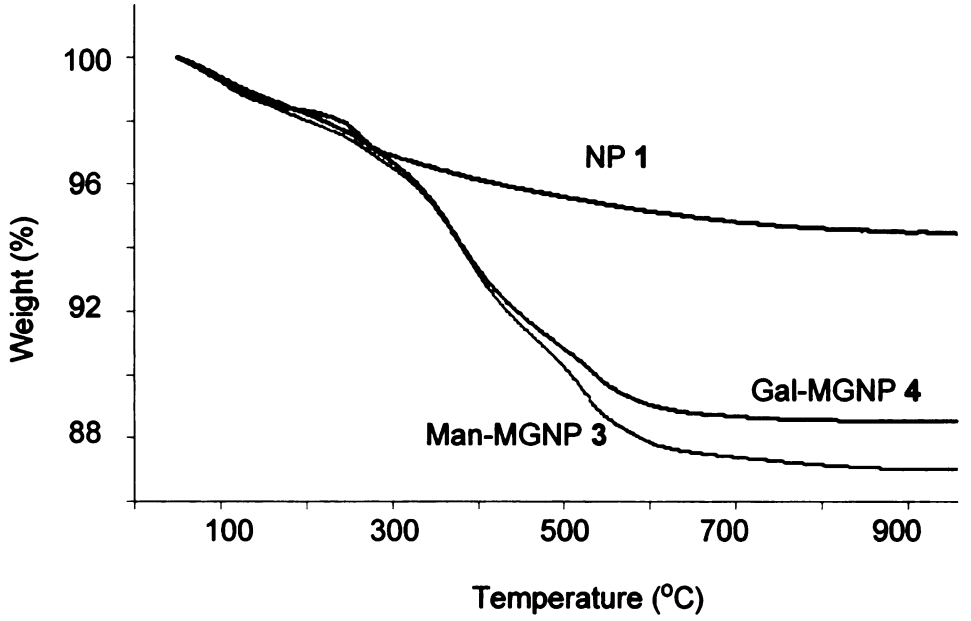

Figure 2-5. TGA curves for NP **1** (blue), Man-MGNP **3** (pink) and Gal-MGNP **4** (green).

2.3. e. High Resolution-Magic Angle Spinning (HR-MAS) ^{1}H NMR

NMR is a critical tool for providing detailed ligand structural features. Unfortunately, there is a serious limitation directly applying ^{1}H NMR to MGNPs due to the field inhomogeneity caused by the inherent superparamagnetism of the particles. Drastic line broadening was observed in spectra recorded with a conventional NMR probe, which led to undistinguishable ^{1}H NMR spectra (**Figure 2-6a**). Recently, HR-MAS NMR was found to be a superior tool to overcome this

problem.[18, 19] Indeed, HR-MAS ^{1}H NMR spectra of MGNPs gave solution-like spectra with a completely resolved splitting pattern, including the correct signal multiplicities and accurate integrations (**Figure 2-6b**). For instance, the anomeric proton of the galactoside ligand on Gal-MGNP **4** was well resolved as a doublet (J = 8.0 Hz) at 4.3 ppm, indicating the configuration of the carbohydrate was unaffected during immobilization. The fact that only one set of peaks from carbohydrates was observed suggested that the carbohydrate coating was homogeneous on the particle surface.

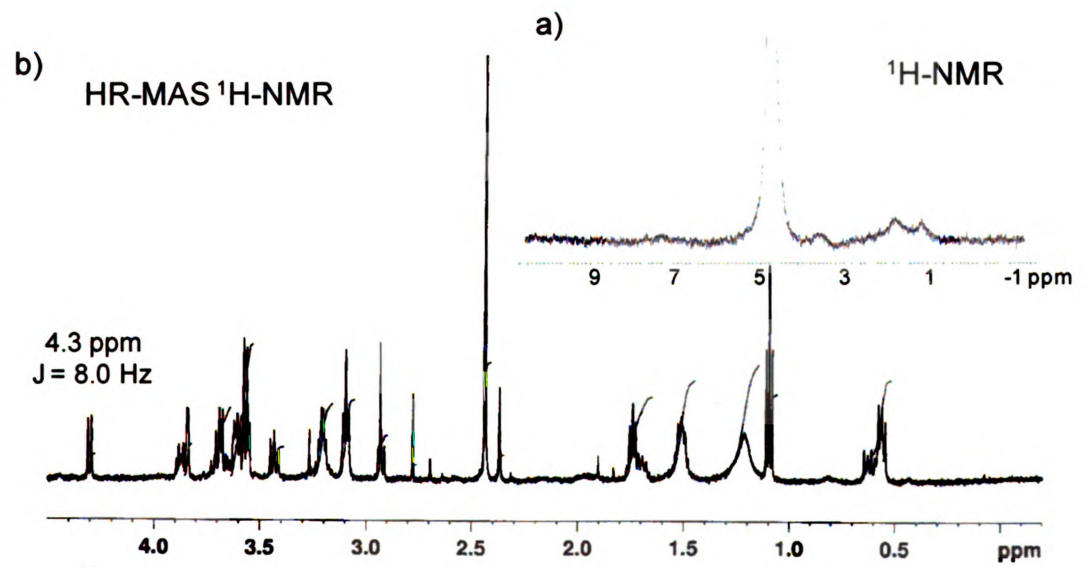

Figure 2-6. a) ^{1}H-NMR spectrum of Gal-MGNP **4** acquired in solution with a conventional 5 mm probe; and b) HR-MAS ^{1}H NMR of the same sample.

2.4. Lectin Binding Assay: MGNP/Con A Interactions

To validate the efficiency of MGNPs and to insure their use as nanoprobes to detect *E. coli*, we first tested carbohydrate-lectin interactions. Hence, the interaction between various MGNPs with a mannose-binding lectin, Con A,[20] was first investigated. Carbohydrate-lectin binding is central in designing our

biosensor.[21] After incubating NPs with fluorescein-labeled Con A overnight, a magnetic field was applied to the mixture through a handheld magnet inducing aggregation of magnetic NPs on the side of the vial. The residual fluorescence of supernatants was then recorded (**Figure 2-7**).

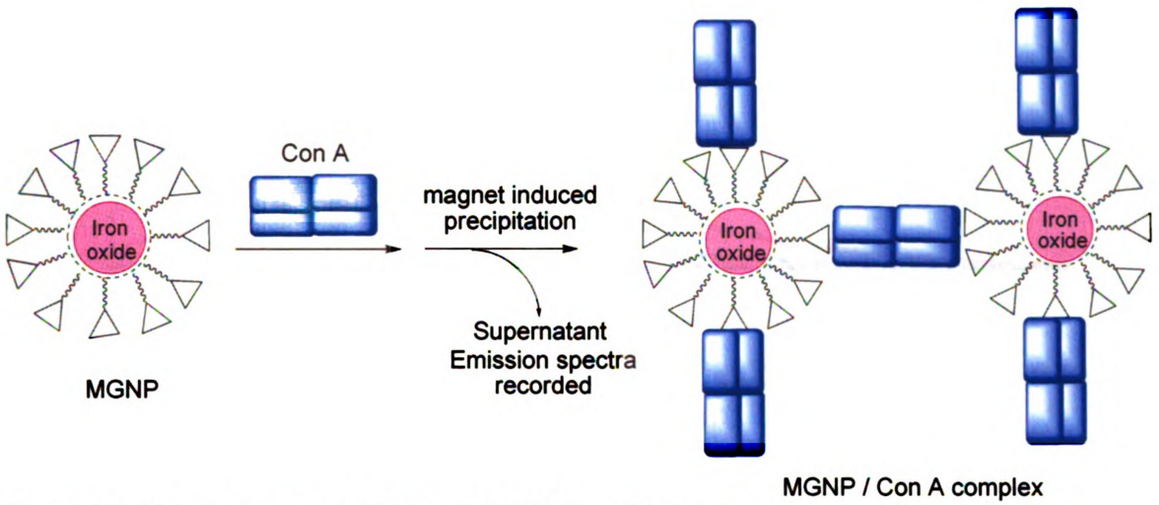

Figure 2-7. Schematic representation of MGNP-Con A interactions.

With MGNP **3**, the emission intensity of the supernatant decreased 87% indicating that most Con A was removed by MGNP **3** (**Figure 2-8a**). Triazole linked MGNP **2** was less efficient accounting for a 60% emission decrease probably because of the low efficiency of the Huisgen reaction with immobilized alkynes.[12] NP **1** without carbohydrates (control) did not remove any Con A, proving that the separation of Con A is due to its interaction with carbohydrates, rather than the nonspecific absorption to NP surface.

To test the separation efficiency dependence on concentration, different amounts of MGNP **3** (0.2 mg, 1 mg, 2 mg, 5mg) were mixed with fluorescein-labeled Con A (100 μg/mL, 2 mL) at 4 °C for 12 hours. The particles were then

subjected to magnetic separation and the fluorescence spectra of the supernatant were recorded.

a)

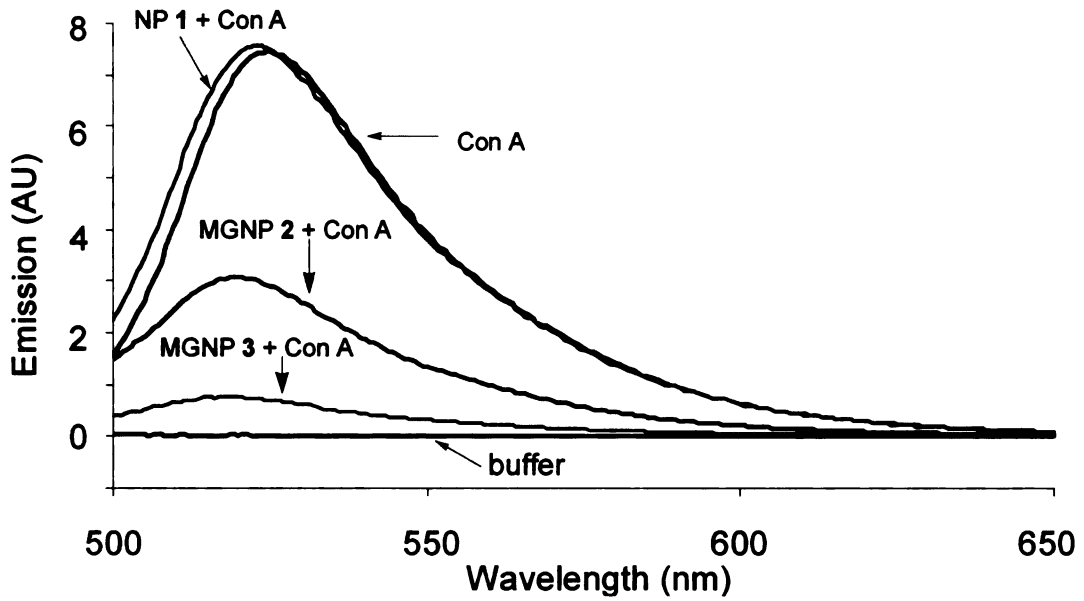

b)

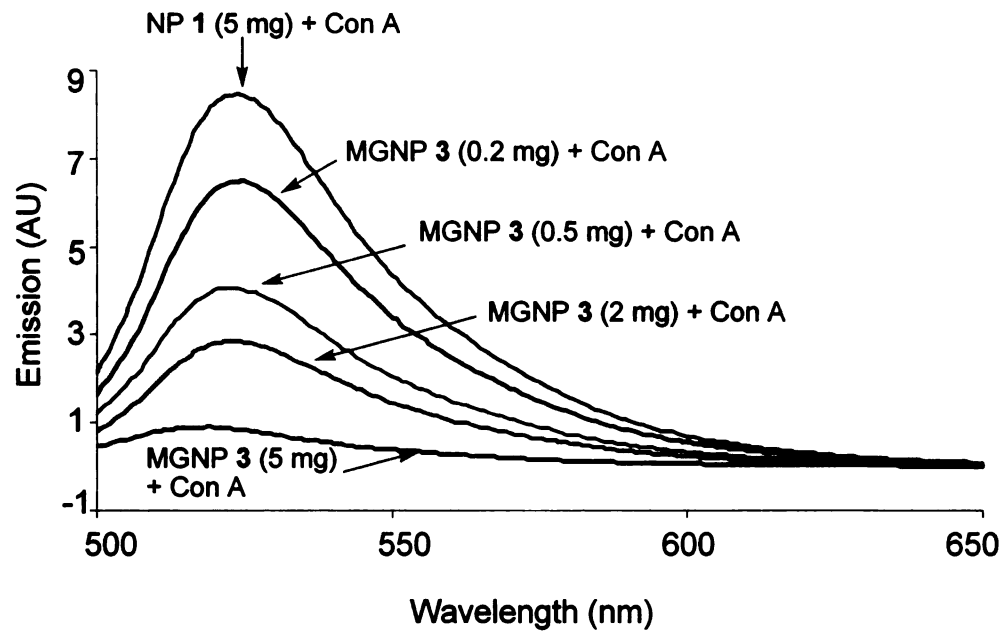

Figure 2-8. Fluorescent emission spectra of the supernatants of fluorescein-labeled Con A solutions (100 µg/mL, 2mL) after incubation a) with MGNPs or NP **1** (5 mg); b) with NP **1** and various amounts of MGNP **3** (0.2 mg, 1 mg, 2 mg, 5mg) and subsequent magnet mediated separation ($\lambda_{excitation}$ = 492 nm).

It was observed that with increasing the concentration of MGNP **3**, the amount of Con A removed by MGNP **3** increased, resulting in decreased fluorescence emission intensity (**Figure 2-8b**). All these results reveal the multivalent appeal of MGNP with ligand clustering leading to strong binding and gave us confidence to use our MGNP system for *E. coli* detection.

2.5. *E. coli* Detection using MGNPs

One of the mechanisms of *E. coli* detection is mediated by interactions between the bacteria and the specific carbohydrate receptors. Herein, *E. coli* strain ORN178 was used to validate the specific binding of MGNP **3** to type 1 fimbriae (called *Fim-H*) of *E. coli* ORN178. Type 1 fimbriae are heteropolymeric mannose binding proteinaceous appendages that obtrude from the surface of many gram-negative bacteria and play a major role in the binding phenomena. After incubating MGNP **3** (2 mg/mL) with solutions of an *E. coli* strain ORN178 (10^3-10^7 cells/mL in PBS buffer) for a few minutes, a magnetic field was applied separating MGNP/*E. coli* aggregates (**Figure 2-9**). The supernatants were carefully removed and the remaining aggregates were washed thoroughly, stained with a fluoresecent dye (PicoGreen), transferred to a glass slide, and imaged. Fluorescent microscopic imaging showed that *E. coli* can be reliably detected with a limit of 10^4 cells/mL (**Figure 2-10**). With NP **1**, no bacteria were observed on the slides.

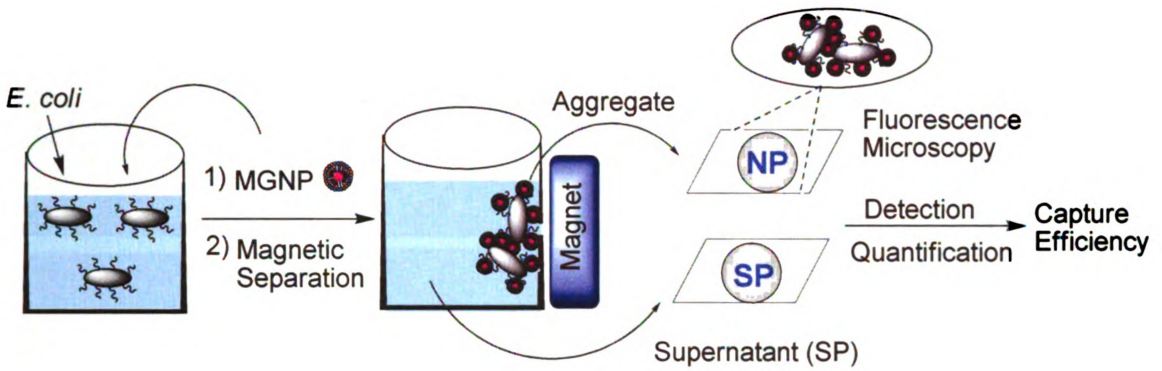

Figure 2-9. Schematic demonstration of *E. coli* detection by MGNPs.

Following the same protocol, we enumerated bacteria in the aggregate and supernatant using the fluorescent microscope. The capture efficiency was calculated by dividing the number of *E. coli* in MGNP aggregate over the total number of cells in both the supernatant and the aggregate. High capture efficiencies up to 88% can be achieved with 45 minute incubation. Next, the effect of incubation time was examined. Interestingly, even in just 5 minutes, *E. coli* can be detected with a capture efficiency of 65%. Indeed, the capture efficiency using MGNP **3** is much higher than the 10-30 % range typically observed with antibody or lectin functionalized magnetic particles,[2, 3, 22] which can be difficult to fabricate because of challenges in immobilizing biomacromolecules. Furthermore, the orientation of the antibody/lectin on a NP surface is difficult to control, which may affect their binding capacities.[23]

MGNP/*E. coli* complexes were then imaged by TEM with MGNP aggregates observed on the surface, at the lateral ends and along the pili[24] of *E. coli* cells (**Figure 2-11**)., Although glyco-nanoparticles have been studied as bioprobes for pathogens,[25, 26] this is the first time that MGNPs have been used for bacterium detection and decontamination.

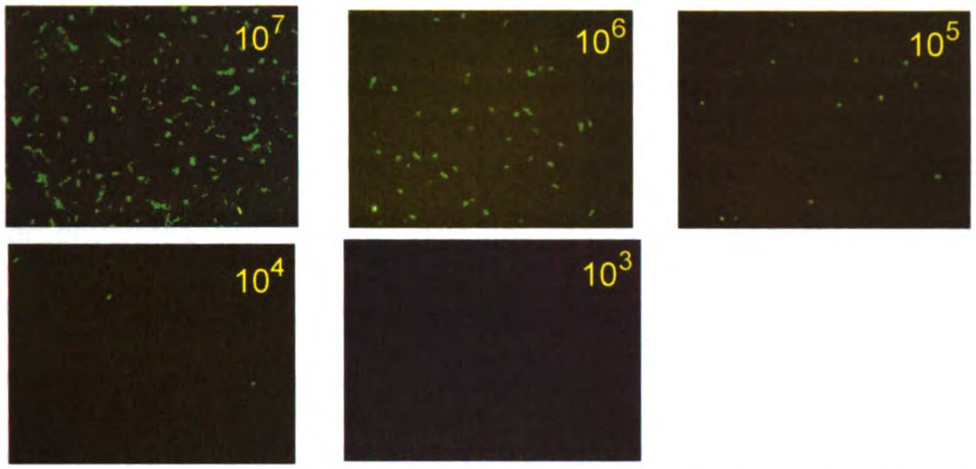

Figure 2-10. Representative fluorescence microscopic images of captured *E. coli*. The concentration of bacteria (cells/mL) incubated with MGNP **3** is indicated on each image.

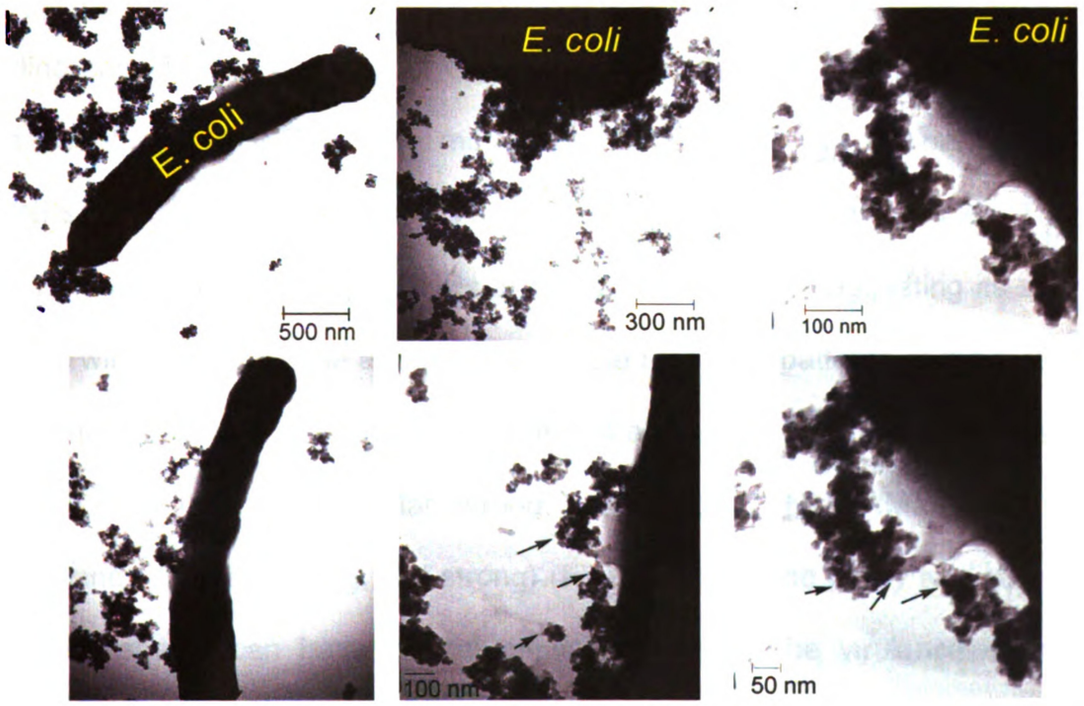

Figure 2-11. TEM images of MGNP **3**/*E. coli* complexes at different magnifications. Arrows indicate where MGNP **3** binds to the pili, which were faintly stained in the pictures. A drop of 1% phosphotungustic acid was used to negatively stain MGNP/*E. coli* aggregates.[27]

2.6. Bacterial Differentiation

Although we presented a full account on the quantification and enumeration of *E. coli* cells, we further investigated the possibility of bacterium

differentiation. It is known that several bacteria may bind with the same carbohydrate albeit with various affinities.[7] This provides a unique opportunity to use a MGNP array system, where the selective binding of a microbe to various carbohydrates will lead to different responses. The resulting characteristic response patterns[28, 29] will then allow differentiation of bacteria. As a proof-of-principle, we investigated the usage of two MGNPs (Man-MGNP **3** and Gal-MGNP **4**) to rapidly detect and differentiate three *E. coli* strains: ORN178, ORN208 a mutant strain with greatly reduced mannose binding affinity,[30] and an environmental strain (ES) isolated from Lake Erie with unknown carbohydrate binding specificity. While 65% of ORN178 was captured by MGNP **3**, only 15% was caught by MGNP **4**. The mutant strain ORN208 was trapped by both MGNPs, although at lower levels. With the ES strain, capture efficiencies of 70% and 75% were achieved by MGNPs **3** and **4**, respectively, suggesting its strong binding with both mannose and galactose. The response patterns of the three *E. coli* strains to Man-MGNP **3** and Gal-MGNP **4** allowed us to easily determine the microbial identity: ORN178 (Man strong, Gal weak), ORN208 (Man weak, Gal weak), and ES (Man strong, Gal strong) (**Figure 2-12**). The ability to distinguish pathogen strains can have clinical applications since the virulence of many pathogens can be correlated with carbohydrate binding specificity.[31] Moreover, the nondestructive nature of MGNP binding can allow the concentration and recovery of pathogens and further analysis by other techniques.[32]

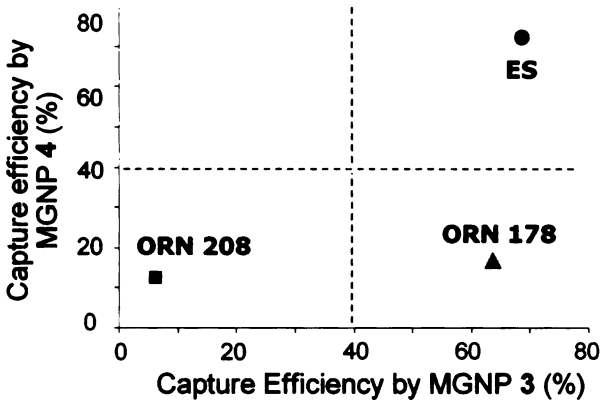

Figure 2-12. *E. coli* strain differentiation by MGNPs **3** and **4**.

In general, we were able to explore a MGNP-based system to not only detect *E. coli* within 5 min, but also remove up to 88% of the target bacteria from the medium. Furthermore, the identities of three different *E. coli* strains were easily determined on the basis of the response patterns to two MGNPs highlighting their potential in biosensing. Thus, we demonstrate the potential of sugar-coated magnetic nanoparticles for fast bacterial detection and removal, which provides new endeavors in pathogen decontamination and diagnostic applications.

2.7. Lipoic Carbohydrate Conjugates: Controlling Nonspecific Adsorption at Biointerfaces for Biosensor and Biomedical Application

Nonspecific adsorption from serum components is a general problem in biosensing and biomedical applications. Nonspecific adsorption of proteins or human serum components on biosensor surfaces of diagnostic devices reduce the accuracy of the bioanalysis and hence pose significant challenges for their use and applications. Therefore, the mechanistic understanding of the protein nonspecific adsorption on surfaces and the development of biointerfaces that

have the ability to resist nonspecific adsorption of protein have attracted significant research interests.[33] A number of blocking reagents have been studied both experimentally and theoretically. For example, biointerfaces modified with blocking reagents such as bovine serum albumin (BSA),[34, 35] PEG,[36, 37] and oligo-ethylene glycol based groups,[38, 39] have been shown to decrease nonspecific protein adsorption. Among them, the most commonly used blocking agents are BSA and PEG containing agents. Herein, we hypothesize that carbohydrates could be suitable candidates for reducing the nonspecific adsorption from serum components as well as the nonspecific cell attachment, and hence will play chief roles in enhancing the detection of harmful microbes and toxins.

The SAM scaffold[40] has recently appeared as one of the most promising model systems for mechanistic study of multivalent interactions. Carbohydrate SAMs offer extensive control over patterns, density, and orientation, which are of tremendous importance to elicit a clear structure-activity relationship between protein and carbohydrate recognition events.[41] More importantly, SAMs have been applied to label-free analysis methods such as QCM.[42] QCM transducer offers the benefits of real-time monitoring of protein adsorption to surface coating and can be used to characterize the properties of carbohydrate biointerfaces.

Herein, in collaboration with Dr. Zeng's laboratory from Oakland University, SAMs of sugar-thiolates on gold platforms were fabricated. It is well known that monolayers form spontaneously by adsorption of thiols from their solutions onto gold surfaces.[43] Six types of lipoic acid carbohydrate conjugates,

namely lipoic mannose (LMan), lipoic galactose (LGal), lipoic glucose (LGlc), lipoic sialic acid (LSia), lipoic N-acetyl glucosamine (LGlNAc), and lipoic fucose (LFuc) were synthesized and their properties toward protein resistance were measured using human serum samples, the most common clinical samples for bioanalysis. Resistance toward Hela cell attachment was also investigated as an example to understand the carbohydrate selectivity at cell surfaces.

As shown in **Figure 2-13**, the structures of the six lipoic carbohydrate derivatives consist of three components. The first component is the cyclic disulfide, which can adsorb strongly to the Au sensor surface via Au-S bond; the second is the OEG chain which can enhance aqueous solubility and form a monolayer; and the third is the carbohydrate linked through their respective reducing end. Preparation of these compounds commenced from the commercially available lipoic acid that was coupled to the Boc-protected diamine using a standard amide coupling condition, followed by removal of the Boc group promoted by trifluoroacetic acid (TFA) yielding lipoic amine (**Figure 2-13a**). The functionalization of carbohydrates with carboxylic acids was performed by reduction of the corresponding azido-propyl glycosides in the presence of succinic anhydride leading to the O-acetyl protected sugar acids in 75-87% yields (**Figure 2-13b**). These were then coupled to lipoic amine using HOBt/HBTU with subsequent protective group removal affording the six lipoic carbohydrate derivatives in good yields.

Figure 2-13. Synthesis of Lipoic Carbohydrate Conjugates.

The carbohydrate-derived lipoic acid derivatives were then studied as protein and cell resistant biomaterials in collaborations with Dr. Zeng's laboratory. The six types of carbohydrates were examined for their abilities to reduce nonspecific adsorption of human serum and Hela cells using QCM.[44] The data suggested that the structures of carbohydrates play an important role in resisting nonspecific binding. Specifically, the resistance was found to increase in the order LFuc < LMan < LGlNAc < LGlc < LSia < LGal, where LGal derivative resisted most nonspecific adsorption (**Figure 2-14A**). Furthermore, the combination of lipoic galactose and BSA was the most effective in reducing the adsorption of even undiluted human serum and the attachment of Hela cells while allowing specific binding (**Figure 2-14B**). Several control experiments have demonstrated that the resistant-ability of mixed LGal and BSA was comparable to the best known system for decreasing nonspecific adsorption.[44] The exact reason for this phenomenon is still not known.

A)

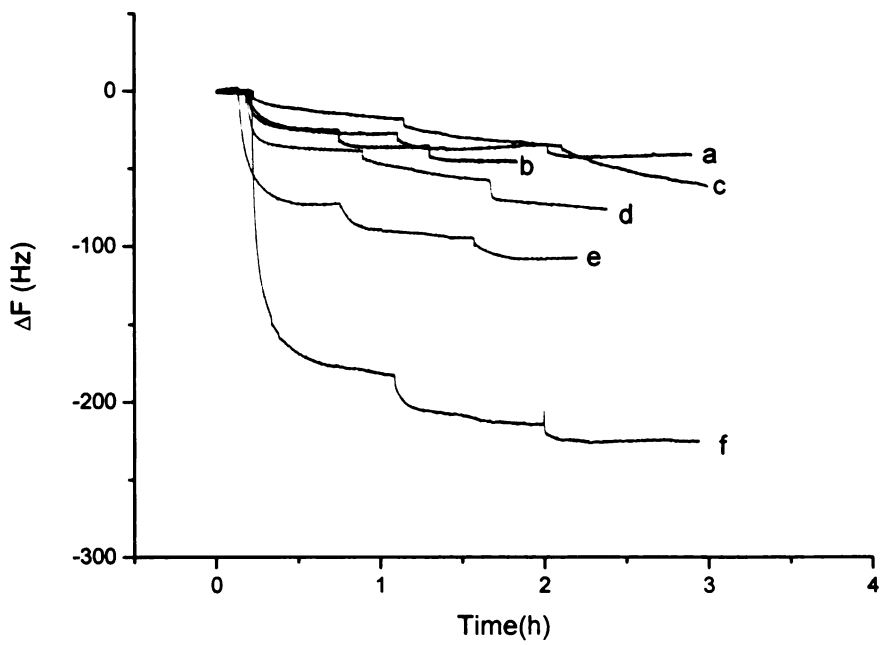

B)

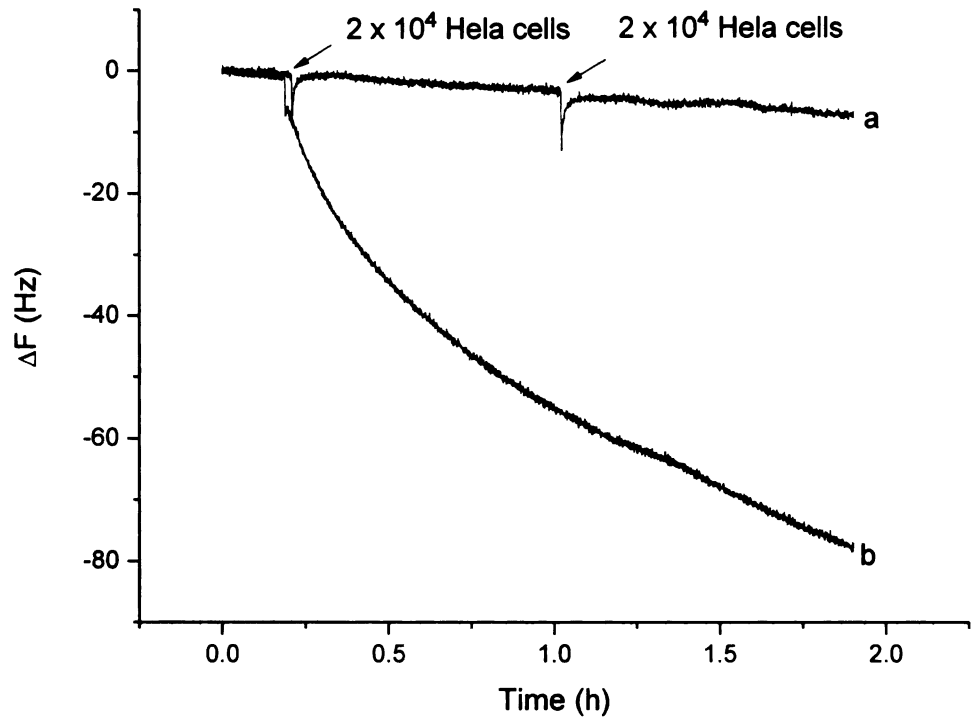

Figure 2-14. A) Blocking effect of various lipoic acid carbohydrate derivatives. (a) LGal, (b) LSia, (c) LGlc, (d) LGlNAc, (e) LMan, (f) LFuc; B) Real-time frequency responses to the addition of 2×10^4 Hela cells onto (a) the mixture of lipoic galactose and BSA modified Au quartz and (b) PEG-thiol modified Au quartz.

2.8. Experimental Section

2.8.a. Materials and Instrumentation

Unless otherwise indicated, all starting materials, reagents and solvents were obtained from commercial suppliers and used as supplied without further purification. Con A-FITC was purchased from Molecular Probes. *E. coli* ORN178 and ORN208 strains were kindly donated by Prof. Orndorff (North Carolina State University). All oxygen and moisture sensitive reactions were carried under nitrogen. Air sensitive solvents were transferred via syringe. Column chromatography was performed employing 230-400 mesh silica gels. Thin-layer

chromatography (TLC) was performed using glass plates pre-coated to a depth of 0.25 mm with 230-400 mesh silica gel impregnated with a fluorescent indicator (254 nm). All compounds were visualized by the use of UV light or a yellow stain containing $Ce(NH_4)_2(NO_3)_6$ (0.5 g) and $(NH_4)_6Mo_7O_{24}.4H_2O$ (24.0g) in 6 % H_2SO_4 (500 mL). Degassed and double deionized water (DDW) was used in all the biological assays.

NMR spectra were recorded on a Varian VXRS-400 or Inova-600 instruments and were referenced using Me_4Si (0 ppm), residual $CHCl_3$ (δ ^{1}H-NMR 7.26 ppm), $CDCl_3$ (δ ^{13}C-NMR 77.0 ppm), residual CHD_2OD (δ ^{1}H-NMR 5.32 ppm), CD_3OD (δ ^{13}C-NMR 49.0 ppm). Assignments of proton and carbon signals were carried out with the aid of gCOSY experiments. ESI mass spectra were recorded on ESQUIRE LC-MS operated in positive ion mode. High-resolution mass spectra were recorded on a Micromass electrospray Tof™ II (Micromass, Wythenshawe, UK) mass spectrometer equipped with an orthogonal electrospray source (Z-spray) operated in positive ion mode, which is located at the Mass Spectrometry and Proteomics Facility, the Ohio State University. XRD was recorded using Rigaku Ultima III multipurpose X-ray diffraction system. FTIR spectra (400-4000 cm^{-1}) were recorded as KBr pellet forms using FTIR Perkin Elmer Spectrum GX with ATR capabilities. Fluorescence emission spectra were recorded on an AMINCO BOWMAN II Luminescence spectrometer provided with a continuous (CW) high power Xe lamp as the excitation source and an excitation wavelength of 492 nm and spectra-recording at 500-650 nm. TGA was carried out on SDT 2960 Simultaneous DTA-TGA equipment and the

samples were heated at a constant heating rate of 10 °C/min from 50 to 1000 °C. TEM images were obtained using a Philips CM10 Mawah-NJ software Image Pro Plus 6.0, operating at 100 kV. Bacterium enumeration was carried out using an epifluorescent microscope (Olympus BX-51) with a 50-W Osram UV mercury lamp.

2.8.b. *E. coli* Detection using MGNPs

E. coli cells were grown overnight in LB media at 37 °C to an approximately 10^9 cells/mL. The culture was then centrifuged and cells washed with Phosphate Buffered Saline (PBS) buffer. MGNPs were added to a 4 ml vial containing *E. coli* solution (10^3-10^7 cells/mL, 1 mL) in PBS buffer, mixed well, and incubated at room temperature with gentle shaking. After incubation, the samples were left on a permanent external magnet for 1 minute. The supernatant was carefully removed by pipetting and the resulting nanoparticles were washed three times and then re-suspended with PBS to the original volume. It is worth mentioning that the successive buffer washing cycles are crucial to remove unbound cells and hence nonspecific binding. All samples were then fixed with 37 % para-formaldehyde (54 µL/mL), sonicated for 2 min. and then stained with a non-specific nucleic acid stain (PicoGreen, 2 µL/mL sample) for 5 minutes. Since aggregation of bacterial cells interferes with accurate optical quantification, the cells were dispersed by sonication. *E. coli* detection and enumeration was carried out using epifluorescent microscopy. Samples were vacuum-filtered through a glass fiber prefilter and black polycarbonate filter (25-mm diameter; 0.22 µm). The filter paper was then air dried, transferred to a microscope slide, covered

with a drop of immersion oil and a cover glass, and imaged. Individual cells were quantified by counting randomly 20 fields per each run and a minimum of 200 cells. The total number of cells on each slide was calculated by multiplying the average number of cell per field by the number of fields (46691) per slide. All measurements were reproducible and the deviations were found to be within 10%.

2.8.c. Evaluation of Capture Efficiency Variation

Four solutions of *E. coli* cells (~ 1.5 x 10^6 cell/mL, 1 mL) were incubated with MGNP **3** (2 mg) each for 45 minutes and the capture efficiency (C. E.) for each incubation was calculated to be 84, 80, 88 and 82 % for four separate experiments. The average capture efficiency for this quadruplicate experiment is 83.5 ± 3.4%.

$$\text{Capture Efficiency (C.E.)} = \frac{\#\text{ of cells in MGNP aggregate}}{\#\text{ of cells in MGNP aggregate} + \#\text{ of cells in supernatant}}$$

2.8.d. HR-MAS ^{1}H NMR Analyses.

HR-MAS experiments were carried out on a Bruker BioSpin FT-NMR Avance 500 equipped with an 11.7 T superconducting ultrashield magnet available at C.I.G.A. (Centro Interdipartimentale Grandi Apparecchiature) of the University of Milan. The HR-MAS probe with internal lock is capable of performing either direct or indirect (inverse) detection experiments. MAS experiments were performed at spinning rates of up to 15 kHz (15 kHz maximum MAS rotation available) using a 50 µL zirconia rotor. All the samples were diluted at different concentrations with deuterated solvents to find out the concentration

limit to the NMR signal broadening. HR-MAS ^{1}H-NMR spectra were obtained using 200-400 scans for each experiment. The sample temperature was dependent on the rotation speed.

2.8.e. QCM Measurement

The QCM cell filled with 1 mL of PBS buffer was placed in a Faraday cage at room temperature. Contents of the QCM cell were continuously stirred before, during, and after the addition of analyte, which was added to the cell in 20 µL volumes. The frequency and series damping resistance of the QCM were monitored using a network/spectrum/ impedance analyzer (Agilent 4395A). The relationship between the change in resonant frequency (ΔF) resulting from a change in mass (Δm), was given by the Sauerbrey's equation, $\Delta F = -2n\Delta m F_0^2 (\rho_q \mu_q)^{-1/2} A^{-1}$, where n is the overtone number, μ_q is the shear modulus of the quartz (2.947×10^{11} g.cm^{-1}.s^{-2}), and ρ_q is the density of the quartz (2.648 g.cm^{-3}). According to the Sauerbrey's equation, our fitted frequency change of 1 Hz corresponds to a mass increase of 1 ng for the 10 MHz quartz crystal used in this work.

2.8. f. Syntheses of MGNPs

1. Synthesis of sugar building blocks (Mannose and Galactose)

Synthesis of mannose amido-acid (M5).

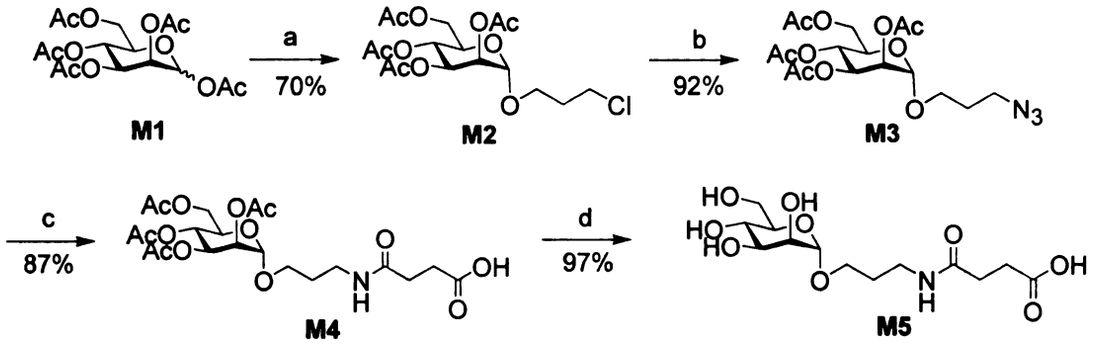

Figure 2-15. Reagents and conditions: a) 3-chloro-1-propanol, $BF_3.Et_2O$, DCM; b) NaN_3, DMF, 80 °C; c) succinic anhydride, H_2/Pd-C, THF, 3h; d) NaOMe, MeOH.

3-Azidopropyl 2,3,4,6-tetra-*O*-acetyl-α-D-mannopyranoside (M3). **M3** was prepared as previously described starting from pentaacetyl mannose **M1**.[45-47] Comparison of NMR spectra with those reported confirms its structure. [45-47]

***O*-Acetyl protected mannose amido-acid (M4).** A solution of **M3** (0.650 g, 1.51 mmol), succinic anhydride (0.230 g, 2.30 mmol) and 10 % Pd/C (0.166 g) in dry THF (20 mL) was stirred at room temperature under H_2. After 3 hours, TLC (EtOAc-hexanes, 1:1) showed complete conversion of starting material (R_f = 0.5) to a major product (R_f = 0.0). The reaction mixture was then filtered off through Celite and concentrated. The residue was purified by column chromatography starting from EtOAc-hexanes 1:1 increasing to MeOH-DCM, 1:10 to afford the product **M4** as a sticky white solid (0.67 g, 88 % yield). ^1H NMR ($CDCl_3$, 600 MHz): δ_H 1.78-1.85 (m, 2H, $OCH_2CH_2CH_2NH$), 1.97 (s, 3H, OAc), 2.03 (s, 3H,

OAc), 2.08 (s, 3H, OAc), 2.13 (s, 3H, OAc), 2.50 (t, J = 6.3 Hz, 2H, $COCH_2CH_2COOH$), 2.64 (t, J = 6.0 Hz, 2H, $COCH_2CH_2COOH$), 3.35 (t, J = 6.0 Hz, 2H, $OCH_2CH_2CH_2NH$), 3.47-3.50 (m, 1H, $OCHHCH_2$), 3.74-3.78 (m, 1H, $OCHHCH_2$), 3.95-3.97 (m, 1H, H-5), 4.11 (dd, J = 2.4, 12.0 Hz, 1H, H-6a), 4.24 (dd, J = 4.8, 12.0 Hz, 1H, H-6b), 4.79 (d, J = 1.2 Hz, 1H, H-1), 5.21 (dd, J = 1.2; 2.4 Hz, 1H, H-2), 5.25-5.27 (m, 2H, H-3, H-4), 6.42 (bs, 1H, NH). ^{13}C NMR ($CDCl_3$, 100 MHz): δ_C 20.9, 21.0, 21.1 (4C, CH_3), 29.2 (1C, CH_2CH_2NH), 30.1 (1C, $COCH_2$), 31.0 (1C, CH2COOH), 37.6 (1C, CH_2CH_2NH), 62.8 (1C, CH_2OAc), 66.3 (1C, CH), 66.8 (1C, CH), 68.7 (1C, CH_2O), 69.4 (1C, CH), 69.7 (1C, CH), 97.8 (1C, $C_{anomeric}$), 170.0 (1C, $CH_3C(O)O$), 170.4 (1C, $CH_3C(O)O$), 170.5 (1C, $CH_3C(O)O$), 171.2 (1C, $CH_3C(O)O$), 172.9 (1C), 175.9 (1C). ESI-MS *m/z* calcd. for $C_{21}H_{31}NNaO_{13}$ $[M + Na]^+$: 528.5; found: 528.4.

Mannose amido-acid (M5). A freshly prepared solution of NaOMe-MeOH (0.35 mL, 1 M) was added to a solution of **M4** (0.350 g, 0.692 mmol) in dry methanol (8 mL) at room temperature under nitrogen. The mixture was stirred for 5 hours, neutralized with Amberlite IR-120 (H^+) ion-exchange resin, filtered, and concentrated. Flash column chromatography (MeOH-DCM, 1:1) of the residue afforded **M5** as a gel like white solid in 97% yield (0.23 g). ^1H NMR (CD_3OD, 600 MHz): δ_H 1.76-1.80 (m, 2H, $OCH_2CH_2CH_2NH$), 2.45 (t, J = 6.9 Hz, 2H, $COCH_2CH_2COOH$), 2.56 (t, J = 6.9 Hz, 2H, $COCH_2CH_2COOH$), 3.23-3.29 (m, 2H, $OCH_2CH_2CH_2NH$), 3.43-3.47 (m, 1H, $OCHHCH_2$), 3.50-3.54 (m, 1H, H-5), 3.58 (t, J = 9.6 Hz, 1H, H-4), 3.68-3.71 (m, 2H, H-3, H-6a), 3.76-3.80 (m, 2H, H-2, $OCHHCH_2$), 3.84 (dd, J = 2.1, 11.7 Hz, 1H, H-6b), 4.74 (d, J = 1.2 Hz, 1H, H-

1). ^{13}C NMR (CD_3OD, 100 MHz): δ_C 29.1 (1C, $CH_2CH_2CH_2NH$), 31.0 (1C, $COCH_2CH_2COOH$), 31.4 (1C, $COCH_2CH_2COOH$), 36.4 (1C, CH_2CH_2NH), 61.7 (1C, CH_2OH), 64.8 (1C, CH_2 CH_2O), 67.5 (1C, CH), 71.0 (1C, CH_2O), 71.4 (1C, CH), 73.5 (1C, CH), 100.5 (1C, $C_{anomeric}$), 174.0 (1C). HR-MS *m/z* calcd. for $C_{13}H_{23}NNaO_9$ $[M + Na]^+$: 360.1271, found: 360.1273.

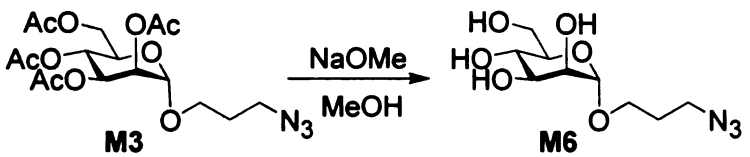

Figure 2-16. Synthesis of Azido-mannose for *Click* Chemistry.

3-α-Azidopropyl D-mannopyranoside (M6). A solution of **M3** (1.35 g, 5.13 mmol) in MeOH (10 mL) was treated with a solution of sodium (23 mg) in MeOH (1 mL). After 1 hour, the solution was acidified with Amberlite IR-120H$^+$ to pH 6. Evaporation of the solvent under reduced pressure afforded **M6** as a white crystalline solid (0.783 g, 95%). ^1H NMR (CD_3OD, 600 MHz): δ_H 1.83-1.88 (m, 2H, $CH_2CH_2N_3$); 3.41 (td, *J* = 6.8, 3.6 Hz, 2H, CH_2N_3); 3.48-3.53 (m, 2H, $OCHHCH_2$ + H-5); 3.60 (t, *J* = 9.6 Hz, 1H, H-4); 3.67 (dd, *J* = 3.2, 9.2 Hz, 1H, H-3); 3.71 (t, *J* = 6.0 Hz, 1H, H'-6); 3.79-3.85 (m, 3H, H-2, H-6", H-7"); 4.74 (d, *J* = 1.6 Hz, 1H, H-1). ^{13}C NMR (CD_3OD, 100 MHz): δ_C 28.8 (1C, $CH_2CH_2N_3$); 56.2 (1C, $CH_2CH_2N_3$); 61.7 (1C, CH_2OH); 64.2 (1C, CH_2CH_2O); 67.4 (1C, CH); 71.0 (1C, CH); 71.4 (1C, CH); 73.6 (1C, CH); 100.5 (1C, $C_{anomeric}$).

Synthesis of galactose amido-acid (G5).

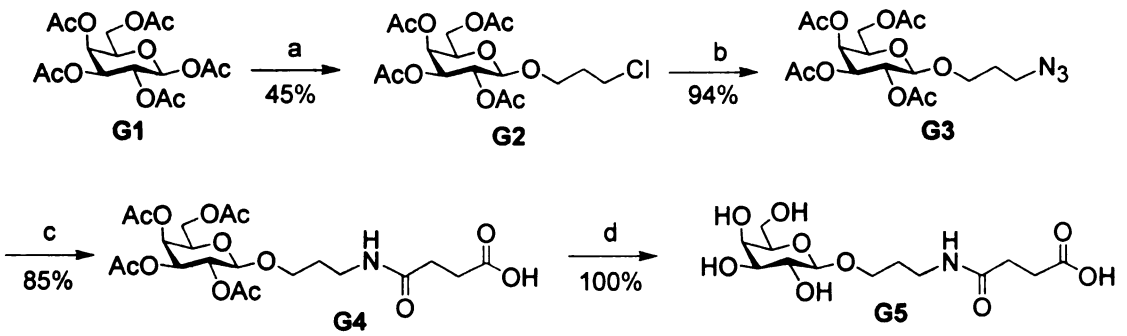

Figure 2-17. Reagents and conditions: a) 3-chloro-1-propanol, $BF_3.Et_2O$, DCM; b) NaN_3, DMF, 80 °C; c) succinic anhydride, H_2/Pd-C, THF, 3h; d) NaOMe, MeOH.

3-Azidopropyl 2,3,4,6-tetra-*O*-acetyl-β-D-galactopyranoside (G3). **G3** was prepared analogously as **M3** starting from commercially available penta-acetyl galactose **G1**.[47, 48] Comparison of NMR spectra with those reported in the literature confirms its structure. [47, 48]

***O*-Acetyl protected galactose amido-acid (G4).** A solution of **G3** (0.510 g, 1.18 mmol), succinic anhydride (0.180 g, 1.80 mmol), and 10 % Pd-C (0.130 g) in dry THF (15 mL) was stirred at room temperature under H_2. After 3 hours, TLC (EtOAc-hexanes, 1:1) showed complete conversion of starting material (R_f = 0.5) to a major product (R_f = 0.0). The reaction mixture was then filtered off through Celite and concentrated. The residue was purified by column chromatography starting from 1:1 EtOAc-hexanes to 1:10 MeOH-DCM to afford the product **G4** as a sticky white solid (0.508 g, 85 % yield). ^1H NMR ($CDCl_3$, 600 MHz): δ_H 1.74-1.86 (m, 2H, $OCH_2CH_2CH_2NH$), 1.99 (s, 3H, OAc), 2.05 (s, 3H, OAc), 2.08 (s, 3H, OAc), 2.17 (s, 3H, OAc), 2.47-2.70 (m, 4H, $COCH_2CH_2COOH$), 3.31-3.38 (m,

1H, CH_2CHHNH), 3.40-3.46 (m, 1H, CH_2CHHNH), 3.56-3.61 (m, 1H, $OCHHCH_2$), 3.92 (td, J = 1.2, 10.2 Hz, 1H, H-5), 3.98-4.03 (m, 1H, $OCHHCH_2$), 4.10-4.15 (m, 1H, H-6a), 4.19-4.24 (m, 1H, H-6b), 4.44 (d, J = 7.6 Hz, 1H, H-1), 5.05 (dd, J = 3.6, 10.4 Hz, 1H, H-3), 5.17 (dd, J = 8.0, 10.8 Hz, 1H, H-2), 5.40 (dd, J = 0.8, 3.2 Hz, 1H, H-4), 6.45 (t, J = 5.6 Hz, 1H, NH). ^{13}C NMR ($CDCl_3$, 100 MHz): δ_C 20.8, 21.9, 21.1 (4C, CH_3), 29.1 (1C, CH_2CH_2NH), 30.6 (1C, $COCH_2$), 30.7 (1C, CH2-COOH), 38.3 (1C, CH_2CH_2NH), 61.5 (1C, CH_2OAc), 67.2 (1C, CH), 69.3 (1C, CH), 69.5 (1C, CH_2O), 70.7 (1C, CH), 71.0 (1C, CH), 101.6 (1C, $C_{anomeric}$), 170.3 (1C, $CH_3C(O)O$), 170.46 (1C, $CH_3C(O)O$), 170.54 (1C, $CH_3C(O)O$), 170.8 (1C, $CH_3C(O)O$), 173.3 (1C), 175.3 (1C). MS-ESI *m/z* calcd. for $C_{21}H_{31}NNaO_{13}$ [M + Na]$^+$: 528.5; found: 528.4.

Galactose amido-acid (G5). A solution of **G4** (0.310 g, 0.613 mmol) in MeOH (5 mL) was treated with a solution of sodium (8.60 mg) in MeOH (0.35 mL) under nitrogen. After 3 h, the solution was acidified with Amberlite IR-120 H^+ to pH=6. Evaporation of the solvent under reduced pressure afforded **G5** as a white sticky solid in quantitative yield (0.206 g). ^{1}H NMR (CD_3OD, 600 MHz): δ_H 1.74-1.79 (m, 2H, $OCH_2CH_2CH_2NH$), 2.44 (t, J = 6.6 Hz, 2H, $COCH_2CH_2COOH$), 2.56 (t, J = 7.2 Hz, 2H, $COCH_2CH_2COOH$), 3.23-3.27 (m, , 1H, OCH_2CH_2CHHNH), 3.31-3.35 (m, , 1H, OCH_2CH_2CHHNH), 3.45 (dd, J = 3.0, 9.6 Hz, 1H,), 3.49-3.52 (m, 2H, H-2, H-5), 3.60 (dt, J = 6.0, 10.2 Hz, 1H, $OCHHCH_2$), 3.68-3.72 (m, 1H, H-6a), 3.73-3.77 (m, 1H, H-6b), 3.81 (dd, J = 1.2, 3.3 Hz, 1H, H-4), 3.92 (dt, J = 6.0, 10.2 Hz, 1H, $OCHHCH_2$), 4.20 (d, J = 7.8 Hz, 1H, H-1). ^{13}C NMR (CD_3OD, 100 MHz): δ_C 29.1 (1C, $CH_2CH_2CH_2NH$), 32.6 (1C, $COCH_2$ CH2COOH), 33.1 (1C,

$COCH_2$ CH_2COOH), 36.5 (1C, CH_2CH_2NH), 61.4 (1C, CH_2OH), 67.2 (1C, CH_2 CH_2O), 69.3 (1C, CH), 71.3 (1C, CH_2O), 73.8 (1C, CH), 75.5 (1C, CH), 103.8 (1C, $C_{anomeric}$), 174.7 (1C). HR-MS *m/z* calcd. for $C_{13}H_{23}NO_9$ $[M + Na]^+$: 360.1271, found: 360.1273.

2. Synthesis of Alkyne-Siloxane (AS) Linker for *Click* Chemistry

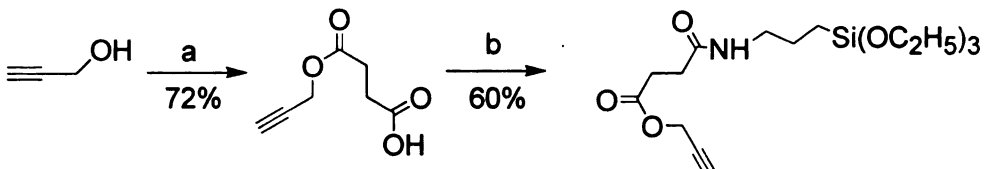

Propargyl Alcohol **Alkyne-Acid (AA)** **Alkyne-Siloxane (AS)**

Figure 2-18. Reagents and conditions: a) succinic anhydride, DMAP, DCM, 6h; b) APTES, EDC, DCM, 12h.

Alkyne-Acid (AA). To a solution of propargyl alcohol (2.06 g, 36.8 mmol) and succinic anhydride (4.65 g, 46.5 mmol) in dry DCM (30 mL), 4-dimethylaminopyridine (DMAP) (4.80 g, 39.3 mmol) was added and the reaction mixture was stirred under nitrogen for 6 hours. After TLC showed complete conversion, the solution was diluted with DCM, acidified with 0.1 M HCl till pH=2 and then extracted with DCM. The organic layer was then dried and concentrated to afford 4.00 g (72 %) of **AA** as a white solid. ^1H NMR ($CDCl_3$, 600 MHz): δ_H 2.47 (t, J = 2.4 Hz, 1H), 2.63-2.70 (m, 4H), 4.68 (d, J = 2.4 Hz, 2H, CH_2O). ^{13}C NMR ($CDCl_3$, 100 MHz) δ_c 28.8, 29.0, 31.2, 52.6, 75.3, 171.6, 178.3. MS (ESI) *m/z* calcd. for $C_7H_8NaO_4$ $[M + Na]^+$: 179.1; found: 179.1.

Prop-2-ynyl succinate amidopropyl triethoxysilane (AS). To a solution of acid **AA** (0.550 g, 3.52 mmol) and 1-[3-(dimethylamino)-propyl]-3-ethylcarbodiimide

hydrochloride (EDC) (1.00 g, 5.22 mmol) in dry DCM (10 mL), APTES (0.942 g, 4.25 mmol) was added and the reaction mixture was stirred under nitrogen. After 12 hours, the solvent was removed under reduced pressure. The residue was purified by column chromatography from 1:1 EtOAc-hexanes to 1:10 MeOH-DCM to give 0.75 g (60 %) of the desired linker **AS** as a clear white crystalline solid. ^{1}H NMR ($CDCl_3$, 600 MHz): δ_H 0.58 (t, J = 12.0 Hz, 2H, CH_2CH_2Si), 1.17 (t, J = 10.8 Hz, 9H, $(OCH_2CH_3)_3$), 1.53-1.60 (m, 2H), 2.43 (t, J = 10.8 Hz, 2H), 2.45 (t, J = 4.2 Hz, 1H), 2.66 (t, J = 10.8 Hz, 2H), 3.18 (q, J = 10.8 Hz, 2H, $NHCH_2CH_2$), 3.76 (q, J = 10.8 Hz, 6H, $(OCH_2CH_3)_3$), 4.63 (d, J = 3.6 Hz, 2H, CH_2OCO), 6.01(bs, 1H, NH). ^{13}C NMR ($CDCl_3$, 100 MHz) δ_C 7.9, 18.5, 23.0, 29.5, 31.0, 42.1, 52.3, 58.6, 75.2, 77.7, 171.1, 172.4. MS (ESI) *m/z* calcd. for $C_{16}H_{29}NNaO_6Si$ $[M + Na]^+$: 382.2; found: 382.3.

3. Synthesis of magnetic Fe_3O_4 NPs and subsequent immobilization

Preparation of silica-coated magnetite nanoparticles (NP 1)

Fe_3O_4 NPs were prepared by slight modification of the co-precipitation method.[14, 15, 49] Briefly, 1M Fe^{3+} and 1M Fe^{2+} were prepared by dissolving the iron salts in 2M HCl solutions, respectively. Then 1 eq. of Fe^{3+} solution was mixed with 0.5 eq. of Fe^{2+} solution in a degassed flask. NH_4OH (30%) was added until pH ~11 was reached where a black material was precipitated. Adjustment of pH ~11-12 is critical to get 6 - 15 nm particle size (confirmed by TEM). After vigorous stirring for 30 minutes at room temperature, the resulting black NPs were isolated by applying a permanent external magnet (Lifesep® 50 SX magnetic separator), washed 6 times with double deionized water and 3

times with ethanol. In an effort to better suit biorecognition purposes, we used PVP as the surfactant and TEOS as the stable coated silica shell. In a typical experimental procedure,[8] a solution of PVP (Mw ~ 55 KDa, 0.65 mL, 25.6 g/L) was added to the bare Fe_3O_4 NPs suspended in DDW (150 mL). The mixture was stirred overnight at room temperature. The resulting nanoparticles were then separated, thoroughly washed by water-acetone mixture and re-suspended in 2-propanol: water (4:1 v/v, 150 mL). NH_4OH solution (0.2 % v/v, 0.3 mL) was added followed by dropwise addition of TEOS (1.5 mL) over 1 hour with continuous stirring. The reaction mixture was stirred overnight, isolated and washed repeatedly with diethyl ether and ethanol leading to silica coated NP **1**.[50]

Preparation of Man-MGNP 2 using Huisgen [2+3] cycloaddition reaction

Alkyne-Siloxane (**AS**) (55 mg) was added to silica coated NP **1** (55 mg) suspended in dry toluene (100 mL) (**Figure 2-1a**). The mixture was sonicated for 12 hours and then stirred overnight. The resulting alkyne-NP were magnetically isolated, washed with water, ethanol, diethyl ether, DMSO and redispersed in DMSO:H_2O (4:1). 3-Azidopropyl α-D-mannopyranoside **M6** (55 mg), $CuSO_4.5H_2O$ (10 mg) and sodium ascorbate (20 mg) were then added to the alkyne-functionalized NP in DMSO:H_2O (4:1, 50 mL) under sonication (**Figure 2-1b**). The reaction mixture was stirred at room temperature for 24 hours under nitrogen. The resulting Man-MGNP **2** were then isolated and washed with water, ethanol and ether successively.

Preparation of MGNPs 3 and 4 using amide (BOP) coupling

To prepare the amine-functionalized NP, NP **1** was suspeneded in dry toluene (150 mL) and sonicated for 30 minutes. APTES (2 % w/v) was then added and stirred at 60 °C overnight (**Figure 2-1a**). The resulting amine-NP was isolated, washed and redispersed in ethanol. To immobilize the surface with sugar using amide bond coupling, amine-NP (450 mg) was washed with DMF twice, redispersed in DMF (150 mL) and sonicated for 30 minutes. The coupling solution was prepared by mixing mannose amido-acid **M5** (0.515 g), benzotriazole-1-yl-oxy-tris-(dimethylamino)-phosphonium hexafluorophosphate (BOP) (1.1 g, 1.5 eq.), 1-hydroxybenzotriazole (HOBT) (0.25 g, 1.3 eq.), and diisopropylethylamine (DIPEA) (1.0 mL, 4 eq.) in DMF (15 mL). The coupling solution was then added dropwise to the amine-NP in DMF under sonication and the reaction mixture was stirred overnight at room temperature (**Figure 2-1c**). The resulting Man-MGNP **3** was then isolated and washed with ether and ethanol. The same protocol was followed to synthesize the analogous Gal-MGNP **4** using galactose amido-acid **G5**.

2.8.f. Synthesis of Lipoic Carbohydrate Derivatives

1. Synthesis of Lipoic Amine

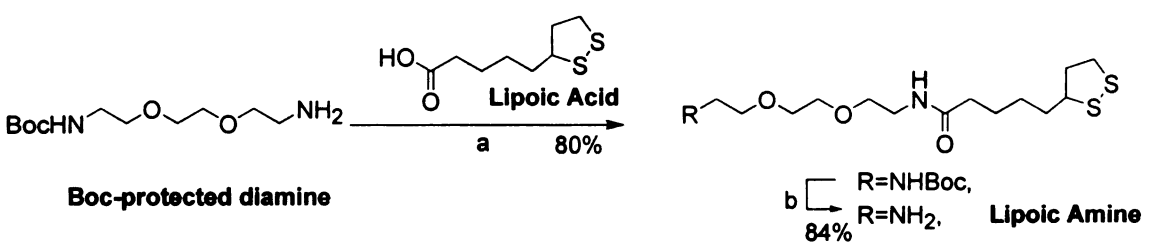

Figure 2-19. Reagents and conditions: a) EDC, Et_3N, DCM, overnight; b) TFA, DCM, 1 h.

Lipoic Amine. A solution of lipoic acid (0.50 g, 2.42 mmol), Boc-protected diamine[51] (1.40 g, 5.64 mmol), *N*-ethyl *N,N'*-dimethylaminopropyl carbodiimide hydrochloride (EDC, 0.930 g, 4.84 mmol) and triethylamine (Et_3N, 1.00 mL, 7.12 mmol) in anhydrous dichloromethane (DCM, 10 mL) was stirred under nitrogen at room temperature for 12 hrs. The reaction mixture was rotary evaporated and the resulting residue was purified by column chromatography eluting with 7% MeOH in CH_2Cl_2 to afford the protected lipoic amide as sticky yellowish oil (0.85 g, 80%). ^1H NMR (500 MHz, $CDCl_3$): δ_H 1.42 (s, 9H, CH_3), 1.40-1.50 (m, 2H, $COCH_2CH_2CH_2CH_2CHS$), 1.60-1.72 (m, 4H, $COCH_2CH_2CH_2CH_2CHS$), 1.85-1.92 (m, 1H, CH_aHCH_2S), 2.18 (t, J = 7.5 Hz, 2H, $COCH_2CH_2CH_2CH_2CHS$), 2.40-2.47 (m, 1H, CHH_bCH_2S), 3.06-3.18 (m, 2H, CH_2S), 3.28-3.32 (m, 2H, $CONHCH_2$), 3.44 (dd, J = 5.5, 10.5 Hz, 2H, $BocNHCH_2$), 3.52-3.57 (m, 1H, $COCH_2CH_2CH_2CH_2CHS$), 3.54 (t, J = 5.0 Hz, 4H, OCH_2CH_2O), 3.58-3.62 (m, 4H, $CH_2OCH_2CH_2OCH_2$), 5.0 (bs, 1H, NH), 6.1 (bs, 1H, NH). ^{13}C NMR (125 MHz, $CDCl_3$): δ_C 25.6, 28.6, 29.1, 34.9, 36.6, 38.67, 38.69, 39.4, 40.45, 40.48, 40.55, 56.7, 70.16, 70.42, 70.47, 162.7, 173.1. HRMS *m/z* calcd. for $C_{19}H_{37}N_2O_5S_2$ $[M+H]^+$: 437.2018; found: 437.2009. Deprotection of lipoic amide (0.85 g, 1.95 mmol) was completed with TFA (2 mL) in CH_2Cl_2 (3 mL) after 1 h. The reaction mixture was evaporated and then purified by flash column chromatography (25% MeOH in CH_2Cl_2) to furnish lipoic amine as a sticky yellowish gelatin in 84% yield (0.55 g). ^1H NMR (500 MHz, CD_3OD): δ_H 1.42-1.48 (m, 2H, $COCH_2CH_2CH_2CH_2CHS$), 1.60-1.78 (m, 4H, $COCH_2CH_2CH_2CH_2CHS$), 1.88-1.95 (m, 1H, CH_aHCH_2S), 2.24 (t, J = 7.0 Hz, 2H, $COCH_2CH_2CH_2CH_2CHS$),

2.45-2.52 (m, 1H, CH$H_b$$CH_2$S), 3.10-3.22 (m, 4H, C$H_2S, CH_2$$NH_2$), 3.38 (t, J = 5.5 Hz, 2H, CONHC$H_2$$CH_2$O), 3.58 (t, J = 5.5 Hz, 2H, CONHCH$_2$CH_2O), 3.58-3.62 (m, 1H, COCH$_2$CH$_2$CH$_2$CH$_2$CHS), 3.66-3.71 (m, 4H, OCH_2CH_2O), 3.74 (t, J = 5.0 Hz, 2H, OCH_2CH$_2$$NH_2$). ^{13}C NMR (125 MHz, CD_3OD): δ_C 25.5 (1C, COCH$_2$CH$_2$CH$_2$CH$_2$CHS), 28.7 (1C, COCH$_2$CH$_2$CH$_2$CH$_2$CHS), 34.6 (1C, COCH$_2$CH$_2$CH$_2$CH$_2$CHS), 35.7 (1C, COCH$_2$CH$_2$CH$_2$CH$_2$CHS), 38.2 (1C, SCH$_2$), 39.0 (1C, CONHCH$_2$), 39.5 (1C, NH$_2$CH$_2$), 40.2 (1C, SCHCH$_2$CH$_2$S), 56.5 (1C, SCHCH$_2$), 66.7 (1C, OCH$_2$CH$_2$NH$_2$), 69.5 (1C, OCH$_2$CH$_2$NHCO), 70.12, 70.19 (2C, OCH$_2$CH$_2$O), 175.1 (1C, NHCO). HR-MS m/z calcd. for $C_{14}H_{29}N_2O_3S_2[M+H]^+$: 337.1620; found: 337.1628.

2. Synthesis of Lipoic Galactose (LGal)

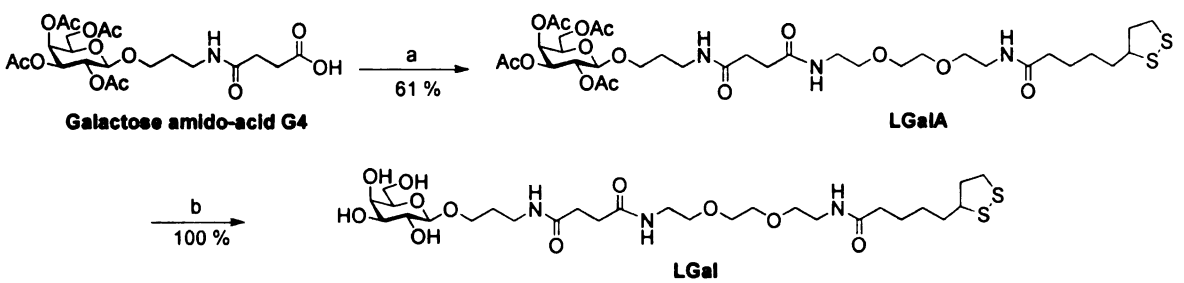

Figure 2-20. Reagents and conditions: a) Lipoic amine, HBTU/HOBT, DIPEA, DMF, 3hrs; b) NaOMe, MeOH, 1h.

General Procedures for *O*-acetyl sugar acids formation, amidation and deprotection. To functionalize the carbohydrates, a solution of the azido propyl glycoside, succinic anhydride (1.5 equiv.) and 10% Pd/C in dry THF was stirred at room temperature under H_2. After 3 h, TLC (EtOAc-hexanes, 1:1) showed complete conversion of starting material to a major product. The reaction mixture was then filtered through Celite and concentrated. The residue was purified by

column chromatography to afford the product *O*-acetyl protected sugar acids as a gel like solid in 75 - 87%yield. A solution of O-acetyl sugar acid, 2-(1H-benzotriazole-1-yl)-1,1,3,3-tetra-methyluronium hexafluorophosphate (HBTU) (1 equiv.), hydroxybenzotriazole (HOBT) (1 equiv.), and DIPEA (3.5 equiv.) in anhydrous DMF was stirred under nitrogen at room temperature for 5 min. Lipoic amine (1.5 equiv.) was then added and the reaction mixture was stirred for 3 h. The solvent was removed, and the resulting mixture was washed with water followed by brine, dried over Na_2SO_4 and rotary evaporated. The residue was purified by column chromatography eluting with 3 - 20% MeOH in DCM to afford the lipoic sugar acetates. Then the solution of lipoic sugar acetate (0.2 M) in MeOH (2 mL) was treated with a solution of 30% NaOMe in MeOH (0.2 mL) under nitrogen. After 1 h, the solution was neutralized with Amberlite IR -120 H^+ to pH=6 (For lipoic sialic acid synthesis, 0.2 mL of water was added to the reaction mixture half an hour prior to neutralization). Evaporation of solvent under reduced pressure afforded the requisite final lipoic carbohydrate derivatives (LGal, LMan, LFuc, LGlNAc, LGlc and LSia) in 45 - 61%yields for the two steps.

Lipoic Galactose Acetate (LGalA). LGalA (0.148 g, 0.180 mmol) was synthesized in 61% yield following the general procedure for amidation starting from galactose amido acid **G4** synthesized before (0.150 g, 0.297 mmol). ^1H NMR (500 MHz, $CDCl_3$): δ_H 1.40-1.48 (m, 2H, $COCH_2CH_2CH_2CH_2CHS$), 1.60-1.73 (m, 4H, $COCH_2CH_2CH_2CH_2CHS$), 1.74-1.80 (m, 2H, $COH_2CH_2CH_2NH$), 1.87-1.93 (m, 1H, CH_aHCH_2S), 1.98 (s, 3H, OCH_3), 2.04 (s, 3H, OCH_3), 2.07 (s, 3H, OCH_3), 2.16 (s, 3H, OCH_3), 2.20 (t, J = 6.5 Hz, 2H,

COCH_2CH$_2$CH$_2$CH$_2$CHS), 2.42-2.48 (m, 1H, CHH_bCH$_2$S), 2.49-2.57 (m, 4H, COCH_2CH_2CO), 3.08-3.13 (m, 1H, CH$_2$CH_aHS), 3.14-3.19 (m, 1H, CH$_2$CHH_bS), 3.22-3.40 (m, 2H, OCH$_2$CH$_2$CH_2NH), 3.41-3.46 (m, 4H, CONHCH_2), 3.53-3.58 (m, 6H, H_2COCH$_2$CH$_2$OCH_2, OCH_aHCH$_2$CH$_2$NH, COCH$_2$CH$_2$CH$_2$CH$_2$CHS), 3.60 (s, 4H, H$_2$COCH_2CH_2OCH$_2$), 3.91 (dt, J = 1.0, 6.0 Hz, 1H, H-5), 3.94-3.99 (m, 1H, OCHH_bCH$_2$CH$_2$NH), 4.10-4.20 (m, 2H, H-6), 4.44 (d, J = 8.0 Hz, 1H, H-1), 5.03 (dd, J = 3.5, 10.5 Hz, 1H, H-3), 5.18 (dd, J = 7.5, 10.5 Hz, 1H, H-2), 5.40 (dd, J = 1.0, 3.5 Hz, 1H, H-4), 6.37, 6.41, 6.61 (t, 3H, NH). ^{13}C NMR (125 MHz, $CDCl_3$): δ_C 20.8, 20.9, 21.1 (4C, CH_3), 25.6 (1C, COCH$_2$CH$_2$CH_2CH$_2$CHS), 29.1 (1C, COCH$_2$CH_2CH$_2$CH$_2$CHS), 29.4 (1C, OCH$_2$CH_2CH$_2$NH), 31.8, 32.0 (2C, HNCOCH_2CH2CONH), 34.9 (1C, COCH$_2$CH$_2$CH$_2$CH_2CHS), 36.5 (1C, COCH_2CH$_2$CH$_2$CH$_2$CHS), 37.6 (1C, NHCH_2CH$_2$CH$_2$O), 38.7 (1C, SCH_2), 39.45, 39.46 (2C, CONHCH_2), 40.5 (1C, SCHCH_2CH$_2$S), 56.7 (1C, SCHCH$_2$), 61.5 (1C, C6), 67.2 (1C, OCH_2CH_2CH$_2$NH), 68.9 (1C, *CH*), 69.2 (1C, *CH*), 70.0 (1C, *CH*), 70.2 (2C, CH$_2$OCH_2CH_2OCH$_2$), 70.46, 70.49 (2C, CH_2OCH$_2$CH$_2$OCH_2), 70.9 (1C, *CH*), 71.0 (1C, *CH*), 101.5 (1C, *C1$_{anomeric}$*), 170.1 (1C, CH$_3$C(O)O), 170.3 (1C, CH$_3$C(O)O), 170.5 (1C, CH$_3$C(O)O), 170.6 (1C, CH$_3$C(O), 172.5, 172.6, 173.2 (3C, NHC(O)CH$_2$). HRMS *m/z* calcd. for $C_{35}H_{57}N_3NaO_{15}S_2$ $[M + Na]^+$: 846.3129; found: 846.3127.

Lipoic Galactose (LGal). LGal (0.0795 g, 0.121 mmol) was synthesized in quantitative yield following the general procedure for deprotection starting from **LGalA** (0.10 g, 0.121 mmol). ^{1}H NMR (500 MHz, CD_3OD): δ_H 1.42-1.48 (m, 2H, COCH$_2$CH$_2$CH_2CH$_2$CHS), 1.60-1.75 (m, 4H, COCH$_2$CH_2CH$_2$CH_2CHS), 1.76-1.82

(m, 2H, $COH_2CH_2CH_2NH$), 1.87-1.93 (m, 1H, CH_aHCH_2S), 2.22 (t, J = 7.5 Hz, 2H, $COCH_2CH_2CH_2CH_2CHS$), 2.44-2.48 (m, 1H, CH_bCH_2S), 2.49 (dt, J = 4.5, 6.5 Hz, 4H, $COCH_2CH_2CO$), 3.08-3.14 (m, 1H, CH_2CH_aHS), 3.16-3.22 (m, 1H, CH_2CH_bS), 3.26-3.32 (m, 2H, $OCH_2CH_2CH_2NH$), 3.34-3.40 (m, 4H, $CONHCH_2$), 3.49 (dd, J = 3.0, 9.0 Hz, 1H, H-3), 3.52-3.54 (m, 2H, H-2, H-5), 3.53-3.57 (m, 5H, $H_2COCH_2CH_2OCH_2$, $COCH_2CH_2CH_2CH_2CHS$), 3.58-3.62 (m, 1H, $OCH_aHCH_2CH_2NH$), 3.63 (s, 4H, $H_2COCH_2CH_2OCH_2$), 3.71-3.80 (m, 2H, H-6), 3.84 (dd, J = 1.0, 3.5 Hz, 1H, H-4), 3.92-3.97 (m, 1H, $OCH_bCH_2CH_2NH$), 4.23 (d, J = 7.0 Hz, 1H, H-1). ^{13}C NMR (125 MHz, CD_3OD): δ_C 25.6 (1C, $COCH_2CH_2CH_2CH_2CHS$), 28.7 (1C, $COCH_2CH_2CH_2CH_2CHS$), 29.1 (1C, $OCH_2CH_2CH_2NH$), 31.20, 31.23 (2C, $HNCOCH_2CH2CONH$), 34.6 (1C, $COCH_2CH_2CH_2CH_2CHS$), 35.7 (1C, $COCH_2CH_2CH_2CH_2CHS$), 36.6 (1C, $NHCH_2CH_2CH_2O$), 38.2 (1C, SCH_2), 39.16, 39.24 (2C, $CONHCH_2$), 40.2 (1C, $SCHCH_2CH_2S$), 56.5 (1C, $SCHCH_2$), 61.5 (1C, C6), 67.2 (1C, $OCH_2CH_2CH_2NH$), 69.2 (1C, *C4*), 69.45, 69.50 (2C, $CH_2OCH_2CH_2OCH_2$), 70.2 (2C, $CH_2OCH_2CH_2OCH_2$), 71.4 (1C, *C2*), 73.9 (1C, *C3*), 75.6 (1C, *C5*), 103.8 (1C, $C1_{anomeric}$), 173.42, 173.56, 174.95 (3C, $NHC(O)CH_2$). HRMS *m/z* calcd. for $C_{27}H_{50}N_3O_{11}S_2$ $[M+H]^+$: 656.2887; found: 656.2880.

3. Synthesis of Lipoic Mannose (LMan)

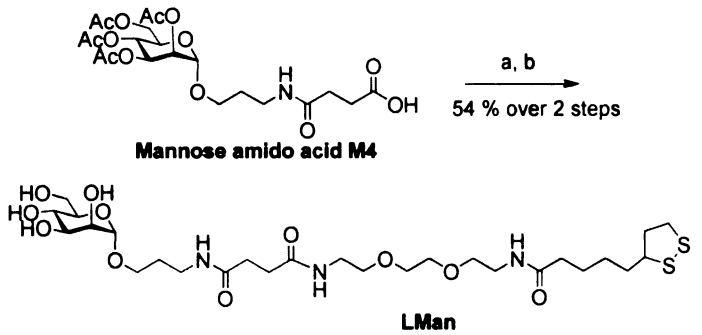

Figure 2-21. Reagents and conditions: a) Lipoic amine, HBTU/HOBT, DIPEA, DMF, 3hrs; b) NaOMe, MeOH, 1h.

Lipoic Mannose Acetate (LManA). LManA (0.0980 g, 0.119 mmol) was synthesized in 60% yield following the general procedure for amidation starting from mannose amido acid **M4** synthesized before (0.100 g, 0.198 mmol). ^{1}H NMR (500 MHz, $CDCl_3$): δ_H 1.42-1.52 (m, 2H, $COCH_2CH_2CH_2CH_2CHS$), 1.58-1.76 (m, 4H, $COCH_2CH_2CH_2CH_2CHS$), 1.78-1.87 (m, 2H, $COH_2CH_2CH_2NH$), 1.88-1.96 (m, 1H, CH_aHCH_2S), 2.00 (s, 3H, OCH_3), 2.06 (s, 3H, OCH_3), 2.12 (s, 3H, OCH_3), 2.16 (s, 3H, OCH_3), 2.22 (t, J = 7.0 Hz, 2H, $COCH_2CH_2CH_2CH_2CHS$), 2.44-2.50 (m, 1H, CHH_bCH_2S), 2.52-2.56 (m, 4H, $COCH_2CH_2CO$), 3.10-3.21 (m, 1H, CH_2CH_2S), 3.33-3.38 (m, 2H, $OCH_2CH_2CH_2NH$), 3.42-3.48 (m, 4H, $CONHCH_2$), 3.49-3.53 (m, 1H, $OCH_aHCH_2CH_2NH$), 3.54-3.60 (m, 5H, $H_2COCH_2CH_2OCH_2$, $COCH_2CH_2CH_2CH_2CHS$), 3.62 (s, 4H, $H_2COCH_2CH_2OCH_2$), 3.72-3.78 (m, 1H, $OCHH_bCH_2CH_2NH$), 3.94-4.00 (m, 1H, H-5), 4.10 (dd, 1H, H-6a), 4.27 (dd, 1H, H-6b), 4.80 (d, 1H, H-1), 5.20-5.24 (m, 1H, H-2), 5.24-5.29 (m, 2H, H-3, H-4), 6.30, 6.40, 6.60 (t, 3H, NH). ^{13}C NMR (125 MHz, $CDCl_3$): δ_C 20.8, 20.9, 21.1 (4C, CH_3), 25.6 (1C, $COCH_2CH_2CH_2CH_2CHS$), 29.1 (1C, $COCH_2CH_2CH_2CH_2CHS$),

29.4 (1C, $OCH_2CH_2CH_2NH$), 31.8, 32.0 (2C, $HNCOCH_2CH2CONH$), 34.9 (1C, $COCH_2CH_2CH_2CH_2CHS$), 36.5 (1C, $COCH_2CH_2CH_2CH_2CHS$), 37.6 (1C, $NHCH_2CH_2CH_2O$), 38.7 (1C, SCH_2), 39.45, 39.46 (2C, $CONHCH_2$), 40.5 (1C, $SCHCH_2CH_2S$), 56.7 (1C, $SCHCH_2$), 61.5 (1C, C6), 67.2 (1C, $OCH_2CH_2CH_2NH$), 68.9 (1C, *CH*), 69.2 (1C, *CH*), 70.0 (1C, *CH*), 70.2 (2C, $CH_2OCH_2CH_2OCH_2$), 70.46, 70.49 (2C, $CH_2OCH_2CH_2OCH_2$), 70.9 (1C, *CH*), 71.0 (1C, *CH*), 101.5 (1C, $C1_{anomeric}$), 170.1 (1C, $CH_3C(O)O$), 170.3 (1C, $CH_3C(O)O$), 170.5 (1C, $CH_3C(O)O$), 170.6 (1C, $CH_3C(O)$, 172.5, 172.6, 173.2 (3C, $NHC(O)CH_2$). HRMS *m/z* calcd. for $C_{35}H_{57}N_3NaO_{15}S_2$ $[M + Na]^+$: 846.3129; found: 846.3127.

Lipoic Mannose (LMan). LMan (0.029 g, 0.044 mmol) was synthesized in 90% yield following the general procedure for deprotection starting from **LManA** (0.040 g, 0.049 mmol). ^1H NMR (500 MHz, CD_3OD): δ_H 1.40-1.52 (m, 2H, $COCH_2CH_2CH_2CH_2CHS$), 1.60-1.82 (m, 6H, $COCH_2CH_2CH_2CH_2CHS$, $COH_2CH_2CH_2NH$), 1.87-1.93 (m, 1H, CH_aHCH_2S), 2.23 (t, *J* = 7.0 Hz, 2H, $COCH_2CH_2CH_2CH_2CHS$), 2.44-2.52 (m, 1H, CHH_bCH_2S), 2.49 (td, *J* = 1.5, 5.5 Hz, 4H, $COCH_2CH_2CO$), 3.08-3.14 (m, 1H, CH_2CH_aHS), 3.16-3.22 (m, 1H, CH_2CHH_bS), 3.24-3.30 (m, 2H, $OCH_2CH_2CH_2NH$), 3.35-3.40 (m, 4H, $CONHCH_2$), 3.44-3.49 (m, 1H, H-3), 3.52-3.62 (m, 7H, $H_2COCH_2CH_2OCH_2$, $OCH_aHCH_2CH_2NH$, $COCH_2CH_2CH_2CH_2CHS$, H-2 or H-5), 3.63 (s, 4H, $H_2COCH_2CH_2OCH_2$) , 3.68-3.74 (m, 2H, H-6), 3.77-3.82 (m, 2H, $OCHH_bCH_2CH_2NH$, H-2 or H-5), 3.85 (dd, *J* = 2.5, 12.0 Hz, 1H, H-4), 4.75 (d, *J* = 1.5 Hz, 1H, H-1). ^{13}C NMR (125 MHz, CD_3OD): δ_C 25.5, 28.7, 29.1, 31.09, 31.13, 34.6, 35.7, 36.5, 38.2, 39.13, 39.21, 40.2, 56.4, 61.8, 63.2, 64.9, 67.5, 69.44,

69.49, 70.1, 71.0, 71.5, 73.5, 100.47, 173.42, 173.59, 174.95. HRMS *m/z* calcd. for $C_{27}H_{50}N_3O_{11}S_2[M+H]^+$:656.2887; found:656.2899.

4. Synthesis of Lipoic Fucose (LFuc)

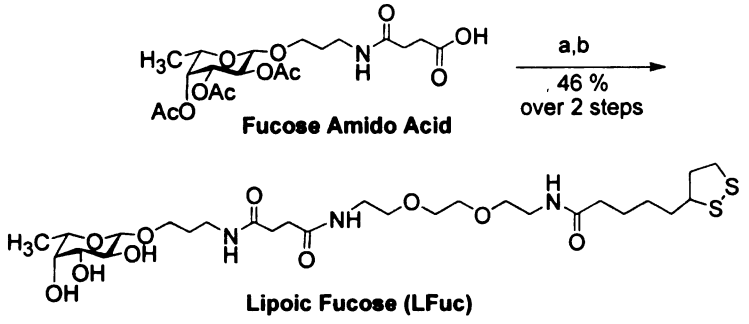

Figure 2-22. Reagents and conditions: a) Lipoic amine, HBTU/HOBT, DIPEA, DMF, 3hrs; b) NaOMe, MeOH, 1h.

Lipoic Fucose Acetate (LFucA). **LFucA** (0.257 g, 0.336 mmol) was synthesized in 50% yield following the general procedure for amidation starting from fucose amido acid (0.300 g, 0.670 mmol). ^{1}H NMR (500 MHz, $CDCl_3$): δ_H 1.14 (d, *J* = 6.0 Hz, 3H, C*H*$_3$), 1.32-1.42 (m, 2H, COCH$_2$CH$_2$C*H*$_2$CH$_2$CHS), 1.52-1.65 (m, 4H, COCH$_2$C*H*$_2$CH$_2$C*H*$_2$CHS), 1.66-1.74 (m, 2H, OCH$_2$C*H*$_2$CH$_2$NH), 1.79-1.85 (m, 1H, C*H*$_a$HCH$_2$S), 1.90 (s, 3H, OC*H*$_3$), 1.98 (s, 3H, OC*H*$_3$), 2.10 (s, 3H, OC*H*$_3$), 2.12 (t, *J* = 7.5 Hz, 2H, COC*H*$_2$CH$_2$CH$_2$CH$_2$CHS), 2.34-2.40 (m, 1H, CH*H*$_b$CH$_2$S), 2.42-2.50 (m, 4H, COC*H*$_2$C*H*$_2$CO), 3.00-3.05 (m, 1H, CH$_2$C*H*$_a$HS), 3.07-3.11 (m, 1H, CH$_2$CH*H*$_b$S), 3.17-3.22 (m, 1H, OCH$_2$CH$_2$C*H*$_a$HNH), 3.24-3.30 (m, 1H, OCH$_2$CH$_2$CH*H*$_b$NH), 3.32-3.37 (m, 4H, CONHC*H*$_2$), 3.45-3.50 (m, 6H, *H*$_2$COCH$_2$CH$_2$OC*H*$_2$, OCH*H*$_b$CH$_2$CH$_2$NH, COCH$_2$CH$_2$CH$_2$CH$_2$C*H*S), 3.52 (s, 4H, H$_2$COC*H*$_2$C*H*$_2$OCH$_2$), 3.75 (dq, *J* = 0.5, 6.5 Hz, 1H, H-5), 3.86-3.91 (m, 1H, OC*H*$_a$H CH$_2$CH$_2$NH), 4.34 (d, *J* = 7.5 Hz, 1H, H-1), 4.94 (dd, *J* = 3.5, 10.5 Hz, 1H, H-3), 5.06 (dd, *J* = 7.5, 10.5 Hz, 1H, H-2), 5.15 (dd, *J* = 0.5, 3.5 Hz, 1H, H-4),

6.50 (dt, J = 5.5, 2H, N*H*), 6.71 (t, J = 5.5, 1H, N*H*). ^{13}C NMR (125 MHz, $CDCl_3$): δ_C 16.2, 20.8, 20.9, 21.0, 25.6, 29.1, 29.3, 31.7, 32.0, 34.8, 36.4, 37.6, 38.6, 39.4, 39.4, 40.4, 53.7, 56.6, 68.7, 69.2, 69.4, 69.9, 70.1, 70.3, 70.4, 70.4, 71.2, 101.3, 170.1, 170.3, 170.8, 172.4, 172.6, 173.2. HRMS *m/z* calcd. for $C_{33}H_{56}N_3O_{13}S_2[M]^+$:766.3255; found:766.3259.

Lipoic Fucose (LFuc). LFuc (0.141 g, 0.220 mmol) was synthesized in 94% yield following the general procedure for deprotection starting from **LFucA** (0.180 g, 0.235 mmol). ^1H NMR (500 MHz, CD_3OD): δ_H 1.28 (d, J = 6.5 Hz, 3H, CH_3), 1.42-1.50 (m, 2H, $COCH_2CH_2CH_2CH_2CHS$), 1.60-1.74 (m, 4H, $COCH_2CH_2CH_2CH_2CHS$), 1.76-1.82 (m, 2H, $COH_2CH_2CH_2NH$), 1.87-1.94 (m, 1H, CH_aHCH_2S), 2.22 (t, J = 7.5 Hz, 2H, $COCH_2CH_2CH_2CH_2CHS$), 2.44-2.48 (m, 1H, CHH_bCH_2S), 2.50 (t, J = 4.0 Hz, 4H, $COCH_2CH_2CO$), 3.09-3.14 (m, 1H, CH_2CH_aHS), 3.17-3.21 (m, 1H, CH_2CHH_bS), 3.25-3.34 (m, 2H, $OCH_2CH_2CH_2NH$), 3.36-3.40 (m, 4H, $CONHCH_2$), 3.48 (dd, J = 2.0, 4.5 Hz, 1H, H-2, H-3), 3.55 (dd, J = 2.5, 5.5 Hz, 1H, H-4), 3.54-3.58 (m, 4H, $H_2COCH_2CH_2OCH_2$), 3.58-3.60 (m, 1H, $OCH_aHCH_2CH_2NH$), 3.60-3.62 (m, 1H, $COCH_2CH_2CH_2CH_2CHS$), 3.63 (s, 4H, $H_2COCH_2CH_2OCH_2$), 3.65 (td, J = 1.0, 7.5 Hz, 1H, H-5), 3.92-3.97 (m, 1H, $OCHH_bCH_2CH_2NH$), 4.23 (d, J = 7.5 Hz, 1H, H-1). ^{13}C NMR (125 MHz, CD_3OD): δ_C 15.7, 25.6, 28.7, 29.1, 31.2, 31.2, 34.6, 35.7, 36.7, 38.2, 39.16, 39.24, 40.2, 56.5, 67.2, 69.46, 69.50, 70.17, 70.18, 70.8, 71.2, 71.9, 74.0, 103.6, 173.4, 173.5, 174.9. HR-MS *m/z* calcd. for $C_{27}H_{50}N_3O_{10}S_2$ $[M+H]^+$: 640.2938; found: 640.2933.

5. Synthesis of Lipoic Glucose (LGlc)

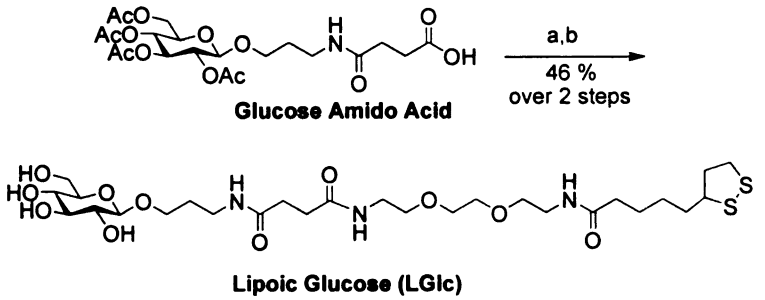

Figure 2-23. Reagents and conditions: a) Lipoic amine, HBTU/HOBT, DIPEA, DMF, 3hrs; b) NaOMe, MeOH, 1h.

Lipoic Glucose Acetate (LGlcA). LGlcA (0.180 g, 0.218 mmol) was synthesized in 50% yield following the general procedure for amidation starting from glucose amido acid (0.220 g, 0.435 mmol). ^{1}H NMR (500 MHz, $CDCl_3$): δ_H 1.38-1.48 (m, 2H, $COCH_2CH_2CH_2CH_2CHS$), 1.60-1.72 (m, 4H, $COCH_2CH_2CH_2CH_2CHS$), 1.72-1.80 (m, 2H, $OCH_2CH_2CH_2NH$), 1.85-1.92 (m, 1H, CH_aHCH_2S), 1.99, 2.01, 2.04, 2.08 (4s, 4 x 3H, $COCH_3$), 2.18 (t, J = 7.0 Hz, 2H, $COCH_2CH_2CH_2CH_2CHS$), 2.40-2.48 (m, 1H, CH_bCH_2S), 2.48-2.55 (m, 4H, $COCH_2CH_2CO$), 3.06-3.18 (m, 2H, CH_2CH_2S), 3.21-3.35 (m, 2H, $OCH_2CH_2CH_2NH$), 3.40-3.45 (m, 4H, $CONHCH_2$), 3.51-3.58 (m, 6H, $H_2COCH_2CH_2OCH_2$, $OCH_aHCH_2CH_2NH$, $COCH_2CH_2CH_2CH_2CHS$), 3.60 (s, 4H, $H_2COCH_2CH_2OCH_2$), 3.67-3.71 (m, 1H, H-5), 3.88-3.93 (m, 1H, OCH_b CH_2CH_2NH), 4.15 (dd, J = 2.5, 12.5 Hz, 1H, H-6a), 4.25 (dd, J = 4.5, 12.5 Hz, 1H, H-6b), 4.47 (d, J = 8.5 Hz, 1H, H-1), 4.96 (dd, J = 8.0, 9.5 Hz, 1H, H-2), 5.06 (t, J = 9.5 Hz, 1H, H-4), 5.20 ((t, J = 9.5 Hz, 1H, H-3), 6.43 (t, J = 5.5 Hz, 1H, NH), 6.49 (t, J = 5.5 Hz, 1H, NH), 6.67 (t, J = 5.5 Hz, 1H, NH). ^{13}C NMR (125 MHz, $CDCl_3$): δ_C 20.83, 20.95, 21.0, 25.6, 29.1, 29.4,

31.8, 32.0, 34.9, 36.5, 37.4, 38.7, 39.43, 39.45, 40.5, 50.8, 56.7, 62.0, 68.55, 68.57, 70.0, 70.2, 70.43, 70.46, 71.5, 72.1, 72.8 101.0, 169.7, 169.9, 170.4, 171.0, 172.57, 172.58, 173.3. HRMS *m/z* calcd. for $C_{35}H_{58}N_3O_{15}S_2$ $[M+H]^+$: 824.3309; found: 824.3305.

Lipoic Glucose (LGlc). LGlc (0.074 g, 0.11 mmol) was synthesized in 93% yield following the general procedure for deprotection starting from **LGlcA** (0.10 g, 0.12 mmol). ^1H NMR (500 MHz, CD_3OD): δ_H 1.42-1.52 (m, 2H, $COCH_2CH_2CH_2CH_2CHS$), 1.60-1.76 (m, 4H, $COCH_2CH_2CH_2CH_2CHS$), 1.76-1.82 (m, 2H, $COH_2CH_2CH_2NH$), 1.87-1.93 (m, 1H, CH_aHCH_2S), 2.22 (t, J = 7.5 Hz, 2H, $COCH_2CH_2CH_2CH_2CHS$), 2.44-2.48 (m, 1H, CH_bCH_2S), 2.50 (t, J = 4.0 Hz, 4H, $COCH_2CH_2CO$), 3.09-3.21 (m, 3H, CH_2CH_2S, $OCH_2CH_2CH_aHNH$), 3.27-3.32 (m, 2H, $OCH_2CH_2CH_bNH$, H-4), 3.33-3.39 (m, 6H, $CONHCH_2$, $COCH_2CH_2CH_2CHS$, H-3), 3.54-3.62 (m, 6H, $H_2COCH_2CH_2OCH_2$, $OCH_aHCH_2CH_2NH$, H-2), 3.63 (s, 4H, $H_2COCH_2CH_2OCH_2$), 3.64-3.69 (m, 2H, H-5, H-6a), 3.88 (dd, J = 2.0, 10.0 Hz, 1H, H-6b), 3.92-3.96 (m, 1H, $OCH_bCH_2CH_2NH$), 4.27 (d, J = 8.0 Hz, 1H, H-1). ^{13}C NMR (125 MHz, CD_3OD): δ_C 25.6, 28.7, 29.2, 31.11, 31.15, 34.6, 35.7, 36.5, 38.2, 39.1, 39.2, 40.2, 56.4, 61.6, 67.2, 69.43, 69.48, 70.2, 70.5, 74.0, 76.8, 76.9, 103.2, 173.45, 173.57, 175.0. HRMS *m/z* calcd. for $C_{27}H_{50}N_3O_{11}S_2$ $[M+H]^+$: 656.2887; found: 656.2875.

6. Synthesis of Lipoic Sialic (LSia)

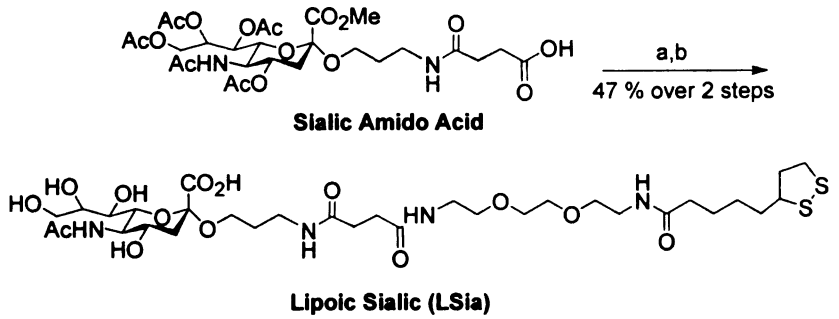

Lipoic Sialic (LSia)

Figure 2-24. Reagents and conditions: a) Lipoic amine, HBTU/HOBT, DIPEA, DMF, 3hrs; b) NaOMe, MeOH, 1h, then 0.2 mL water.

Lipoic Sialic Acetate (LSiaA). LSiaA (0.085 g, 0.088 mmol) was synthesized in 52% yield following the general procedure for amidation starting from sialic amido acid (0.11 g, 0.17 mmol). ^{1}H NMR (500 MHz, $CDCl_3$): δ_H 1.38-1.50 (m, 2H, $COCH_2CH_2CH_2CH_2CHS$), 1.60-1.76 (m, 6H, $COCH_2CH_2CH_2CH_2CHS$, $OCH_2CH_2CH_2NH$), 1.87-1.95 (m, 2H, CH_aHCH_2S, H-3ax.), 1.86, 2.01, 2.02, 2.13 (5s, 5 x 3H, $COCH_3$, $NHCOCH_3$), 2.19 (t, J = 7.5 Hz, 2H, $COCH_2CH_2CH_2CH_2CHS$), 2.40-2.48 (m, 1H, CH_bCH_2S), 2.50 (bs, 4H, $COCH_2CH_2CO$), 2.63 (dd, J = 5.0, 10.5 Hz, 1H, H-3eq.), 3.07-3.18 (m, 2H, CH_2CH_2S), 3.25-3.34 (m, 3H, $OCH_2CH_2CH_2NH$, $OCH_aHCH_2CH_2NH$), 3.40-3.45 (m, 4H, $CONHCH_2$), 3.52-3.57 (m, 5H, $H_2COCH_2CH_2OCH_2$, $COCH_2CH_2CH_2CH_2CHS$), 3.60 (s, 4H, $H_2COCH_2CH_2OCH_2$), 3.74-3.78 (m, 1H, $OCH_bCH_2CH_2NH$), 3.79 (s, 3H, CO_2CH_3), 4.02-4.08 (m, 2H, H-5, H-9a), 4.10 (dd, J = 2.0, 11.0 Hz, 1H, H-6), 4.30 (dd, J = 3.0, 12.5 Hz, 1H, H-9b), 4.80-4.86 (m, 1H, H-4), 5.31 (dd, J = 2.0, 8.5 Hz, 1H, H-7), 5.35-5.38 (m, 1H, H-8), 5.48 (d, J = 9.5 Hz, 1H, NHAc), 6.41 (t, J = 5.5 Hz, 1H, NH), 6.49 (t, J = 5.5 Hz, 1H, NH), 6.60 (t, J = 5.0 Hz, 1H, NH). ^{13}C NMR (125 MHz, $CDCl_3$): δ_C 21.05, 21.12, 21.4,

23.4, 25.6, 29.1, 29.4, 31.80, 31.96, 34.9, 36.5, 37.1, 38.1, 38.7, 39.4, 40.5, 49.5, 53.1, 53.7, 56.7, 62.8, 63.5, 67.5, 68.5, 69.2, 70.0, 70.2, 70.45, 70.47, 72.7, 99.0, 168.6, 170.4, 170.5, 170.6, 171.05, 171.16, 172.3, 172.5, 173.3. HRMS *m/z* calcd. for $C_{41}H_{67}N_4O_{18}S_2$ $[M+H]^+$: 967.2815; found : 967.2809.

Lipoic Sialic Acid (LSia). LSia (0.047 g, 0.059 mmol) was synthesized in 95% yield following the general procedure for deprotection starting from **LSiaA** (0.060 g, 0.062 mmol) except that 0.2 mL of water was added to the reaction mixture half an hour prior to neutralization. ^{1}H NMR (500 MHz, CD_3OD): δ_H 1.42-1.52 (m, 2H, $COCH_2CH_2CH_2CH_2CHS$), 1.60-1.80 (m, 7H, $COCH_2CH_2CH_2CH_2CHS$, $COH_2CH_2CH_2NH$, H-3ax.), 1.87-1.94 (m, 1H, CH_aHCH_2S), 2.00 (s, 3H, $NHCOCH_3$), 2.23 (t, J = 7.5 Hz, 2H, $COCH_2CH_2CH_2CH_2CHS$), 2.44-2.48 (m, 1H, CH_bCH_2S), 2.50 (bs, 4H, $COCH_2CH_2CO$), 2.71 (dd, J = 5.0, 12.5 Hz, 1H, H-3eq.), 3.09-3.21 (m, 2H, CH_2CH_2S), 3.25-3.28 (m, 2H, $OCH_2CH_2CH_2NH$), 3.36-3.40(m, 4H, $CONHCH_2$), 3.48-3.53 (m, 1H, $OCH_aHCH_2CH_2NH$), 3.54-3.61 (m, 7H, $H_2COCH_2CH_2OCH_2$, $COCH_2CH_2CH_2CH_2CHS$, H-5, H-8), 3.62-3.66 (m, 1H, H-7), 3.63 (s, 4H, $H_2COCH_2CH_2OCH_2$), 3.70-3.80 (m, 2H, H-4, H-6), 3.82-3.88 (m, 3H, H-9, $OCH_bCH_2CH_2NH$). ^{13}C NMR (125 MHz, CD_3OD): δ_C 19.6, 21.5, 25.6, 28.7, 29.2, 31.2, 34.6, 35.7, 36.4, 38.2, 39.2, 39.3, 40.2, 40.5, 52.7, 56.4, 61.4, 63.5, 67.6, 69.0, 69.43, 69.48, 70.16, 71.7, 73.8, 98.7, 170.8, 173.5, 173.6, 174.0, 174.2, 175.0. HRMS *m/z* calcd. for $C_{32}H_{57}N_4O_{14}S_2$ $[M+H]^+$: 785.3034; found : 785.3030.

7. Synthesis of Lipoic N-acetyl glucosamine (LGlNAc)

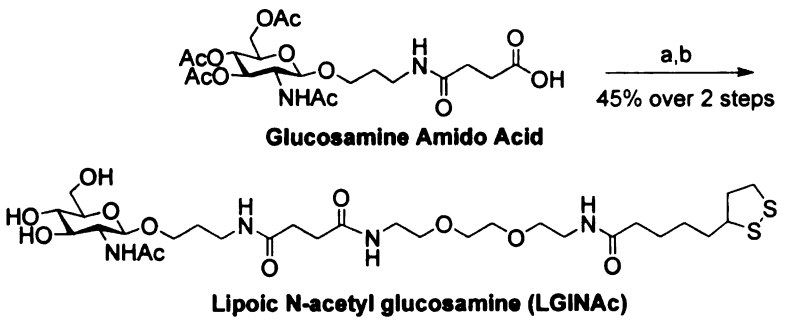

Figure 2-25. Reagents and conditions: a) Lipoic amine, HBTU/HOBT, DIPEA, DMF, 3hrs; b) NaOMe, MeOH, 1h.

Lipoic N-acetyl Glucosamine Acetate (LGNAcA). LGlNAcA (0.114 g, 0.139 mmol) was synthesized in 50% yield following the general procedure for amidation starting from glucosamine amido acid (0.140 g, 0.278 mmol). ^{1}H NMR (500 MHz, $CDCl_3$): δ_H 1.40-1.50 (m, 2H, $COCH_2CH_2CH_2CH_2CHS$), 1.60-1.72 (m, 5H, $COCH_2CH_2CH_2CH_2CHS$, $OCH_2CH_aHCH_2NH$), 1.72-1.80 (m, 1H, $OCH_2CHH_bCH_2NH$), 1.85-1.92 (m, 1H, CH_aHCH_2S), 1.92, 1.99, 2.00, 2.06 (4s, 3 x 3H, $COCH_3$, 3H, $NHCOCH_3$), 2.19 (t, J = 7.5 Hz, 2H, $COCH_2CH_2CH_2CH_2CHS$), 2.40-2.48 (m, 1H, CHH_bCH_2S), 2.48-2.58 (m, 4H, $COCH_2CH_2CO$), 3.06-3.18 (m, 3H, CH_2CH_2S, $OCH_2CH_2CH_aHNH$), 3.40-3.47 (m, 5H, $CONHCH_2$, $OCH_aHCH_2CH_2NH$), 3.51-3.58 (m, 6H, $H_2COCH_2CH_2OCH_2$, $OCH_2CH_2CHH_bNH$, $COCH_2CH_2CH_2CH_2CHS$), 3.60 (s, 4H, $H_2COCH_2CH_2OCH_2$), 3.68-3.72 (m, 1H, H-5), 3.94-4.00 (m, 2H, H-2, $OCHH_b$ CH_2CH_2NH), 4.11 (dd, J = 2.5, 12.5 Hz, 1H, H-6a), 4.25 (dd, J = 4.5, 12.0 Hz, 1H, H-6b), 4.54 (d, J = 8.5 Hz, 1H, H-1), 5.06 (t, J = 10.0 Hz, 1H, H-4), 5.16 ((t, J = 9.5 Hz, 1H, H-3), 6.35 (bs, 1H, N*H*), 6.65 (m, 2H, N*H*), 6.92 (d, J = 8.5 Hz, 1H, N*H*Ac). ^{13}C NMR (125 MHz, $CDCl_3$): δ_C 20.86, 20.96, 21.0, 23.4, 25.6, 29.1, 29.4, 31.80, 31.83, 34.9, 36.53, 36.57, 38.7, 39.46,

39.54, 40.5, 54.5, 56.7, 62.3, 67.9, 68.9, 69.9, 70.2, 70.46, 70.50, 72.0, 73.3, 101.6, 169.6, 170.99, 171.08, 171.14, 172.66, 172.73, 173.3. HRMS *m/z* calcd. for $C_{35}H_{58}N_4NaO_{14}S_2$ $[M+Na]^+$: 845.3875; found: 845.3868.

Lipoic N-acetyl Glucosamine (LGINAc). LGINAc (0.046 g, 0.066 mmol) was synthesized in 90% yield following the general procedure for deprotection starting from **LGINAcA** (0.060 g, 0.073 mmol). ^1H NMR (500 MHz, CD_3OD): δ_H 1.42-1.52 (m, 2H, $COCH_2CH_2CH_2CH_2CHS$), 1.60-1.72 (m, 4H, $COCH_2CH_2CH_2CH_2CHS$), 1.72-1.78 (m, 2H, $COH_2CH_2CH_2NH$), 1.87-1.94 (m, 1H, CH_aHCH_2S), 2.01 (s, 1H, $NHCOCH_3$), 2.23 (t, J = 7.0 Hz, 2H, $COCH_2CH_2CH_2CH_2CHS$), 2.44-2.48 (m, 1H, CH_bCH_2S), 2.50 (t, J = 3.0 Hz, 4H, $COCH_2CH_2CO$), 3.09-3.21 (m, 3H, CH_2CH_2S, $OCH_2CH_2CH_aHNH$), 3.27-3.34 (m, 2H, $OCH_2CH_2CH_bNH$, H-4), 3.35-3.40 (m, 5H, $CONHCH_2$, $COCH_2CH_2CH_2CH_2CHS$), 3.45 (dd, J = 8.5, 10.5 Hz, 1H, H-3), 3.53-3.62 (m, 6H, $H_2COCH_2CH_2OCH_2$, $OCH_aHCH_2CH_2NH$, H-2), 3.63 (s, 4H, $H_2COCH_2CH_2OCH_2$), 3.64-3.72 (m, 2H, H-5, H-6a), 3.88-3.94 (m, 2H, H-6b, $OCH_bCH_2CH_2NH$), 4.40 (d, J = 8.5 Hz, 1H, H-1). ^{13}C NMR (125 MHz, CD_3OD): δ_C 21.9, 25.6, 28.7, 29.3, 31.11, 31.14, 34.6, 35.7, 36.3, 38.2, 39.1, 39.2, 40.2, 56.3, 56.4, 61.7, 66.9, 69.44, 69.48, 70.15, 70.17, 71.0, 75.1, 76.8, 101.6, 172.8, 173.45, 173.57, 175.0. HRMS *m/z* calcd. for $C_{29}H_{52}N_4$ Na $O_{11}S_2$ $[M+Na]^+$: 719.3804; found: 719.3806.

2.9. References

1. Lingwood, C. A., **Oligosaccharide receptors for bacteria: a view to a kill.** *Curr. Opin. Chem. Biol.* **1998,** *2*, 695-700.

2. Chang, S.-C.; Adriaens, P., **Nano-immunodetection and quantification of mycobacteria in metalworking fluids.** *Env. Eng. Sci.* **2007,** *24*, 58-72.

3. Porter, J.; Robinson, J.; Pickup, R.; Edwards, C., **An evaluation of lectin-mediated magnetic bead cell sorting for the targeted separation of enteric bacteria.** *J. Appl. Microbiol.* **1998,** *84*, 722-732.

4. Hatch, D. M.; Weiss, A. A.; Kale, R. R.; Iyer, S. S., **Biotinylated bi- and tetra-antennary glycoconjugates for Escherichia coli detection.** *ChemBioChem* **2008,** *9*, 2433-2442.

5. Gu, H.; Xu, K.; Xu, C.; Xu, B., **Biofunctional magnetic nanoparticles for protein separation and pathogen detection.** *Chem. Commun.* **2006**, 941-949.

6. Zhao, X.; Hilliard, L. R.; Mechery, S. J.; Wang, Y.; Bagwe, R. P.; Jin, S.; Tan, W., **A rapid bioassay for single bacterial cell quantitation using bioconjugated nanoparticles.** *Proc. Nat. Acad. Sci., USA* **2004,** *101*, 15027-15032.

7. Mammen, M.; Choi, S.-K.; Whitesides, G. M., **Polyvalent interactions in biological systems: Implications for design and use of multivalent ligands and inhibitors.** *Angew. Chem. Int. Ed.* **1998,** *37*, 2754-2794.

8. Yoon, T.-J.; Kim, J. S.; Kim, B. G.; Yu, K. N.; Cho, M.-H.; Lee, J.-K., **Multifunctional nanoparticles possessing a "magnetic motor effect" for drug or gene delivery.** *Angew. Chem. Int. Ed.* **2005,** *44*, 1068-1071.

9. Bruce, I. J.; Sen, T., **Surface modification of magnetic nanoparticles with alkoxysilanes and their application in magnetic bioseparations.** *Langmuir* **2005,** *21*, 7029-7035.

10. Yamaura, M.; Camilo, R. L.; Sampaio, L. C.; Macedo, M. A.; Nakamura, M.; Toma, H. E., **Preparation and characterization of (3-aminopropyl)triethoxysilane-coated magnetite nanoparticles.** *J. Magn. Magn. Mater.* **2004,** *279*, 210-217.

11. Koh, I.; Wang, X.; Varughese, B.; Isaacs, L.; Ehrman, S. H.; English, D. S., **Magnetic iron oxide nanoparticles for biorecognition: Evaluation of surface coverage and activity.** *J. Phys. Chem. B* **2006,** *110*, 1553-1558.

12. Lin, P.-C.; Ueng, S.-H.; Yu, S.-C.; Jan, M.-D.; Adak, A. K.; Yu, C.-C.; Lin, C.-C., **Surface modification of magnetic nanoparticle via Cu(I)-catalyzed alkyne-azide [2 + 3] cycloaddition.** *Org. Lett.* **2007,** *9*, 2131-2134.

13. Kell, A. J.; Simard, B., **Vancomycin architecture dependence on the capture efficiency of antibody-modified microbeads by magnetic nanoparticles.** *Chem. Commun.* **2007**, 1227-1229.

14. Cheng, F. Y.; Su, C. H.; Yang, Y. S.; Yeh, C. S.; Tsai, C. Y.; Wu, C. L.; Wu, M. T.; Shieh, D. B., **Characterization of aqueous dispersions of Fe_3O_4 nanoparticles and their biomedical applications.** *Biomaterials* **2005,** *26*, 729-738.

15. Ma, M.; Zhang, Y.; Yu, W.; Shen, H.-y.; Zhang, H.-q.; Gu, N., **Preparation and characterization of magnetite nanoparticles coated by amino silane.** *Colloids Surf., A* **2003,** *212*, 219-226.

16. Liu, X.; Ma, Z.; Xing, J.; Liu, H., **Preparation and characterization of amino-silane modified superparamagnetic silica nanospheres.** *J. Magn. Magn. Mater.* **2004,** *270*, 1-6.

17. Klotz, M.; Ayral, A.; Guizard, C.; Menager, C.; Cabuil, V., **Silica coating on colloidal maghemite particles.** *J. Colloid Interface Sci.* **1999,** *220*, 357-361.

18. Polito, L.; Colombo, M.; Monti, D.; Melato, S.; Caneva, E.; Prosperi, D., **Resolving the structure of ligands bound to the surface of superparamagnetic iron oxide nanoparticles by high-resolution magic-angle spinning NMR spectroscopy.** *J. Am. Chem. Soc.* **2008,** *130*, 12712-24.

19. Polito, L.; Monti, D.; Caneva, E.; Delnevo, E.; Russo, G.; Prosperi, D., **One-step bioengineering of magnetic nanoparticles via a surface diazo transfer/azide-alkyne click reaction sequence.** *Chem. Commun.* **2008**, 621-623.

20. Lis, H.; Sharon, N., **Lectins: carbohydrate-specific proteins that mediate cellular recognition.** *Chem. Rev.* **1998,** *98*, 637-674.

21. Jelinek, R.; Kolusheva, S., **Carbohydrate biosensors.** *Chem. Rev.* **2004,** *104*, 5987-6015.

22. Chang, S.-C.; Anderson, T. I.; Bahrman, S. E.; Gruden, C. L.; Khijniak, A. I.; Adriaens, P., **Comparing recovering efficiency of immunomagnetic separation and centrifugation of *mycobacteria* in metalworking fluids.** *J. Ind. Microbiol. Biotechnol.* **2005,** *32*, 629-638.

23. Luk, Y.-Y.; Tingey, M. L.; Dickson, K. A.; Raines, R. T.; Abbott, N. L., **Imaging the binding ability of proteins immobilized on surfaces with different orientations by using liquid crystals** *J. Am. Chem. Soc.* **2004,** *126*, 9024-9032.

24. Kim, B.-S.; Yang, W.-Y.; Ryu, J.-H.; Yoo, Y.-S.; Lee, M., **Carbohydrate-coated nanocapsules from amphiphilic rod–coil molecule: Binding to bacterial type 1 pili.** *Chem. Commun.* **2005**, 2035-2037.

25. Schofield, C. L.; Field, R. A.; Russell, D. A., **Glyconanoparticles for the Colorimetric Detection of Cholera Toxin.** *Anal. Chem.* **2007,** *79*, 1356-1361 and references cited therein.

26. Disney, M. D.; Zheng, J.; Swager, T. M.; Seeberger, P. H., **Detection of bacteria with carbohydrate-functionalized fluorescent polymers.** *J. Am. Chem. Soc.* **2004,** *126*, 13343-13346.

27. Lin, C.-C.; Yeh, Y.-C.; Yang, C.-Y.; Chen, C.-L.; Chen, G.-F.; Chen, C.-C.; Wu, Y.-C., **Selective binding of mannose-encapsulated gold nanoparticles to type 1 pili in Escherichia coli.** *J. Am. Chem. Soc.* **2002,** *124*, 3508-3509.

28. Miranda, O. R.; You, C.-C.; Phillips, R.; Kim, I.-B.; Ghosh, P. S.; Bunz, U. H. F.; Rotello, V. M., **Array-based sensing of proteins using conjugated polymers.** *J. Am. Chem. Soc.* **2007,** *129*, 9856-9857.

29. Wright, A. T.; Anslyn, E. V., **Differential receptor arrays and assays for solution-based molecular recognition.** *Chem. Soc. Rev.* **2006,** *35*, 14-28.

30. Harris, S. L.; Spears, P. A.; Havell, E. A.; Hamrick, T. S.; Horton, J. R.; Orndorff, P. E., **Characterization of *Escherichia coli* type 1 pilus mutants with altered binding specificities.** *J. Bacteriol.* **2001,** *183*, 4099–4102.

31. Stevens, J.; Blixt, O.; Tumpey, T. M.; Taubenberger, J. K.; Paulson, J. C.; Wilson, I. A., **Structure and receptor specificity of the hemagglutinin from an H5N1 influenza virus** *Science* **2006,** *312*, 404-410.

32. Tang, Y.-W.; Procop, G. W.; Persing, D. H., **Molecular diagnostics of infectious diseases** *Clin. Chem.* **1997,** *43*, 2021-2038.

33. Senaratne, W.; Andruzzi, L.; Ober Christopher, K., **Self-assembled monolayers and polymer brushes in biotechnology: current applications and future perspectives.** *Biomacromolecules* **2005,** *6*, 2427-48.

34. Brorson, S.-H., **Bovine serum albumin (BSA) as a reagent against non-specific immunogold labeling on LR-White and epoxy resin.** *Micron* **1997,** *28*, 189-195.

35. Papavassiliou, A. G.; Bohmann, D., **Optimization of the signal-to-noise ratio in south-western assays by using lipid-free BSA as blocking reagent.** *Nucleic Acids Res.* **1992,** *20*, 4365-6.

36. Huang, N.-P.; Voeroes, J.; De Paul, S. M.; Textor, M.; Spencer, N. D., **Biotin-derivatized poly(L-lysine)-g-poly(ethylene glycol): A novel polymeric interface for bioaffinity sensing.** *Langmuir* **2002,** *18*, 220-230.

37. Uchida, K.; Otsuka, H.; Kaneko, M.; Kataoka, K.; Nagasaki, Y., **A reactive poly(ethylene glycol) layer to achieve specific surface plasmon resonance sensing with a high S/N ratio: The substantial role of a short underbrushed PEG layer in minimizing nonspecific adsorption.** *Anal. Chem.* **2005,** *77*, 1075-1080.

38. Andruzzi, L.; Senaratne, W.; Hexemer, A.; Sheets, E. D.; Ilic, B.; Kramer, E. J.; Baird, B.; Ober, C. K., **Oligo(ethylene glycol) containing polymer brushes as bioselective surfaces.** *Langmuir* **2005,** *21*, 2495-2504.

39. Zareie, H. M.; Boyer, C.; Bulmus, V.; Nateghi, E.; Davis, T. P., **Temperature-responsive self-assembled monolayers of oligo(ethylene glycol): Control of biomolecular recognition.** *ACS Nano* **2008,** *2*, 757-765.

40. Revell, D. J.; Knight, J. R.; Blyth, D. J.; Haines, A. H.; Russell, D. A., **Self-Assembled carbohydrate monolayers: Formation and surface selective molecular recognition.** *Langmuir* **1998,** *14*, 4517-4524.

41. Houseman, B. T.; Mrksich, M., **Model systems for studying polyvalent carbohydrate binding interactions.** *Top. Curr. Chem.* **2002,** *218*, 1-44.

42. Shen, Z.; Huang, M.; Xiao, C.; Zhang, Y.; Zeng, X.; Wang, P. G., **Nonlabeled quartz crystal microbalance biosensor for bacterial detection using carbohydrate and lectin recognitions.** *Anal. Chem.* **2007,** *79*, 2312-2319.

43. Mrksich, M., **A surface chemistry approach to studying cell adhesion.** *Chem. Soc. Rev.* **2000,** *29*, 267-273.

44. Wang, Y.; El-Boubbou, K.; Kouyoumdjian, H.; Sun, B.; Huang, X.; Zeng, X., **Lipoic acid glyco-conjugates, a new class of agents for controlling nonspecific adsorption of blood serum at biointerfaces for biosensor and biomedical applications.** *Langmuir* **2010,** *26*, 4119-25.

45. Hayes, W.; Osborn, H. M. I.; Osborne, S. D.; Rastall, R. A.; Romagnoli, B., **One-pot synthesis of multivalent arrays of mannose mono- and disaccharides.** *Tetrahedron* **2003,** *59*, 7983-7996.

46. Davis, B. G.; Wood, S. D.; Maughan, M. A. T., **Towards an unprotected self-activating glycosyl donor system: bromobutyl glycosides.** *Can. J. Chem.* **2002,** *80*, 555-558.

47. Ladmiral, V.; Mantovani, G.; Clarkson, G. J.; Cauet, S.; Irwin, J. L.; Haddleton, D. M., **Synthesis of neoglycopolymers by a combination of "Click**

Chemistry" and living radical polymerization. *J. Am. Chem. Soc.* **2006,** *128*, 4823-4830.

48. Joosten John, A. F.; Loimaranta, V.; Appeldoorn Chantal, C. M.; Haataja, S.; El Maate Fatna, A.; Liskamp Rob, M. J.; Finne, J.; Pieters Roland, J., **Inhibition of Streptococcus suis adhesion by dendritic galabiose compounds at low nanomolar concentration.** *J. Med. Chem.* **2004,** *47*, 6499-508.

49. Srinivasan, B.; Huang, X., **Functionalization of magnetic nanoparticles with organic molecules: Loading level determination and evaluation of linker length effect on immobilization.** *Chirality* **2008,** *20*, 265-277.

50. Lu, Y.; Yin, Y.; Mayers, B. T.; Xia, Y., **Modifying the surface properties of superparamagnetic iron oxide nanoparticles through a sol-gel approach.** *Nano Lett.* **2002,** *2*, 183-186.

51. Pastorin, G.; Wu, W.; Wieckowski, S.; Briand, J.-P.; Kostarelos, K.; Prato, M.; Bianco, A., **Double functionalization of carbon nanotubes for multimodal drug delivery.** *Chem. Commun.* **2006**, 1183-1184.

CHAPTER 3

Magnetic Glyco-Nanoparticles: A Tool to Detect, Differentiate, and Unlock the Glyco-Codes of Cancer *via* MRI

3.1. Cancer Facts

Cancer is the second leading cause of death in the United States and is expected to surpass cardiovascular diseases in 2012.[1] Statistically, nearly half of all men and over one third of all women in the United States will contract cancer during their lifetimes, and one in four will die from it.[1] The estimated annual cost of cancer to the United States is around ~ $110 billion. Thus, early detection and prevention are the most effective means for the control and treatment of the disease.

Cancer usually appears as a tumor, while not all tumors are cancerous. Noncancerous tumors (benign) do not spread or metastasize to other parts of the body and are rarely life-threatening. Cancerous tumors (malignant) develop when cells in the body begin to grow and metastasize in an uncontrolled manner (out-of-control growth of abnormal cells).

3.2. Cancer Detection and Diagnosis

Conventional cancer diagnosis depends on the cell pathology and histological assessment where biopsy, endoscopy, and imaging are employed.[2] Imaging techniques including X-ray, computed tomography (CT), ultrasound (US), positron emission tomography (PET), optical coherence tomography (OCT), laser-induced fluorescence endoscopy, and MRI are usually applied.[3] MRI uses radio-frequency waves and a strong magnetic field (~ 1.5-3 T) to provide

remarkably clear and detailed pictures of internal organs and tissues.[4] The MRI technique has proven very valuable for the diagnosis of a broad range of pathologic conditions including cancer, heart, vascular, and stroke problems.[5]

Molecular, proteomic and genomic technologies, on the other hand, offer the promise of a comprehensive understanding of cancer at the molecular level.[6] These technologies determine how the genes, proteins and DNA in cancer cells behave and interact by expressing these molecular signatures as patterns enabling personalized cancer medicine through analysis of gene-expression blueprints.[7-9] Indeed, cancer cells have diverse biological capabilities that are conferred by numerous genetic aberrations. Mining the cancer genome for aberrations and alternations has become a major activity in cancer research, because it is widely understood that these aberrations provide potential clues to identify molecular biomarkers (biological indicators) that aid in early detection, diagnosis, and targeted therapy.[7] Detection of cancer-specific DNA mutations, abnormal DNA methylation patterns, and DNA replication proteins have been explored. Molecular alterations in tumors can be revealed using technologies that assess changes in the content or sequence of DNA, its transcription into mRNA, the production of proteins or the synthesis of various metabolic products.[9] The challenge in this approach, however, is to discover the correct cancer biomarkers and to identify which molecular abnormalities contribute to cancer and which are simply 'noise' at the genomic level. Although there has been success in the genomic approach, the translation of emerging insights from the genome into the

clinical practice of cancer medicine has not yet been fully attained.[8] New and better diagnostic tools to attain treatments are certainly needed.

Nowadays, nanotechnology is revolutionizing the biotechnology industries, clinical and medical fields at both the diagnostic and therapeutic fronts. The use of functionally-targeted nanoparticles in medicine is one of the important directions that bio-nanotechnology is taking. Indeed, their applications in imaging,[10-12] targeting,[13-15] drug delivery,[16-18] cancer cell diagnostics[19-22] and therapeutics[23-26] have been active fields of research. Although NPs exhibit similar size dimensions to many common biomolecules such as proteins and DNA, complete understanding of the bio-conversation between those entities and its effective clinical translation is still to be explored.[27] Research concerning the interactions between organic/inorganic nanocomposites and biological cells will enable new developments in nano-biotechnology to reach their fullest potential.

3.3. Glyco-conjugates as Cancer Biomarkers

Cancer is a complex group of diseases. Each malignant cell type has molecular signatures that distinguish it from the healthy counterpart. The availability of simple and fast methods to identify the unique cellular characteristics can greatly benefit cancer treatment and improve the clinical outcomes for patients.[21, 28-30] Currently, the majority of methods for cancer detection target biomarkers such as mutated DNA/RNA and over-expressed antigens.[28-33] This requires extensive prior knowledge on the presence of the specific markers,[31, 34] which can be very time consuming to acquire. Furthermore, as tumor cells have high tendencies to mutate,[35, 36] their antigenic

variants may escape the detection leading to false negative results. An appealing alternative is to take advantage of cell surface receptor mediated recognition events. Receptor binding is often critical to cell functions and usually cannot be abolished without affecting cell viability. In addition, cell surface receptors would be easier to target without requiring the probes to cross the cellular membrane as compared to intracellular markers.

An attractive target for receptor mediated interaction is carbohydrates and, in particular glycoconjugates, which play important roles in cancer development and metastasis.[37-42] Carbohydrates are uniquely suited for encoding biological information because of their rich structural variations.[43-45] Aberrant glycosylations on tumor cell surfaces have been extensively probed by antibodies and plant derived lectins.[42, 46, 47] This led to the identification of characteristic tumor associated carbohydrate molecules,[40, 42] which has greatly facilitated the development of carbohydrate based anti-cancer vaccine studies.[37, 48, 49] In comparison, the understanding of carbohydrate-binding properties of tumors is not as advanced. Cancer cells can interact with the extracellular matrix in their microenvironment through endogenous receptors binding with carbohydrates.[50-52] These interactions vary depending on the physiological state of the cells, as supported by the ground breaking histological studies of tumor tissues.[53-55] Therefore, the ability to characterize and distinguish carbohydrate binding profiles of a variety of cells can expedite both the mechanistic understanding of their roles in disease development and the expansion of diagnostic and therapeutic tools.[56-58] As the distinctions among cancer cell subtypes and

malignant vs. normal cells can often be subtle, a suitable tool is needed to *quantitatively* analyze the fine characteristics in carbohydrate binding of various cell types.

3.4. Nanoparticles for Cancer Detection

As mentioned earlier, nanotechnology has begun to play increasingly important roles in cancer research.[34] Using antibody immobilized nanoparticles, various types of cancer cells were detected both *in vitro*[28] and *in vivo*.[59] Recently, instead of relying on the specific antibodies, structurally related cationic gold nanoparticles bearing fluorescent polymers on the surface were prepared.[21] The differential electrostatic and hydrophobic interactions between the gold nanoparticles and cells were reflected in changes of fluorescence intensity upon cell binding, which allowed the differentiation of tumor from normal cells as well as closely related tumor cells. Herein, we explore the possibility of using a MGNP based system to detect and profile various cell types based on their carbohydrate binding abilities. MGNPs provide an appealing platform for biological detection. The spherical nanoparticles have large surface areas, which allow the attachment of multiple carbohydrates leading to enhanced avidity with carbohydrate receptors through multivalent binding.[43, 60, 61] Unlike the toxic heavy metal containing nanoparticles such as quantum dots,[62, 63] the magnetite nanoparticles have been approved for clinical uses with minimum cytotoxicity.[64, 65] Furthermore, the super-paramagnetic nature of this MGNPs can allow cell detection *via* MRI without the need to pre-label the cells.[65-68]

One challenge, however, in using MGNPs and carbohydrates for molecular recognition is that multiple cell types may bind with the same carbohydrate structure albeit having different affinities. To address this issue, we envision that by pooling the responses from an array of MGNPs, the various cell types may be differentiated through pattern recognition.[21, 69-71] Furthermore, the information obtained on the physiologically relevant carbohydrate-receptor interaction can not only enhance our understanding of the roles carbohydrate play in cancer but also guide the development of potential therapeutics such as agents against cancer adhesion. Although glyco-nanoparticles have been previously employed for elegant studies of carbohydrate-mediated biological interactions,[72-83] MGNPs have not been utilized to detect and systematically profile mammalian cells.

3.5. Synthesis and Characterization of MGNPs

The synthesis of MGNPs commenced from the tetraethoxysilane coated magnetite nanoparticle (NP **1**) prepared earlier on which amino groups were introduced via silanization with APTES (**Figure 3-1a**). Carboxylic acid derivatives of four types of naturally occurring monosaccharides, namely, Man, Gal, fucose (Fuc), and sialic acid (Sia), were then immobilized onto the amine functionalized nanoparticles through amide coupling reactions leading to MGNP **2** – **5** respectively.

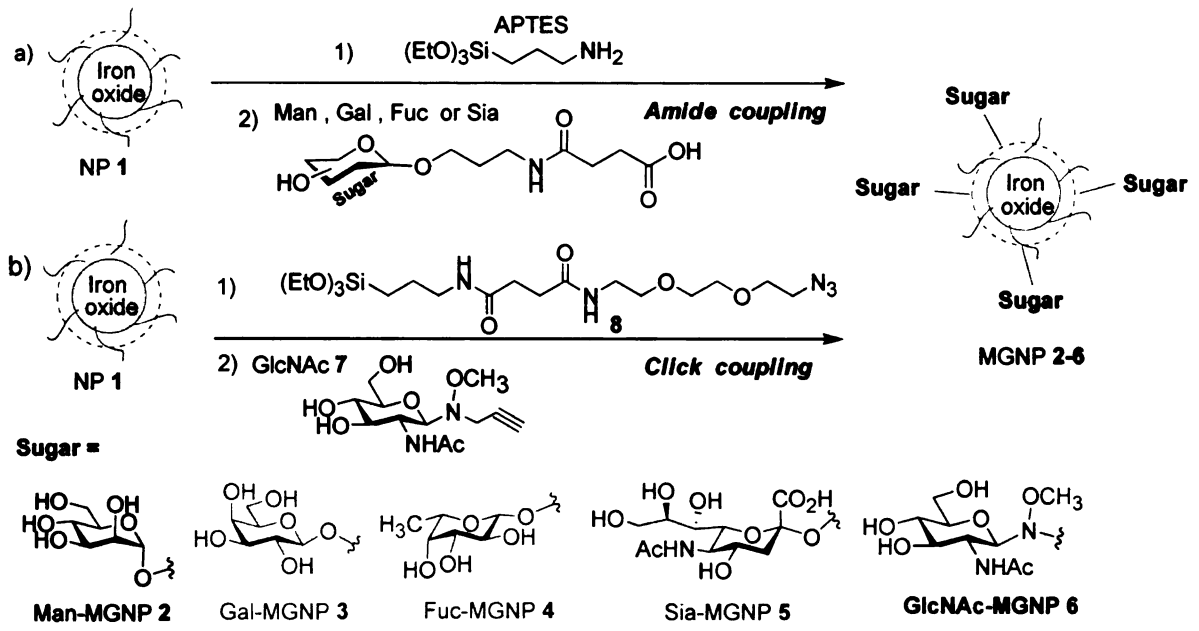

Figure 3-1. Syntheses of MGNPs.

In an alternative method, we synthesized GlcNAc-MGNP **6** *via* click chemistry. To this end, we explored the possibility of using a native unprotected sugar. The free reducing sugar GlcNAc was chemoselectively ligated with a methoxy amine linker producing GlcNAc derivative **7** containing a terminal alkyne at the reducing end (**Figure 3-2**).[84-86] NP **1** was then modified with the azido siloxane derivative **8**, which was subsequently coupled with alkynyl-GlcNAc **7** through the copper catalyzed Huisgen click reaction[87-89] to yield GlcNAc-MGNP **6** (**Figure 3-1b**). It is advantageous to use the native unprotected sugar as this opens up an avenue for future incorporation of natural polysaccharides without extensive synthetic manipulations.

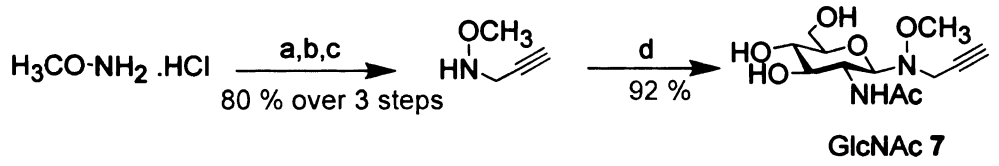

Figure 3-2. a) Benzoyl chloride, pyridine, CH_2Cl_2, 0 °C to r.t.,2 hrs; b) 3-bromopropyne, K_2CO_3, acetone, reflux for 8 hrs; c) 6% MeOH in HCl, reflux for 2 hrs; d) *N*-acetyl glucosamine, 0.1 M acetate buffer (pH=6.5) / DMF (3:1), 50 °C, 24 hrs.

As usual, all MGNPs assembled were characterized by a variety of techniques, including TEM, NMR, TGA, FT-IR, and XRD. TEM images of MGNPs indicated that the diameters of NPs were around ~ 6 nm and TGA showed that about 8% of the dry weight of MGNPs was due to carbohydrates. XRD showed the expected composition of magnetite Fe_3O_4 NPs and the patterns of the nanocrystals were assigned to the reflections of the structure of Fe_3O_4. FT-IR analysis was consistent with the expected peaks discussed before. Moreover, HR-MAS ^{1}H-NMR spectra of MGNPs gave solution-like spectra indicating that the NPs are indeed functionalized with the requisite sugars and that the carbohydrate-coating was homogenous on the particle surface.[90]

3.6. Validation of MGNP Binding Specificities

Although glyco-nanoparticles have been previously utilized to probe carbohydrate-receptor interactions,[72-83] it is important to validate that the carbohydrates immobilized on MGNPs retain their biological recognition specificity. This was probed using four lectins, i.e., *Concanavalin A* (Con A, a Man selective lectin),[91] *Wheat Germ Agglutinin* (WGA, a GlcNAc and Sia selective lectin),[92, 93] a *Bandeiraea Simplicifolia* isolectin (BS-I, a Gal selective lectin)[94] and Lotus *Tetragonolobus Purpureas Agglutinin* (TPA, a Fuc selective

lectin).[95] Upon incubation of a fluorescently labeled lectin with a MGNP, if the MGNP can bind with the lectin, subsequent application of an external magnetic field to the sample would remove the fluorescent lectin from the solution leading to a reduction of fluorescent intensity of the supernatant. Con A is a well characterized Man selective lectin with weak Gal binding affinities.[91] Incubation of Man-MGNP **2** (1 mg/mL) with FITC-labeled Con A (100 μg/mL) followed by magnetic separation led to a 89% reduction in fluorescent intensity of the solution, while the same amount of the weakly bound Gal-MGNP **3** was able to remove only 8% of the Con A (**Figure 3-3a**). This is consistent with the known carbohydrate binding preferences of Con A.[91] The addition of a solution of free mannose (18 mg/mL, 100 mM) to Man-MGNP **2**/Con A mixture did not increase the intensity of residual emission of the supernatant after magnetic separation and high concentration of mannose (180 mg/mL, 1 M) was required to partially disrupt the Con A/Man-MGNP **2** complex. These results reveal that multivalent display of carbohydrate ligands on MGNP resulted in strong lectin binding.

In contrast to Con A, the Gal selective FITC-BS-I[94] strongly bound with Gal-MGNP **3**, producing 91% reduction of the solution emission intensity (**Figure 3-3b**). At the same time, as BS-I has weak affinities with mannose,[94] incubation of Man-MGNP **2** with FITC-BS-I only decreased emission intensity a little. The same phenomena were observed with WGA and TPA.[90] WGA bound tightly with GlcNAc-MGNP **6** and Sia-MGNP **5** but not with Gal-MGNP **3** and TPA interacted strongly with Fuc-MGNP **4** as predicted based on their known binding specificities.[92, 93, 95, 96]

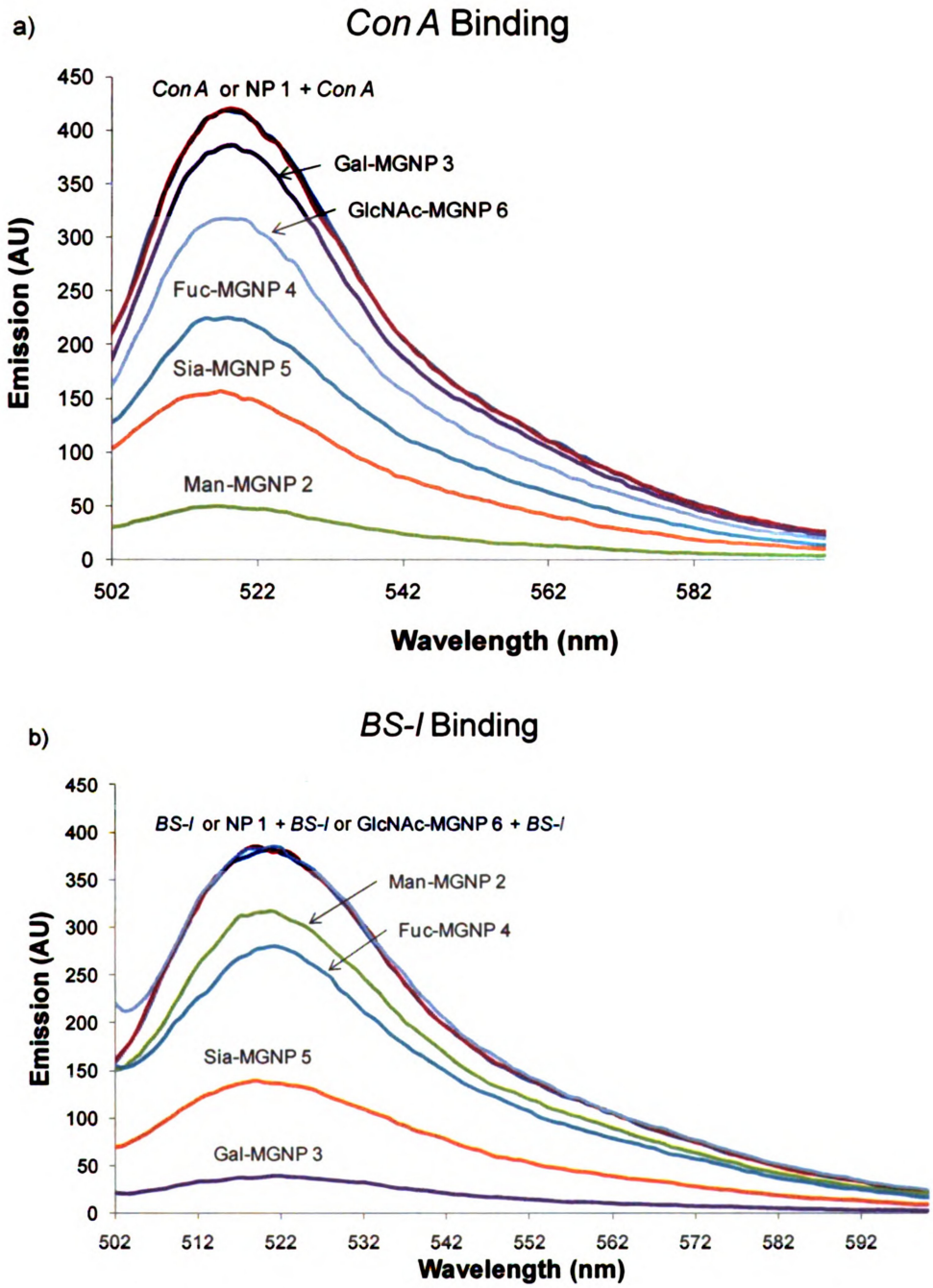

Figure 3-3. Fluorescent emission intensities of supernatents of FITC-labeled a) Con A, b) BS-I (100 μg/mL) upon incubation with various MGNPs **2-6** or control NP **1** (1 mg/mL) followed by magnet mediated separation ($\lambda_{excitation}$ = 494 nm).

In addition, NP **1** devoid of carbohydrates on the surface could not remove any proteins from the solution suggesting that the non-specific absorption on NP

surface is minimal. These observations coupled with the good specificities obtained in the *E. coli* detection experiments (section 2.5) unequivocally demonstrated that the MGNPs are not promiscuous in binding and the carbohydrates immobilized on MGNPs maintain the same biological recognition preference as the free forms in solution.

3.7. Monitoring MGNP Binding by MRI

After establishing the specificity of MGNPs using fluorescence experiments, we moved on to examine the utility of MRI to monitor the interaction of MGNPs with their biological targets. MRI measures the relaxation time of water protons in a magnetic field, which is commonly used to non-invasively visualize the internal structures and functions *in vivo*. Using MRI to monitor MGNP allows multiple samples to be measured simultaneously within a single scan,[97] thus enabling rapid response time and shortening multi-analyte data acquisition. Furthermore, when the MRI methodology for MGNP monitoring is established, it can be translated to *in vivo* applications without the need to develop a new detection technology.

Magnetic NPs can serve as MRI contrast agents, where they decrease the transverse relaxation time (T2) producing a negative contrast from the environment by virtue of signal reduction.[67, 98, 99] In the presence of a crosslinking receptor, due to the small sizes of MGNPs, multiple MGNPs can bind with the receptor assembling into clusters (**Figure 3-4**).

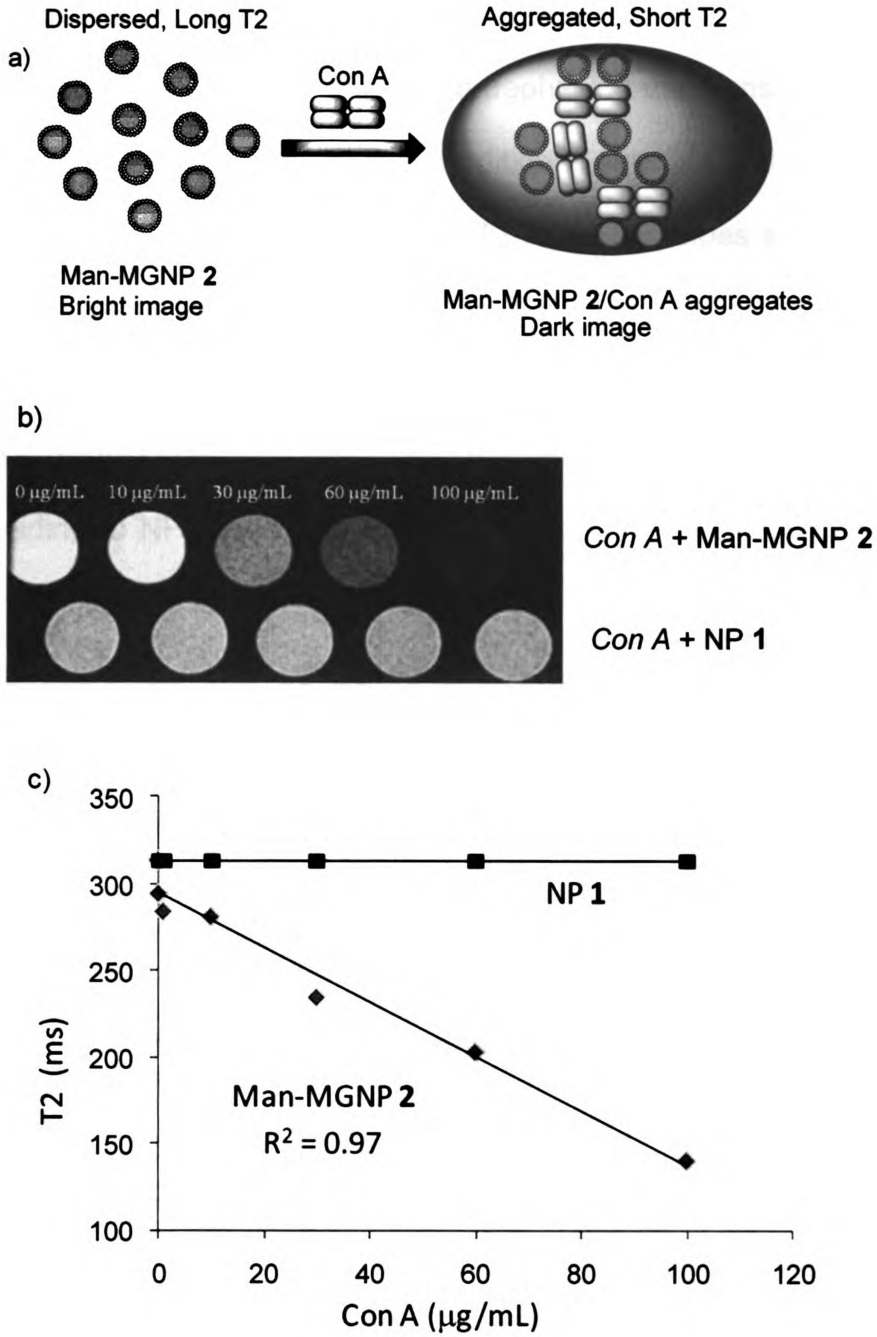

Figure 3-4. a) Incubation of Man-MGNP **2** (shown as pink balls) with Con A, a tetrameric mannose selective lectin (shown as blue rectangles) resulted in the formation of aggregates, leading to shorter T2 relaxation time and consequently a darkened MRI image. b) T2 weighted MRI images of Man-MGNP **2** (20 μg/mL) and NP **1** (20 μg/mL) upon incubation with increasing concentrations of Con A. c) T2 changed linearly upon incubation of Man-MGNP **2** with increasing concentrations of Con A, while incubation with NP **1** devoid of carbohydrates did not lead to any change.

With their increased sizes, the aggregates create larger local magnetic field gradients and thus become more efficient at dephasing the spins of surrounding water protons as the motional averaging condition is satisfied at the nanoparticle size regime.[100, 101] This leads to lowering of T2 relaxation times as described by the magnetic relaxation switching theory.

Our detection assay was first tested using Con A. As one Con A contains four mannose binding sites,[102] it can crosslink multiple mannose containing Man-MGNP **2**, leading to NP aggregation, which should result in the reduction of T2 relaxation time (**Figure 3-4a**). Due to the superparamagnetic nature of the magnetic nanoparticles, only 20 μg/mL of MGNP was needed for detection. When Man-MGNP **2** was mixed with increasing concentrations of Con A, the binding equilibrium was shifted more towards the aggregates. This led to a sequential decrease of the brightness of the corresponding T2 weighted MR images (**Figure 3-4b**). Quantification of the images showed an excellent linear correlation between Con A concentration and T2 relaxation time, with as little as 0.1 μg/mL (1 nM) of Con A detected (**Figure 3-4c**). In contrast, the control NP **1** devoid of mannose did not cause any change in T2, signifying that the contrast change was due to the specific binding between Man-MGNP **2** and Con A. In addition, incubation of the GlcNAc selective WGA with GlcNAc-MGNP **6** led to a linear decrease of T2 relaxation time with increasing concentrations of WGA, while the mixture of WGA with the non binding Gal-MGNP **3** did not produce any T2 changes. These results corroborated the fluorescence studies and confirmed

MGNP binding specificities which gave us great confidence to apply this technology to cancer cell study.

3.8. Mammalian Cells Selectively Bound with MGNPs as Detected by MRI

Building on the success of lectin and *E. coli* detection, we evaluated the utility of MGNPs in monitoring mammalian cell interactions and cancer cell detection. The use of carbohydrates as the recognition elements can provide functional information on cell surface active carbohydrate receptors. This is complementary to the usage of antibodies, as the latter monitor the presence of particular antigenic structures, which can be absent in some cancer cell mutants. In addition, an antibody is commonly limited to binding a specific target, while carbohydrate ligands can be used to monitor a range of cells, thus reducing the number of reagents required for study.

A normal breast cell line 184B5 and nine types of representative cancer cells were used for our study including human ovarian adenocarcinoma SKOV-3, colon HT29, kidney A498, lung A549, and breast cancer MCF-7/Adr-res and the closely related murine melanoma cell lines B16F10 and B16F1, mammary adenocarcinoma TA3-ST and TA3-HA. Each type of cells at two concentrations (10^5 and 10^6 cells/mL) was incubated with MGNP **2-6** or the control NP **1**, and the T2 relaxation times of all the samples were recorded. Thirty samples were measured at the same time with our MRI setup. While no significant T2 changes were observed with any cells upon mixing with the NP **1**, the ten cell lines produced a large variation in T2 reductions upon MGNP incubation with the T2

changes normalized against the largest ΔT2 within each MGNP category (**Figure 3-5**).

The decrease of the absolute values of T2 upon MGNP incubation can be explained due to particle agglomeration upon cell binding. At a higher cell concentration (10^6 cells/mL, **Figure 3-5b**), more MGNPs were bound leading to larger ΔT2 compared with lower cell concentration (10^5 cells/mL) for each cell line (**Figure 3-5a**). Furthermore, when the cells were pre-incubated with a solution of a free monosaccharide (100 mM) and then treated with the MGNP bearing the same carbohydrate, T2 changes were less due to the competitive binding of the free monosaccharide with cells. These observations were consistent with the notion that T2 reduction was induced by the specific MGNP/cell interactions.

3.9. Biological Implications of Carbohydrate-receptors on Cancer Cells

Based on the MR responses, in most of the cell lines examined, bindings with Fuc-MGNP **4** and Sia-MGNP **5** were observed (**Figure 3-5**), suggesting these cell lines have active fucose and sialic acid receptors.[56] B16F1, B16F10, MCF-7/Adr-res, and SKOV-3 were found to interact with β-galactoside. This is of special interest since it confirmed the previously reported galactoside binding of the B16F10[56] presumably through galectins, a family of galactose specific lectins as well as the high expression level of galectins on MCF-7/Adr-res[103] cells. Furthermore, HT29, MCF-7/Adr-res, 184B5, A498, and SKOV-3 express functioning GlcNAc receptors as suggested by their interactions with GlcNAc-MGNP **6**. Moreover, MCF-7/Adr-res, 184B5, SKOV-3, B16F10, B16F1, A549 and A498 bind mannose.[104]

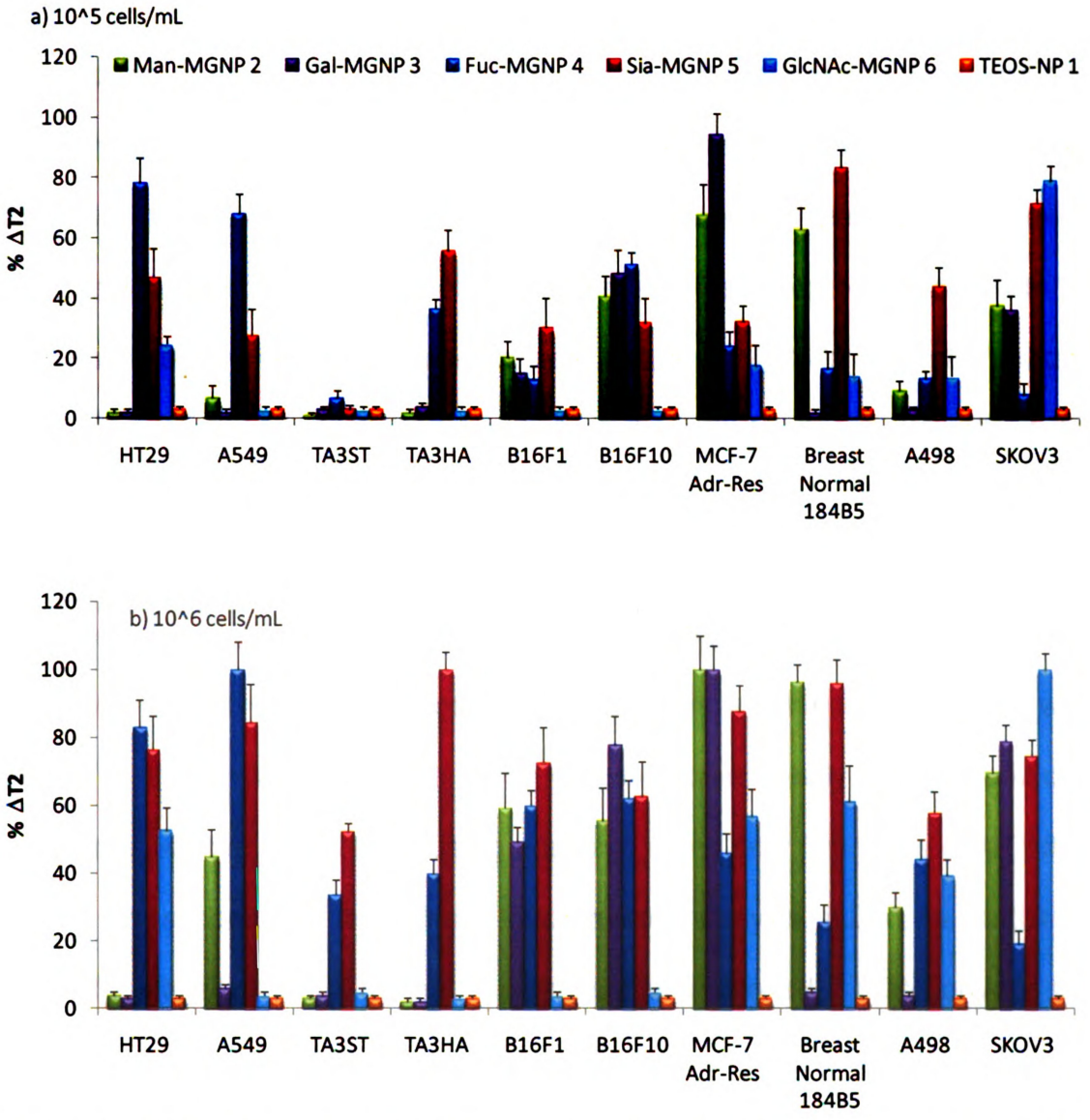

Figure 3-5. a) Percentage changes of T2 relaxation time (% ΔT2) obtained upon incubating MGNPs **2-6** or the control NP **1** (20 μg/mL) with ten cell lines (10^5 cells/mL). The ΔT2 was calculated by dividing the T2 differences between MGNP and MGNP/cancer cell by the corresponding highest ΔT2 from each MGNP category. b) % ΔT2 obtained upon incubating MGNPs **2-6** or the control NP **1** (20 μg/mL) with ten cell lines (10^6 cells/mL). The above data represent the averages of 8 individual measurements with the error bars showing standard deviations.

The sugar free nanoprobe NP **1** did not bind to any cells in our study, evidence to the importance of intrinsic carbohydrate-protein interactions involved and the exclusion of nonspecific interactions as the cause of binding. The wealth of new information generated on the sugar binding preferences of these cell lines can be very useful for cancer research. Although some of the receptors responsible for binding are not determined yet, the magnetic nature of MGNPs can help facilitate the enrichment and identification of carbohydrate receptors on these cells in the future through magnet mediated separation.

3.10. Establishment of MR Responses as Molecular Signatures for Full Differentiation of All Ten Cell Lines *via* LDA Analysis

With the diverse MR signature in hand, we examined whether it was possible to differentiate all ten cell lines. This was a particularly stringent test due to the large number of cell lines being analyzed using only five types of MGNPs. In order to accomplish this, linear discriminant analysis (LDA), a statistical method for classification of groups of objects, was employed.[70] LDA converts the ΔT2 values of each cell line to canonical linear discriminants (LDs), which are linear combinations of the original data weighted by coefficients producing the greatest analyte discrimination. LDA is a powerful technique, which has been successfully applied to the detection of a variety of targets including carbohydrates, proteins, and cells.[21, 70, 71, 105-107] All T2 changes (6 types of NPs, 10 cell types, 8 repetitions) at each cell concentration were submitted to LDA and LDs were generated. Based on the LDA patterns, the ten cell lines were easily clustered into ten respective groups (**Figure 3-6**). At the 10^5 cells/mL concentration, the first three LDs contain 49.5, 25.3 and 17.5% of the variations

respectively, which account for 92.3% of the total variations. Validation of the LDA was carried out using a jackknife matrix method,[108] where all but one measurement out of each group was treated as a new training set. The group memberships of the omitted observations were then predicted based on the new training set, which were accurately classified in all the cases tested. This highlights that despite the simple structures of the monosaccharides utilized, the T2 changes of the MGNP array can be employed as characteristic molecular signatures for each cell line.

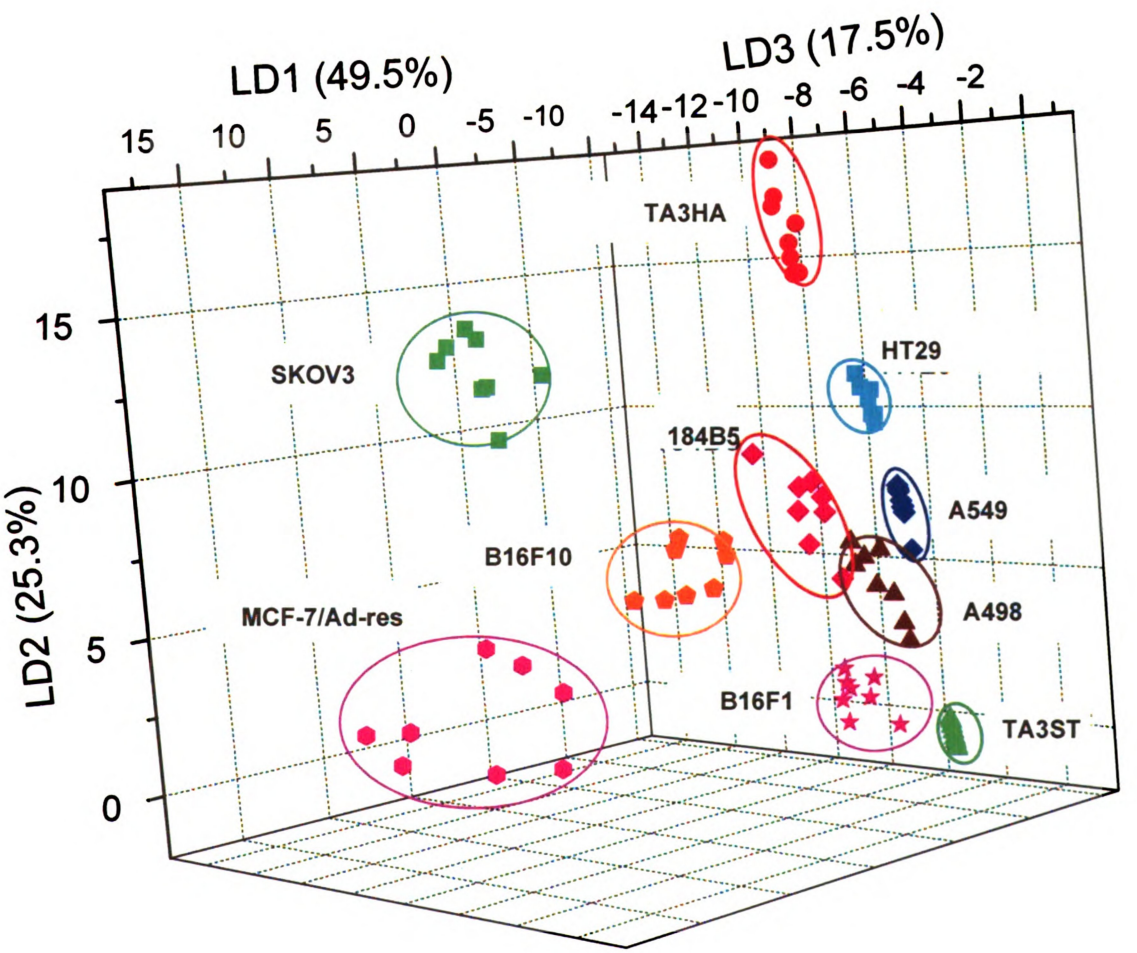

Figure 3-6. LDA plots for the first three LDs of ΔT2 patterns obtained with the MGNP array upon binding with the ten cell lines (10^5 cells/mL). Full differentiation of the ten cell lines was achieved.

3.11. Detection of Cancer Cells *vs* Normal Cells based on the MR Signature

A major hurdle for cancer treatment and early cancer detection is the identification of pertinent cellular signatures to allow the differentiation of normal cells from their cancerous counterparts. We envision that this can be achieved by analysis of the respective cellular characteristics towards carbohydrate binding. As a proof-of-principle, the $\Delta T2$ of the breast cancer MCF-7/Adr-res cells *vs* the normal breast endothelial cells 184B5 upon MGNP binding were examined in detail. As the trend of binding is the same qualitatively at both cell concentrations, we focused mainly on T2 changes at 10^5 cells/mL. The interactions with Man-MGNP **2**, Fuc-MGNP **4** and GlcNAc-MGNP **6** were found to be very similar between the two cell lines (**Figure 3-7a**). However, the MCF-7/Adr-res cells caused a significantly larger $\Delta T2$ upon binding with Gal-MGNP **3** as compared with the normal breast cells 184B5, which enabled easy detection of breast cancer cells. This corroborated with literature that MCF-7/Adr-res cells contain the cancer-specific galactoside binding galectins which are absent in non-cancer cell lines.[103] Modification of the galactoside ligand structures[109] as well as optimization of ligand density and nanoparticle surface chemistry can further improve the selectivity in binding for future *in vivo* applications.

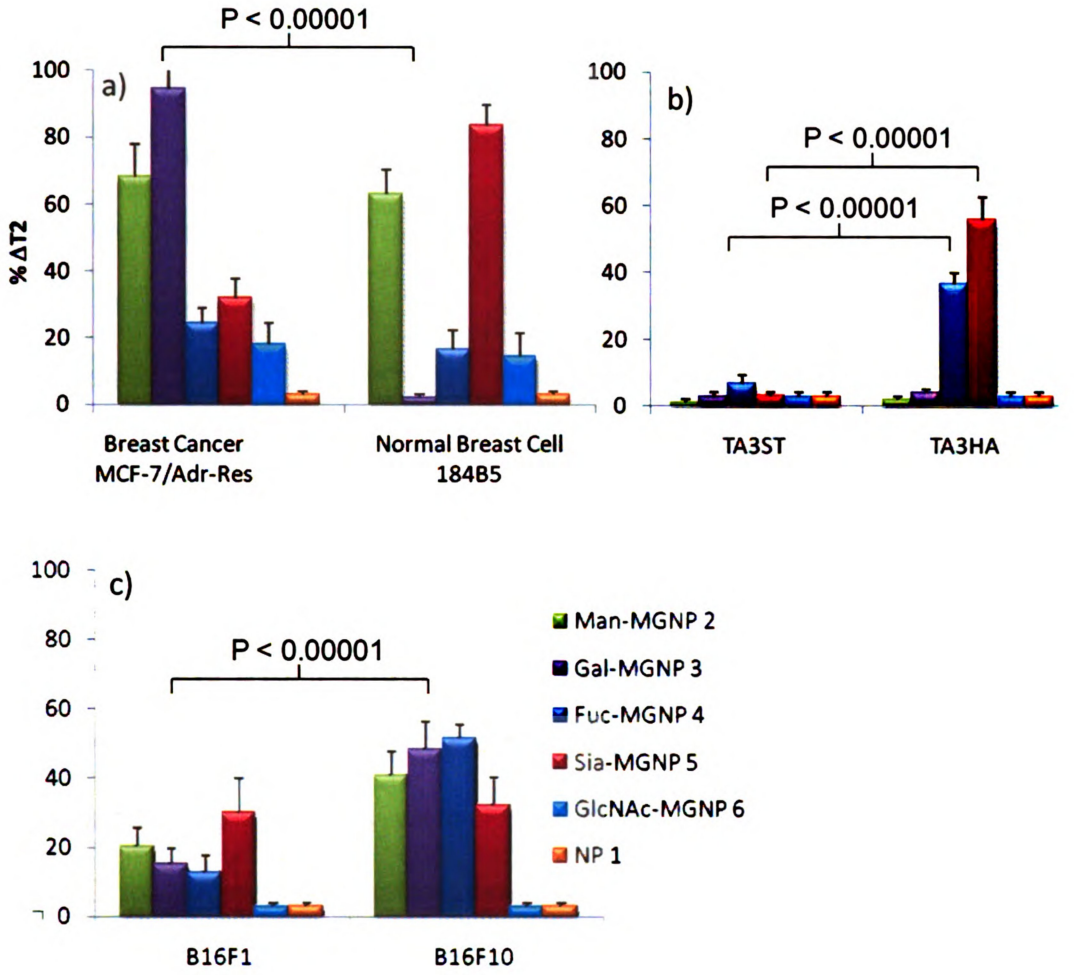

Figure 3-7. % ΔT2 obtained upon incubating MGNPs **2-6** or the control NP **1** (20 μg/mL) with a) breast cancer MCF-7/Adr-res vs normal breast cell 184B5; b) TA3ST vs TA3HA cell lines; and c) B16F1 vs B16F10 (10^5 cells/mL). Significant differences in binding with MGNPs were observed differentiating these cell lines.

3.12. Differentiation of Closely Related Isogenic Cancer Cells including Metastatic Cancer Cells

Besides the differentiation of cancer *vs* normal cells, the MR data also enabled the distinction between closely related isogenic sublines of cancer cells. Isogenic cancer cells are derived from the same parent cell line, presenting significant challenges for identification. One example is the mouse mammary carcinoma cells TA3HA and TA3ST. These two types of cells originated from the same parent cell line with TA3HA expressing the mucin like cell surface

glycoprotein epiglycanin absent in TA3ST.[110] Despite this subtle difference, TA3HA showed significantly stronger interactions with the Fuc-MGNP **4** and Sia-MGNP **5** (**Figure 3-7b**).

Another example of closely related cells are the widely used B16F10 and B16F1 mouse melanoma cells, where no qualitative differences in protein composition, galactose or sialic acid content on the cell surfaces or the membrane fluidity were observed before.[111] The quantitative nature of the MGNP approach uncovered the subtle difference between these two cell lines with B16F10 showing larger T2 change ($P<0.00001$) upon binding with Gal-MGNP 3 as compared to B16F1 (**Figure 3-7c**), which is likely due to the higher level of galectins expressed on B16F10 cells.[56] This is consistent with the observation that galactoside mimetics were more potent in preventing the adhesion of B16F10 to extracellular matrix component than that of B16F1.[56] B16F10 also caused larger $\Delta T2$ with Man-MGNP **2** and Fuc-MGNP **4** at 10^5 cells/mL. These results indicate that despite the overall similarity, there are quantitative changes in carbohydrate binding between the B16F1 cells and its metastatic variant B16F10.

3.13. Cellular Uptake and Bio-compatibility of MGNPs

In order to gain insights into how MGNPs interact with cells, cellular staining experiments were performed. Besides their properties as MRI contrast agents, MGNPs can be visualized by Prussian blue staining, which yields an intense blue color upon reaction with the magnetite core of MGNPs allowing easy tracking of the particles.

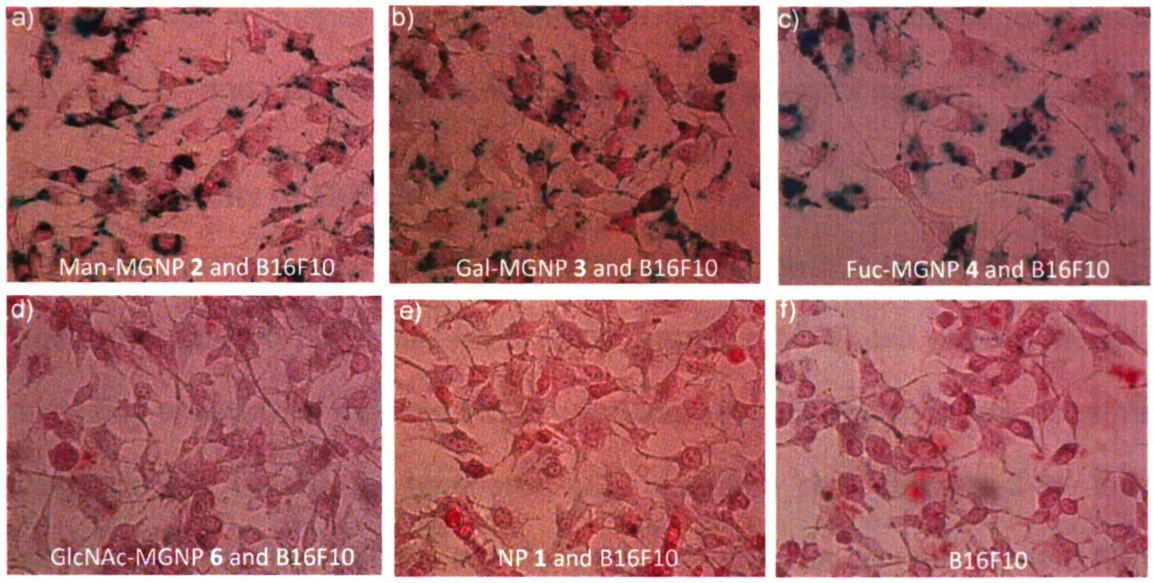

Figure 3-8. Prussian blue staining images of 20 μg/mL of a) Man-MGNP **2**; b) Gal-MGNP **3**; c) Fuc-MGNP **4**; d) GlcNAc-MGNP **6**; and e) control NP **1** incubated with B16F10 cancer cells after unbound particles were removed by washing and f) B16F10 cells. The images clearly indicated the high intracellular uptake of Man-MGNP **2**, Gal-MGNP **3** and Fuc-MGNP **4**. No Prussian blue stains were visible with the non-binding GlcNAc-MGNP **6** and the control NP **1** proving the selectivity in binding.

As an example, B16F10 cells were incubated with MGNPs (20 μg/mL), washed extensively with buffer to remove all unbound nanoparticles and stained with Prussian Blue. As Man-MGNP **2**, Gal-MGNP **3** and Fuc-MGNP **4** caused the biggest T2 changes when incubated with B16F10, strong blue stains were observed both on cell surface and inside the cells suggesting a significant cellular surface binding and cellular uptake (**Figure 3-8a-c**). In contrast, the non-binding GlcNAc-MGNP **6** and control particle NP **1** without any carbohydrates did not show much staining (**Figure 3-8d-f**). The same phenomena were observed with other cell lines as well. The correlations between Prussian Blue staining and $\Delta T2$ changes proved that the MR changes were indeed due to NP binding with the cells. The selective uptake and intracellular accumulation of specific MGNPs in cancer cells and the ability of MGNPs to differentiate normal cells from tumor

cells bode well for further development of MGNPs as vehicles for targeted drug delivery[112, 113] and magnetic induced hyperthermia therapy of cancer.[114]

3.14. Cytotoxicity of MGNPs

Next, we examined the toxicity of the MGNPs towards the cells by 3-(4,5-dimethylthiazol-2-yl)-2,5-diphenyltetrazolium bromide (MTT) cell viability assays. Incubation of cells with different MGNPs for one week did not show any negative effects on cell viability as compared with untreated cells (**Figure 3-9**). This demonstrates that the MGNPs are biocompatible and can be used as safe MRI contrast agents.

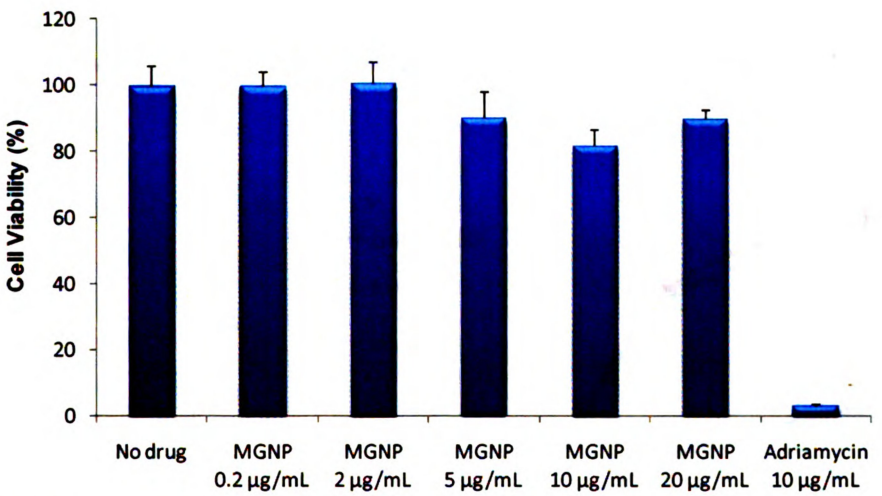

Figure 3-9. As an example, MTT assay of A498 cells incubated with Fuc-MGNP **4** showed no cytotoxicity after one week incubation, while Adriamycin killed most of the cells.

3.15. Anti-adhesive Properties of MGNPs

Tumor metastasis is associated with poor prognosis of cancers.[47] One of the critical steps in metastasis is the adhesion of circulating tumor cells to endothelium at the target location. It has been demonstrated that cell adhesion inhibitors can be a potential treatment for metastatic diseases.[115-117]

The MRI signature from MGNPs provides detailed information on how tumor cells interact with each carbohydrate, which is valuable for guiding the development of anti-adhesive agents, as the strongly binding MGNPs can reduce the adhesion of cancer cells to the matrix by blocking the cell surface receptors. According to the MRI signature, Gal-MGNP **3** interacted strongly with B16F10 cells, which led us to measure its anti-adhesive properties as a proof-of-principle study. Upon incubation of B16F10 cells with Gal-MGNP **3**, the number of cells adhered to the surface was reduced by more than 50% (**Figure 3-10**). In contrast, the non-binding NP **1** showed little effect on cell adhesion. Modification of the monosaccharide ligands immobilized on MGNPs may strengthen the binding with the cells, further enhancing the anti-adhesive effects.

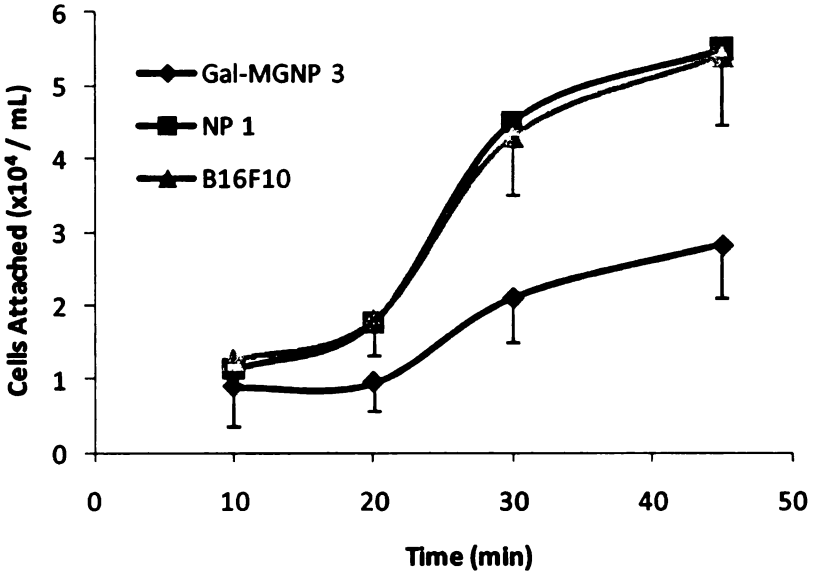

Figure 3-10. The adhesion of mouse melanoma B16F10 (~ 5 x 10^4 cells/mL) to the surface was significantly reduced by incubation with Gal-MGNP **3** (blue line), while the control NP **1** (green line) had no effect on cell adhesion as compared to cells without treatment with any NPs (red line). Error bars indicate standard deviations (triplicate readings).

In conclusion, a new approach based on the multi-channel MR responses of MGNPs to qualitatively and quantitatively map the carbohydrate binding characteristics of a variety of cancer cells was developed. Validated through binding with a series of lectins and a well characterized *E. coli* system, the carbohydrates immobilized on MGNPs were found to retain their biological recognition and binding specificities. Although the monosaccharides utilized in this study are fairly simple in structures and multiple cells may bind with the same carbohydrate, the selective carbohydrate-receptor binding with the MGNP array amplified the small structural differentials. The resulting combined array responses allowed the detection of cancer cells as well as the differentiation of closely related isogenic cancer cell subtypes without detailed prior knowledge on endogenous carbohydrate receptors, while the wealth of information generated and magnetic nature of the MGNPs can facilitate future identification of the receptors. The LDA pattern recognition method was applied to decipher the glyco-code of tumor cell binding, which may be a useful and general protocol to analyze carbohydrate-receptor interactions.

The strongly binding MGNPs were found to be internalized by tumor cells, and they significantly reduced the cancer cell adhesion. As the MGNP array measures the physiologically related carbohydrate-receptor interactions, which are involved in a variety of cellular functions including endocytosis, cell-matrix and cell-cell communications, the knowledge gained from this new addition to the glyco-nanotechnology toolbox can enhance our understanding of cancer cell functions. This can provide leads for further ligand optimization to improve the

specificity in carbohydrate receptor recognition, which in turn can enable the application of MGNPs for *in vivo* cancer detection through MRI in the future.

3.16. Experimental Section

3.16. a. Cells and Culture Conditions

Unless otherwise indicated, all starting materials, reagents and solvents were obtained from commercial suppliers (Sigma-Aldrich or Fisher Scientific) and used as supplied without further purification. All fluorescein labeled lectins were purchased from Aldrich. All cell lines were purchased from the American Type Culture Collection (ATCC) [Cell line designation (Catalog No.), type] unless otherwise noted: 184B5 (CRL-8799), normal breast cell; A498 (HTB-44), kidney cancer; A549 (CCL-185), lung cancer; HT29 (HTB-38), colon cancer; SKOV-3 (HTB-77), ovarian cancer; B16-F10 (CRL-6475), metastatic mouse melanoma; B16-F1 (CRL-6323), less metastatic mouse melanoma. The MCF-7/Adr-res (breast cancer Adriamycin resistant) cell line was obtained from the National Cancer Institute. Two murine mammary carcinoma cell lines (TA3-HA, TA3-ST) were kind gifts from Dr. John Hilkens, Netherlands Cancer Institute. All cell lines were grown as monolayer cultures on tissue culture dishes in phenol red free DMEM (Invitrogen, Carlsbad, CA) supplemented with 10% fetal bovine serum (FBS) (Sigma), penicillin G (Sigma, 61.4 μg/mL), streptomycin (Sigma, 100 μg/mL) and L-Glutamine (Sigma, 292 μg/mL) at 37°C in an atmosphere of 5% CO_2 and 95% air. All cells were grown to log-phase, trypsinized with trypsin-EDTA solution (0.25 % trypsin, 1 mM EDTA) to detach the cells, washed twice by

centrifugation to remove any residual trypsin and re-suspended in the appropriate media.

3.16. b. MRI and Relaxivity Measurement

Magnetic resonance imaging studies were carried on a 3T Signa® HDx MR scanner (GE Healthcare, Waukesha, WI). Thirty test tube samples were scanned simultaneously in a standard quadrature birdcage head coil. For T2 measurements, a multi-echo fast spin-echo sequence (time of repetition = 500 ms, receiver bandwidth = ± 31.25 kHz, field of view = 20 cm, slice thickness = 3 mm, gap = 3 mm, number of excitation = 1, and matrix size = 256 × 128) was used to simultaneously collect a series of data points at seven different echo times (*TE*) 15-60 ms with an increment of 7.50 ms at two slice locations. For each sample, the region of interest (ROI) (circles of 4.5 mm radius) was drawn at the center of each test tube at both slice locations. The T2 was calculated based on the semi-log linear regression of the mean signal intensity values at the ROI and the corresponding *TE*s. Specifically, $1/T2 = -[(\ln S_n - \ln S_m)/(TE_n - TE_m)]$, where S_n and S_m are voxel signal intensity values at *TE* values of TE_n and TE_m.

3.16. c. Detection of Cancer Cells using MGNPs

Cell suspensions (10^5 or 10^6 cells/mL) were prepared in phenol red free DMEM media supplemented with 0.20 % bovine serum albumin. Aliquots of these cultures were placed in sterile tubes and MGNPs **2-6** (final concentration 20 μg/mL) were added. NP **1** without any carbohydrates was used as the control. The tubes were incubated with gentle mixing at 37 °C. The T2 values MGNP/cell

suspensions and MGNP in the absence of cells were then recorded *via* MRI. MRI experiments were performed 8 times for each cell line at both cell concentrations. The largest T2 value change upon binding with cells for each MGNP was set as 100%. The ΔT2 % for each cell line was calculated as the percentage of change relative to the largest T2 changes for the respective MGNP. LDA was performed using the statistical computing and graphics software R.

3.16. d. Prussian Blue Staining

Different cancer cell lines were seeded onto 24-well plate. After incubation for 12 hrs at 37 °C, nanoparticles were added to the plate in a final concentration of 20 μg/mL per well. After 12 hrs, the supernatant was removed and cells were washed three times with PBS, treated with 10% formalin solution (0.50 mL) for 5 minutes to fix the cells, and then washed with PBS. Prussian blue staining was then performed. To each well was added a 1:1 mixture of 4% potassium ferrocyanide(II) trihydrate and 2% HCl solution (0.50 mL), and cells were incubated for 30 minutes at 37 °C in the dark, counterstained with nuclear fast red for 3 min, and then washed three times with PBS. The Prussian blue staining images were assessed by an inverted light microscope.

3.16. e. Cell Viability

Adherent cancer cells (10^5 cells/mL) were plated in each well (100 μL/well) of a 96-well plate. MGNP at the desired concentrations (from 0.2, 2, 5, 10, 20 μg/mL per well) as well as Adriamycin (10 μg/mL) were then added respectively. After incubation for 5 days at 37 °C in 5% CO_2, aqueous MTT solution (5 mg/mL,

20 μL) was added to each well. After incubation for 4 hrs at 37 °C, the supernatant was removed from each well and DMSO (100 μL) was added to dissolve the converted dye. Absorption at 550 nm was then measured on a plate reader to determine the cell viability. Each result was the average of triplicate readings for each concentration. The absorbance from the untreated cells was set as 100% viability. Cell viabilities with various concentrations of MGNPs and Adriamycin were calculated by dividing the respective absorbance by that from the untreated cells.

3.16. f. Anti-adhesive Assay

Cancer cells were detached using 2 mM EDTA in PBS, washed with PBS, counted to final concentration of ~ 5 x 10^4 cells/mL and incubated with Gal-MGNP (20 μg/mL) for 3 h at 37 °C in DMEM containing 10 % FBS. The cells were then immediately seeded in a 24-well plate and incubated at 37 °C. After 10, 20, 30 and 45 minutes of incubation, the medium and the floating cells were carefully removed by aspiration, and the attached layers were washed twice with PBS. The firmly attached cells were then counted under an inverted light microscope. Cell adhesion curves were generated after counting triplicate wells (20 different homogeneous fields per each well).

3.16. g. Preparation of MGNPs

1. Syntheses of Carboxylic Acid-functionalized Sugars

a- Synthesis of Fucose Amido-acid (Fuc)

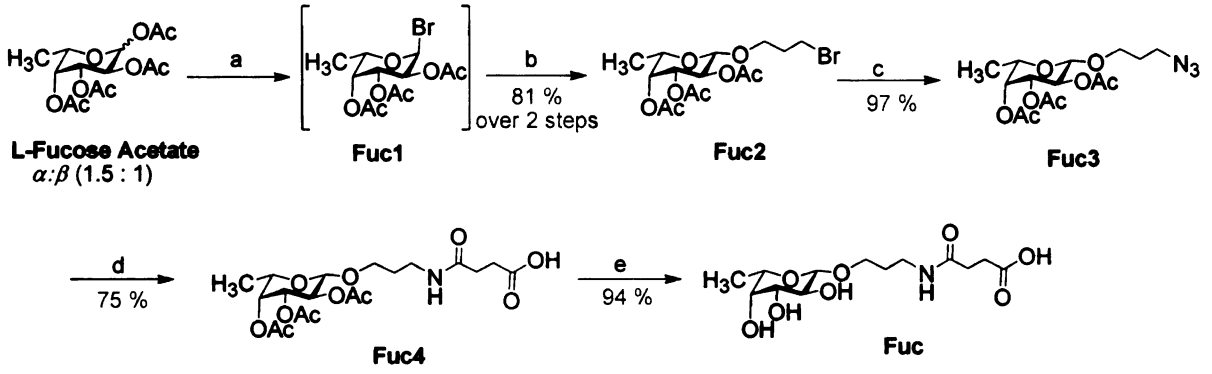

Figure 3-11. a) 33% HBr in AcOH, CH_2Cl_2, 2 hrs; b) 3-bromo-1-propanol, MS 4Å, Ag_2CO_3, CH_2Cl_2, 18 hrs; c) NaN_3, DMF, 80 °C, 18 hrs; d) succinic anhydride, H_2/Pd-C, THF, 3 hrs; e) NaOMe/MeOH, 1h.

Bromopropyl 2,3,4-tri-*O*-acetyl-β-L-fucose (Fuc2). To a cooled solution of L-fucose tetraacetate[118] (1.50 g, 4.51 mmol) in dry CH_2Cl_2 (15.0 mL), 33% HBr-AcOH (9 mL) was slowly added, and the mixture was stirred for 2 hrs at room temperature under nitrogen. The reaction mixture was concentrated and the resulting orange oil was azeotroped with toluene (5x). Then, a solution of the residue in dry CH_2Cl_2 (20 mL) containing activated molecular sieves (4 Å; 1.5 g) was stirred for 15 min at room temperature under nitrogen. 3-Bromo-1-propanol (0.750 mL, 8.63 mmol) was added and stirring was continued for another 30 min. Silver carbonate (1.65 g, 5.98 mmol) was then added, and the obtained suspension was stirred overnight. The reaction mixture was then diluted with CH_2Cl_2 and filtered through Celite. The filtrate was washed with saturated aq. $NaHCO_3$ and brine repeatedly, dried over Na_2SO_4, filtered, and concentrated.

Column chromatography (30% EtOAc in Hexane) of the residue afforded **Fuc2** as a white foam (1.50 g, 81% over two steps). ^{1}H NMR (500 MHz, $CDCl_3$): δ_H 1.18 (d, J = 6.5 Hz, 3H, CH_3), 1.93-2.00 (m, 1H, OCH_2CH*H*$_b$$CH_2Br$), 1.94, 2.03, 2.12 (3s, 3 x 3H, CH_3CO), 2.10-2.18 (m, 1H, OCH_2C*H*$_a$$HCH_2Br$), 3.44 (dd, J = 5.5, 7.5 Hz, 2H, OCH_2CH_2C*H*$_2$Br), 3.59-3.64 (m, 1H, OC*H*$_a$$HCH_2CH_2Br$), 3.78 (dq, J = 1.0, 6.5 Hz, 1H, H-5), 3.94-3.98 (m, 1H, OCH*H*$_b$ CH_2CH_2Br), 4.41 (d, J = 7.5 Hz, 1H, H-1), 4.98 (dd, J = 3.5, 10.0 Hz, 1H, H-3), 5.12 (dd, J = 7.5, 10.5 Hz, 1H, H-2), 5.19 (dd, J = 1.0, 3.5 Hz, 1H, H-4). ^{13}C NMR (125 MHz, $CDCl_3$): δ_C 16.2, 20.8, 20.9, 21.0, 30.5, 32.5, 67.3, 69.2, 69.3, 70.4, 71.5, 101.5, 169.8, 170.4, 170.9. HRMS *m/z* calcd. for $C_{15}H_{23}BrNaO_8$ $[M+Na]^+$: 433.0474; found: 433.0472.

Azidopropyl 2,3,4-tri-*O*-acetyl-β-L-fucose (Fuc3). Bromopropyl 2,3,4-tri-*O*-acetyl-β-L-fucose **Fuc2** (0.920, 2.24 mmol) and NaN_3 (1.16 g, 17.8 mmol) were dissolved in DMF (15.0 mL), and refluxed for 18 hrs at 80 °C under nitrogen. The mixture was then concentrated *in vacuo*, diluted with CH_2Cl_2 and washed with water, dried over Na_2SO_4, filtered, and concentrated affording the product **Fuc3** as a white foamy solid (0.810 g, 97%). ^{1}H NMR (500 MHz, $CDCl_3$): δ_H 1.22 (d, J = 6.0 Hz, 3H, CH_3), 1.77-1.93 (m, 2H, OCH_2C*H*$_2$$CH_2Br$), 1.98, 2.06, 2.17 (3s, 3 x 3H, CH_3CO), 3.35-3.39 (m, 2H, OCH_2CH_2C*H*$_2$Br), 3.56-3.60 (m, 1H, OCH*H*$_b$$CH_2CH_2Br$), 3.81 (dq, J = 1.0, 6.5 Hz, 1H, H-5), 3.95-3.99 (m, 1H, OC*H*$_a$H CH_2CH_2Br), 4.43 (d, J = 8.0 Hz, 1H, H-1), 5.01 (dd, J = 3.5, 10.5 Hz, 1H, H-3), 5.18 (dd, J = 8.0, 10.5 Hz, 1H, H-2), 5.23 (dd, J = 1.0, 3.5 Hz, 1H, H-4). ^{13}C NMR (125 MHz, $CDCl_3$): δ_C 16.3, 20.8, 20.9, 21.0, 29.2, 48.2, 66.5, 69.2, 69.4,

70.5, 71.5, 101.4, 169.8, 170.4, 170.9. HRMS *m/z* calcd. for $C_{15}H_{24}O_8N_3$ $[M+H]^+$: 374.1563; found: 374.1565.

***O*-Acetyl fucose amido-acid (Fuc4).** A mixture of fucoside **Fuc3** (0.770 g, 2.06 mmol), succinic anhydride (0.300 g, 3.00 mmol) and 10 % Pd/C (0.250 g) in dry THF (20.0 mL) was stirred at room temperature under H_2. After 3 hrs, the reaction mixture was filtered off through Celite and concentrated. Purification by column chromatography eluting 5% MeOH in CH_2Cl_2 afforded **Fuc4** (0.690 g, 75% yield). ^{1}H NMR (500 MHz, $CDCl_3$): δ_H 1.21 (d, *J* = 6.5 Hz, 3H, C*H*$_3$), 1.70-1.84 (m, 2H, OCH$_2$C*H*$_2$CH$_2$NH), 2.16, 2.05, 1.96 (3s, 3 x 3H, C*H*$_3$CO), 2.51-2.67 (m, 4H, OCC*H*$_2$C*H*$_2$COOH), 3.26-3.32 (m, 1H, OCH$_2$CH$_2$CH*H*$_b$NH), 3.36-3.42 (m, 1H, OCH$_2$CH$_2$C*H*$_a$HNH), 3.52-3.56 (m, 1H, OCH*H*$_b$CH$_2$CH$_2$Br), 3.81 (dq, *J* = 1.0, 6.5 Hz, 1H, H-5), 3.96-4.00 (m, 1H, OC*H*$_a$HCH$_2$CH$_2$NH), 4.40 (d, *J* = 7.5 Hz, 1H, H-1), 5.02 (dd, *J* = 3.5, 10.5 Hz, 1H, H-3), 5.13 (q, *J* = 7.5, 10.5 Hz, 1H, H-2), 5.22 (dd, *J* = 1.0, 3.5 Hz, 1H, H-4), 6.56 (t, *J* = 5.5 Hz, 1H, N*H*). ^{13}C NMR (125 MHz, $CDCl_3$): δ_C 16.2, 20.8, 20.9, 21.1, 29.1, 30.3, 30.7, 38.2, 69.3, 69.4, 69.5, 70.4, 71.2, 101.4, 170.4, 170.5, 170.9, 173.0, 176.2. HRMS *m/z* calcd. for $C_{19}H_{30}O_{11}N$ $[M+H]^+$: 448.1819; found: 448.1817.

Fucose amido-acid (Fuc). Deprotection of O-acetyl fucose amido-acid **Fuc4** (0.200 g, 0.447 mmol) using NaOMe/MeOH (0.50 mL, 5.40 M) in dry methanol (2.00 mL) afforded the final product **Fuc** as a foamy white solid in 94 % yield (0.135 g) after flash column chromatography (30 % MeOH in DCM). ^{1}H NMR (CD_3OD, 500 MHz): δ_H 1.27 (d, *J* = 6.5 Hz, 3H, C*H*$_3$), 1.76-1.82 (m, 2H, OCH$_2$C*H*$_2$CH$_2$NH), 2.48 (t, *J* = 7.0 Hz, 2H, COC*H*$_2$CH$_2$COOH), 2.58 (t, *J* = 7.0

Hz, 2H, $COCH_2CH_2COOH$), 3.24-3.38 (m, 2H, $OCH_2CH_2CH_2NH$), 3.49-3.51 (m, 2H, H-2, H-3), 3.56-3.63 (m, 2H, H-4, OCH_bCH_2), 3.64-3.67 (m, 1H, H-5), 3.88-3.93 (m, 1H, OCH_aHCH_2), 4.21 (d, J = 7.5 Hz, 1H, H-1). ^{13}C NMR (CD_3OD, 500 MHz): δ_C 15.7, 29.1, 29.9, 30.8, 36.6, 67.1, 70.8, 71.2, 71.8, 74.0, 103.5, 173.6, 176.1. HRMS *m/z* calcd. for $C_{13}H_{23}NNaO_8$ $[M + Na]^+$: 344.1321; found: 344.1313.

b- Synthesis of Sialic Amido-acid (Sia)

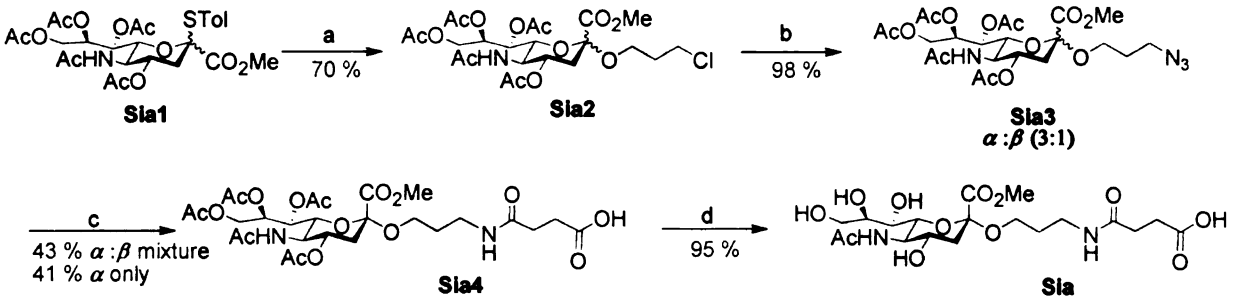

Figure 3-12. a) 3-chloro-1-propanol, NIS, TfOH, 3Å MS, CH_2Cl_2:CH_3CN, -40 °C to r.t. 3 hrs; b) NaN_3, DMF, 80 °C, 12 hrs; c) succinic anhydride, H_2/Pd-C, THF, 3 hrs; d) NaOMe/MeOH, 2hrs.

***O*-Acetyl sialic chloride (Sia2). Sia1**[119] (3.01 g, 6.32 mmol) and 3-chloro-1-propanol (0.840 g, 10.1 mmol) were dissolved in a mixture of anhydrous CH_2Cl_2:CH_3CN (30:30 mL) under N_2 in the presence of 3 Å molecular sieves. After stirring at room temperature for 30 minutes, *N*-iodosuccinimide (NIS) (1.42 g, 6.32 mmol) was added and the mixture was stirred for additional 30 minutes at room temperature. The reaction was cooled down to -40 °C and trifluoromethanesulfonic acid (TfOH) (0.0700 g, 0.880 mmol) was slowly added. A change of color to dark red was observed. After 3 hrs, the reaction mixture was diluted with CH_2Cl_2 washed with 20% $Na_2S_2O_3$ (x2), and then water (x3). The organic phase was then dried and concentrated. Column chromatography

(hexanes–EtOAc, 1:1) yielded **Sia2** (2.514 g, 70% yield). The chemical shift for H-3eq of the α anomer was characterized by the downfield shifted δ_H = 2.51 (dd, *J* = 4.5, 12.5 Hz, 1H, H-3eq.), as opposed to H-3eq. of the *β* anomer with δ_H = 2.40 (dd, *J* = 4.5, 12.5 Hz, 1H, H-3eq.).[120] ^{1}H NMR (500 MHz, $CDCl_3$) for α anomer: δ_H 1.86-1.94 (m, 1H, H-3ax.), 1.90-1.96 (m, 2H, $OCH_2CH_2CH_2Cl$), 1.80, 1.96, 1.97, 2.06, 2.07 (5s, 5 x 3H, $COCH_3$), 2.51 (dd, *J* = 4.5, 12.5 Hz, 1H, H-3eq.), 3.33-3.37 (m, 1H, $OCH_aHCH_2CH_2Cl$), 3.54 (t, *J* = 6.5 Hz, 2H, $OCH_2CH_2CH_2Cl$), 3.73 (s, 3H, CO_2CH_3), 3.76-3.80 (m, 1H, $OCHH_bCH_2CH_2Cl$), 4.00-4.08 (m, 3H, H-5, H-6, H-9a), 4.26 (dd, *J* = 3.0, 12.5 Hz, 1H, H-9b), 4.74-4.80 (m, 1H, H-4), 5.26 (dd, *J* = 2.5, 8.5 Hz, 1H, H-7), 5.30-5.40 (m, 1H, H-8). ^{13}C NMR (125 MHz, $CDCl_3$): δ_C 20.88, 20.95, 20.98, 21.21, 23.23, 32.76, 38.13, 41.55, 49.39, 52.92, 61.49, 62.63, 67.61, 69.09, 69.36, 72.79, 98.93, 168.58, 170.27, 170.29, 170.49, 170.82, 171.06. HRMS *m/z* calcd. for $C_{23}H_{34}ClNNaO_{13}$ $[M+Na]^+$: 591.1923; found: 591.1915.

***O*-Acetyl sialic azide (Sia3).** *O*-Acetyl sialic chloride **Sia2** (0.650 g, 1.14 mmol) and NaN_3 (0.595 g, 9.15 mmol) were dissolved in DMF (15.0 mL), and refluxed for 12 hrs at 80 °C under nitrogen. The mixture was then concentrated *in vacuo*, diluted with CH_2Cl_2, washed with water, dried over Na_2SO_4, filtered, and concentrated to yield the compound as a α:*β* (3:1) mixture (0.650 g, 98%). The chemical shift for H-3eq. of the α anomer was characterized by the downfield shifted δ_H = 2.55 (dd, *J* = 4.5, 12.5 Hz, 1H, H-3eq.), as opposed to H-3eq. of the *β* anomer with δ_H = 2.42 (dd, *J* = 4.5, 12.5 Hz, 1H, H-3eq.). ^{1}H NMR (500 MHz, $CDCl_3$) for α anomer: δ_H 1.77-1.83 (m, 2H, $OCH_2CH_2CH_2N_3$), 1.86-1.94 (m, 1H,

H-3ax.), 1.85, 2.00, 2.02, 2.11, 2.12 (5s, 5 x 3H, $COCH_3$), 2.55 (dd, J = 4.5, 12.5 Hz, 1H, H-3eq.), 3.28-3.33 (m, 1H, $OCH_aHCH_2CH_2N_3$), 3.36 (t, J = 6.5 Hz, 2H, $OCH_2CH_2CH_2N_3$), 3.78 (s, 3H, CO_2CH_3), 3.79-3.84 (m, 1H, $OCHH_bCH_2CH_2N_3$), 4.02-4.14 (m, 3H, H-5, H-6, H-9a), 4.30 (dd, J = 3.0, 12.5 Hz, 1H, H-9b), 4.76-4.84 (m, 1H, H-3), 5.30 (dd, J = 2.5, 8.5 Hz, 1H, H-7), 5.36-5.40 (m, 1H, H-8). ^{13}C NMR (125 MHz, $CDCl_3$): δ_C 20.95, 20.98, 21.02, 21.04, 21.08, 21.2, 21.3, 23.3, 28.9, 29.3, 31.6, 36.7, 37.6, 38.2, 48.3, 48.4, 49.4, 49.5, 52.9, 53.0, 60.8, 61.8, 62.7, 67.6, 68.80, 68.84, 69.1, 69.3, 72.1, 72.4, 72.7, 98.8, 98.9, 162.8, 167.6, 168.6, 170.2, 170.3, 170.5, 170.78, 170.85, 170.90, 171.1. HRMS *m/z* calcd. for $C_{23}H_{34}N_4NaO_{13}$ $[M+Na]^+$: 597.2020; found: 597.2003.

***O*-Acetyl sialic amido-acid (Sia4).** A mixture of **Sia3** (0.240 g, 0.420 mmol), succinic anhydride (0.0750 g, 0.750 mmol) and 10 % Pd/C (0.0500 g) in dry THF (10.0 mL) was stirred at room temperature under H_2. After 3 hrs, the reaction mixture was filtered off through Celite and concentrated. Purification by column chromatography using 5-20 % MeOH in CH_2Cl_2 afforded **Sia4** as α:β (2.5:1) mixture (0.115 g, 43 % yield). Elution at 25 % MeOH in CH_2Cl_2 and increasing gradually to pure MeOH yields exclusively α product as a foamy white solid (0.110 g, 41 % yield). Overall yield 84 %. ^1H NMR (500 MHz, CD_3OD): δ_H 1.72-1.78 (m, 2H, $OCH_2CH_2CH_2NH$), 1.78-1.88 (m, 1H, H-3ax.), 1.85, 1.99, 2.02, 2.11, 2.15 (5s, 5 x 3H, $COCH_3$), 2.49 (t, 4H, J = 4.0 Hz, $OCCH_2CH_2COOH$), 2.63 (dd, J = 4.5, 12.5 Hz, 1H, H-3eq.), 3.22-3.28 (m, 2H, $OCH_2CH_2CH_2NH$), 3.30-3.36 (m, 1H, $OCH_aHCH_2CH_2NH$), 3.76-3.82 (m, 1H, $OCHH_bCH_2CH_2NH$), 3.83 (s, 3H, CO_2CH_3), 3.96 (t, J = 10.5 Hz, 1H, H-5), 4.08 (dd, J = 5.5, 12.5 Hz, 1H, H-9a),

4.18 (dd, *J* = 2.0, 10.5 Hz, 1H, H-6), 4.30 (dd, *J* = 2.5, 12.5 Hz, 1H, H-9b), 4.76-4.84 (m, 1H, H-4), 5.34 (dd, *J* = 2.0, 9.0 Hz, 1H, H-7), 5.38-5.42 (m, 1H, H-8). ^{13}C NMR (125 MHz, CD_3OD): δ_C 19.56, 19.60, 19.8, 20.1, 21.6, 29.3, 31.8, 32.1, 36.6, 38.0, 52.2, 62.4, 62.6, 67.5, 68.4, 69.6, 72.1, 98.9, 168.5, 170.4, 170.60, 170.65, 171.3, 172.3, 174.5. HRMS *m/z* calcd. for $C_{27}H_{40}N_2NaO_{16}$ $[M + Na]^+$: 671.2276; found: 671.2273.

Sialic amido-acid (Sia). Sia4 (32.0 mg, 0.0493 mmol) was de-*O*-acetylated in dry MeOH (2.00 mL) containing 0.200 mL of freshly prepared 1M NaOMe in MeOH. The reaction was complete after 2 hrs at room temperature. The solution was carefully neutralized with Amberlite 120 (H^+) resin till pH=6.5. The reaction mixture was then filtered and evaporated. Flash column chromatography (40 % MeOH in DCM) afforded the final product **Sia** (22.0 mg) in 95 % yield. ^1H NMR (500 MHz, CD_3OD): δ_H 1.70-1.78 (m, 3H, H-3ax., $OCH_2CH_2CH_2NH$), 2.02 (s, 3H, $NHCOCH_3$), 2.45 (bs, 4H, $OCCH_2CH_2COOH$), 2.67 (dd, *J* = 4.5, 13.0 Hz, 1H, H-3eq.), 3.25 (t, *J*=6.5 Hz, 2H, $OCH_2CH_2CH_2NH$), 3.36 (s, 3H, CO_2CH_3), 3.42-3.46 (m, 1H, $OCH_bH_bCH_2CH_2NH$), 3.51 (d, *J* = 8.5 Hz, 1H, H-9a), 3.62 (d, *J* = 10.0 Hz, 1H, H-9b), 3.64-3.72 (m, 2H, $OCH_aH_aCH_2CH_2NH$, H-5), 3.78-3.88 (m, 4H, H-4, H-6, H-7, H-8). ^{13}C NMR (500 MHz, CD_3OD): δ_C 21.7, 29.3, 32.7, 36.2, 40.3, 48.7, 52.3, 52.5, 61.7, 63.5, 67.3, 69.2, 71.3, 73.6, 99.0, 169.9, 173.9, 174.9, 180.2. HRMS *m/z* calcd. for $C_{19}H_{32}N_2NaO_{12}$ $[M + Na]^+$: 503.1853; found: 503.1848.

2. Synthesis of Alkynyl-GlcNAc (7) for *Click* Chemistry

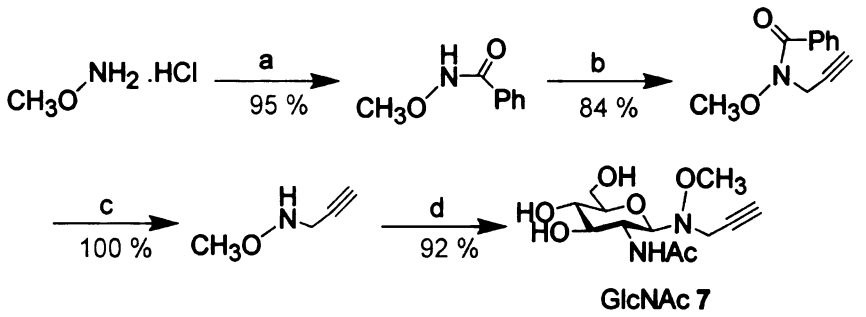

Figure 3-13. a) Benzoyl chloride, pyridine, CH_2Cl_2, 0 °C to r.t.,2 hrs; b) 3-bromopropyne, K_2CO_3, acetone, reflux for 8 hrs; c) 6% MeOH in HCl, reflux for 2 hrs; d) *N*-acetyl glucosamine, 0.1 M acetate buffer (pH=6.5) / DMF (3:1), 50 °C, 24 hrs.

***N*-2-propynyl-*O*-methoxyamine.** *N*-2-propynyl-*O*-methoxyamine was synthesized by slight modification of literature procedures.[121, 122] Briefly, protection of *N*-methoxyamine hydrochloride with benzoyl chloride, *N*-alkylation with 3-bromopropyne, followed by benzoyl deprotection yielded the product as hydrochloride salt. ^{1}H NMR (500 MHz, D_2O): δ_H 2.87 (t, J = 2.5 Hz 1H), 3.80 (s, 3H), 4.06 (d, J = 2.5 Hz, 2H). ^{13}C NMR (500 MHz, D_2O): δ_C 39.2, 62.2, 72.0, 78.4. HRMS *m/z* calcd. for C_4H_8NO $[M + H]^+$: 86.0606; found: 86.0603.

***N*-2-propynyl-*N*-(β-D-glucosamine)-*O*-methylhydroxylamine (7).** A solution of GlcNAc (0.200 g, 0.904 mmol) and *N*-2-propynyl-*O*-methoxyamine (0.300 g, 2.53 mmol) in a mixture of 0.1 M aqueous sodium acetate buffer pH 6.5 / DMF (3:1) was stirred at 50 °C for 24 h. The solvent was evaporated and flash column chromatography (15 % MeOH in DCM) afforded alkynyl-GlcNAc **7** as exclusively β anomer (92 %, 0.240 g). Repeating the same procedure without adding DMF decreased the yield to 30 %. ^{1}H NMR (500 MHz, CD_3OD): δ_H 1.98 (s, 3H, NHCOC*H*$_3$), 2.57 (t, J = 3.0 Hz, 1H, $CH_2C{\equiv}CH$), 3.16-3.20 (m, 1H), 3.33 (s, 1H), 3.39 (t, J = 9.0 Hz, 1H), 3.57 (s, 3H, OC*H*$_3$), 3.66 (dd, J = 6.0, 12.0 Hz, 1H), 3.70

(dd, J = 3.0, 16.0 Hz, 1H), 3.81-3.85 (m, 2H), 3.90 (t, J = 9.5 Hz, 1H), 4.30 (d, J = 10.0 Hz, 1H, H-1). ^{13}C NMR (500 MHz, CD_3OD): δ_C 21.9, 41.4, 52.6, 61.45, 61.67, 70.5, 72.3, 76.6, 78.5, 79.5, 90.5, 172.7. HRMS *m/z* calcd. for $C_{12}H_{20}N_2NaO_6$ $[M + Na]^+$: 311.1219; found: 311.1207.

3. Synthesis of Azido Siloxane Derivative (8)

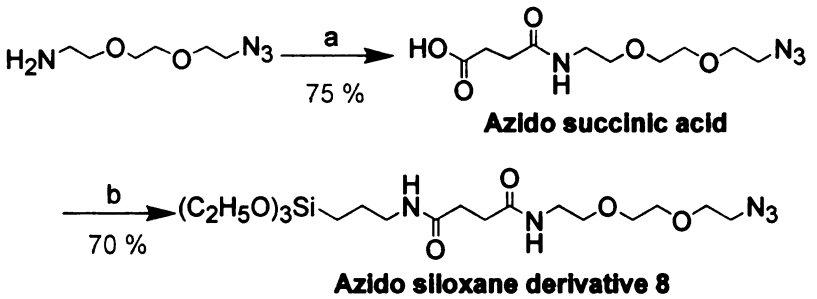

Figure 3-14. a) Succinic anhydride, DMAP, CH_2Cl_2, 12 hrs; b) APTES, EDC, CH_2Cl_2, 8 hrs.

Azido succinic acid. A solution of azido amine derivative[123] (0.200 g, 1.15 mmol), succinic anhydride (0.140 g, 1.40 mmol), 4-dimethylaminopyridine (DMAP) (0.210 g, 1.72 mmol) in dry CH_2Cl_2 (10.0 mL) was stirred under nitrogen at room temperature for 12 hrs. The solvent was evaporated to afford a yellowish solid (0.250 g) in 75 % yield. ^1H NMR ($CDCl_3$, 600 MHz): δ_H 2.49 (t, J = 6.0 Hz, 2H), 2.61 (t, J = 6.0 Hz, 2H), 3.35 (t, J = 4.0 Hz, 2H), 3.41 (q, 2H), 3.52 (t, J = 3.5 Hz, 2H), 3.58-3.62 (m, 4H), 3.64 (t, J = 4.0 Hz, 2H), 6.82 (bs, 1H, N*H*). HRMS *m/z* calcd. for $C_{10}H_{18}N_4NaO_5$ $[M + Na]^+$: 297.1175; found: 297.1177.

Azido siloxane derivative (8). To a solution of azido succinic acid (0.200, 0.689 mmol) and EDC (0.300 g, 1.56 mmol) in dry CH_2Cl_2 (10.0 mL), APTES (0.280 g, 1.27 mmol) was added and the reaction mixture was stirred at room temperature

under nitrogen. After 8 hrs, the solvent was removed under reduced pressure. The residue was purified by column chromatography (2 to 5 % MeOH in DCM) to afford 0.230 g of azido siloxane derivative **8** as a white solid in 70 % yield. ^{1}H NMR ($CDCl_3$, 500 MHz): δ_H 0.59 (t, *J* = 8.0 Hz, 2H, CH_2Si), 1.19 (t, *J* = 7.0 Hz, 9H, $(OCH_2CH_3)_3$), 1.53-1.61 (m, 2H), 2.47 (t, *J* = 3.5 Hz, 4H, $COCH_2CH_2CO$), 3.18 (q, *J* = 6.4 Hz, 2H), 3.40 (dt, *J* = 5.0, 17.2 Hz, 4H), 3.51 (t, *J* = 2.8 Hz, 2H), 3.58-3.63 (m, 4H), 3.66 (t, *J* = 5.2 Hz, 2H), 3.78 (q, *J* = 7.2 Hz, 6H, $(OCH_2CH_3)_3$), 6.38 (bs, 2H, N*H*). HRMS *m/z* calcd. for $C_{19}H_{39}N_5NaO_7Si[M + Na]^+$: 500.2571; found: 500.2575.

4. Synthesis of MGNPs (2-6)

Amine-NP. MGNPs were prepared by slight modification of the co-precipitation method described earlier. Briefly, 0.22 micron filtered 1M aqueous solution of ferric chloride hexahydrate $FeCl_3.6H_2O$ (20.0 mmol, 5.41 g, 5.00 mL) and polyvinylpyrrolidone PVP (Mw ~ 55 KDa) (0.0256 g/mL, 0.650 mL) were mixed with vigorous stirring under nitrogen in a degassed flask for 15 min. To the above mixture was added a freshly prepared 0.22 micron filtered solution (10.0 mmol, 2.00 g, 2.50 mL) of ferrous chloride tetrahydrate ($FeCl_2.4H_2O$). Ammonium hydroxide NH_4OH (30%) (~20.0 mL) was then added until pH of ~11-12 was reached. Black precipitates started to form indicating nanoparticle formation. After vigorous stirring for 1 hr at 80 °C, the resulting black NPs were isolated by applying a permanent external magnet (Lifesep® 50 SX magnetic separator), washed 6 times with DDW and 3 times with ethanol. To further protect the magnetite core, we coated the nanoparticles with a silica shell using

tetraethoxysilane (TEOS). In a typical experimental procedure, the nanoparticles were re-suspended in 2-propanol: water (4:1 v/v, 150 mL). NH_4OH solution (0.2 % v/v, 0.300 mL) was added followed by dropwise addition of TEOS (4.50 mmol, 1.00 mL) over 1 hr with continuous stirring. The reaction mixture was stirred overnight, isolated and washed repeatedly with diethyl ether and ethanol to yield silica coated magnetic nanoparticle **1** (TEOS-NP **1**). To prepare the amine functionalized NP, TEOS-NP **1** was suspended in ethanol (150 mL) and DDW (1.50 mL) and sonicated for 30 minutes. 3-aminopropyl triethoxysilane (APTES) (2 % w/v, 12.8 mmol, 3.00 mL) was then added and stirred at 60 °C overnight. The resulting Amine-NP was isolated, washed and re-dispersed in ethanol.

MGNPs (2-5). To immobilize the surface with carbohydrates (e.g. fucose) using the amide bond linkage, amine functionalized NP (80.0 mg) was washed twice with DMF, re-dispersed in DMF (50.0 mL) and sonicated for 30 minutes. The coupling solution was prepared by mixing fucose amido-acid **Fuc** (110 mg, 0.342 mmol), benzotriazole-1-yl-oxy-tris-(dimethylamino)-phosphonium hexafluorophosphate (BOP) (230 mg, 0.520 mmol, 1.50 eq.), 1-hydroxybenzotriazole (HOBT) (50.0 mg, 0.370 mmol, 1.10 eq.), and diisopropylethylamine (DIPEA) (0.230 mL, 1.39 mmol, 4 eq.) in DMF (10.0 mL). The coupling solution was then added dropwise to amine NP **2** in DMF under sonication. The reaction mixture was stirred overnight at room temperature. The resulting nanoparticles were isolated by magnet, washed 3x with ethanol and 3x with water to afford **Fuc-MGNP 4** (~ 80.0 mg dry weight). The same protocol was followed to synthesize the analogous Man, Gal and Sia-MGNPs. For Sia-

MGNPs, the last step involved deprotection of methyl ester using 0.2 M aqueous NaOH (100 μl) to afford **Sia-MGNP 5** (~ 15.0 mg dry weight).

Azide NP. The synthesis of Azide NP was carried out in a similar manner to the previously prepared Amine NP employing the azido siloxane linker instead. Briefly, azido siloxane derivative **8** (70.0 mg, 0.150 mmol) was added to NP **1** (100 mg) suspended in THF: Ethanol (100: 25 mL) and stirred at 60 °C for 48 hrs. The resulting **Azide NP** (130 mg) were isolated by magnet and washed several times with ethanol, water and diethyl ether.

MGNP 6. Alkynyl-GlcNAc **7** (150 mg, 0.520 mmol), $CuSO_4.5H_2O$ (6.5 mg, 0.026 mmol) and sodium ascorbate (50.0 mg, 0.260 mmol) were added to Azide-NP **9** (100 mg) in t-BuOH : H_2O (1:1, 40 mL). The reaction mixture was stirred at room temperature for 24 hrs, isolated and washed with water and ethanol successively to afford **GlcNAc-MGNP 6** (160 mg).

3.16. h. Characterization of MGNPs

1. TEM

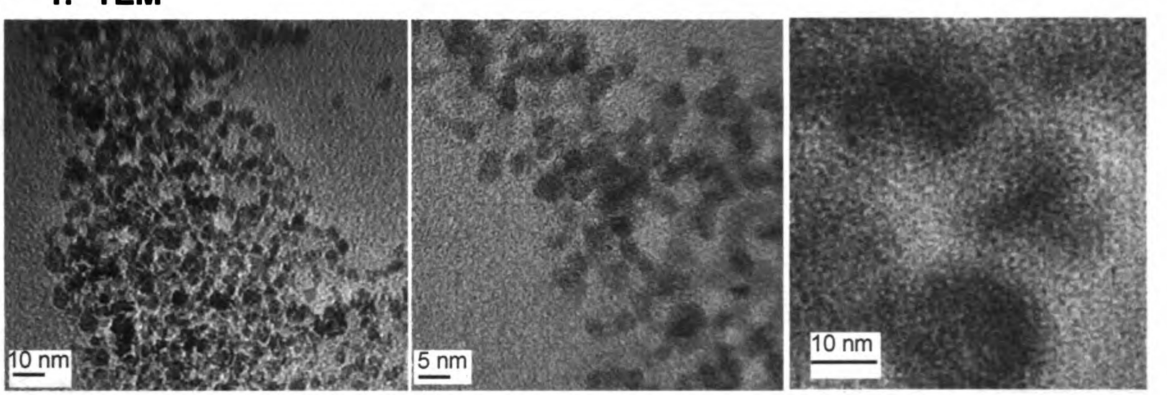

Figure 3-15. TEM images of MGNP shows that NP core is ~ 5 – 10 nm.

2. FT-IR

FT-IR spectra for MGNP **2-5** were identical to those reported previously. FT-IR spectra for azido-NP and GlcNAc-MGNP **6** are shown below in **Figure 3-16**. The fact that azido-NP was indeed coated with azide was proven by the appearance of a strong absorbance at 2095 cm^{-1} due to N=N=N stretching. The success of *click* reaction was confirmed by the disappearance of the azide peak in GlcNAc-MGNP **6** spectra.

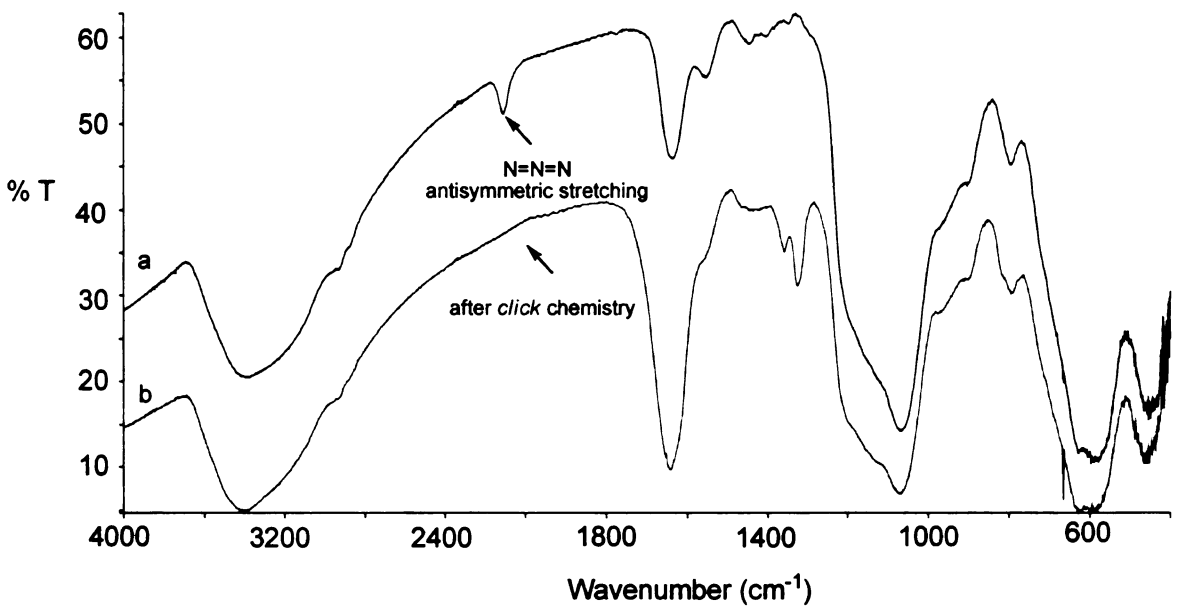

Figure 3-16. FT-IR spectra of a-) Azido-NP b-) GlcNAc-MGNP **6**.

3. TGA

As shown in **Figure 3-17,** all MGNPs **(2-5)** exhibited a weight loss between 11 and 14% compared to NP **1** with a weight loss of only 5.5%, implying the presence of organic molecules on the surface of MGNPs. TGA analysis showed that ~ 8% of the dry weight of the particles was due to the carbohydrate moieties, which led to an estimate of 500 copies of carbohydrates on each particle. On the

other hand, Azido-NP showed a weight loss of 13% compared to the GlcNAc-MGNP **6** with a weight loss of 19%, indicating that the MGNP surface was indeed functionalized with GlcNAc.

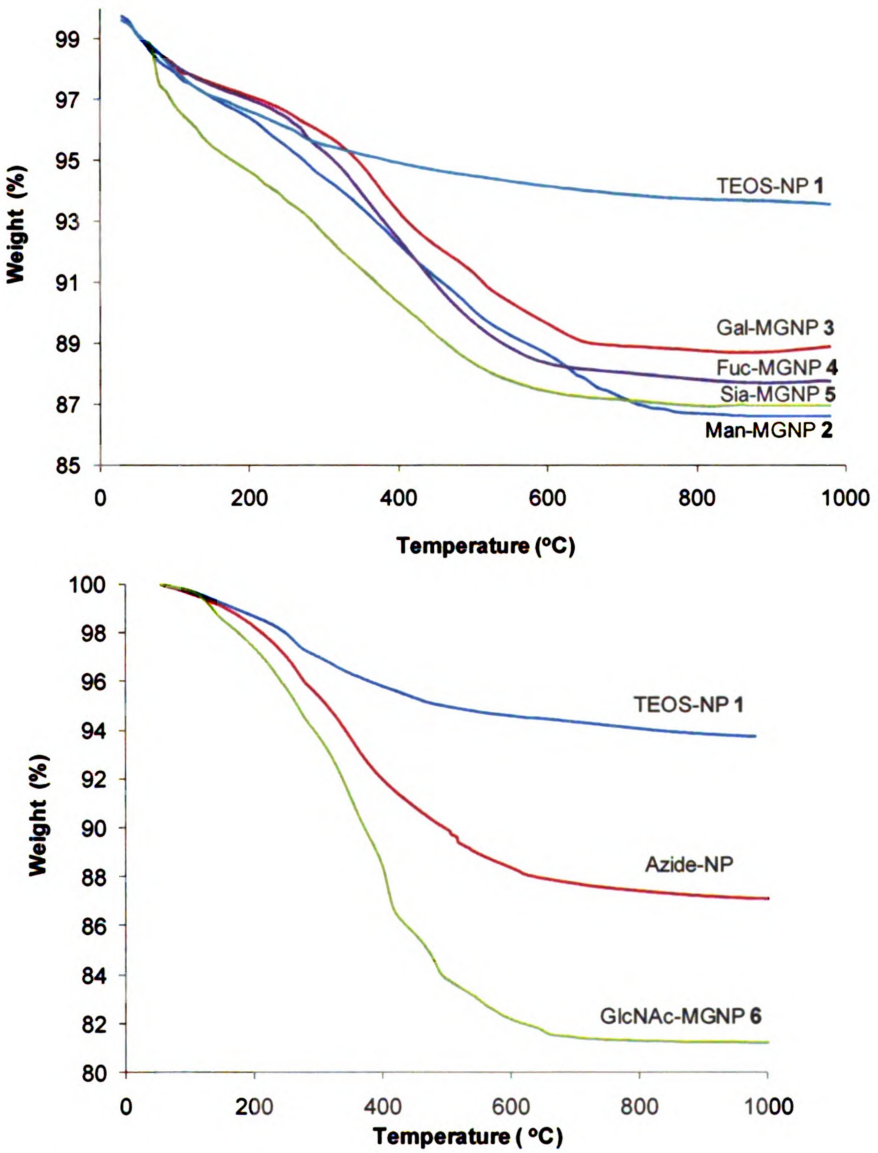

Figure 3-17. a) TGA curves for TEOS-NP **1** (light blue), Man-MGNP **2** (dark blue), Gal-MGNP **3** (red), Fuc-MGNP **4** (violet), and Sia-MGNP **5** (green). b) TGA curves for TEOS-NP **1** (blue), Azide-NP **9** (red), and GlcNAc-MGNP **10** (green). All samples were heated at a constant heating rate of 10 °C/min from 50 to 1000 °C under nitrogen.

3.17. References

1. **American Cancer Society.** *Cancer Facts and Figures* **2009** (see American Cancer Society website for further information).

2. Nakamura, R. M.; Grody, W. W.; Wu, J. T.; Nagle, R. B., *Cancer Diagnostics: Current and Future Trends.* Humana Press: 2004; p 520.

3. Glasspool, R. M.; Evans, T. R., **Clinical imaging of cancer metastasis.** *Eur. J. Cancer* **2000,** *36*, 1661-70.

4. Mitchell, D. G.; Cohen, M., *MRI Principles.* Elsevier Science Health Science Div 2003; p 416.

5. Choudhury, R. P.; Fuster, V.; Badimon, J. J.; Fisher, E. A.; Fayad, Z. A., **MRI and characterization of atherosclerotic plaque emerging applications and molecular imaging.** *Arterioscler. Thromb. Vasc. Biol.* **2002,** *22*, 1065-1074 and references therein.

6. Balmain, A.; Gray, J.; Ponder, B., **The genetics and genomics of cancer.** *Nat. Genet.* **2003,** *33*, 238-244.

7. van 't Veer, L. J.; Bernards, R., **Enabling personalized cancer medicine through analysis of gene-expression patterns.** *Nature* **2008,** *452*, 564-570.

8. Chin, L.; Gray, J. W., **Translating insights from the cancer genome into clinical practice.** *Nature* **2008,** *452*, 553-563.

9. Sawyers, C. L., **The cancer biomarker problem.** *Nature* **2008,** *452*, 548-552.

10. Montet, X.; Montet-Abou, K.; Reynolds, F.; Weissleder, R.; Josephson, L., **Nanoparticle imaging of integrins on tumor cells.** *Neoplasia* **2006,** *8*, 214-222.

11. Gao, X.; Cui, Y.; Levenson, R. M.; Chung, L. W. K.; Nie, S., **In vivo cancer targeting and imaging with semiconductor quantum dots.** *Nat. Biotechnol.* **2004,** *22*, 969-976.

12. Lee, J.-H.; Huh, Y.-M.; Jun, Y.-w.; Seo, J.-w.; Jang, J.-t.; Song, H.-T.; Kim, S.; Cho, E.-J.; Yoon, H.-G.; Suh, J.-S.; Cheon, J., **Artificially engineered magnetic particles for ultra-sensitive molecular imaging.** *Nat. Med.* **2006,** *13*, 95-99.

13. Weissleder, R.; Kelly, K.; Sun, E. Y.; Shtatland, T.; Josephson, L., **Cell-specific targeting of nanoparticles by multivalent attachment of small molecules.** *Nat. Biotechnol.* **2005,** *23*, 1418-1423.

14. Qian, X.; Peng, X.-H.; Ansari, D. O.; Yin-Goen, Q.; Chen, G. Z.; Shin, D. M.; Yang, L.; Young, A. N.; Wang, M. D.; Nie, S., ***In vivo* tumor targeting and spectroscopic detection with surface-enhanced Raman nanoparticle tags.** *Nat. Biotechnol.* **2008,** *26*, 83-90.

15. Yang, L.; Peng, X.-H.; Wang, Y. A.; Wang, X.; Cao, Z.; Ni, C.; Karna, P.; Zhang, X.; Wood, W. C.; Gao, X.; Nie, S.; Mao, H., **Receptor-targeted nanoparticles for in vivo imaging of breast cancer.** *Clin. Cancer Res.* **2009,** *15*, 4722-4732.

16. Park, J.-H.; von Maltzahn, G.; Xu, M. J.; Fogal, V.; Kotamraju, V. R.; Ruoslahti, E.; Bhatia, S. N.; Sailor, M. J., **Cooperative nanomaterial system to sensitize, target, and treat tumors.** *Proc. Natl. Acad. Sci.* **2009**, 1-6.

17. Park, J.-H.; von Maltzahn, G.; Zhang, L.; Schwartz, M. P.; Ruoslahti, E.; Bhatia, S. N.; Sailor, M. J., **Magnetic iron oxide nanoworms for tumor targeting and imaging.** *Adv. Mater.* **2008,** *20*, 1630-1635.

18. McCarthy, J. R.; Kelly, K. A.; Sun, E. Y.; Weissleder, R., **Targeted delivery of multifunctional magnetic nanoparticles.** *Nanomedicine* **2007,** *2*, 153-167.

19. Liu, X.; Dai, Q.; Austin, L.; Coutts, J.; Knowles, G.; Zou, J.; Chen, H.; Huo, Q., **A one-step homogeneous immunoassay for cancer biomarker detection using gold nanoparticle probes coupled with dynamic light scattering.** *J. Am. Chem. Soc.* **2008,** *130*, 2780-2782.

20. Jun, Y.-w.; Huh, Y.-M.; Choi, J.-s.; Lee, J.-H.; Song, H.-T.; Kim, S.; Yoon, S.; Kim, K.-S.; Shin, J.-S.; Suh, J.-S.; Cheon, J., **Nanoscale size effect of magnetic nanocrystals and their utilization for cancer diagnosis via magnetic resonance imaging.** *J. Am. Chem. Soc.* **2005,** *127*, 5732-5733.

21. Bajaj, A.; Miranda, O. R.; Kim, I.-B.; Phillips, R. L.; Jerry, D. J.; Bunz, U. H. F.; Rotello, V. M., **Detection and differentiation of normal, cancerous, and metastatic cells using nanoparticle-polymer sensor arrays.** *Proc. Nat. Acad. Sci.* **2009,** *106*, 10912-10916.

22. Stoeva, S. I.; Lee, J.-S.; Smith, J. E.; Rosen, S. T.; Mirkin, C. A., **Multiplexed detection of protein cancer markers with biobarcoded nanoparticle probes.** *J. Am. Chem. Soc.* **2006,** *128*, 8378-8379.

23. Jain, P. K.; Huang, X.; El-Sayed, I. H.; El-Sayed, M. A., **Noble metals on the nanoscale: optical and photothermal properties and some applications in imaging, sensing, biology, and medicine.** *Acc. Chem. Res.* **2008,** *41*, 1578-1586.

24. Brigger, I.; Dubernet, C.; Couvreur, P., **Nanoparticles in cancer therapy and diagnosis.** *Adv. Drug Delivery Rev.* **2002,** *54*, 631-651.

25. Cipolla, L.; Peri, F.; Airoldi, C., **Glycoconjugates in cancer therapy.** *Anti-Cancer Agents Med. Chem.* **2008,** *8*, 92-121.

26. Huang, X.; Neretina, S.; El-Sayed, M. A., **Gold nanorods: from synthesis and properties to biological and biomedical applications.** *Adv. Mater.* **2009,** *21*, 4880-4910 and references therein.

27. Mailaender, V.; Landfester, K., **Interaction of nanoparticles with cells.** *Biomacromolecules* **2009,** *10*, 2379-2400.

28. Lee, H.; Yoon, T.-J.; Figueiredo, J.-L.; Swirski, F. K.; Weissleder, R., **Rapid detection and profiling of cancer cells in fine-needle aspirates.** *Proc. Nat. Acad. Sci., USA* **2009,** *106*, 12459-12464.

29. Wingren, C.; Borrebaeck, C. A. K., **Antibody microarray analysis of directly labelled complex proteomes.** *Curr. Opin. Biotech.* **2008,** *19*, 55-61.

30. Nagrath, S.; Sequist, L. V.; Maheswaran, S.; Bell, D. W.; Irimia, D.; Ulkus, L.; Smith, M. R.; Kwak, E. L.; Digumarthy, S.; Muzikansky, A.; Ryan, P.; Balis, U. J.; Tompkins, R. G.; Haber, D. A.; Toner, M., **Isolation of rare circulating tumour cells in cancer patients by microchip technology.** *Nature* **2007,** *450*, 1235-1239.

31. Pantel, K.; Brakenhoff, R. H.; Brandt, B., **Detection, clinical relevance and specific biological properties of disseminating tumour cells.** *Nature Rev. Cancer* **2008,** *8*, 329-340.

32. Uhr, J. W., **Cancer diagnostics: one-stop shop.** *Nature* **2007,** *450*, 1168-1169.

33. Ludwig, J. A.; Weinstein, J. N., **Biomarkers in cancer staging, prognosis and treatment selection.** *Nature Rev. Cancer* **2005,** *5*, 845-856.

34. Ferrari, M., **Cancer nanotechnology: opportunities and challenges.** *Nature Rev. Cancer* **2005,** *5*, 161-171.

35. Hynes, N. E.; MacDonald, G., **ErbB receptors and signaling pathways in cancer.** *Curr. Opin. Cell Biol.* **2009,** *21*, 177-184.

36. Klein, C. A.; Blankenstein, T. J. F.; Schmidt-Kittler, O.; Petronio, M.; Polzer, B.; Stoecklein, N. H.; Riethmüller, G., **Genetic heterogeneity of single disseminated tumour cells in minimal residual cancer.** *Lancet* **2002,** *360*, 683-689.

37. Freire, T.; Bay, S.; Vichier-Guerre, S.; Lo-Man, R.; Leclerc, C., **Carbohydrate antigens: synthesis aspects and immunological applications in cancer.** *Mini-Rev. Med. Chem.* **2006,** *6*, 1357-1373.

38. Hakomori, S., **Glycosylation defining cancer malignancy: New wine in an old bottle.** *Proc. Nat. Acad. Sci., USA* **2002,** *99*, 10231-10233.

39. Gorelik, E.; Galili, U.; Raz, A., **On the role of cell surface carbohydrates and their binding proteins (lectins) in tumor metastasis.** *Cancer Metas. Rev.* **2001,** *20*, 245-277.

40. Danishefsky, S. J.; Allen, J. R., **From the laboratory to the clinic: A retrospective on fully synthetic carbohydrate-based anticancer vaccines.** *Angew. Chem. Int. Ed.* **2000,** *39*, 836-863 and referencec cited therein.

41. Durand, G.; Seta, N., **Protein glycosylation and diseases: Blood and urinary oligosaccharides as markers for diagnosis and therapeutic monitoring.** *Clin. Chem.* **2000,** *46*, 795-805.

42. Hakomori, S.; Zhang, Y., **Glycosphingolipid antigens and cancer therapy.** *Chem. Biol.* **1997,** *4*, 97-104.

43. Gabius, H.-J., **Glycans: Bioactive signals decoded by lectins.** *Biochem. Soc. Trans.* **2008,** *36*, 1491-1496.

44. Gabius, H.-J.; Siebert, H.-C.; André, S.; Jiménez-Barbero, J.; Rüdiger, H., **Chemical biology of the sugar code.** *ChemBioChem* **2004,** *5*, 740-764.

45. Varki, A., **Biological roles of oligosaccharides: All of the theories are correct.** *Glycobiology* **1993,** *3*, 97-130.

46. Dai, Z.; Zhou, J.; Qiu, S.-J.; Liu, Y.-K.; Fan, J., **Lectin-based glycoproteomics to explore and analyze hepatocellular carcinomarelated glycoprotein markers.** *Electrophoresis* **2009,** *30*, 2957-2966 and references cited therein.

47. Kawaguchi, T., **Cancer metastasis: characterization and identification of the behavior of metastatic tumor cells and the cell adhesion molecules, including carbohydrates.** *Current Drug Targets: Cardiovasc. Haemato. Disorders* **2005,** *5*, 39-64.

48. Buskas, T.; Thompson, P.; Boons, G.-J., **Immunotherapy for cancer: synthetic carbohydrate-based vaccines.** *Chem. Commun.* **2009**, 5335-5349.

49. Kuberan, B.; Linhardt, R. J., **Carbohydrate based vaccines.** *Curr. Org. Chem.* **2000,** *4*, 635-677.

50. Barthel, S. R.; Gavino, J. D.; Descheny, L.; Dimitroff, C. J., **Targeting selectins and selectin ligands in inflammation and cancer.** *Exp. Opin. Ther. Targets* **2007,** *11*, 1473-1491.

51. Kannagi, R.; Izawa, M.; Koike, T.; Miyazaki, K.; Kimura, N., **Carbohydrate-mediated cell adhesion in cancer metastasis and angiogenesis.** *Cancer Sci.* **2004,** *65*, 377-384.

52. Lahm, H.; Andre, S.; Hoeflich, A.; Kaltner, H.; Siebert, H.-C.; Sordat, B.; von der Lieth, C.-W.; Wolf, E.; Gabius, H.-J., **Tumor galectinology: Insights into the complex network of a family of endogenous lectins.** *Glycoconjugate J.* **2004,** *20*, 227-238.

53. Gabius, H.-J., **Glycohistochemistry: The why and how of detection and localization of endogenous lectins.** *Anat. Histol. Embryol.* **2001,** *30*, 3-31.

54. Kayser, K.; Bovin, N. V.; Zemlyanukhina, T. V.; Donaldo-Jacinto, S.; Koopmann, J.; Gabius, H.-J., **Cell type-dependent alterations of binding of synthetic blood group antigen-related oligosaccharides in lung cancer.** *Glycoconjugate J.* **1994,** *11*, 339-344.

55. Kayser, K.; Heil, M.; Gabius, H.-J., **Is the profile of binding of a panel of neoglycoproteins useful as a diagnostic marker in human lung cancer?** *Path. Res. Pract.* **1989,** *184*, 621-629.

56. Kim, E. Y. L.; Gronewold, C.; Chatterjee, A.; Von der Lieth, C.-W.; Kliem, C.; Schmauser, B.; Wiessler, M.; Frei, E., **Oligosaccharide mimics containing galactose and fucose specifically label tumour cell surfaces and inhibit cell adhesion to fibronectin.** *ChemBioChem* **2005,** *6*, 422-431.

57. Lerchen, H.-G.; Baumgarten, J.; Piel, N.; Kolb-Bachofen, V., **Lectin-mediated drug targeting: discrimination of carbohydrate-mediated cellular uptake between tumor and liver cells with neoglycoconjugates carrying fucose epitopes regioselectivity modified in the 3-position.** *Angew. Chem., Int. Ed.* **1999,** *38*, 3680-3683.

58. Rye, P. D.; Bovin, N. V., **Selection of carbohydrate-binding cell phenotypes using oligosaccharide-coated magnetic particles.** *Glycobiology* **1997,** *7*, 179-182.

59. Gao, X.; Cui, Y.; Levenson, R. M.; Chung, L. W. K.; Nie, S., ***In vivo* cancer targeting and imaging with semiconductor quantum dots.** *Nature Biotech.* **2004,** *22*, 969-979.

60. Mammen, M.; Choi, S.-K.; Whitesides, G. M., **Polyvalent interactions in biological systems: Implications for design and use of multivalent ligands and inhibitors.** *Angew. Chem. Int. Ed.* **1998,** *37*, 2754-2794.

61. Lee, Y. C.; Lee, R. T., **Carbohydrate-protein interactions: basis of glycobiology.** *Acc. Chem. Res.* **1995,** *28*, 321-327.

62. Chang, E.; Thekkek, N.; Yu, W. W.; Colvin, V. L.; Drezek, R., **Evaluation of quantum dot cytotoxicity based on intracellular uptake.** *Small* **2006,** *2*, 1412-1417.

63. Derfus, A. M.; Chan, W. C. W.; Bhatia, S. N., **Probing the cytotoxicity of semiconductor quantum dots.** *Nano Lett.* **2004,** *4*, 11-18.

64. Bourrinet, P.; Bengele, H. H.; Bonnemain, B.; Dencausse, A.; Idee, J. M.; Jacobs, P. M.; Lewis, J. M., **Preclinical safety and pharmacokinetic profile of ferumoxtran-10, an ultrasmall superparamagnetic iron oxide magnetic resonance contrast agent.** *Invest. Radiol.* **2006,** *41*, 313-324.

65. Gupta, A. K.; Gupta, M., **Synthesis and surface engineering of iron oxide nanoparticles for biomedical applications.** *Biomaterials* **2005,** *26*, 3995-4021.

66. Anzai, Y.; Piccoli, C. W.; Outwater, E. K.; Stanford, W.; Bluemke, D. A.; Nurenberg, P.; Saini, S.; Maravilla, K. R.; Feldman, D. E.; Schmiedl, U. P.; Brunberg, J. A.; Francis, I. R.; Harms, S. E.; Som, P. M.; Tempany, C. M., **Evaluation of neck and body metastases to nodes with ferumoxtran 10-enhanced MR imaging: phase III safety and efficacy study.** *Radiology* **2003,** *228*, 777-788.

67. Wang, Y.-X. J.; Hussain, S. M.; Krestin, G. P., **Superparamagnetic iron oxide contrast agents: physicochemical characteristics and applications in MR imaging.** *Eur. Radiol.* **2001,** *11*, 2319-2331.

68. Weissleder, R.; Elizondo, G.; Wittenberg, J.; Rabito, C. A.; Bengele, H. H.; Josephson, L., **Ultrasmall superparamagnetic iron oxide: Characterization of a new class of contrast agents for MR imaging.** *Radiology* **1990,** *175*, 489-493.

69. Collins, B. E.; Wright, A. T.; Anslyn, E. V., **Combining molecular recognition, optical detection, and chemometric analysis.** *Top. Curr. Chem.* **2007,** *277*, 181-218.

70. Wright, A. T.; Anslyn, E. V., **Differential receptor arrays and assays for solution-based molecular recognition.** *Chem. Soc. Rev.* **2006,** *35*, 14-28.

71. Jurs, P. C.; Bakken, G. A.; McClelland, H. E., **Computational methods for the analysis of chemical sensor array data from volatile analytes.** *Chem. Rev.* **2000,** *100*, 2649-2678.

72. Barrientos, A., G.; de la Fuente, J. M.; Jiménez, M.; Solís, D.; Cañada, F. J.; Martín-Lomas, M.; Penadés, S., **Modulating glycosidase degradation and lectin recognition of gold glyconanoparticles.** *Carbohydr. Res.* **2009,** *344*, 1474-1478.

73. Liang, C.-H.; Wang, C.-C.; Lin, Y.-C.; Chung-Hsuan Chen, C.-H.; Wong, C.-H.; Wu, C.-Y., **Iron oxide/gold core/shell nanoparticles for ultrasensitive detection of carbohydrate-protein interactions.** *Anal. Chem.* **2009**, ASAP.

74. Marradi, M.; Alcántara, D.; de la Fuente, J. M.; García-Martín, M. L.; Cerdán, S.; Penadés, S., **Paramagnetic Gd-based gold glyconanoparticles as probes for MRI: tuning relaxivities with sugars.** *Chem. Commun.* **2009**, 3922-3924.

75. van Kasteren, S. I.; Campbell, S. J.; Serres, S.; Anthony, D. C.; Sibson, N. R.; Davis, B. G., **Glyconanoparticles allow pre-symptomatic in vivo imaging of brain disease.** *Proc. Natl. Acad. Sci., USA* **2009,** *106*, 18-23.

76. Kikkeri, R.; Lepenies, B.; Adibekian, A.; Laurino, P.; Seeberger, P. H., **In vitro imaging and in vivo liver targeting with carbohydrate capped quantum dots.** *J. Am. Chem. Soc.* **2009,** *131*, 2110-2112.

77. Thygesen, M. B.; Sauer, J.; Jensen, K. J., **Chemoselective capture of glycans for analysis on gold nanoparticles: carbohydrate oxime tautomers provide functional recognition by proteins.** *Chem. Eur. J.* **2009,** *15*, 1649-1660.

78. Mukhopadhyay, B.; Martins, M. B.; Karamanska, R.; Russell, D. A.; Field, R. A., **Bacterial detection using carbohydrate-functionalized CdS quantum dots: a model study exploiting E. coli recognition of mannosides.** *Tetrahedron Lett.* **2009,** *50*, 886-889.

79. Sundgren, A.; Barchi, J. J., **Varied presentation of the Thomsen–Friedenreich disaccharide tumor-associated carbohydrate antigen on gold nanoparticles.** *Carbohydr. Res.* **2008,** *343*, 1594-1604.

80. El-Boubbou, K.; Gruden, C.; Huang, X., **Magnetic glyco-nanoparticles: a unique tool for rapid pathogen detection, decontamination, and strain differentiation.** *J. Am. Chem. Soc.* **2007,** *129*, 13392-13393.

81. de Souza, A. C.; Halkes, K. M.; Meeldijk, J. D.; Verkleij, A. J.; Vliegenthart, J. F. G.; Kamerling, J. P., **Gold glyconanoparticles as probes to explore the carbohydrate-mediated self-recognition of marine sponge cells.** *ChemBioChem* **2005,** *6*, 828-831.

82. Hone, D. C.; Haines, A. H.; Russell, D. A., **Rapid, quantitative colorimetric detection of a lectin using mannose-stabilized gold nanoparticles.** *Langmuir* **2003,** *19*, 7141-7144.

83. Lin, C.-C.; Yeh, Y.-C.; Yang, C.-Y.; Chen, G.-F.; Chen, Y.-C.; Wu, Y.-C.; Chen, C.-C., **Quantitative analysis of multivalent interactions of carbohydrate-encapsulated gold nanoparticles with concanavalin A.** *Chem. Commun.* **2003**, 2920-2921.

84. Liu, Y.; Feizi, T.; Campanero-Rhodes, M. A.; Childs, R. A.; Zhang, Y.; Mulloy, B.; Evans, P. G.; Osborn, H. M. I.; Otto, D.; Crocker, P. R.; Chai, W., **Neoglycolipid probes prepared via oxime ligation for microarray analysis of oligosaccharide-protein interactions.** *Chem. Biol.* **2007**, 847-859.

85. Bohorov, O.; Andersson-Sand, H.; Hoffmann, J.; Blixt, O., **Arraying glycomics: A novel bi-functional spacer for one-step microscale derivatization of free reducing glycans.** *Glycobiology* **2006,** *16*, 21C-27C.

86. Peri, F.; Jiménez-Barbero, J.; García-Aparicio, V.; Tvaroška, I.; Nicotra, F., **Synthesis and conformational analysis of novel N(OCH3)-linked disaccharide analogues.** *Chem. Eur. J.* **2004,** *10*, 1433-1444.

87. Polito, L.; Monti, D.; Caneva, E.; Delnevo, E.; Russo, G.; Prosperi, D., **One-step bioengineering of magnetic nanoparticles via a surface diazo transfer/azide-alkyne click reaction sequence.** *Chem. Commun.* **2008**, 621-623.

88. Lin, P.-C.; Ueng, S.-H.; Yu, S.-C.; Jan, M.-D.; Adak, A. K.; Yu, C.-C.; Lin, C.-C., **Surface modification of magnetic nanoparticle via Cu(I)-catalyzed alkyne-azide [2 + 3] cycloaddition.** *Org. Lett.* **2007,** *9*, 2131-2134.

89. Wang, Q.; Chan, T. R.; Hilgraf, R.; Fokin, V. V.; Sharpless, K. B.; Finn, M. G., **Bioconjugation by copper(I)-catalyzed azide-alkyne [3 + 2] cycloaddition.** *J. Am. Chem. Soc.* **2003,** *125*, 3192-3193.

90. El-Boubbou, K.; Zhu David, C.; Vasileiou, C.; Borhan, B.; Prosperi, D.; Li, W.; Huang, X., **Magnetic glyco-nanoparticles: a tool to detect, differentiate, and unlock the glyco-codes of cancer via magnetic resonance imaging.** *J. Am. Chem. Soc.* **2010,** *132*, 4490-9.

91. Shimura, K.; Kasai, K., **Determination of the affinity constants of Concanavalin A for monosaccharides by fluorescence affinity probe capillary electrophoresis.** *Anal. Biochem.* **1995,** *227*, 186-194.

92. Nagata, Y.; Burger, M. M., **Wheat germ agglutinin.** *J. Biol. Chem.* **1974,** *249*, 3116-3122.

93. Vornholt, W.; Hartmann, M.; Keusgen, M., **SPR studies of carbohydrate-lectin interactions as useful tool for screening on lectin sources.** *Biosen. Bioelectron.* **2007,** *22*, 2983-2988.

94. Hayes, C. E.; Goldstein, I. J., **An a-D-galactosyl-binding lectin from Bandeiraea Simplicifolia seeds: Isolation by affinity chromatography and characterization.** *J. Biol. Chem.* **1974,** *249*, 1904-1914.

95. Liener, I. E.; Sharon, N.; Goldstein, I. J., *The lectins: Properties, functions, and applications in biology and medicine*. Academic Press: Orlando 1986.

96. Wright, C. S., **Structural comparison of the two distinct sugar binding sites in wheat germ agglutinin isolectin II.** *J. Mol. Biol.* **1984,** *178*, 91-104.

97. Lee, H.; Sun, E.; Ham, D.; Weissleder, R., **Chip–NMR biosensor for detection and molecular analysis of cells.** *Nature Med.* **2008,** *14*, 869-874.

98. Thorek, D. L. J.; Chen, A. K.; Czupryna, U.; Tsourkas, A., **Superparamagnetic iron oxide nanoparticle probes for molecular imaging.** *Ann. Biomed. Eng.* **2005,** *34*, 23-38.

99. Weissleder, R.; Papisov, M., **Pharmaceutical iron oxides for MR imaging.** *Rev. Mag. Res. Med* **1992,** *4*, 1-20.

100. Rocha, A.; Gossuinb, Y.; Mullera, R. N.; Gillis, P., **Superparamagnetic colloid suspensions: water magnetic relaxation and clustering.** *J. Magn. Magn. Mater.* **2005,** *293*, 532-539.

101. Yung, K.-T., **Empirical models of transverse relaxation for spherical magnetic perturbers.** *Magn. Reson. Imaging* **2003,** *21*, 451-463.

102. Derewenda, Z.; Yariv, J.; Helliwell, J. R.; Kalb, A. J.; Dodson, E. J.; Papiz, M. Z.; Wan, T.; Campbell, J., **The structure of the saccharide-binding site of concanavalin A.** *EMBO J.* **1989,** *8*, 2189-2193.

103. Satelli, A.; Rao, P. S.; Gupta, P. K.; Lockman, P. R.; Srivenugopal, K. S.; Rao, U. S., **Varied expression and localization of multiple galectins in different cancer cell lines.** *Oncology Rep.* **2008,** *19*, 587-594.

104. Chandrasekaran, S.; Tanzer, M. L.; Giniger, M. S., **Characterization of oligomannoside binding to the surface of murine melanoma cells. Potential relationship to oligomannoside-initiated cell spreading.** *J. Biol. Chem.* **1994,** *269*, 3367-73.

105. Zhang, T.; Edwards, N. Y.; Bonizzoni, M.; Anslyn, E. V., **The use of differential receptors to pattern peptide phosphorylation.** *J. Am. Chem. Soc.* **2009,** *131*, 11976-11984.

106. Jagt, R. B. C.; Gomez-Biagi, R. F.; Nitz, M., **Pattern-based recognition of heparin contaminants by an array of self-assembling fluorescent receptors.** *Angew. Chem. Int. Ed.* **2009,** *48*, 1995 –1997.

107. Miranda, O. R.; You, C.-C.; Phillips, R.; Kim, I.-B.; Ghosh, P. S.; Bunz, U. H. F.; Rotello, V. M., **Array-based sensing of proteins using conjugated polymers.** *J. Am. Chem. Soc.* **2007,** *129*, 9856-9857.

108. Yang, M. C. K.; Robinson, D. H., *Understanding and learning statistics by computer.* World Scientific Publishing Company: 1986.

109. Delaine, T.; Cumpstey, T.; Ingrassia, L.; Le Mercier, M.; Okechukwu, P.; Leffler, H.; Kiss, R.; Nilsson, U. J., **Galectin-inhibitory thiodigalactoside ester derivatives have antimigratory effects in cultured lung and prostate cancer cells.** *J. Med. Chem.* **2008,** *51*, 8109-8114.

110. Miller, D. K.; Cooper, A. G., **Kinetics of release of glucosamine-labeled glycoproteins from the TA3-Ha murine adenocarcinoma cell.** *J. Biol. Chem.* **1978,** *253*, 8798-8803.

111. Raz, A.; McLellan, W. L.; Hart, I. R.; Bucana, C. D.; Hoyer, L. C.; Sela, B. A.; Dragsten, P.; Fidler, I. J., **Cell surface properties of B16 melanoma variants with differing metastatic potential.** *Cancer Res.* **1980,** *40*, 1645-1651.

112. Davis, B. G.; Robinson, M. A., **Drug delivery systems based on sugar-macromolecule conjugates.** *Curr. Opin. Drug Disc. Dev.* **2002,** *5*, 279-288.

113. Yamazaki, N.; Kojima, S.; Bovin, N. V.; André, S.; Gabius, S.; Gabius, H.-J., **Endogenous Lectins as Targets for Drug Delivery.** *Adv. Drug Del. Rev.* **2000,** *43*, 225-244.

114. Thiesen, B.; Jordan, A., **Clinical applications of magnetic nanoparticles for hyperthermia.** *Int. J. Hypertherm.* **2008,** *24*, 467-474.

115. Rojo, J.; Diaz, V.; de la Fuente, J. M.; Segura, I.; Barrientos, A. G.; Riese, H. H.; Bernad, A.; Penadés, S., **Gold glyconanoparticles as new tools in antiadhesive therapy.** *ChemBioChem* **2004,** *5*, 291-297.

116. Zhu, D.; Cheng, C.-F.; Pauli, B. U., **Blocking of lung endothelial cell adhesion molecule-1 (Lu-ECAM-1) inhibits murine melanoma lung metastasis.** *J. Clin. Invest.* **1992,** *89*, 1718-1724.

117. Meromsky, L.; Lotan, R.; Raz, A., **Implications of endogenous tumor cell surface lectins as mediators of cellular interactions and lung colonization.** *Cancer Res.* **1986,** *46*, 5270-52.

118. Wang, Z.; Zhou, L.; El-Boubbou, K.; Ye, X.-S.; Huang, X., **Multi-component one-pot synthesis of the tumor-associated carbohydrate antigen Globo-H based on preactivation of thioglycosyl donors.** *J. Org. Chem.* **2007,** *72*, 6409-6420.

119. Jing, Y. **Fluorous thiols in oligosaccharide synthesis and iterative one-pot synthesis of tumor associated carbohydrate antigen LewisX pentasaccharide**. M.S. thesis, The University of Toledo, **2005**.

120. Boons, G.-J.; Demchenko, A. V., **Recent advances in O-sialylation.** *Chem. Rev.* **2000,** *100*, 4539-4565.

121. Moore, D. H.; Cannon, J. G.; McIsaac, W. M.; Ho, B. T., **Compounds with potential enzyme inhibitory activity. Hydroxylamine analogs of 2-propynylamine.** *J. Med. Chem.* **1969,** *12*, 45-8.

122. Miyata, O.; Koizumi, T.; Asai, H.; Iba, R.; Naito, T., **Imino 1,2-Wittig rearrangement of hydroximates and its application to synthesis of cytoxazone.** *Tetrahedron* **2004,** *60*, 3893-3914.

123. Natarajan, A.; Du, W.; Xiong, C.-Y.; DeNardo, G. L.; DeNardo, S. J.; Gervay-Hague, J., **Construction of di-scFv through a trivalent alkyne-azide 1,3-dipolar cycloaddition.** *Chem. Commun.* **2007**, 695-697.

CHAPTER 4

Hyaluronan Magnetic Glyco-Nanoparticles (HA-MGNPs) for Detection and Molecular Imaging of Atherosclerosis

4.1. Introduction

Atherosclerosis is a silent systemic disease that is characterized by the build-up of patchy deposits of fatty materials (atheromas or atherosclerotic plaques) within the walls of medium and large-sized arteries, leading to reduced or blocked blood flow. With time, the plaques weaken and rupture leading to thrombosis and occlusion and thus can cause heart attacks or strokes. Although enormous clinical efforts and drug trials have had a major impact on decreasing coronary events,[1] it will be necessary to better understand atherogenesis to provide a rational basis for the design of novel diagnostics and therapeutics to further reduce the risk. Until recently, there has been no effective way to detect the presence of atherosclerosis in patients unless it has reached a relatively advanced stage. Thus, it is imperative to better understand the secrets behind this disease so as to assess prevention and treatment methods.

Atherosclerosis is a very complex disease. The pathogenesis of atherosclerosis is not well understood. Previous studies indicate that hyaluronic acid or hyaluronan (HA) are present in regions of atherosclerotic lesions and its principal receptor, CD44, participate in many stages of atherosclerosis.[2-4] In fact, the pathogenesis includes recruitment of inflammatory cells to the vessel wall and activation of vascular cells. CD44 and HA represent a significant receptor-carbohydrate ligand pair mediating an activation-dependent pathway of lymphocyte / endothelial cell adhesion.[2] It has been demonstrated that HA is

upregulated in atherosclerotic lesions and that CD44, expressed on both inflammatory and vascular cells, promotes the recruitment of macrophages to atherosclerotic lesions via multiple mechanisms.[5] These findings place HA at the beginning of the inflammatory response,[6] a critical step in the formation of the atherosclerotic lesion. Not only is HA important in the initial stages of leukocyte extravasation but also its accumulation in the early lesions may promote inflammatory cell retention by serving as an anchor for these cells. All this imply that inhibition of CD44 binding with HA may provide an effective means for reducing the development of atherosclerotic lesions.

The unique interactions between CD44 and HA have been exploited for targeted delivery of agents to tumor cells.[7-10] HA/CD44 binding has been shown to facilitate CD44 mediated uptake killing tumor cells,[7] target and deliver genes into the ocular epithelial cells with high transfection levels,[11] decrease breast cancer metastasis, increase antitumor activity in syngeneic and xenograft tumor models[10] and image cancer.[12] However to date, CD44 has not been explored for atherosclerotic plaque binding. In this work, we will examine the possibility to use CD44 as a molecular target for site specific delivery of imaging and therapeutic agents to study atherosclerosis. We hypothesized that superparamagnetic polyvalent HA-functionalized magnetic glyco-nanoparticles can be utilized for the detection and imaging of atherosclerotic plaques.

4.2. Biological Significance of Hyaluronan and CD44

HA is a naturally occurring, non-sulfated glycosaminoglycan GAG (a class of negatively charged polysaccharides) found predominantly in extracellular matrices (ECM), cartilages and the vitreous body of eyes.[13] It plays vital roles in biological events such as cell adhesion, cell migration, inflammation and also mediates cell proliferation making it not only a structural component of tissues, but also an active, signaling molecule.[13] HA is comprised of linear, unbranched, repeating units consisting of glucuronic acid-β-1,3-N-acetyl glucosamine (GlcU-β-1,3-GlcNAc) connected through β-1,4 glycosidic linkages (**Figure 4-1**). HA, along with the other GAGs present in the ECM, provides compressive strength to tissues and promote wound repair.[6, 14] Its negative charge, hydrophilicity and long polymer length result in large amounts of water being bound with the matrix.[15] In addition to providing a hydrated space around cells, it regulates the traffic of growth factors and other signals due to its pore size and charge density. HA can be transformed *in vivo* into oligosaccharide fragments (sHA) ranging from di- to deca-saccharides with tandem repeats of the β-1,4-GlcU-β-1,3-GlcNAc where each respective size is characterized by its own function and properties.[16-18] In general, HA attracts considerable attention due to its apparent ability to influence cell behavior.

Hyaluronic acid (HA)

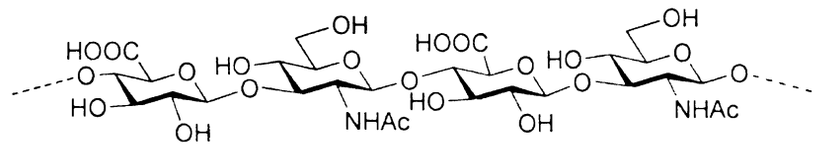

Figure 4-1. Structure of hyaluronic acid (HA).

The cell-HA interaction is a true receptor-ligand interaction where the principal receptor in question is identified as CD44,[19] which is a transmembrane glycoprotein present richly on plasma membrane domains, facing open intercellular spaces, rich in HA. CD44 is expressed on both inflammatory and vascular cells and can mediate adhesion of T lymphocytes to endothelium and smooth muscle cells (SMCs), release of inflammatory mediators from macrophages and T lymphocytes, and proliferation of vascular SMCs.[20] A few years ago, research concerning CD44 has expanded rapidly and CD44 has been implicated in cell migration during angiogenesis, tumor invasion and metastasis.[21] CD44 has a large HA-binding domain (HABD) that is necessary for its functional activity.[22] The majority of the proteoglycan-rich pericellular matrix can be displaced by reagents that compete with CD44-HA binding such as anti-CD44 antibodies and sHA hexasaccharides (HA_6). Competitive binding analyses with sHA showed that the smallest HA unit that could competitively bind HA polymers is a hexasaccharide (HA_6), but that octasaccharide (HA_8) to dodecasaccharide (HA_{12}) are more efficient competitors.[22] This confirms that the minimum size of oligosaccharide required to displace high molecular HA from cell surface CD44 is between 6 and 10 saccharide units (HA_6-HA_{10}) depending on the cell background.[19] Recently, the crystal structure of HA binding to CD44 has been revealed (**Figure 4-2**).[23]

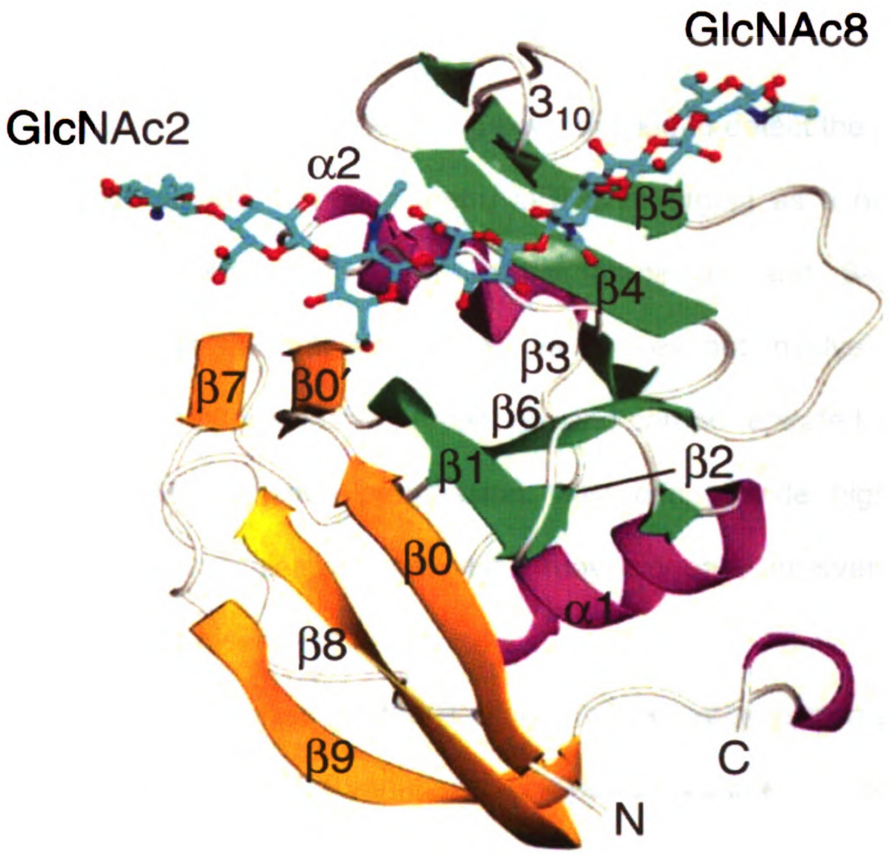

Figure 4-2. Crystal structure of CD44 complexed with HA.

It was shown that hyaluronan binding at the cell surface is a complex interplay of multivalent binding events affected by the size of the multivalent hyaluronan ligand, the quantity and density of cell surface CD44.[19] Since binding of a CD44 containing cell to HA substrate involves multiple weak receptor-ligand interactions, we will assess ligand binding of CD44 by preparing multivalent HA functionalized on magnetic nanoparticles.

4.3. Atherosclerotic Plaque Detection using HA-MGNPs

4.3. a. Plaque Imaging *via* MRI

Numerous imaging modalities have been applied to detect the progression of atherosclerotic plaque.[24] Among them, MRI is emerging as a non-invasive, nondestructive technique with high spatial resolution and 3-dimensional capability.[25] MRI has minimal side-effects as it does not involve the use of radioactive compounds or invasive procedures and can be repeated sequentially over time to monitor disease progression. MRI can provide high-resolution images of multiple vascular regions which may aid early intervention in the treatment of vascular diseases.[26]

In principle, MRI relies on the detection of the water proton's relaxation rate in a magnetic field.[27] The variations of water environment in body tissues create MR images. Briefly, in MRI, the subject is placed in a strong high-external magnetic field which aligns the protons. The MR image is based on the radiofrequency signal, typically from water protons, following administration of an RF pulse. The emitted signal varies according to the water concentration and to the spin-lattice longitudinal (T1) and spin-spin transverse (T2) relaxation times. Fortunately, the T1 and T2 relaxation times vary among different types, providing a highly useful means of generating image contrast. Although MRI has good spatial resolution, but it has relatively low sensitivity compared to other techniques. However, resolution can be improved by the use of contrast agents that target specific cells or molecules improving the sensitivity of MRI.[28]

An important feature of MRI imaging is that it can improve the precision of diagnosis and enable earlier detection of the disease, perhaps allowing intervention even "*before symptoms occur*" or "*irreparable damage*" has been inflicted (i.e. what we refer as *"early detection"*). In general, effective imaging necessitates the proper density of the target molecule, the high affinity of the ligand to its receptor, and the payload of contrast that can be delivered to it. Using a combination of MRI contrast generated in so called T1-weighted (T1w) and T2-weighted (T2w) images, it has been possible to determine both plaque anatomy and composition in experimental animals[29, 30] and carotid artery of humans.[31] However, identifying suitable biomarkers and imaging the plaque at early stages to locate the disease is still not translated into clinical applications. As a more precise understanding of the plaque formation and evolution, MRI studies are required to be assessed. This objective necessitates the development of novel contrast agents targeting molecules within cells or within the extracellular matrix of the evolving plaque.

In fact, atherosclerosis presents a number of potential targets, including, endothelial cell adhesion molecules, extracellular matrix, thrombosis, neovasculature $\alpha_v\beta_3$ integrins, oxidized LDL, matrix metalloproteinases, and macrophages.[26, 32-35] Nevertheless, there are challenges to implement these targeted technologies into the clinical practice. Molecular imaging using targeted contrast agents to cell adhesion molecules upregulated on the endothelial surfaces of the arteries is a promising approach and has the potential of detecting the atherosclerotic lesions non-invasively. The expression of CD44,

predominantly on endothelial cells, mediates leukocyte recruitment to sites of inflammation and is an early event in atherogenesis.[32, 33] Their endothelial location makes such molecules potentially accessible to targeting by intravascular imaging agents.

4.3. b. Nanoparticles as Imaging Agents

The promise offered by nanotechnology and the recent development achieved in molecular imaging open a great deal of opportunities on both the diagnostic and therapeutic fronts.[36] Indeed, imaging molecules and cells involve signal enhancement through the use of purpose-built contrast agents. The contrast agent must identify the target with high specificity and should possess physical properties that permit its sufficient localization to the target. This consequently provides intense signal enhancement within the imaged volume so as to be distinguishable from the unenhanced tissue.[28] Other considerations of such agent include its fast clearance from the body, cytotoxicity, biodegradability and immunogenicity.[37]

Direct imaging of the atherosclerotic plaques by MRI has been studied.[24, 38] The quality of MR images can be greatly enhanced by delivering a paramagnetic contrast agent to the region of interest, with the most popular contrast agents being paramagnetic Gadolinium (Gd) compounds such as Gd-DTPA.[39] To further improve detection, Gd has been attached onto ligands to target several different components of plaques.[26] However, the recent association of Gd with nephrogenic systemic fibrosis, an untreatable disease, has spawned great interests in alternative agents for MR molecular imaging.[40]

Moreover, specific targeting was typically achieved with peptides or monoclonal antibodies.[41] However, such approaches are limited by potential toxicity, immunogenic responses and larger sizes compared to HA-MGNPs. Indeed, the most successful approaches have involved the synthesis of nanocomposites that combine target specificity with the capacity to carry a substantial payload of superparamagnetic agent.[42] Functionalized iron oxide nanoparticles have proven to be effective T2/T2* imaging contrast agents,[43-45] where they shorten relaxation times producing a sharp negative contrast by virtue of signal reduction. They can be utilized as targeted-packaged units and thus concentrated at specific sites. Recently, SPIONs have received much attention because of their applications in a variety of fields such as biosensing, imaging, drug delivery and therapy.[46] Their applications in MRI have ranged from non-targeted to targeted detection.[47] For instance, cross-linked dextran-coated superparamagnetic iron oxide nanoparticles have been functionalized with different biomolecules and used for *in vitro* detection of different targets including oligonucleotides,[48] proteins and intracellular labeling,[49] viruses,[50] and enantiomeric impurities.[51] For *in vivo* purposes, studies have shown that modified nanoparticles can both target and image the atherosclerotic biomarkers.[52-56] Indeed, researchers have shown that MRI can noninvasively detect atherosclerotic plaques in living mice,[57, 58] rabbits[30] and humans.[59] SPIONs have been shown to be more taken up by macrophages than other cells.[60, 61] In recent studies, injection of ultrasmall SPIONs into hyperlipidemic rabbits resulted in significant T2* decrease in the aortic wall after 5 days, which after histopathology showed accumulation in macrophages

embedded in the atherosclerotic plaque.[34] Similar observations have been reported in human carotid arteries where ultrasmall SPIONs were accumulated in macrophages.[62] This is indeed a solid proof that USPION-enhanced MRI can be utilized for *in vivo* detection of macrophages in human plaques. MRI has also been used to monitor monocyte recruitment into developing atherosclerotic plaques.[63] Imaging of apolipoprotein E-deficient ($ApoE^{-/-}$) mice 6 days after administration of SPION demonstrated the localization of iron particles to the regions of accumulating macrophages in the diseased sections of aorta. Combined with their high contrast enhancement abilities, low toxicities and flexible surface chemistry, SPIONs can be excellent MRI probes and effective delivery vehicles.[64] Several SPIONs such as Feridex and Ferumoxtran[61] have been approved by FDA for use in humans as passive MRI contrast agents.

Herein, we hypothesized that certain features associated with plaques' vulnerability including inflammation, endothelial adhesion molecule expression, macrophage recruitment, and the role CD44/HA plays in those chief events may allow us to use novel HA-MGNP as potential contrast probes to detect inflammation early and image the atherosclerotic plaque. Thus, highly colloidal, biocompatible and well dispersed HA-MGNPs will be prepared. Taking advantage of the iron oxide core for imaging and CD44/HA binding events for targeting, their potential use in targeted-detection and enhanced-imaging of atherosclerotic plaque will be investigated

4.4. Synthesis of HA-MGNPs

HA-MGNPs are made of Fe_3O_4 core coated by hyaluronic acid polymer (~ 16 KDa) rendering the NPs dispersed, colloidal and thus appropriate for *in vivo* imaging.

We showed in the previous chapters the successful utilization of MGNPs immobilized with carbohydrates for pathogen and cancer detection *in vitro*. As discussed earlier, the characteristics and properties of the nanoparticles are extremely important, as those factors determine their use for *in vivo* or *in vitro* applications. For *in vitro,* the size restrictions are not so severe as for *in vivo*. For *in vivo* application, magnetic nanoparticles should be stable in water at neutral pH and physiological salinity. The colloidal stability will depend mainly on the dimensions (sufficiently small so that precipitation will not occur), charge and surface of the nanoparticles (steric and electrostatic stabilization).

Despite the large number of reports on the synthesis of superparamagnetic nanoparticles with different methods, including co-precipitation and thermal decomposition,[65, 66] we investigated the use of a sol-gel co-precipitation process at elevated temperatures to form colloidal, stable and polymeric coated superparamagnetic nanoparticles. Particularly, for the preparation of HA-MGNPs, we used a modified synthetic procedure with controlled passivation of the polymeric sugar on the surface of the nanoparticle.[67, 68] Briefly, the synthesis of colloidal superparamagnetic iron oxides by the cold gelation process involves two steps: (i) the neutralization of iron salts (Fe^{2+} and Fe^{3+}) with base (NH_4OH) at 0° C to form a weakly paramagnetic gel, followed by, (ii) heating to convert the paramagnetic gel to a superparamagnetic colloid. The newly devised

nanoparticles are composed of magnetic iron oxide core, encapsulated by a 10 kDa dextran coating. To develop more stable and amino-functionalized nanoparticles, the dextran coating has been cross-linked with epichlorohydrin to yield magnetic dextran-coated nanoparticles (MDNP), and then treated with ammonia to provide functional amino groups on the surface affording amine-MGNP (**Figure 4-3**). Amino groups can then react with the acid functionality of HA polymer (~ 16KDa) in aqueous media using triazine-activated amidation[69] allowing attachment of hyaluronan polymer onto the NP surface.

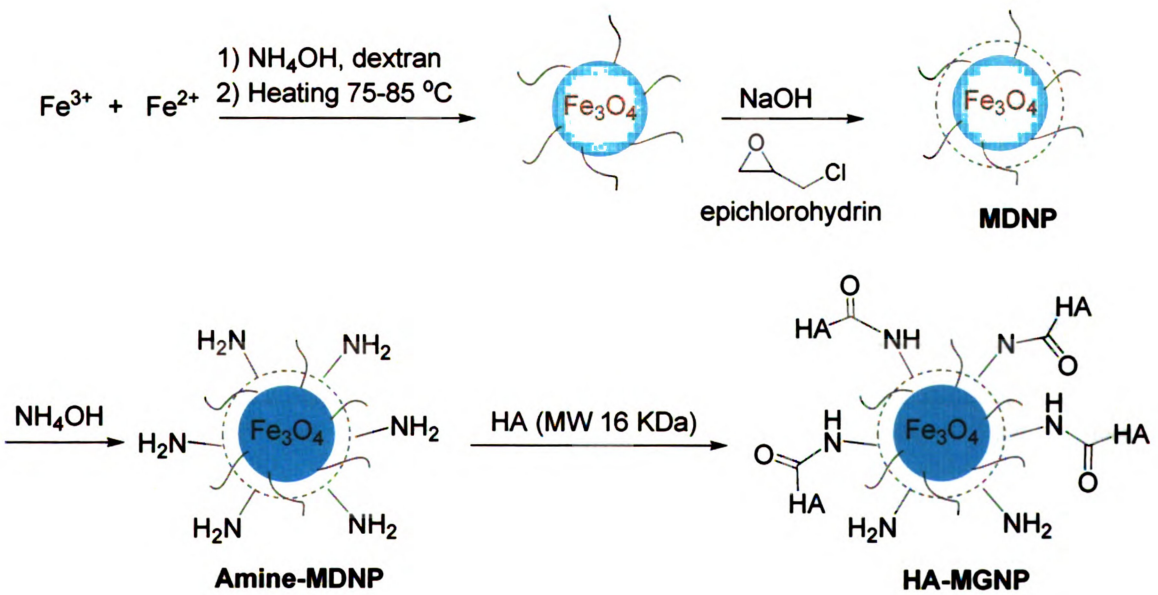

Figure 4-3. Synthesis of HA-MGNP.

HA-MGNPs were thoroughly characterized by a variety of techniques including FT-IR, TEM, TGA and NMR. TGA analysis demonstrated that ~ 90% of the particle weight was from dextran and HA coating (**Figure 4-4**). TEM images showed that the HA-MGNPs were highly mono-dispersed with the average core diameter of ~ 6 nm (**Figure 4-5a**). HR-MAS NMR spectrum of our HA-MGNP

gave solution like resolution, with the molar ratio of 1:3 between dextran to HA (**Figure 4-5b**). With the HA coating, it is most likely dextran is completely shielded by the HA, thus not interfering with the desired biological recognition of NP through HA. HA-MGNPs are highly colloidal, monodispersed, can be simply prepared in large-scales, thus suitable for MRI targeted applications.

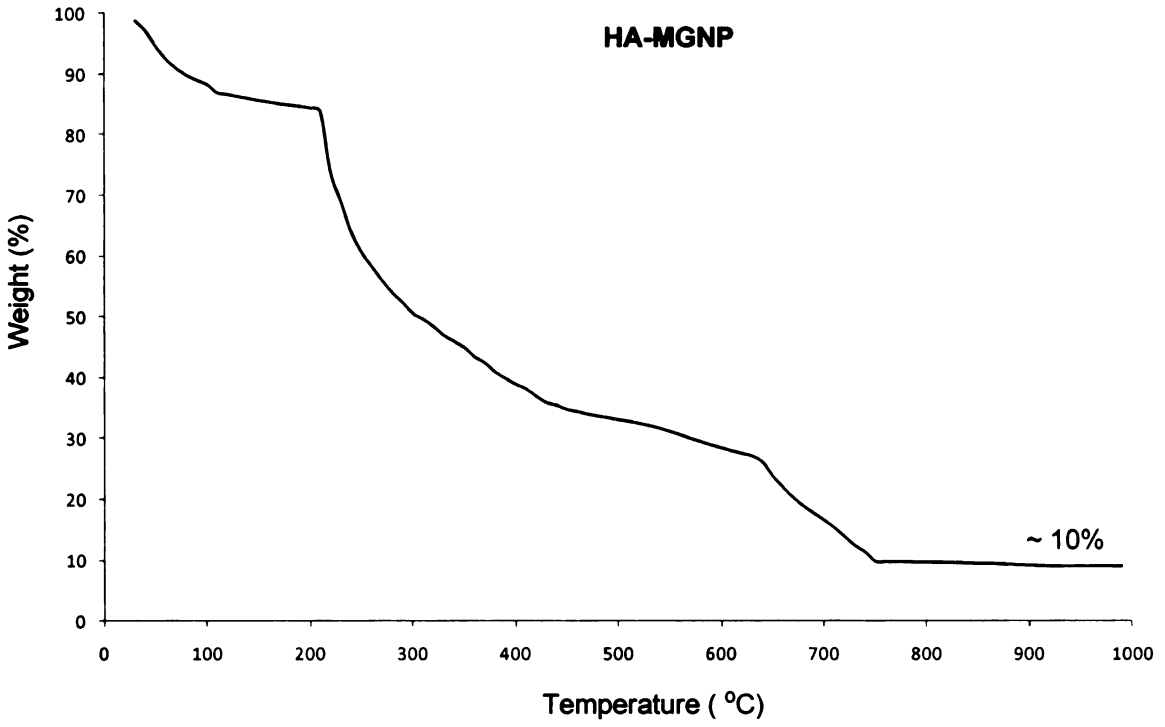

Figure 4-4. TGA for HA-MGNP showed that ~ 90% of the particle weight was from dextran and HA coating. Sample was heated at a constant heating rate of 20 °C/min from 50 to 1000 °C under nitrogen.

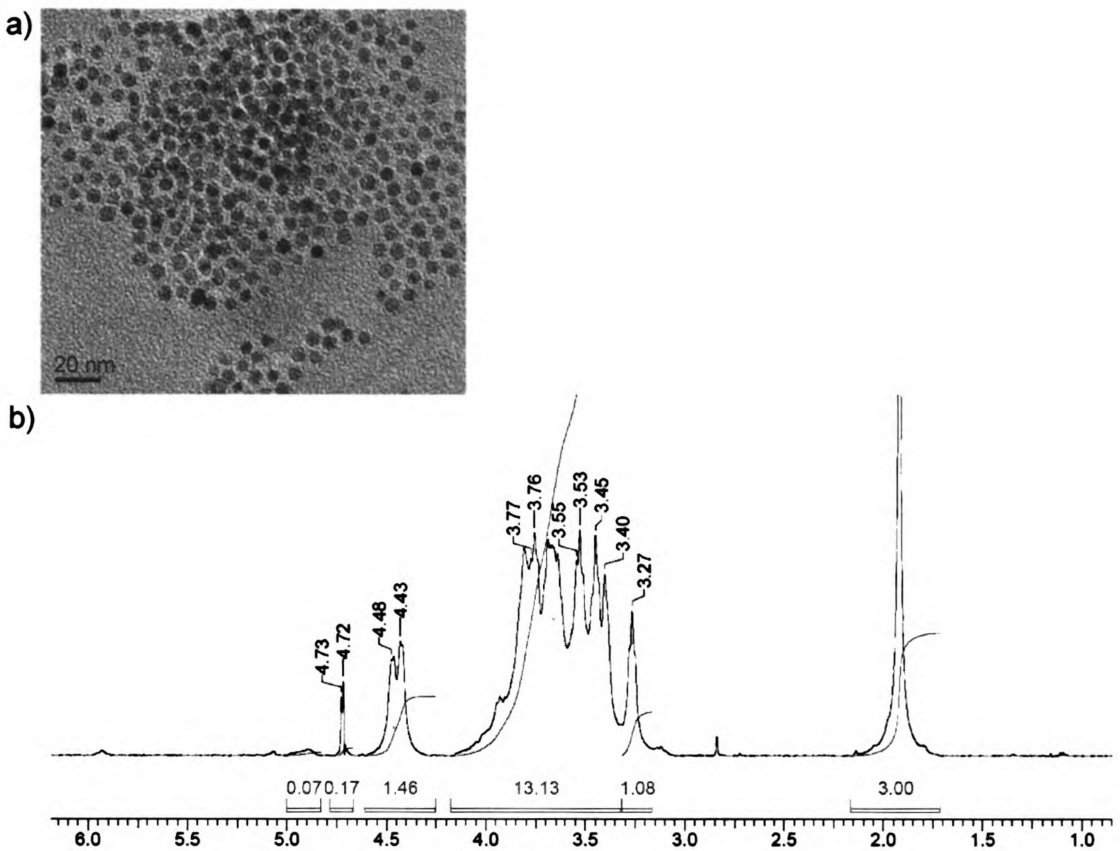

Figure 4-5. a) TEM of HA-MGNP (scale bar is 20 nm) and b) HR-MAS ^{1}H-NMR of HA-MGNP.

4.5. HA-MGNPs as Nanoprobes for Diagnosis and Imaging of Injured Rabbit

In order to examine imaging of atherosclerotic plaques, we first incubated HA-MGNP with both normal rabbit artery tissue and rabbit atherosclerotic artery tissues *in vitro*. The unbound HA-MGNP was removed from the tissue by thorough washing. The presence of the NPs in the tissues was first detected by Prussian blue staining with nuclear fast red counterstaining. The healthy rabbit artery tissue showed little Prussian blue staining demonstrating that it did not bind much with HA-MGNP (**Figure 4-6a**). In contrast, HA-MGNP bound to the atherosclerotic tissue strongly while the vessel wall remained unstained (**Figure 4-6b,c**). Incubation of HA-MGNP with atherosclerotic tissue in the presence of

high concentration of free HA completely abolished the HA-MGNP binding. Furthermore, the control MDNP without HA coating did not stain the atherosclerotic tissue either, suggesting the HA-MGNP/plaque tissue interactions were due to specific binding with HA. The presence of HA-MGNP on plaque tissue was easily detected by MRI, as the selective darkening of the plaque was observed due to the adhesion of NPs to the tissue (**Figure 4-6d**). This indicates that HA-MGNP can be used to selectively target and image the atherosclerotic plaques.

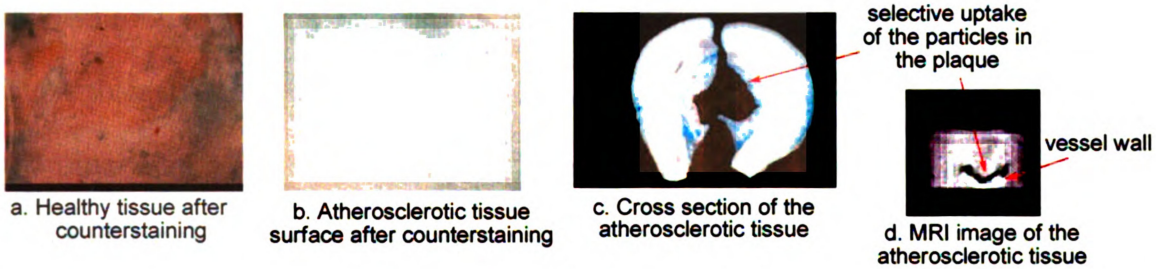

Figure 4-6. Binding of HA-MGNP with rabbit artery tissues after removal of unbound particles. a) healthy non-atherosclerotic tissue surface; b) atherosclerotic tissue surface; c) cross section of the atherosclerotic tissue; and d) MRI image of the atherosclerotic tissue.

With the promising *ex vivo* imaging results in hand, we moved to demonstrate the feasibility of *in vivo* imaging using an *injured* atherosclerotic rabbit model. Full plaques will develop in rabbit aortas injured through a balloon de-endothelialization process followed by feeding with a high (1%) cholesterol diet for six months. The de-endothelialization mimics the ox-LDL induced arterial injury, recruiting macrophages to the injury site as in the early stage of plaque development.[70, 71] In order to examine whether we can detect early plaque formation, a rabbit's aorta was injured through the balloon-catheter procedure and fed it the high cholesterol diet for three weeks. This is an injured rabbit model

where full plaque did not have time to completely develop. Our hypothesis is that if we can detect early inflammatory lesions of the disease (i.e. the key for the progression of the disease), we might be able to stratify clinical risks. The earliest molecular changes and protein signaling occur on the endothelial surfaces of the aorta and vasculature and are chief contributors to initiation of atherosclerosis. Thus, targeting CD44 upregulated on the endothelium under inflammatory conditions is ideal for next generation of diagnostics and therapeutics. HA-MGNP (1.5 mg Fe total/kg of body weight) was hence injected into the ear vein of the injured rabbit. Excitingly we observed selective darkening of the rabbit artery wall by high-resolution 3D T2*-weighted MRI with a voxel size of 0.2 mm^3 fifteen minutes after HA-MGNP injection (**Figure 4-7a,b**). It is worth mentioning that there was only a little plaque developed at this stage without much stenosis, and that pinpoints the advantages of our approach. The rabbit was then sacrificed with its aorta imaged *ex vivo* by high-resolution 3D T2*-weighted MRI (**Figure 4-7c**) with a voxel size of 0.06 mm^3. It should be emphasized that the dosage in our study is much lower than that ~ 56 mg Fe/kg[34] and 11 mg Fe/kg[72] adapted in two studies utilizing SPION as a *passive* contrast agent to image the atherosclerotic plaques in rabbit aorta. This highlights the advantage of *active* targeting.

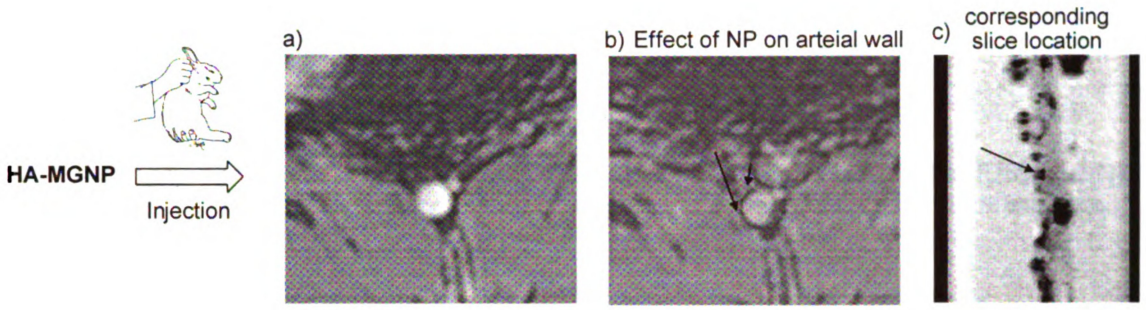

Figure 4-7. MRI images of rabbit artery. a) *in vivo* image before HA-MGNP injection; b) *in vivo* image after HA-MGNP injection; and c) *ex vivo* image following HA-MGNP injection and artery removal with the arrow showing corresponding *in vivo* slice location.

The same study was repeated as shown in Figure 4-5. Interestingly, injection of the control Feridex (FDA approved dextran coated nanoparticle) at the same dose showed no affinity for endothelial cells with no darkening in the arterial wall (**Figure 4-8a,b**). Selective darkening of the rabbit artery wall after HA-MGNP injection was observed as before (**Figure 4-8d**). This proves the reliability of our results and the selectivity of HA-MGNP as targeted-disease specific molecular imaging agents, which can have great impacts on atherosclerosis treatment.

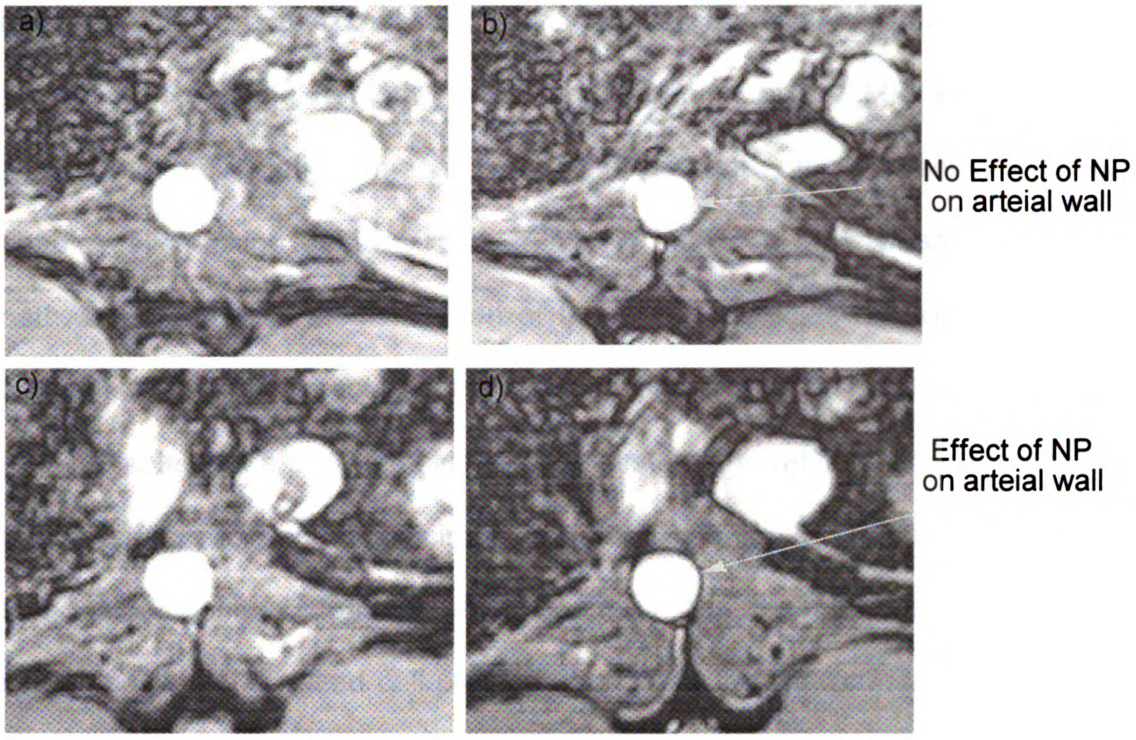

Figure 4-8. MRI images of rabbit artery. a) *in vivo* image before Feridex injection; b) *in vivo* image after Feridex (1.5 mg Fe/kg) injection; c) *in vivo* image before HA-MGNP injection; d) *in vivo* image after HA-MGNP (1.5 mg Fe/kg) injection.

Moreover, in a separate study, HA-MGNP was injected into two rabbits to test toxicity. It is known that both the magnetite NP and HA are highly biocompatible. Indeed, in our study, no toxicities or apparent adverse effects on these rabbits were observed two months following NP injection. Achieving good successful results for the injured rabbit, detection of atherosclerotic plaque at more advanced stages seems promising

4.6. Current Studies and Future Insights

Recent studies point to evidence that indicates dextran-NPs are not as proficient as currently believed.[73, 74] One of the main limitation of typically synthesized and dextran-functionalized iron oxide for biomedical applications is

the presence of a thick polymer that increases the overall hydrodynamic radii (~ 150 nm) causing not only possible dampening of the MR signal but also shorter blood-circulation times. They do not present sufficient cellular uptake to enable cell tracking because of a relatively inefficient fluid phase endocytosis pathway.[73] Targeted biodistribution of these nanoparticles remains a challenge because of a quick process known as opsonization that renders the particles recognizable by the body's major defense system, the reticulo-endothelial system (RES) leading to decreased circulation blood half-life.[73] Moreover, surprisingly, some cases point to situations where dextran-magnetite nanoparticles resulted in cell damage and reduced cell proliferation.[73] As a result, for *in vivo* applications, there is a need to explore novel nanoparticles with proper surface modification that would ensure the particles to be non-toxic, biocompatible and stable to the RES.

As discussed earlier, magnetic nanocomposites are not biocompatible without the aid of a protective hydrophilic layer on the surface to serve as a buffer for bio-cellular interactions. However, sometimes this layer will be thick affecting the overall hydrodynamic size of the particles in media and hence their *in vivo* efficacy. Ideally, the size of the nanoparticles should be small enough to escape capture by macrophages in RES, mainly liver and spleen, but large enough to prevent their rapid leakage into blood capillaries, making it a challenging issue for the synthetic chemists. Indeed, the size of the nanoparticles should be ~ 50 nm to reach tumor tissues by passing through these 2 particular vascular structures. Moreover, functionalizing the surface with hydrophilic compounds is important as

it protects them from opsonization by repelling plasma proteins. Thus, it is of immense value to design MNPs that satisfy the above 2 requirements as those NPs will have the ability to circulate longer in the bloodstream[62] and greater chance of reaching targeted tumor tissues.[75, 76] As a result, there is a push for finding and developing new surface-modifying and targeting contrast nano-agents.

Consequently, we planned the synthesis of HA-coated magnetic nanoparticles in an alternative method without using the dextran layer. Instead of using the co-precipitation or sol-gel method explored earlier, we anticipated the use of the thermal-decomposition technique that usually offers better control over crystallinity, monodispersity and uniformity of nanoparticles and thus higher relaxivity. The hydrophobic inorganic nanocrystals (coated with oleic acid) formed will be then transferred to aqueous solutions through a "robust ligand exchange" method that uses the hydrophilic HA polymer to *directly* replace the original hydrophobic ligands (oleic acids) at an elevated temperature (~ 110 °C) in a 2-solvent system. This method offers several advantages: a) more exchange efficacy at elevated temperature; b) ideal dispersant characteristics (HA is a long hydrocarbon polymeric chain with carboxylate and hydroxyl groups); c) strong coordination to the nanocrystal surface through multiple anchoring groups; d) excellent solubility in water (abundant uncoordinated groups facing water); e) good stability; f) direct immobilization of the target molecule HA; g) two-phase reaction system and h) fast, simple and scalable.

Experimentally, a basic solution of polymeric HA dissolved in basic aqueous solution (pH > 9) will be rapidly injected into a pre-heated toluene solution containing oleic-Fe_3O_4 nanocrystals (prepared by the thermal-decomposition method discussed in chapter one) and refluxed. The composition, size, and morphology of the as synthesized particles can all be tailored, which, in combination with their nanoscale magnetic phenomena, makes them potentially suitable for *in vivo* applications. Preparation and characterization of such particles and mechanistic investigation onto their size, shape and quality-control is in progress.

Both HA-MGNPs and the newly optimized *directly*-HA coated nanoparticles will be evaluated for their abilities to image atherosclerotic plaques *in vivo*. As HA-MGNP targets CD44, a marker for inflammation, we hypothesize that we will be able to use HA-MGNP to follow the plaque development. Our preliminary imaging results suggest that detection of early stages of atherosclerosis development can be achieved with HA-MGNP, which would be difficult to accomplish using the traditional methods such as angiography as there is no significant stenosis. In the preliminary *in vivo* studies, MR images were acquired 15 minutes after injection and the rabbit was sacrificed. NPs were found to be close to the surface of the injury. In the fully developed plaque rabbit model, we will increase the circulation time between injection and MR imaging to test whether the NP will circulate longer in the blood enabling penetration deep inside the plaques. We will also study the biodistribution and rate of clearance of NPs from the body.

Overall, the innovation of our work lies in the development of a nano-based platform technology that can not only detect early and unstable plaques but also have the potential to be functionalized with therapeutic agents. Image-based therapeutics will provide conclusive evidence that the drug is reaching the desired site and the molecular effect can be easily monitored. The advantages of our approach are: 1) CD44 is a novel plaque component for targeting. By using HA-MGNPs, active targeting can greatly reduce the amount of agents required, lowering the risk of side effects; 2) the NP system can be used to deliver a variety of therapeutic agents with the capability to non-invasively monitor the effects of the therapeutics (in process); 3) due to the small sizes of NP, it can potentially penetrate plaques deeply allowing drug and imaging agent delivery to the core; and 4) the NP system is highly biocompatible.

4.7. Conclusion

In conclusion, as a part of our carbohydrate-based nano-program, we devised "smart" nanoparticles that can be used as sensing, imaging, and targeting agents for pathogen detection, cancer differentiation and plaque progression. We believe that carbohydrate-coated nanoparticles are an important addition to the stock of diagnostic and disease-fighting nanoparticles. We would have been missing vast opportunities not to recruit the "sugar-code" to cellular information transfer and clinical applications. Indeed, we proved that designed carbohydrate-functionalized magnetic bio-nanocomposites can be valuable not only as MR contrast enhancement and imaging agents, but also as excellent targeting and sensing vehicles. Although the development of discrete, highly-

colloidal, ultrasmall, biocompatible, stable, high contrast and targeted magnetic glyco-nanoparticles probes is still in its early stages, they have a massive potential to bring significant advances to the biomedical field at both the diagnostic and therapeutic fronts. Target selectivity and receptor specificity is the single most significant factor if MRI is to establish itself in the next decade. We believe that tailored MGNPs could pave the way to *in vivo* diagnosis of the early stages of diseases. Ultimately, the goal is to enable clinicians to better identify people at the highest risk of the disease and to fine-tune therapies to reduce the saddle of diseases in affected patients. To achieve this aim, we should start from ourselves, from the chemistry labs and let me conclude by what Prof. Gregory M. Lanza said: "We should not be sitting in the lab generating nanoparticles and then looking for what they could be used for.... We should seek a medical problem and ask what kind of particle might overcome it and then try to create it".

4.8. Experimental Section

4.8. a. Synthesis of Colloidal and Monodispersed HA-MGNPs

1) Preparation of Crosslinked Dextran-coated Fe_3O_4 Nanoparticles (MDNPs)

$FeCl_3.6H_2O$ (0.32 g, 1.2 mmol) and 4.5 g dextran (~ 9-11 KDa) were mixed in 0.22 µm filtered aqueous solution (10 mL), vigorously stirred and cooled to 0 °C. $FeCl_2.4H_2O$ (0.13 g, 0.65 mmol) was then dissolved in 0.45 mL of 0.22 µm filtered aqueous solution and added slowly to the above cooled mixture. While being rapidly stirred, cooled 30% NH_4OH solution (0.45 mL) was added dropwise to the above acidic solution. At this stage, the greenish suspension was heated to ~85° C for 90 min. The mixture was then cooled, resulting in the

formation of black superparamagnetic colloidal suspension. Ammonium chloride and excess dextran were removed by extensive dialysis (14 KDa cutoff), followed by ultrafiltration (30 KDa *Mw* cutoff membrane). After several washes, the colloidal product was concentrated by ultrafiltration and 0.22 μm filtered to a total volume of 45 mL (3.0 mmol Fe total). To the superparamagnetic colloid (1.2 mmol Fe, 2 mL), was added 5 M NaOH (10 mL), distilled water (4 mL), and epichlorohydrin (51 mmol, 4 mL). The mixture was stirred at room temperature for 24 hrs. Excess epichlorohydrin was then removed by dialysis (14 KDa cutoff) against 10 changes of distilled water to yield MDNP. Amination was achieved by the addition of 30% NH_4OH solution (8 mL) to MDNP (30 mL, ~80 mg total weight), followed by heating at 37° C for 36 hrs. The resulting mixture was then dialyzed (14 KDa cutoff) against 10 changes of distilled water to afford amine-MGNP.

2) Preparation of HA-coated Magnetite Nanoparticles (HA-MGNP)

Triazine-activated amidation of HA was performed using previously reported procedure.[69] Briefly, 100 mg of hyaluronic acid sodium salt (~ 16 KDa) was dissolved in distilled water (5 mg/mL), mixed with Amberlit H^+ and stirred at room temperature for 4 hrs until pH ~3. The resulting mixture was then filtered and rotary-evaporated under high vacuum to obtain hyaluronic acid in protonated form. 4-methylmorpholine (NMM) (50 μL, 0.45 mmol) was added to protonated hyaluronic acid (83 mg, 0.22 mmol carboxylic acid) dissolved in water:acetonitrile (ratio 3:2, 6.5 mL) mixture. The above solution was then cooled to 4 °C, and 2-chloro-4,6-dimethoxy-1,3,5-triazine (30 mg, 0.17 mmol) was added and stirred at

room temperature for 1 h. Amine-MGNP (10 mL, ~30 mg total dried weight) was then added and stirring continued for 24 hrs at room temperature. The reaction was then neutralized with resin and filtered. Extensive dialysis (14 kDa *Mw* cutoff) of the solution against deionized water, followed by ultrafiltration (100 KDa *Mw* cutoff membrane) and 0.22 μm filtration afforded HA-MGNP (~5.5 mg Fe total).

4.8. b. HR-MAS ^{1}H NMR

HR-MAS NMR experiments were carried out on a Varian Inova-500 NMR spectrometer equipped with a 4 mm gHX Nanoprobe (Variannmr Inc., Palo Alto, CA) available at the University of Tennessee Health Science Center (Memphis, TN). The HR-MAS probe with internal lock is capable of performing either direct or indirect (invese) detection experiments. MAS experiments were performed at spinning rates of up to 2.5 kHz using a 40 μL glass rotor. All HA-MGNP samples were dissolved in D_2O solvent and were further diluted at different concentrations with D_2O to find out the concentration limit to the NMR signal broadening. HR-MAS ^{1}H NMR spectra were obtained using 100-600 scans for each experiment. The sample temperature was regulated with an accuracy of ±0.1 °C.

4.8. c. Injured Atherosclerotic Rabbit

New Zealand White rabbits weighing between 2 and 3.5 kg were exposed to the following preparatory regime: the control group consisted of normal rabbits (n=3) that were fed a regular diet for 8 months. Atherosclerotic rabbits (n=3) underwent balloon-induced arterial wall injury, then were fed a diet of 1% cholesterol (Harlan-Sprague Dawley, Inc, Indianapolis, Ind) for 2 months followed by a regular diet for 2 months for a total of 4 months. Under general anesthesia

(ketamine 50 mg/kg and xylazine 20 mg/kg IM), balloon-induced de-endothelialization of the aorta was performed with a 4F Fogarty arterial embolectomy catheter (Baxter Healthcare Corp, Irvine, Calif) introduced *via* a right femoral artery cutdown. The catheter was advanced in a retrograde fashion to the ascending aorta, inflated with 1 mL of air, and pulled back to the iliofemoral artery. This was repeated 3 times; the femoral artery was then ligated, and the skin incision was sutured. Details of model have been reported previously.[77, 78]

4.8. d. Magnetic Resonance Imaging

Imaging was performed before injection, 15 min, 3 hrs, and 6 hrs after intravenous injection in the marginal ear vein of either HA-MGNP or the control Feridex (1.5 mg Fe total, 5 mL total volume). Under general anesthesia (ketamine 50 mg/kg and xylazine 20 mg/kg IM), the rabbits were held in a supine position on plastic boards with medical tape to minimize motion artifact and were placed inside the MRI coil for scanning. MRI rabbit experiments were carried on a GE 3T Signa® HDx MR scanner (GE Healthcare, Waukesha, WI) with an 8-channel knee coil. After a 3-plane localizer, we first used a 2D time-of-flight (TOF) pulse sequence to localize the rabbit aorta with the following parameters: Axial scan, anterior-posterior frequency direction, flow compensation, flip angle = 60 degree, echo time (TE) = 4.4 ms, time of repetition (TR) = 23 ms , receiver bandwidth (rBW) = +/- 15.6 kHz, field of view (FOV) = 14 cm, slice thickness = 2 mm, # of slices = 79, acquisition matrix = 256 x 128, number of excitation (NEX) = 1, and scan time = 4 min 4 sec. Then we acquired high-resolution 3D fast spoiled gradient recalled echo (FSGR) images to cover the rabbit aorta with the

center around the kidney and liver regions with the following parameters: Axial scan, anterior-posterior frequency direction, flip angle = 15 degree, TE = 9.3 ms, TR = 18.9 ms, rBW = +/- 7.8 kHz, field of view = 12 cm, slice thickness = 1 mm, # of slices = 90, acquisition matrix = 256 x 256, NEX = 2, and scan time = 14 min 31 sec. T2*-weighted ability of the FSPGR sequence was used to detect the effect of the nanoparticles before injection, 15 minutes after injection, three hours and six hours later at the same locations.

4.8. e. Histology and Tissue Staining

All procedures were performed according to the Michigan State University Animal Care and Use Committee of the Deaconess Hospital. Rabbits were killed by an overdose of intravenous pentobarbital and potassium chloride. The aorta and iliofemoral arteries were dissected and excised, and the intimal surface was exposed by an anterior longitudinal incision of the vessel. Cross-sectional tissue samples (1 cm in length) were taken from the thoracic aorta, 3 and 6 cm distal to the aortic valve; from the abdominal aorta, 7 and 4 cm proximal to the iliac bifurcation; and from the iliofemoral arteries. The samples were fixed, serially dehydrated in alcohol, and embedded in paraffin. Inverted light microscopy was performed on tissue sections mounted on glass slides and subsequently scanned for the presence of iron after standard histochemical staining (Prussian blue iron staining). Briefly, healthy non-atherosclerotic rabbit artery tissue and atherosclerotic rabbit artery tissue were incubated with HA-MGNPs or the control MDNP (1 mg/mL) for 12 hrs. After 12 hrs, iron-oxide labeled tissues were washed thoroughly, fixed with formalin, incubated for 30 min at 37 °C in the dark

with Perl's reagent (2 % potassium ferrocyanide(II) trihydrate and 3.7 % HCl solution), and counterstained with nuclear fast red (for making contrast between blue iron particles and red nucleus).

4.9. References

1. Ross, S. D., et al., **Clinical outcomes in statin treatment trials: a meta-analysis.** *Arch. Intern. Med.* **1999,** *159*, 1793–1802.

2. DeGrendele, H. C.; Estess, P.; Siegelman, M. H., **Requirement for CD44 in activated T cell extravasation into an inflammatory site.** *Science* **1997,** *278*, 672–675.

3. Jain, M.; Q., H.; Lee, W. S.; Kashiki, S.; Foster, L. C.; Tsai, J. C.; Lee, M.; Haber, E., **Role of CD44 in the reaction of vascular smooth muscle cells to arterial wall injury.** *J. Clin. Invest.* **1996,** *97*, 596-603.

4. Protasiewicz, J.; Adamiec, R., **The role of CD44 in pathogenesis of atherosclerosis.** *Pol. Merkur. Lekarski.* **2005,** *19*, 559-562.

5. McKee, C. M.; Penno, M. B.; Cowman, M.; Bao, C.; Noble, P. W., **Hyaluronan (HA) fragments induce chemokine gene expression in alveolar macrophages. The role of HA size and CD44.** *J. Clin. Invest.* **1996,** *98*, 2403–2413.

6. Weigel, P. H.; Fuller, G. M.; LeBoeuf, R. D., **A model for the role of hyaluronic acid and fibrin in the early events during the inflammatory response and wound healing.** *J. Theor. Biol.* **1986,** *11*, 219-234.

7. Eliaz, R. E.; Szoka, F. C., Jr., **Liposome-encapsulated doxorubicin targeted to CD44: a strategy to kill CD44-overexpressing tumor cells.** *Cancer Res.* **2001,** *61*, 2592-2601.

8. de la Fuente, M.; Seijo, B.; Alonso, M. J., **Novel hyaluronan-based nanocarriers for transmucosal delivery of macromolecules.** *Macromol. Biosci.* **2008,** *8*, 441-450.

9. Peer, D.; Margalit, R., **Loading mitomycin C inside long circulating hyaluronan targeted nano-liposomes increases its antitumor activity in three mice tumor models.** *Int. J. Cancer* **2004,** *108*, 780-9.

10. Peer, D.; Margalit, R., **Tumor-targeted hyaluronan nanoliposomes increase the antitumor activity of liposomal doxorubicin in syngeneic and human xenograft mouse tumor models.** *Neoplasia* **2004,** *6*, 343-353.

11. de la Fuente, M.; Seijo, B.; Alonso Maria, J., **Novel hyaluronic acid-chitosan nanoparticles for ocular gene therapy.** *Invest. Ophthalmol. Vis. Sci.* **2008,** *49*, 2016-24.

12. Lee, Y.; Lee, H.; Kim, Y. B.; Kim, J.; Hyeon, T.; Park, H.; Messersmith, P. B.; Park, T. G., **Bioinspired surface immobilization of hyaluronic acid on**

monodisperse magnetite nanocrystals for targeted cancer imaging. *Adv. Mater.* **2008,** *20*, 4154-4157.

13. Lapcik, L., Jr. ; Lapcik, L.; De Smedt, S.; Demeester, J.; Chabrecek, P., **Hyaluronan: Preparation, structure, properties, and applications.** *Chem. Rev.* **1998,** *98*, 2663-2684.

14. Raman, R.; Sasisekharan, V.; Sasisekharan, R., **Structural insights into biological roles of protein-glycosaminoglycan interactions.** *Chem. Biol.* **2005,** *12*, 267-277.

15. Alberts, B.; Johnson, A.; Lewis, J.; Raff, M.; Roberts, K.; Walter, P., *Molecular Biology of the Cell.* Fourth ed.; 2002.

16. Tammi, R.; MacCallum, D.; Hascall, V. C.; Pienimaki, J.-P.; Hyttinen, M.; Tammi, M., **Hyaluronan bound to CD44 on keratinocytes is displaced by hyaluronan decasaccharides and not hexasaccharides.** *J. Biol. Chem.* **1998,** *273*, 28878-28888.

17. Xu, H.; Ito, T.; Tawada, A.; Maeda, H.; Yamanokuchi, H.; Isahara, K.; Yoshida, K.; Uchiyama, Y.; Asari, A., **Effect of hyaluronan oligosaccharides on the expression of heat shock protein 72.** *J. Biol. Chem.* **2002,** *277*, 17308-17314.

18. Tawada, A.; Masa, T.; Oonuki, Y.; Watanabe, A.; Matsuzaki, Y.; Asari, A., **Large-scale preparation, purification, and characterization of hyaluronan oligosaccharides from 4-mers to 52-mers.** *Glycobiology* **2002,** *12*, 421-426.

19. Lesley, J.; Hascall, V. C.; Tammi, M.; Hyman, R., **Hyaluronan binding by cell Surface CD44.** *J. Biol. Chem.* **2000,** *275*, 26967-26975.

20. Cuff, C. A.; Kothapalli, D.; Azonobi, I.; Chun, S.; Zhang, Y.; Belkin, R.; Yeh, C.; Secreto, A.; Assoian, R. K.; Rader, D. J.; Puré, E., **The adhesion receptor CD44 promotes atherosclerosis by mediating inflammatory cell recruitment and vascular cell activation.** *J. Clin. Invest.* **2001,** *108*, 1031–1040.

21. Trochon, V.; Mabilat, C.; Bertrand, P.; Legrand, Y.; Smadja-Joffe, F.; Soria, C.; Delpech, B.; Lu, H., **Evidence of involvement of CD44 in endothelial cell proliferation, migration and angiogenesis in vitro.** *Int. J. Cancer* **1996,** *66*, 664-668.

22. Teriete, P.; Banerji, S.; Noble, M.; Blundell, C. D.; Wright, A. J.; Pickford, A. R.; Lowe, E.; Mahoney, D. J.; Tammi, M. I.; Kahmann, J. D.; Campbell, I. D.; Day, A. J.; Jackson, D. G., **Structure of the regulatory hyaluronan binding domain in the inflammatory leukocyte homing receptor CD44.** *Molecular cell* **2004,** *13*, 483-496.

23. Banerji, S.; Wright, A. J.; Noble, M.; Mahoney, D. J.; Campbell, I. D.; Day, A. J.; Jackson, D. G., **Structures of the Cd44-hyaluronan complex provide insight into a fundamental carbohydrate-protein interaction.** *Nat. Struct. Mol. Biol.* **2007,** *14*, 234-239.

24. Fayad, Z. A.; Fuster, V., **Clinical imaging of the high-risk or vulnerable atherosclerotic plaque.** *Circ. Res.* **2001,** *89*, 305-316.

25. Choudhury, R. P.; Fuster, V.; Badimon, J. J.; Fisher, E. A.; Fayad, Z. A., **MRI and characterization of atherosclerotic plaque emerging applications and molecular imaging.** *Arterioscler. Thromb. Vasc. Biol.* **2002,** *22*, 1065-1074 and references therein.

26. Briley-Saebo Karen, C.; Mulder Willem, J. M.; Mani, V.; Hyafil, F.; Amirbekian, V.; Aguinaldo Juan Gilberto, S.; Fisher Edward, A.; Fayad Zahi, A., **Magnetic resonance imaging of vulnerable atherosclerotic plaques: current imaging strategies and molecular imaging probes.** *J. Magn. Reson. Imaging* **2007,** *26*, 460-79.

27. van Geuns, R. J.; Wielopolski, P. A.; de Bruin, H. G.; Rensing, B. J.; van Ooijen, P. M.; Hulshoff, M.; Oudkerk, M.; de Feyter, P. J., **Basic principles of magnetic resonance imaging.** *Prog. Cardiovasc. Dis.* **1999,** *42*, 149-56.

28. Corot, C.; Robert, P.; Idee, J.-M.; Port, M., **Recent advances in iron oxide nanocrystal technology for medical imaging.** *Adv. Drug Delivery Rev.* **2006,** *58*, 1471-1504.

29. Helft, G.; Worthley, S. G.; Fuster, V.; Zaman, A. G.; Schechter, C.; Osende, J. I.; Rodriguez, O. J.; Fayad, Z. A.; Fallon, J. T.; Badimon, J. J., **Atherosclerotic aortic component quantification by noninvasive magnetic resonance imaging: an in vivo study in rabbits.** *J. Am. Coll. Cardiol.* **2001,** *37*, 1149-54.

30. Skinner, M. P.; Yuan, C.; Mitsumori, L.; Hayes, C. E.; Raines, E. W.; Nelson, J. A.; Ross, R., **Serial magnetic resonance imaging of experimental atherosclerosis detects lesion fine structure, progression and complications in vivo.** *Nat. Med.* **1995,** *1*, 69-73.

31. Hatsukami, T. S.; Ross, R.; Polissar, N. L.; Yuan, C., **Visualization of fibrous cap thickness and rupture in human atherosclerotic carotid plaque in vivo with high-resolution magnetic resonance imaging.** *Circulation* **2000,** *102*, 959-64.

32. Cybulsky, M. I.; Gimbrone, M. A., Jr., **Endothelial expression of a mononuclear leukocyte adhesion molecule during atherogenesis.** *Science* **1991,** *251*, 788-91.

33. Nakashima, Y.; Raines, E. W.; Plump, A. S.; Breslow, J. L.; Ross, R., **Upregulation of VCAM-1 and ICAM-1 at atherosclerosis-prone sites on the endothelium in the apoE-deficient mouse.** *Arterioscler., Thromb., Vasc. Biol.* **1998,** *18*, 842-851.

34. Ruehm, S. G.; Corot, C.; Vogt, P.; Kolb, S.; Debatin, J. F., **Magnetic resonance imaging of atherosclerotic plaque with ultrasmall superparamagnetic particles of iron oxide in hyperlipidemic rabbits.** *Circulation* **2001,** *103*, 415-422.

35. Stary, H. C.; Chandler, A. B.; Dinsmore, R. E.; Fuster, V.; Glagov, S.; Insull, W., Jr.; Rosenfeld, M. E.; Schwartz, C. J.; Wagner, W. D.; Wissler, R. W., **A definition of advanced types of atherosclerotic lesions and a histological classification of atherosclerosis. A report from the Committee on vascular lesions of the council on arteriosclerosis, American Heart Association.** *Arterioscler. Thromb. Vasc. Biol.* **1995,** *15*, 1512-31.

36. Thorek , L. J. D.; Chen , K. A.; Czupryna, J.; Tsourkas, A., **Superparamagnetic iron oxide nanoparticle probes for molecular imaging.** *Ann. Biomed. Eng.* **2006,** *34*, 23-38.

37. Jain, T. K.; Reddy, M. K.; Morales, M. A.; Leslie-Pelecky, D. L.; Labhasetwar, V., **Biodistribution, clearance, and biocompatibility of iron oxide magnetic nanoparticles in rats.** *Mol. Pharmaceutics* **2008,** *5*, 316-327.

38. Fayad, Z. A.; Fuster, V.; Fallon, J. T.; Jayasundera, T.; Worthley, S. G.; Helft, G.; Aguinaldo, J. G.; Badimon, J. J.; Sharma, S. K., **Noninvasive *in vivo* human coronary artery lumen and wall imaging using black-blood magnetic resonance imaging.** *Circulation* **2000,** *102*, 506-10.

39. Yasuda, S.; Ikuta, K.; Uwatoku, T.; Oi, K.; Abe, K.; Hyodo, F.; Yoshimitsu, K.; Sugimura, K.; Utsumi, H.; Katayama, Y.; Shimokawa, H., ***In vivo* magnetic resonance imaging of atherosclerotic lesions with a newly developed evans blue-DTPA-Gadolinium contrast medium in apolipoprotein-E-deficient mice.** *J. Vasc. Res.* **2008,** *45*, 123-128.

40. Pan, D.; Caruthers Shelton, D.; Hu, G.; Senpan, A.; Scott Mike, J.; Gaffney Patrick, J.; Wickline Samuel, A.; Lanza Gregory, M., **Ligand-directed nanobialys as theranostic agent for drug delivery and manganese-based magnetic resonance imaging of vascular targets.** *J. Am. Chem. Soc.* **2008,** *130*, 9186-7.

41. Lanza, G. M.; Wallace, K. D.; Scott, M. J.; Cacheris, W. P.; Abendschein, D. R.; Christy, D. H.; Sharkey, A. M.; Miller, J. G.; Gaffney, P. J.; Wickline, S. A., **A novel site-targeted ultrasonic contrast agent with broad biomedical application.** *Circulation* **1996,** *94*, 3334-3340.

42. Yu, M. K.; Jeong, Y. Y.; Park, J.; Park, S.; Kim, J. W.; Min, J. J.; Kim, K.; Jon, S., **Drug-loaded superparamagnetic iron oxide nanoparticles for combined cancer imaging and therapy in vivo.** *Angew. Chem., Int. Ed.* **2008,** *47*, 5362-5365.

43. Frias, J. C.; Lipinski, M. J.; Albelda, M. T.; Ibanez, B.; Soriano, C.; Garcia-Espana, E.; Jimenez-Borreguero, L. J.; Badimon, J. J., **Nanoparticles as contrast agents for MRI of atherosclerotic lesions.** *Clin. Med.: Cardiol.* **2008,** *2*, 173-179.

44. Thorek Daniel, L. J.; Chen Antony, K.; Czupryna, J.; Tsourkas, A., **Superparamagnetic iron oxide nanoparticle probes for molecular imaging.** *Ann. Biomed. Eng.* **2006,** *34*, 23-38.

45. Weissleder, R.; Elizondo, G.; Wittenberg, J.; Rabito, C. A.; Bengele, H. H.; Josephson, L., **Ultrasmall superparamagnetic iron oxide: characterization of a new class of contrast agents for MR imaging.** *Radiology* **1990,** *175*, 489-93.

46. Smith Bryan, R.; Heverhagen, J.; Knopp, M.; Schmalbrock, P.; Shapiro, J.; Shiomi, M.; Moldovan Nicanor, I.; Ferrari, M.; Lee Stephen, C., **Localization to atherosclerotic plaque and biodistribution of biochemically derivatized superparamagnetic iron oxide nanoparticles (SPIONs) contrast particles for magnetic resonance imaging (MRI).** *Biomed. Microdevices* **2007,** *9*, 719-27.

47. Qiao, R.; Yang, C.; Gao, M., **Superparamagnetic iron oxide nanoparticles: from preparations to in vivo MRI applications.** *J. Mater. Chem.* **2009,** *19*, 6274-6293.

48. Josephson, L.; Perez, J. M.; Weissleder, R., **Magnetic nanosensors for the detection of oligonucleotide sequences.** *Angew. Chem., Int. Ed.* **2001,** *40*, 3204-3206.

49. Josephson, L.; Tung, C.-H.; Moore, A.; Weissleder, R., **High-efficiency intracellular magnetic labeling with novel superparamagnetic-Tat peptide conjugates.** *Bioconjugate Chem.* **1999,** *10*, 186-191.

50. Perez, J. M.; Simeone, F. J.; Saeki, Y.; Josephson, L.; Weissleder, R., **Viral-induced self-assembly of magnetic nanoparticles allows the detection of viral particles in biological media.** *J. Am. Chem. Soc.* **2003,** *125*, 10192-10193.

51. Tsourkas, A.; Hofstetter, O.; Hofstetter, H.; Weissleder, R.; Josephson, L., **Magnetic relaxation switch immunosensors detect enantiomeric impurities.** *Angew. Chem., Int. Ed.* **2004,** *43*, 2395-2399.

52. Nahrendorf, M.; Jaffer, F. A.; Kelly, K. A.; Sosnovik, D. E.; Aikawa, E.; Libby, P.; Weissleder, R., **Noninvasive vascular cell adhesion molecule-1**

imaging identifies inflammatory activation of cells in atherosclerosis. *Circulation* **2006,** *114*, 1504-1511.

53. McCarthy, J. R.; Jaffer, F. A.; Weissleder, R., **A macrophage-targeted theranostic nanoparticle for biomedical applications.** *Small* **2006,** *2*, 983-987.

54. Kang, H. W.; Torres, D.; Wald, L.; Weissleder, R.; Bogdanov, A. A., **Targeted imaging of human endothelial-specific marker in a model of adoptive cell transfer.** *Lab. Invest.* **2006,** *86*, 599-609.

55. Kelly, K. A.; Allport, J. R.; Tsourkas, A.; Shinde-Patil, V. R.; Josephson, L.; Weissleder, R., **Detection of vascular adhesion molecule-1 expression using a novel multimodal nanoparticle.** *Circ. Res.* **2005,** *96*, 327-336.

56. Schellenberger, E. A.; Bogdanov, A., Jr.; Hogemann, D.; Tait, J.; Weissleder, R.; Josephson, L., **Annexin V-CLIO: A nanoparticle for detecting apoptosis by MRI.** *Mol. Imaging* **2002,** *1*, 102-107.

57. Choudhury, R. P.; Aguinaldo, J. G.; Rong, J. X.; Kulak, J. L.; Kulak, A. R.; Reis, E. D.; Fallon, J. T.; Fuster, V.; Fisher, E. A.; Fayad, Z. A., **Atherosclerotic lesions in genetically modified mice quantified in vivo by non-invasive high-resolution magnetic resonance microscopy.** *Atherosclerosis* **2002,** *162*, 315-321.

58. Hockings, P. D.; Roberts, T.; Galloway, G. J.; Reid, D. G.; Harris, D. A.; Vidgeon-Hart, M.; Groot, P. H. E.; Suckling, K. E.; Benson, G. M., **Repeated three-dimensional magnetic resonance imaging of atherosclerosis development in innominate arteries of low-density lipoprotein receptor-knockout mice.** *Circulation* **2002,** *106*, 1716-1721.

59. Fayad, Z. A.; Fuster, V., **Characterization of atherosclerotic plaques by magnetic resonance imaging.** *Ann. N. Y. Acad. Sci.* **2000,** *902*, 173-86.

60. Moore, A.; Weissleder, R.; Bogdanov, A., Jr., **Uptake of dextran-coated monocrystalline iron oxides in tumor cells and macrophages.** *J. Magn. Reson. Imaging* **1997,** *7*, 1140-5.

61. Muller, K.; Skepper, J. N.; Tang, T. Y.; Graves, M. J.; Patterson, A. J.; Corot, C.; Lancelot, E.; Thompson, P. W.; Brown, A. P.; Gillard, J. H., **Atorvastatin and uptake of ultrasmall superparamagnetic iron oxide nanoparticles (Ferumoxtran-10) in human monocyte-macrophages: Implications for magnetic resonance imaging.** *Biomaterials* **2008,** *29*, 2656-2662.

62. Kooi, M. E.; Cappendijk, V. C.; Cleutjens, K. B. J. M.; Kessels, A. G. H.; Kitslaar, P. J. E. H. M.; Borgers, M.; Frederik, P. M.; Daemen, M. J. A. P.; van Engelshoven, J. M. A., **Accumulation of ultrasmall superparamagnetic**

particles of iron oxide in human atherosclerotic plaques can be detected by *in vivo* magnetic resonance imaging. *Circulation* **2003,** *107*, 2453-2458.

63. Litovsky, S.; Madjid, M.; Zarrabi, A.; Casscells, S. W.; Willerson James, T.; Naghavi, M., **Superparamagnetic iron oxide-based method for quantifying recruitment of monocytes to mouse atherosclerotic lesions in vivo: enhancement by tissue necrosis factor-alpha, interleukin-1beta, and interferon-gamma.** *Circulation* **2003,** *107*, 1545-9.

64. Sharma, R.; Kwon, S., **New applications of nanoparticles in cardiovascular imaging.** *J. Exp. Nanosci.* **2007,** *2*, 115-126.

65. Tartaj, P.; Morales, M. d. P.; Veintemillas-Verdaguer, S.; Gonzalez-Carreno, T.; Serna, C. J., **The preparation of magnetic nanoparticles for applications in biomedicine.** *J. Phys. D: Appl. Phys.* **2003,** *36*, R182-R197.

66. Lu, A. H.; Salabas, E. L.; Schueth, F., **Magnetic nanoparticles: Synthesis, protection, functionalization, and application.** *Angew. Chem., Int. Ed.* **2007,** *46*, 1222-1244.

67. Pittet, M. J.; Swirski, F. K.; Reynolds, F.; Josephson, L.; Weissleder, R., **Labeling of immune cells for in vivo imaging using magnetofluorescent nanoparticles.** *Nat. Protoc.* **2006,** *1*, 73-79.

68. Palmacci, S.; Josephson, L.; Groman, E. V. Synthesis of polymer-covered superparamagnetic oxide colloids for magnetic resonance contrast agents or other applications. 93-US7682-9505669, 1995.

69. Bergman, K.; Elvingson, C.; Hilborn, J.; Svensk, G.; Bowden, T., **Hyaluronic acid derivatives prepared in aqueous media by triazine-activated amidation.** *Biomacromolecules* **2007,** *8*, 2190-2195.

70. Libby, P., **Inflammation in atherosclerosis.** *Nature* **2002,** *420*, 868-874.

71. Moreno, P. R.; Falk, E.; Palacios, I. F.; Newell, J. B.; Fuster, V.; Fallon, J. T., **Macrophage infiltration in acute coronary syndromes. Implications for plaque rupture.** *Circulation* **1994,** *90*, 775-8.

72. Schmitz, S. A.; Coupland, S. E.; Gust, R.; Winterhalter, S.; Wagner, S.; Kresse, M.; Semmler, W.; Wolf, K. J., **Superparamagnetic iron oxide-enhanced MRI of atherosclerotic plaques in Watanabe hereditable hyperlipidemic rabbits.** *Invest. Radiol.* **2000,** *35*, 460-71.

73. Berry, C. C.; Curtis, A. S. G., **Functionalisation of magnetic nanoparticles for applications in biomedicine.** *J. Phys. D: Appl. Phys.* **2003,** *36*, R198-R206.

74. Berry, C. C.; Wells, S.; Charles, S.; Curtis, A. S. G., **Dextran and albumin derivatized iron oxide nanoparticles: influence on fibroblasts in vitro.** *Biomaterials* **2003,** *24*, 4551-4557.

75. Sun, C.; Veiseh, O.; Gunn, J.; Fang, C.; Hansen, S.; Lee, D.; Sze, R.; Ellenbogen, R. G.; Olson, J.; Zhang, M., ***In vivo*** **MRI detection of gliomas by chlorotoxin-conjugated superparamagnetic nanoprobes.** *Small* **2008,** *4*, 372-379.

76. Zhang, C.; Jugold, M.; Woenne, E. C.; Lammers, T.; Morgenstern, B.; Mueller, M. M.; Zentgraf, H.; Bock, M.; Eisenhut, M.; Semmler, W.; Kiessling, F., **Specific targeting of tumor angiogenesis by RGD-conjugated ultrasmall superparamagnetic iron oxide particles using a clinical 1.5-T magnetic resonance scanner.** *Cancer Res.* **2007,** *67*, 1555-1562.

77. Abela, G. S.; Picon, P. D.; Friedl, S. E.; Gebara, O. C.; Miyamoto, A.; Federman, M.; Tofler, G. H.; Muller, J. E., **Triggering of plaque disruption and arterial thrombosis in an atherosclerotic rabbit model.** *Circulation* **1995,** *91*, 776-84.

78. Aziz, K.; Berger, K.; Claycombe, K.; Huang, R.; Patel, R.; Abela George, S., **Noninvasive detection and localization of vulnerable plaque and arterial thrombosis with computed tomography angiography/positron emission tomography.** *Circulation* **2008,** *117*, 2061-70.

Appendices

Supplementary Materials

A.1. NMR spectra for Chapter 2

^{1}H-NMR ($CDCl_3$, 600 MHz)

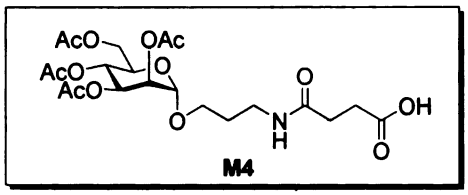

M4

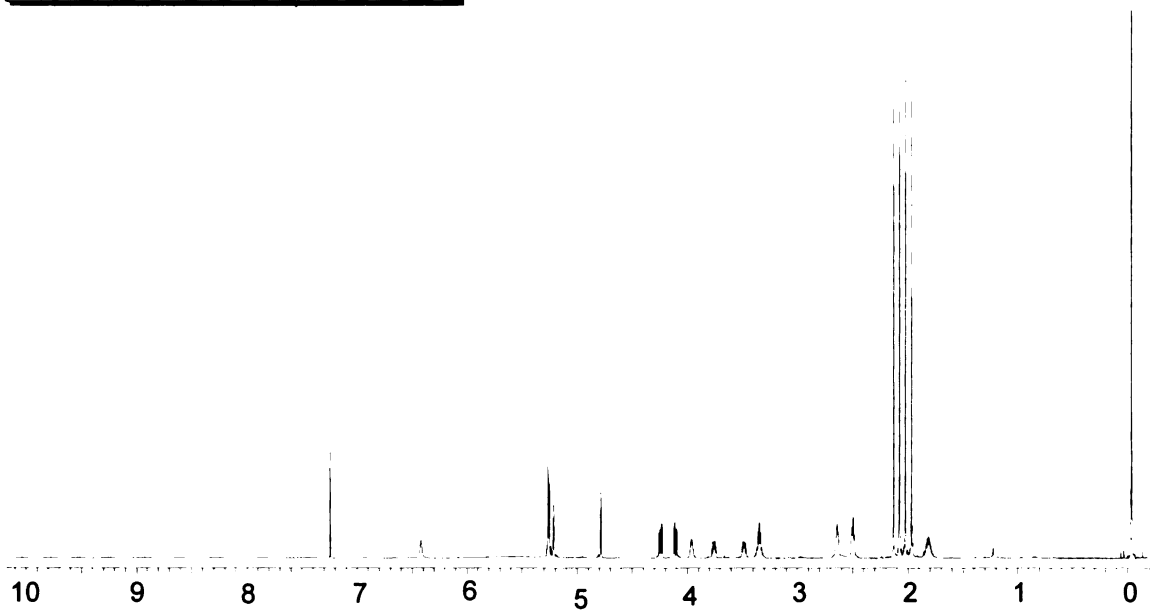

^{13}C-NMR ($CDCl_3$, 100 MHz)

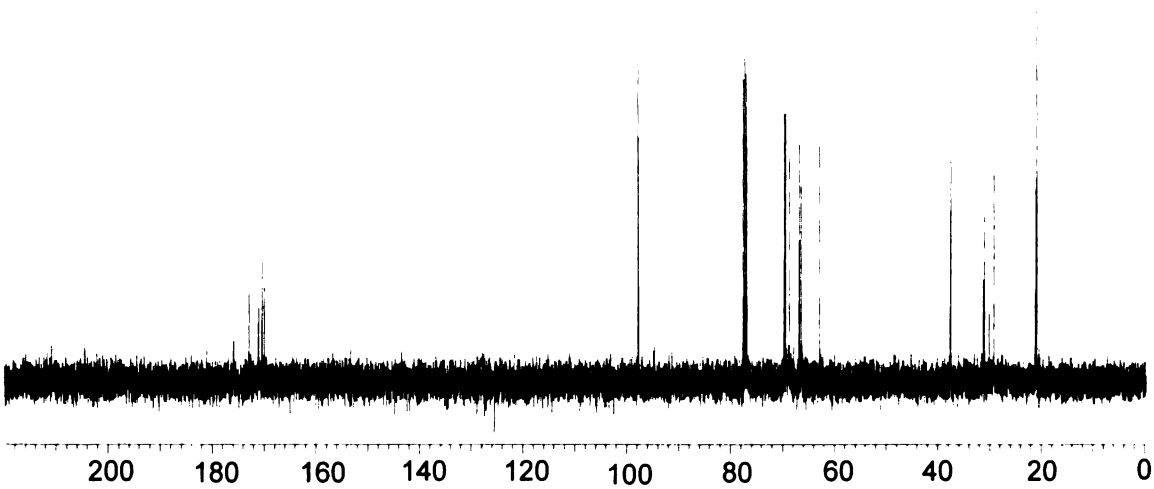

^{1}H-NMR (CD_3OD, 600 MHz)

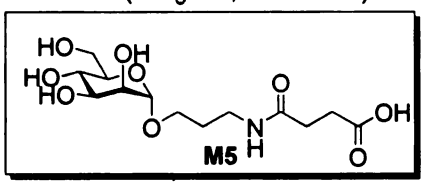

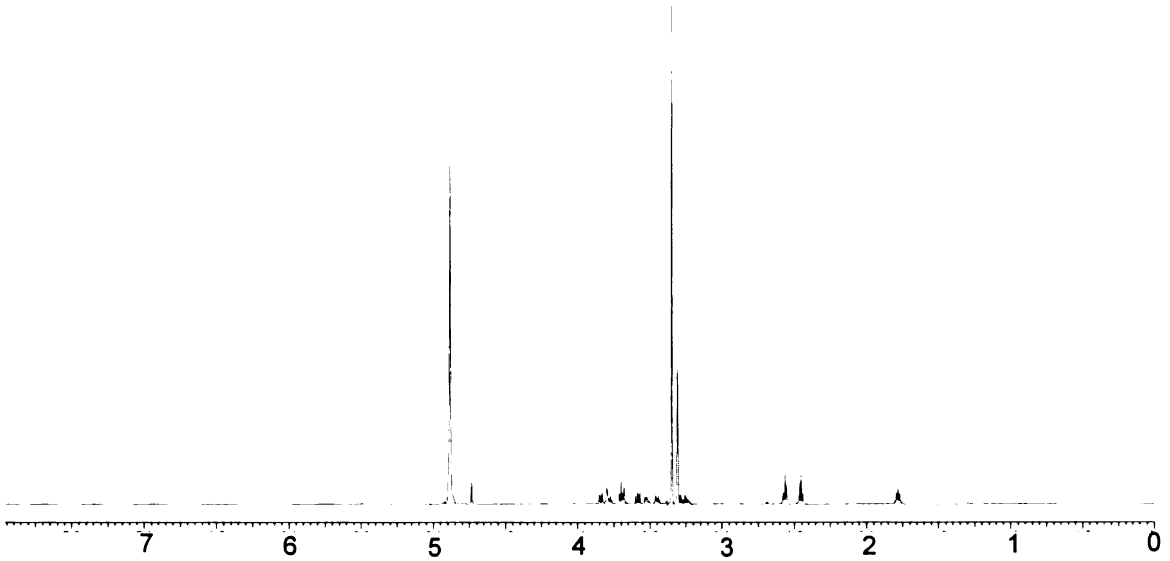

^{13}C-NMR (CD_3OD, 100 MHz)

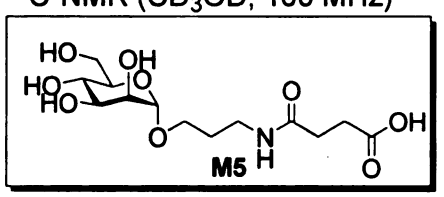

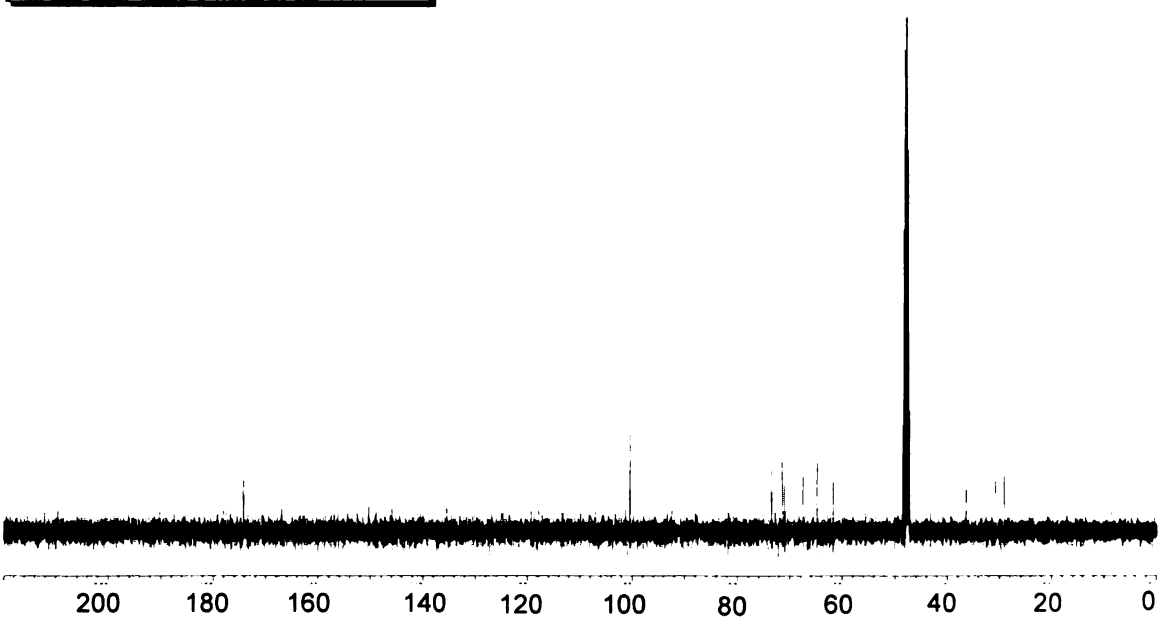

^{1}H-NMR (CD_3OD, 600 MHz)

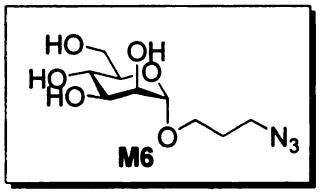

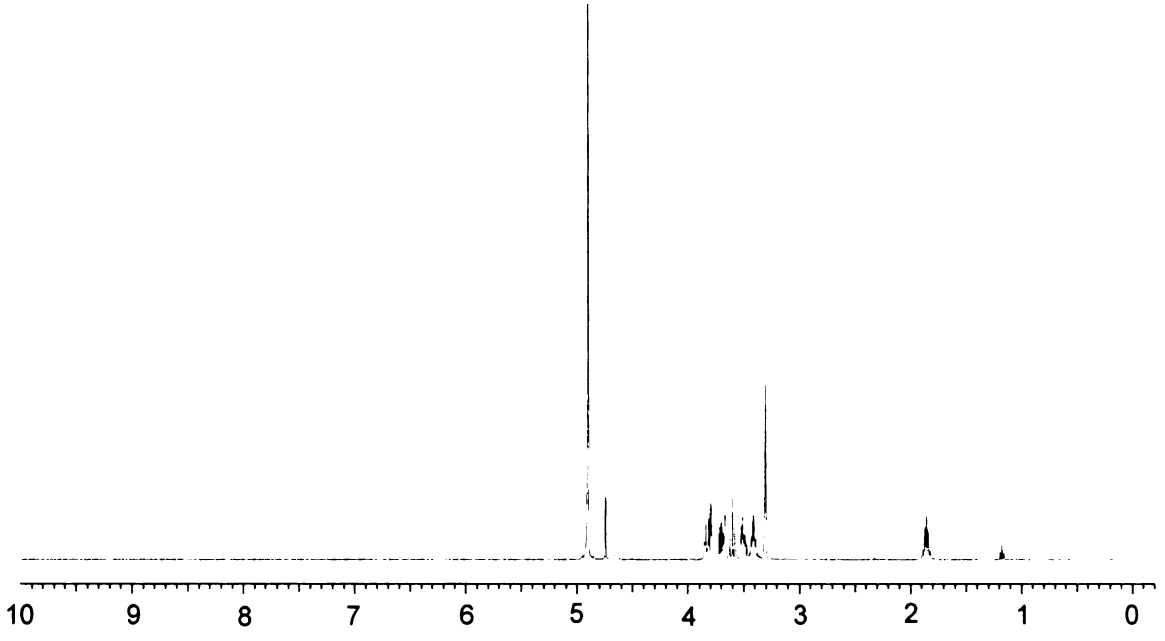

^{13}C-NMR (CD_3OD, 100 MHz)

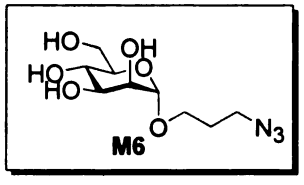

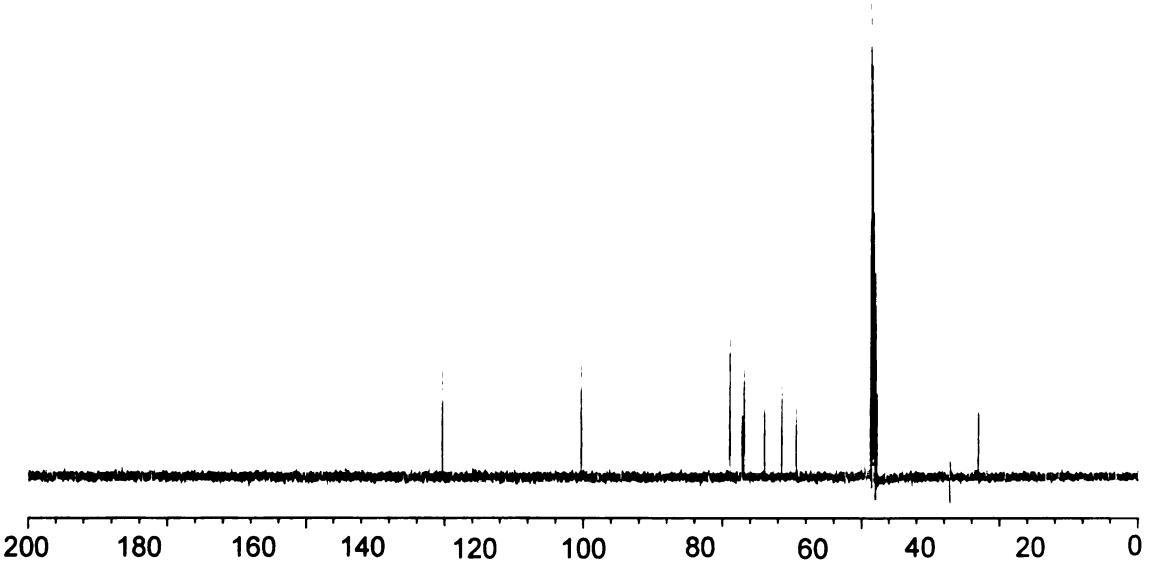

^{1}H-NMR ($CDCl_3$, 600 MHz)

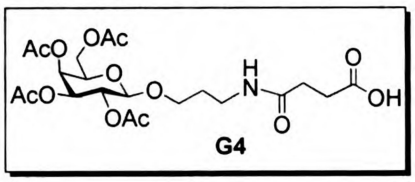

G4

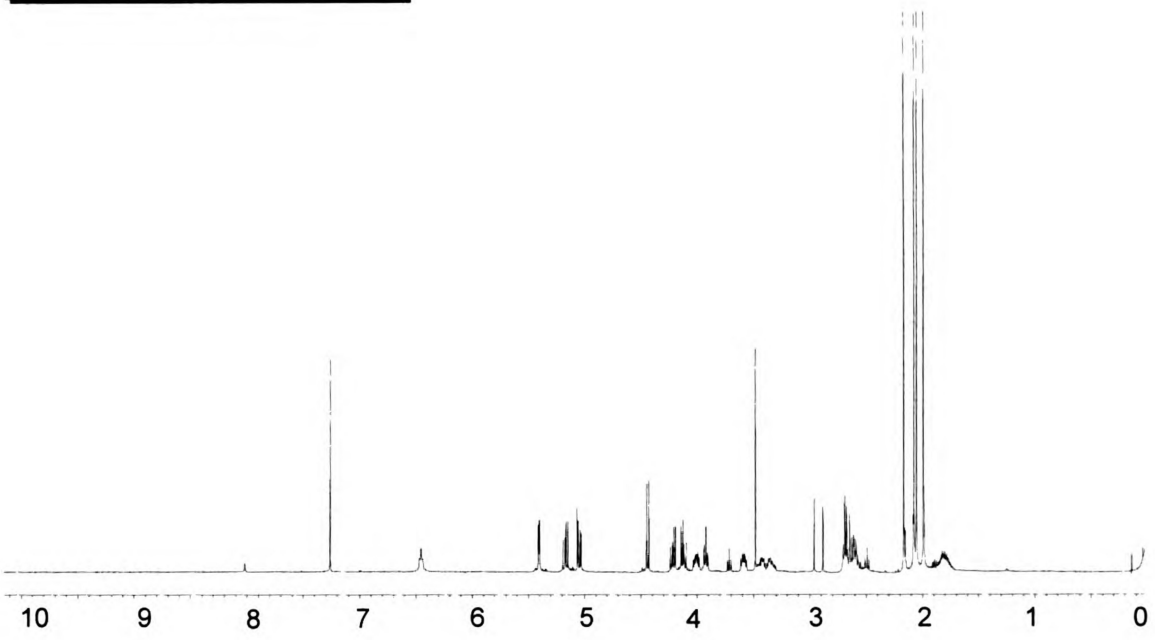

^{13}C-NMR ($CDCl_3$, 100 MHz)

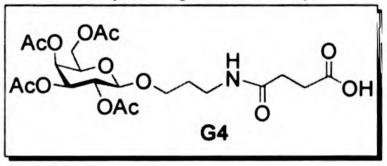

G4

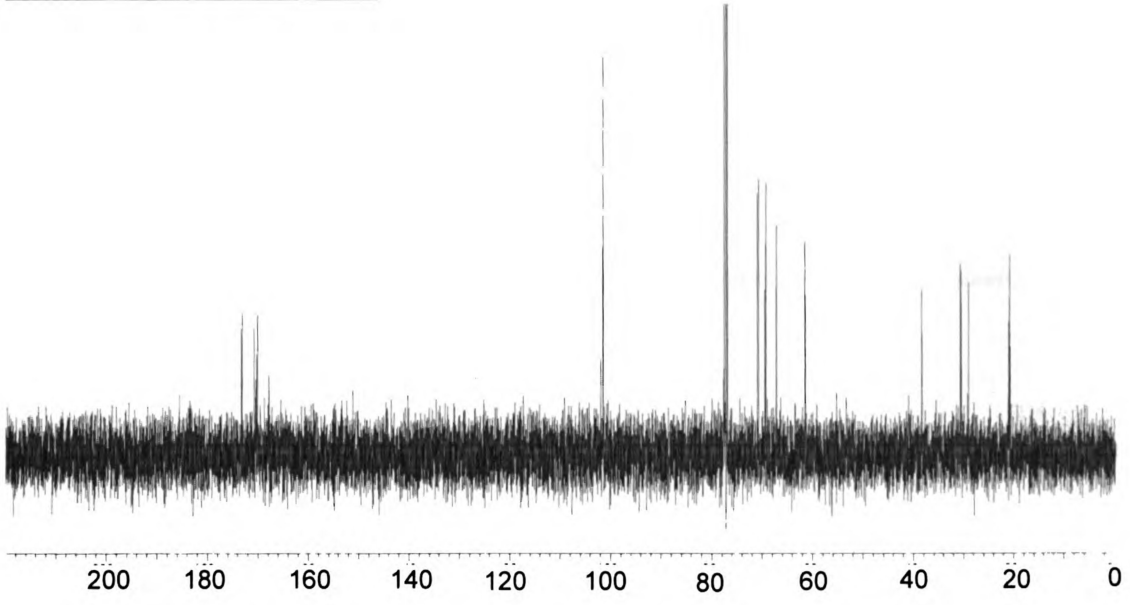

^{1}H-NMR (CD_3OD, 600 MHz)

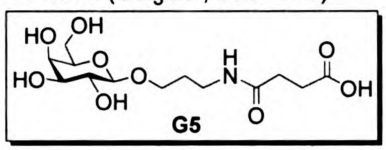

G5

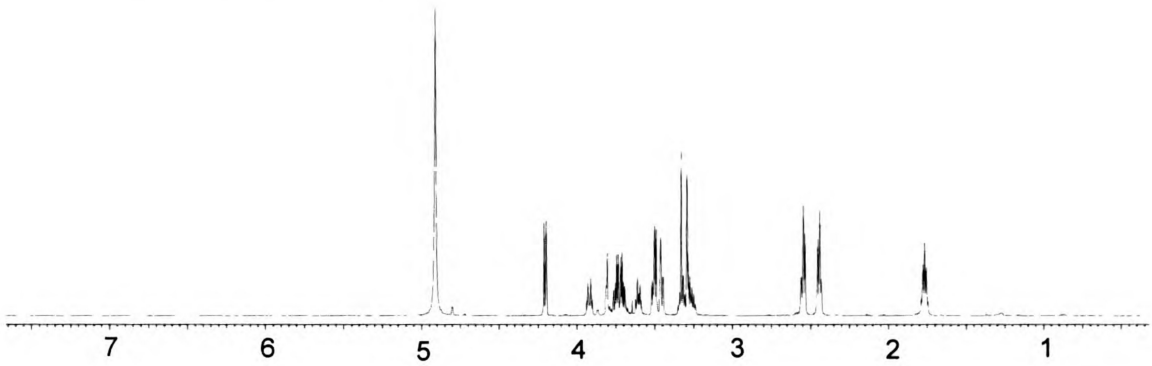

^{13}C-NMR (CD_3OD, 100 MHz)

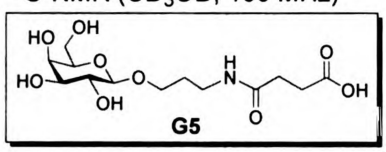

G5

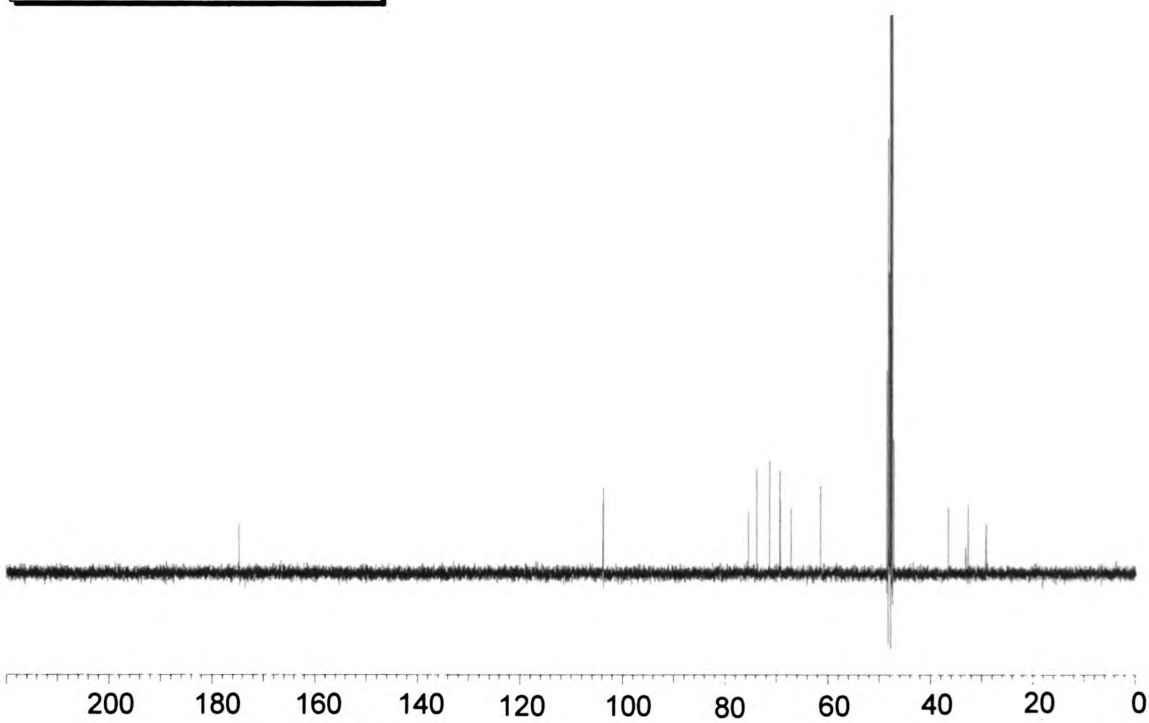

^{1}H-NMR ($CDCl_3$, 600 MHz)

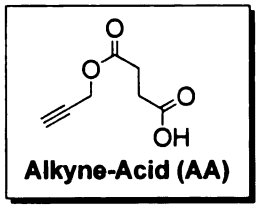

Alkyne-Acid (AA)

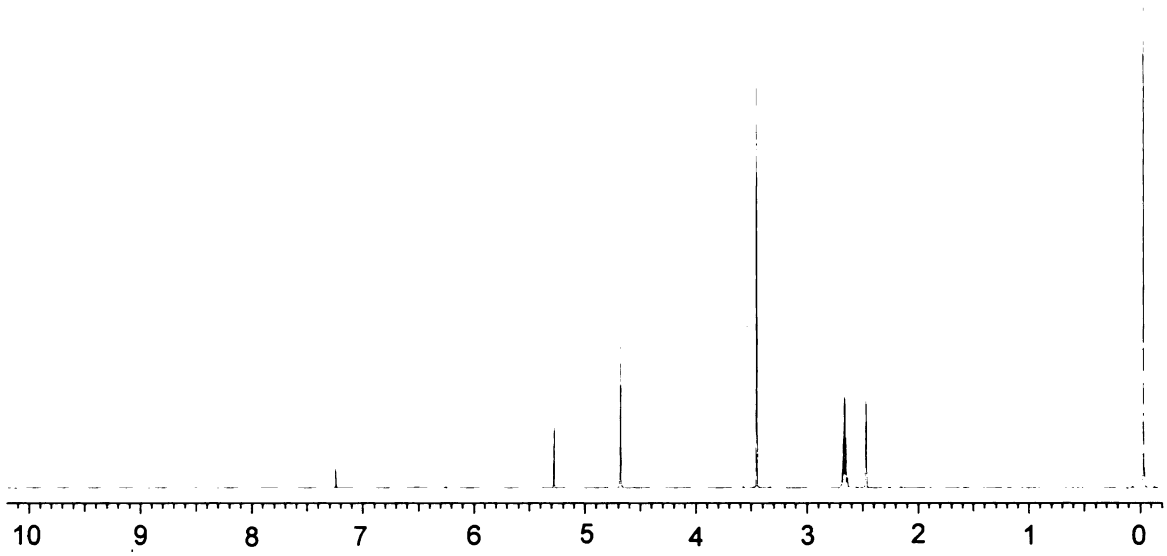

^{13}C-NMR ($CDCl_3$, 100 MHz)

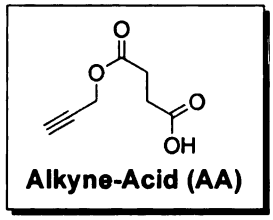

Alkyne-Acid (AA)

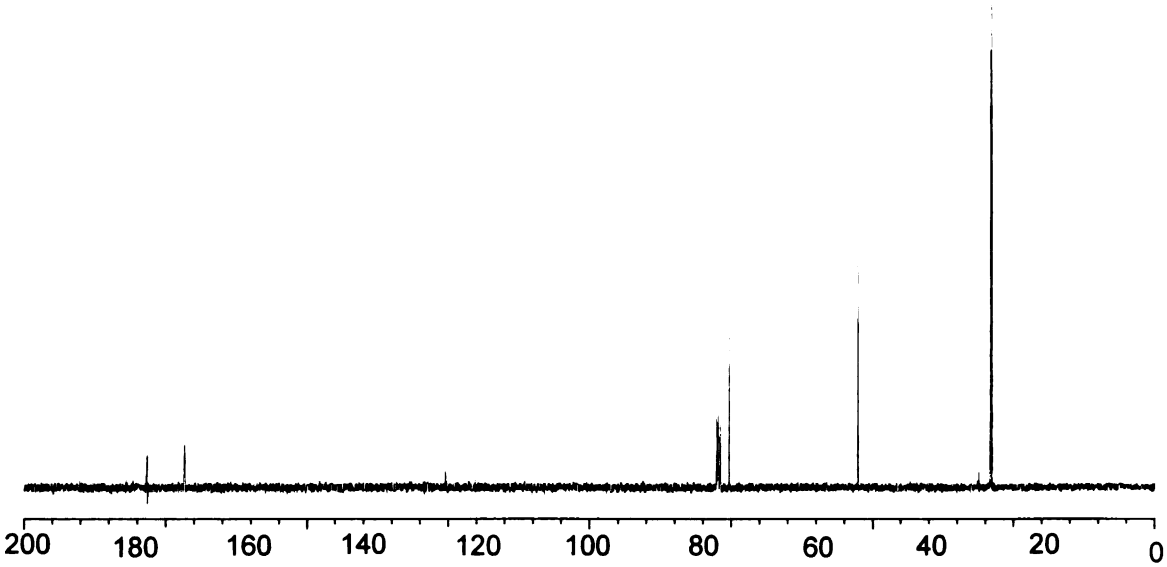

^{1}H-NMR ($CDCl_3$, 600 MHz)

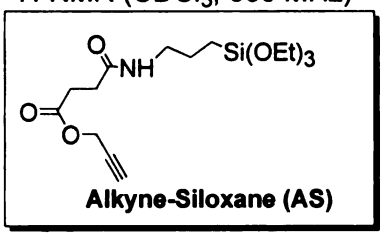

Alkyne-Siloxane (AS)

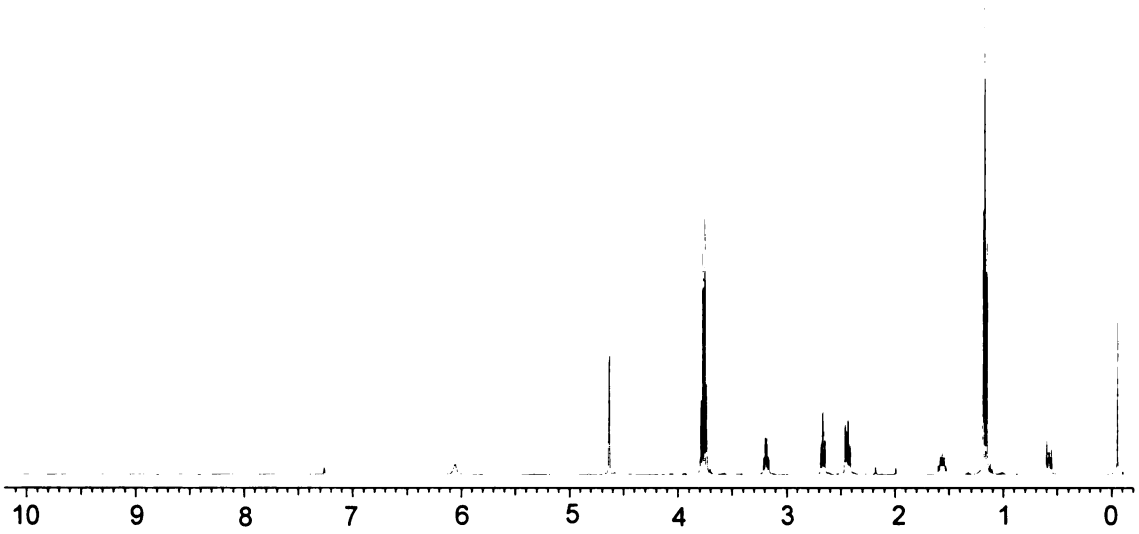

^{13}C-NMR ($CDCl_3$, 100 MHz)

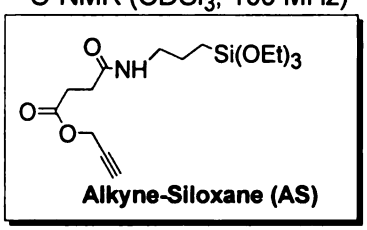

Alkyne-Siloxane (AS)

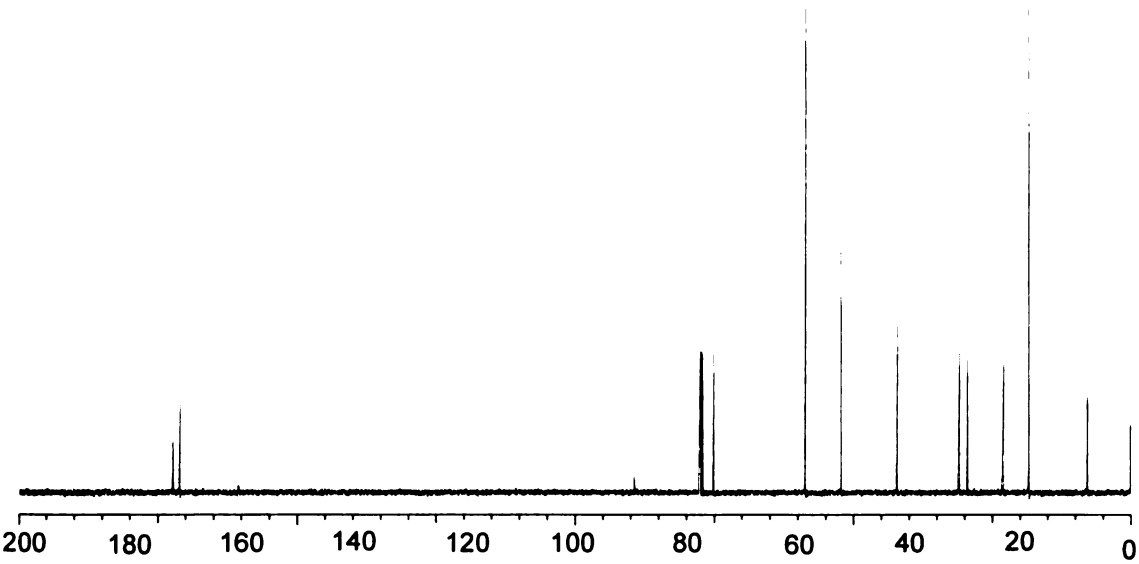

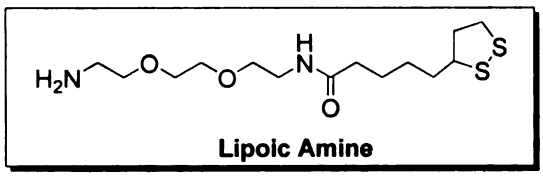

Lipoic Amine

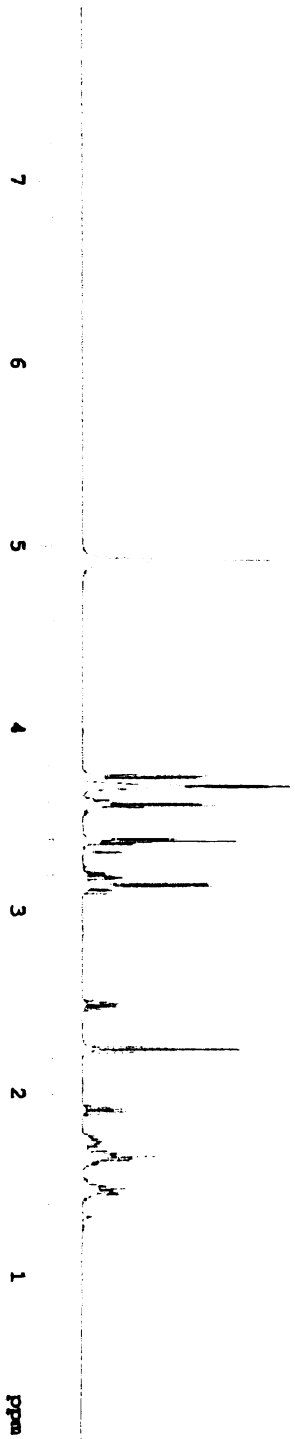

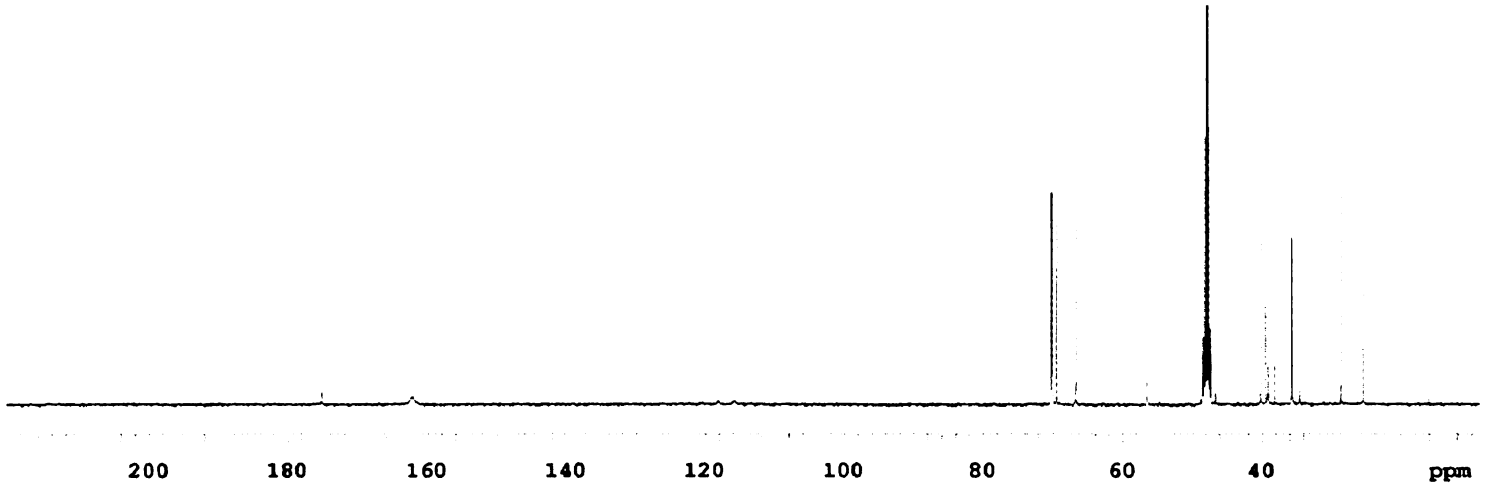
200
180
160
140
120
100
80
60
40
ppm

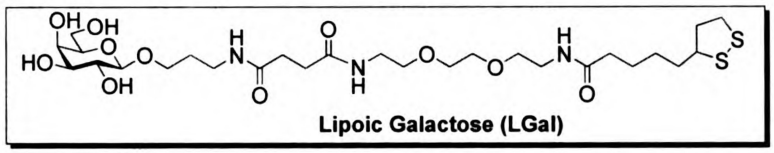

Lipoic Galactose (LGal)

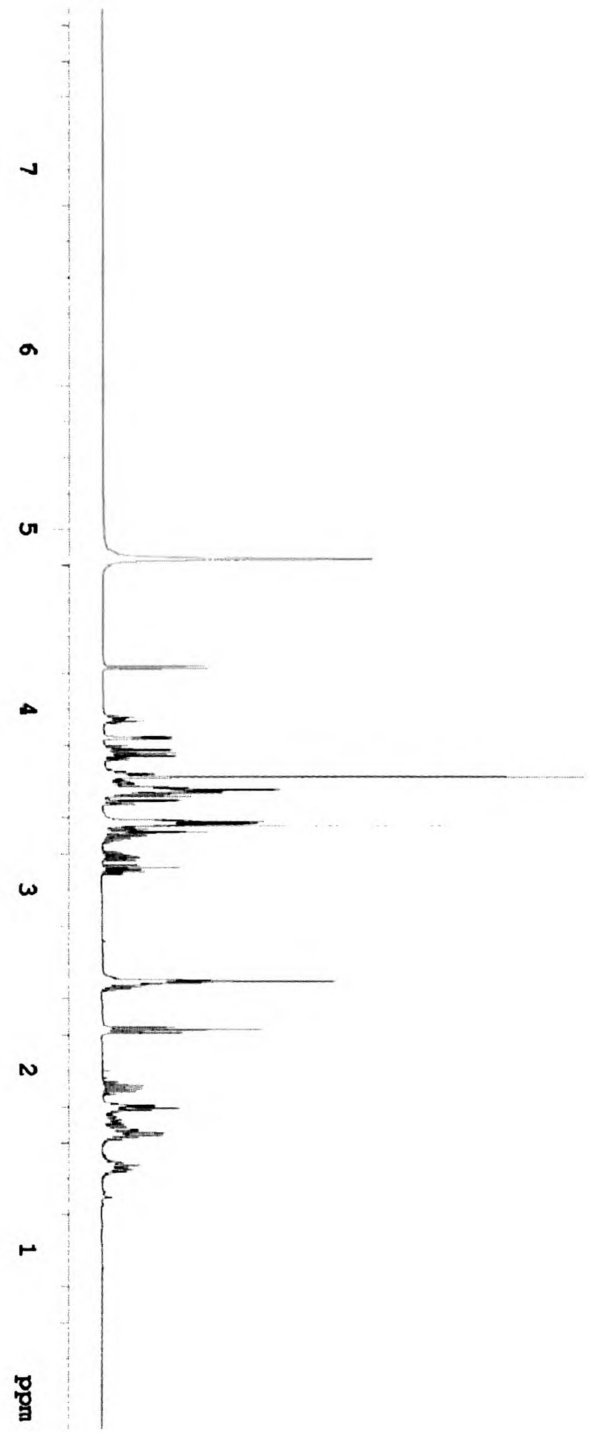

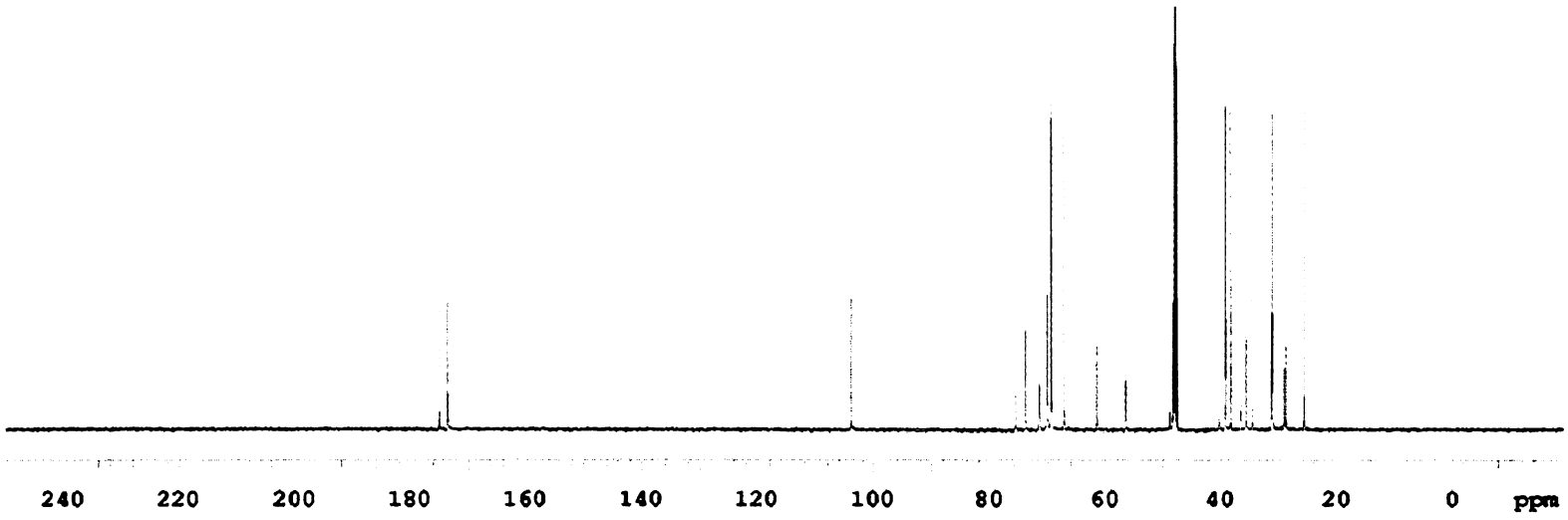
240
220
200
180
160
140
120
100
80
60
40
20
0
ppm

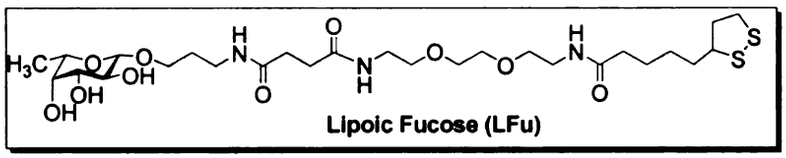
Lipoic Fucose (LFu)

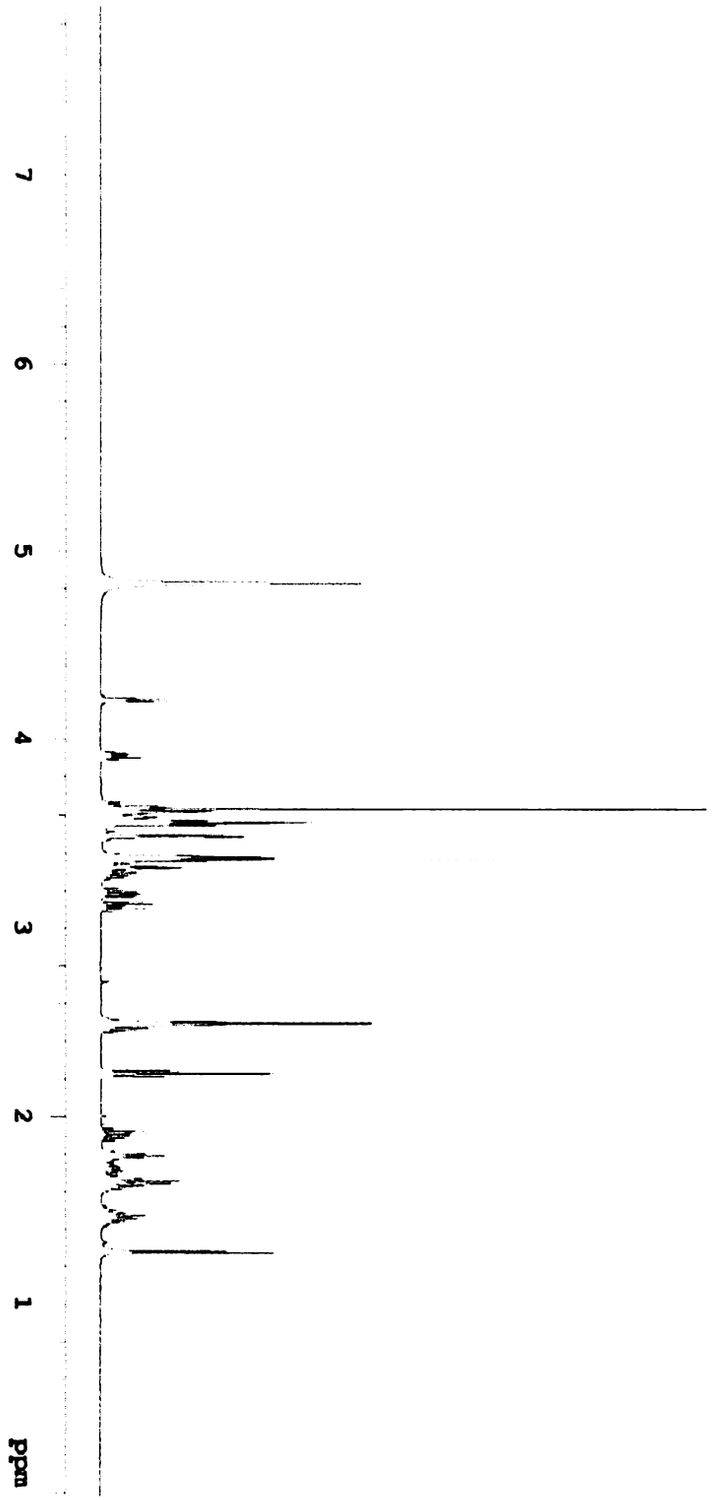
7
6
5
4
3
2
1
ppm

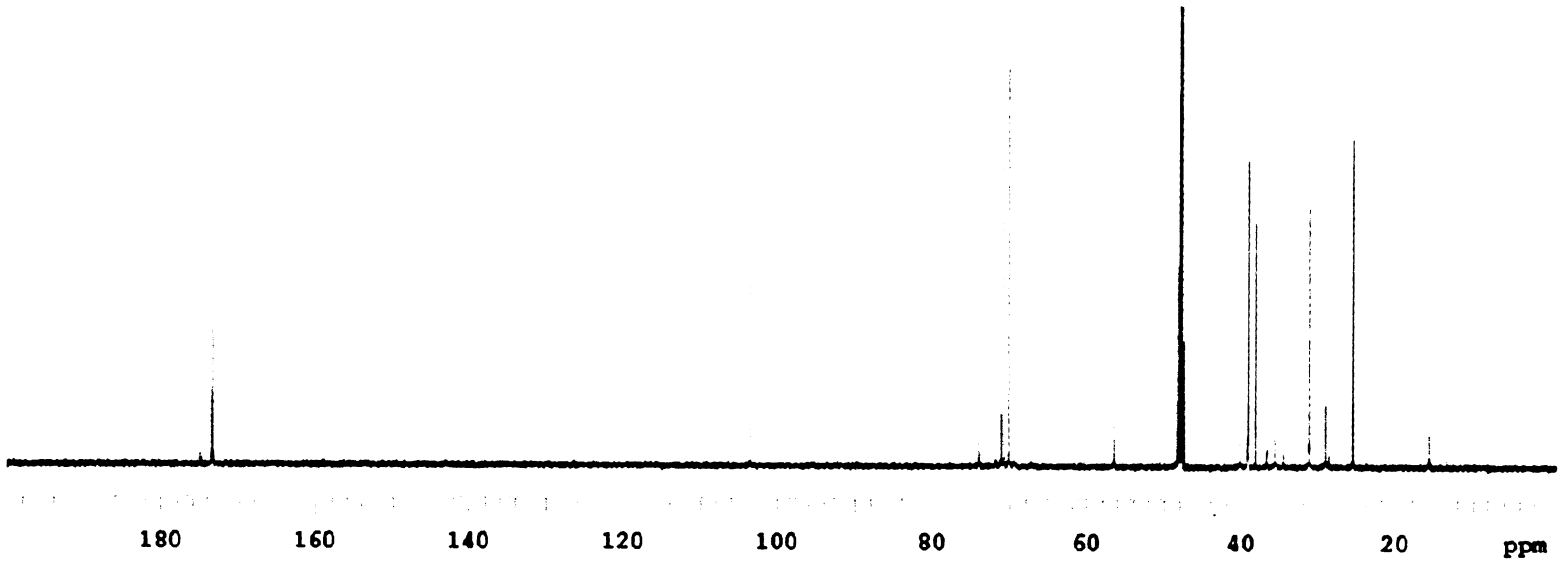
180
160
140
120
100
80
60
40
20
ppm

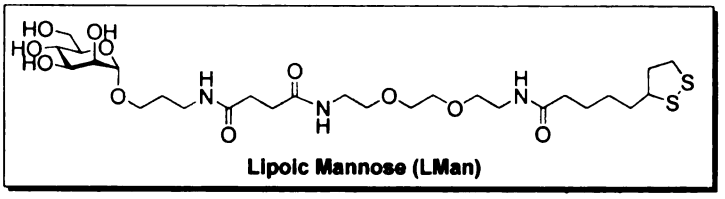

Lipoic Mannose (LMan)

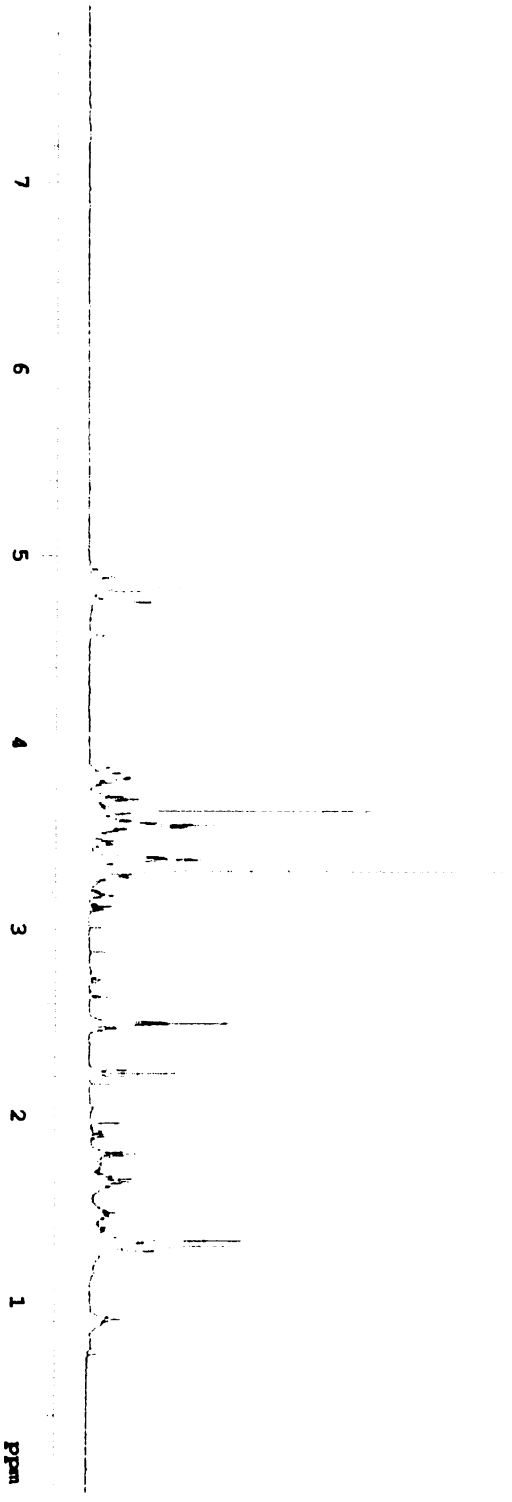

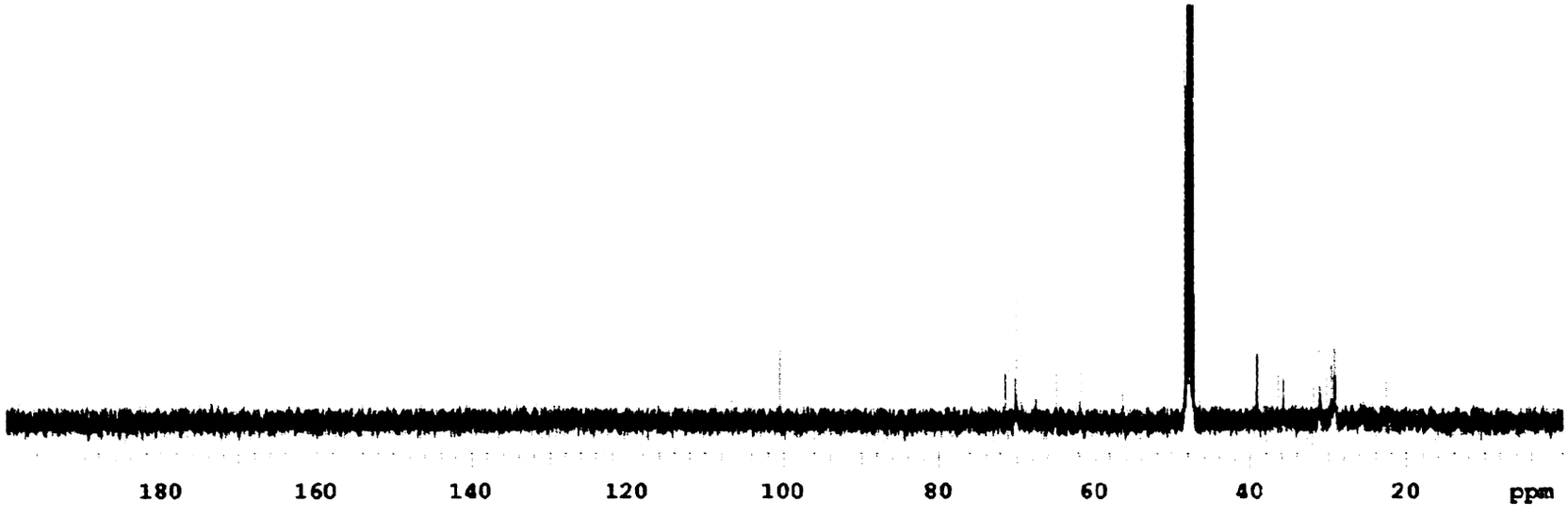
180
160
140
120
100
80
60
40
20
ppm

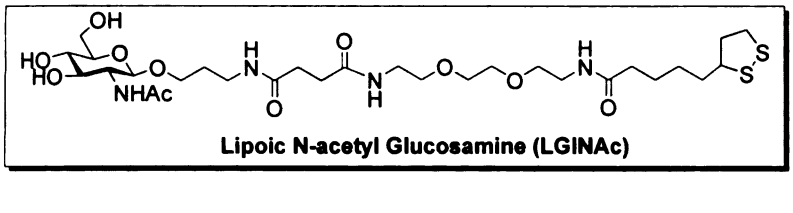

Lipoic N-acetyl Glucosamine (LGINAc)

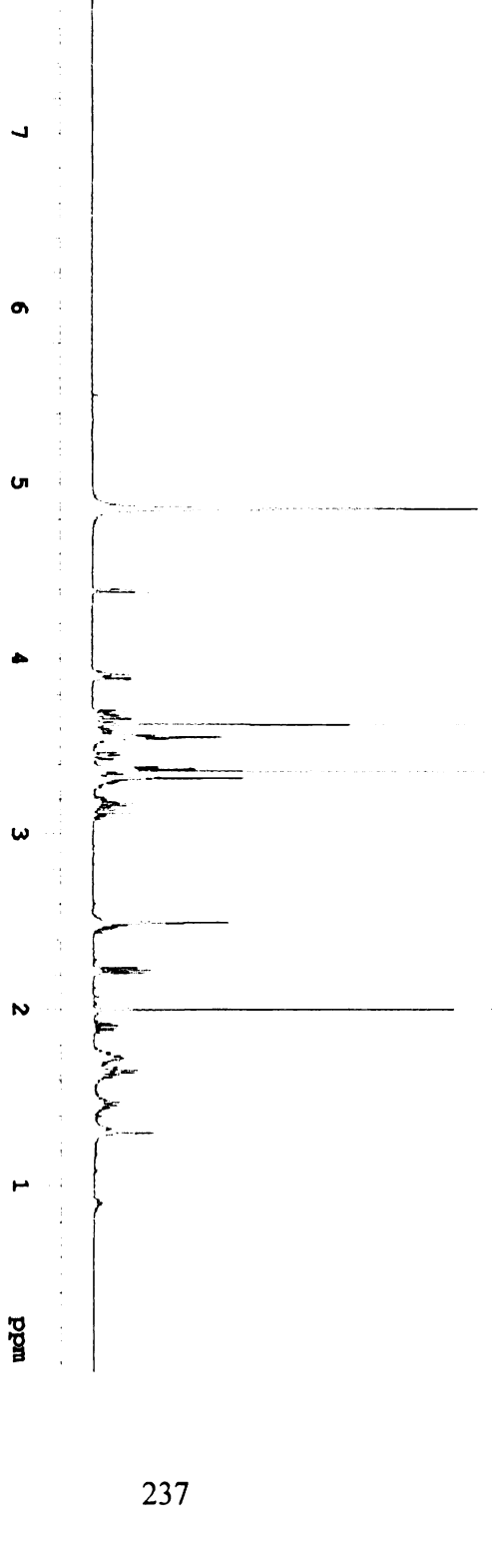

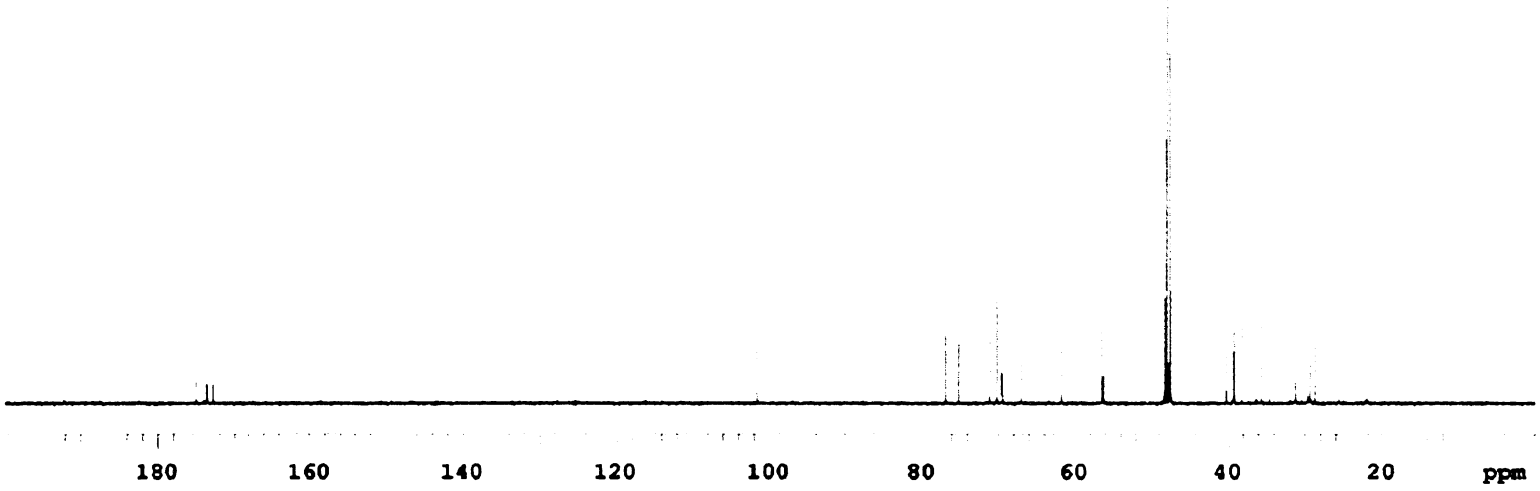
180
160
140
120
100
80
60
40
20
ppm

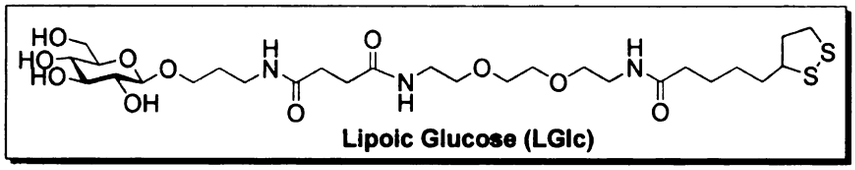

Lipoic Glucose (LGlc)

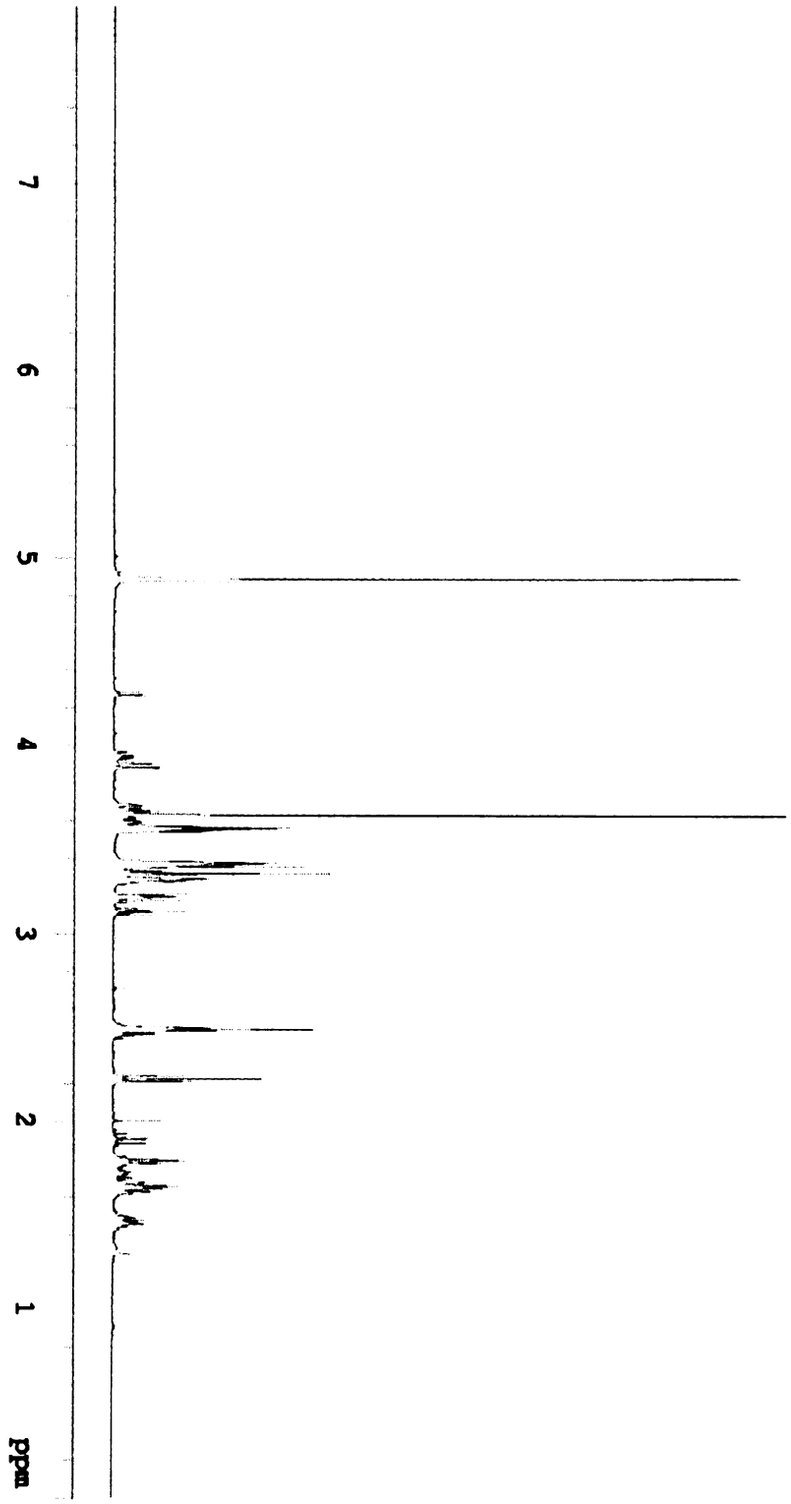

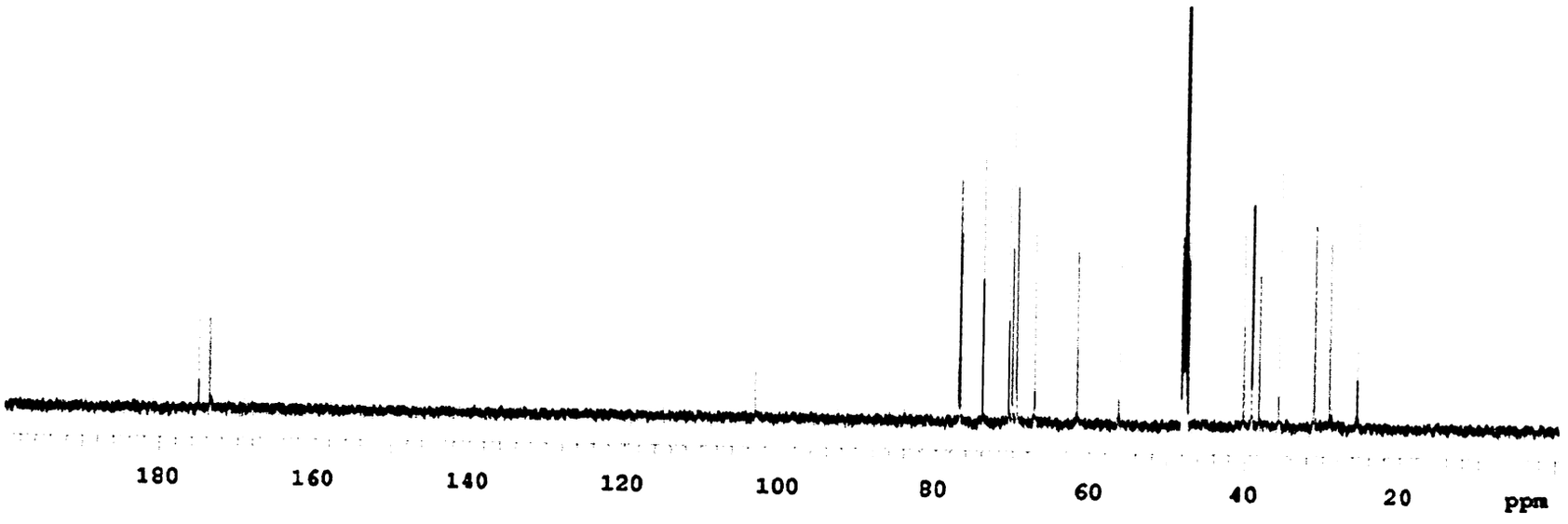
180
160
140
120
100
80
60
40
20
ppm

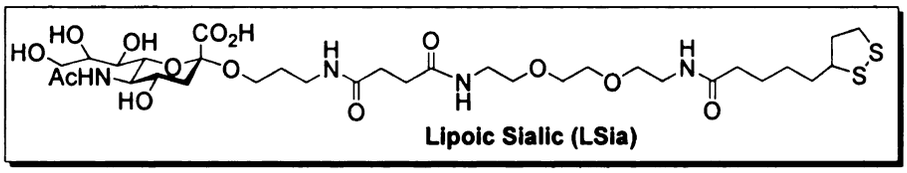

Lipoic Sialic (LSia)

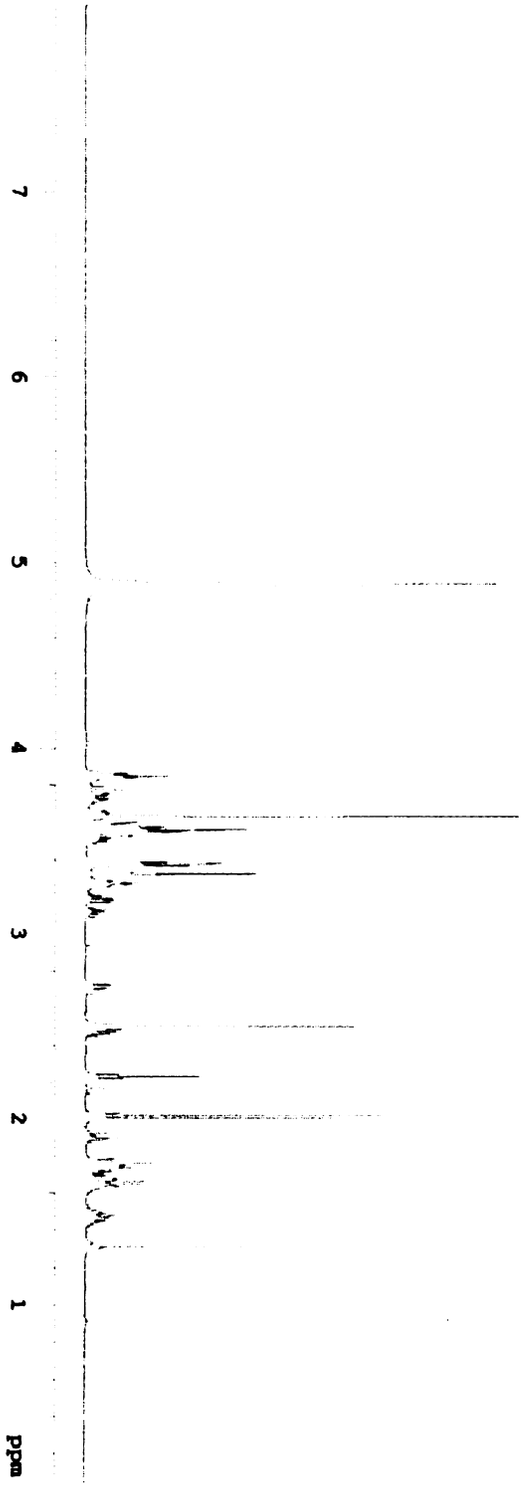

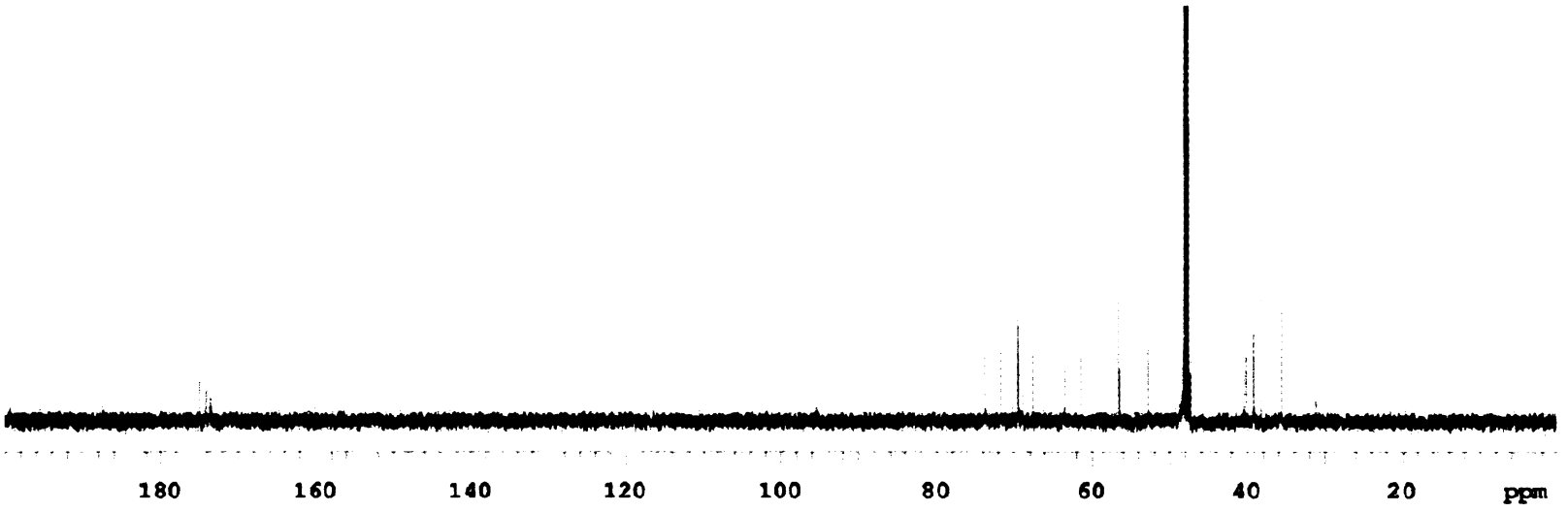
180
160
140
120
100
80
60
40
20
ppm

A.2. NMR spectra for Chapter 3

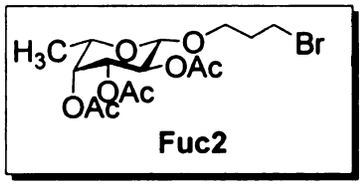

Fuc2

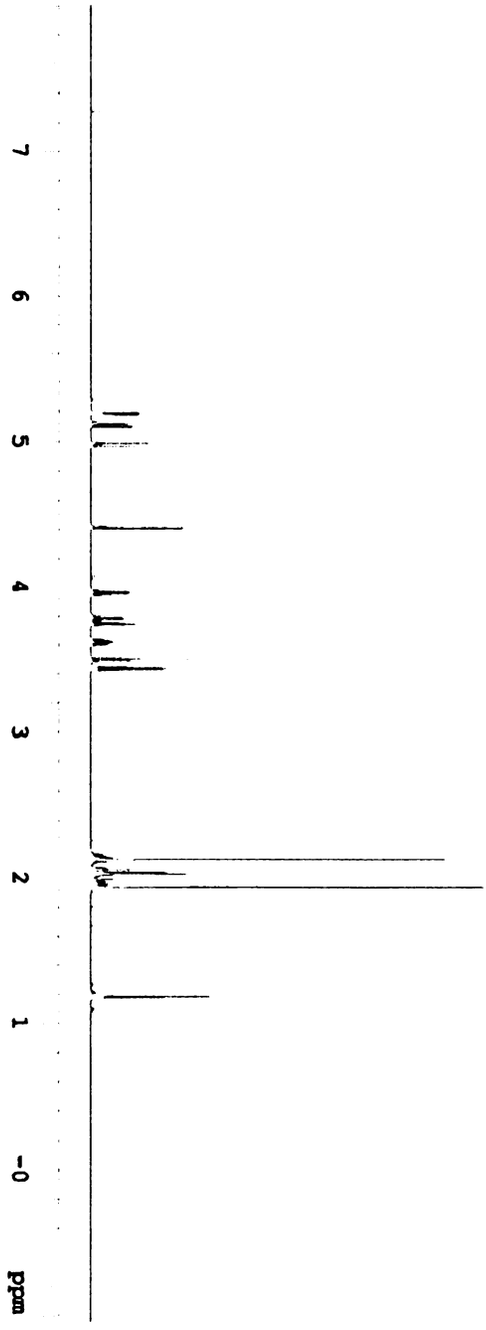

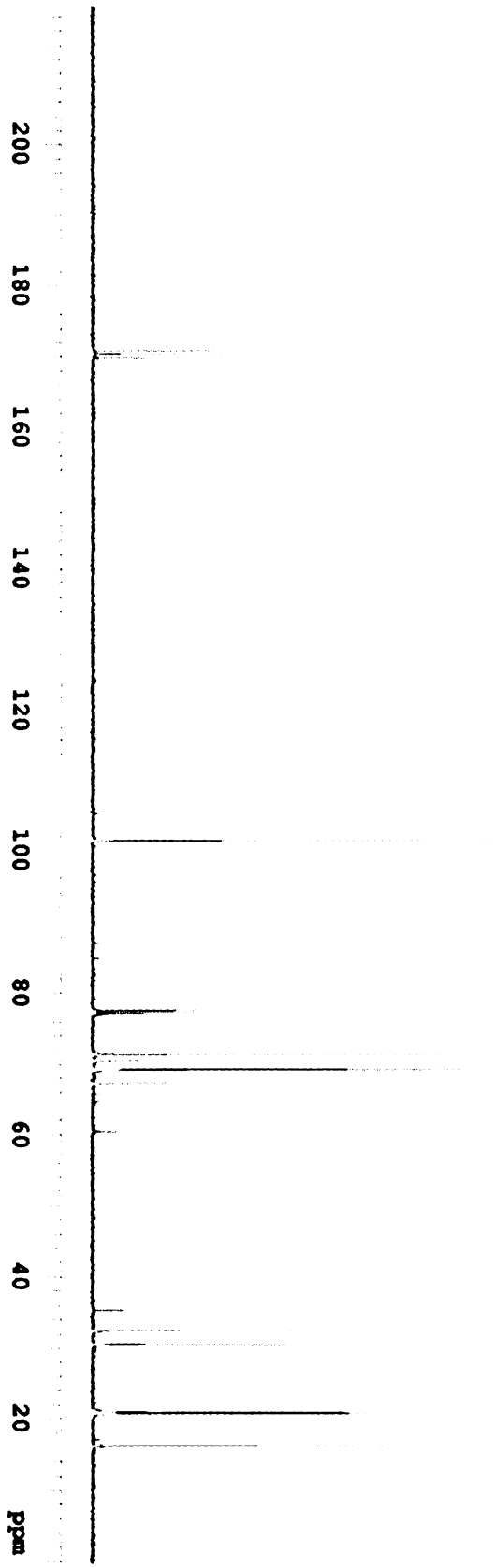
200
180
160
140
120
100
80
60
40
20
ppm

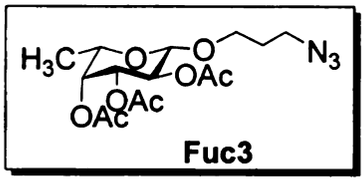
H3C
O
OAc
N3
OAc
OAc
Fuc3

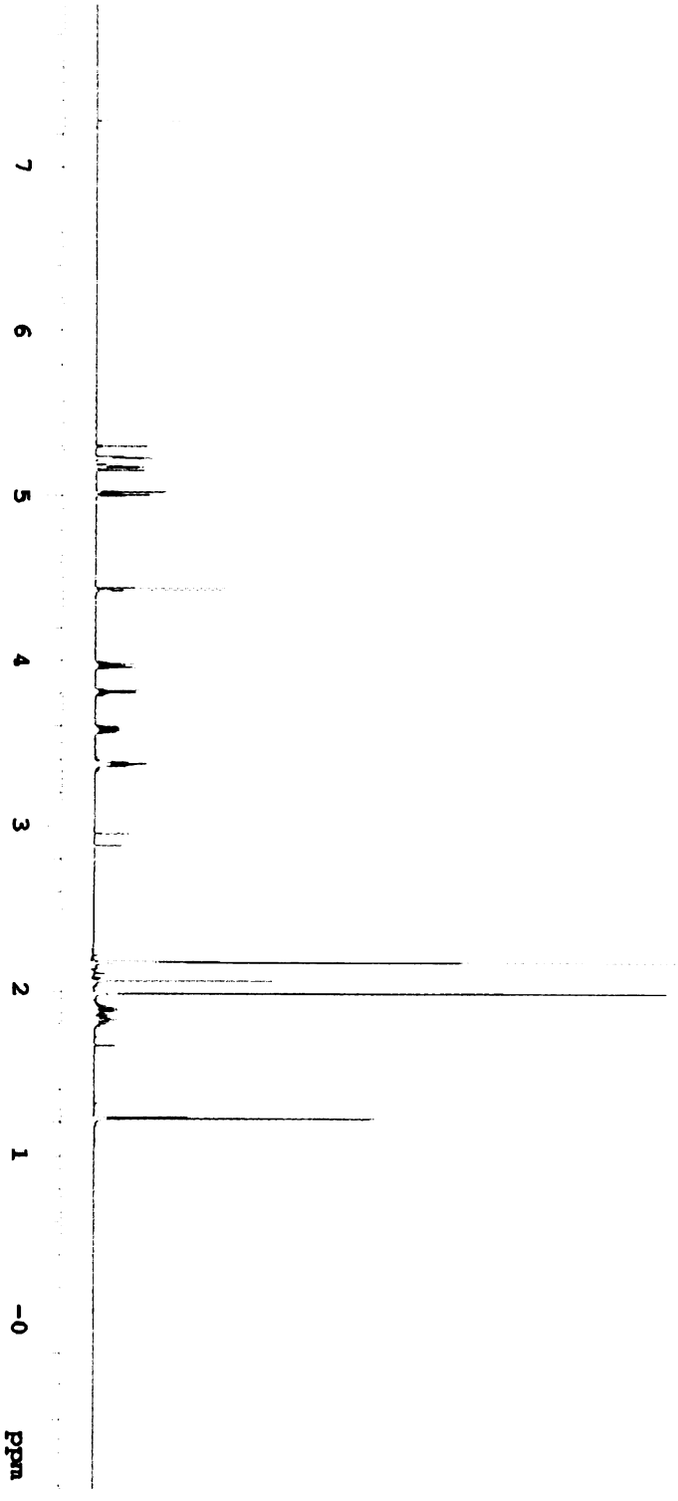
7
6
5
4
3
2
1
-0
ppm

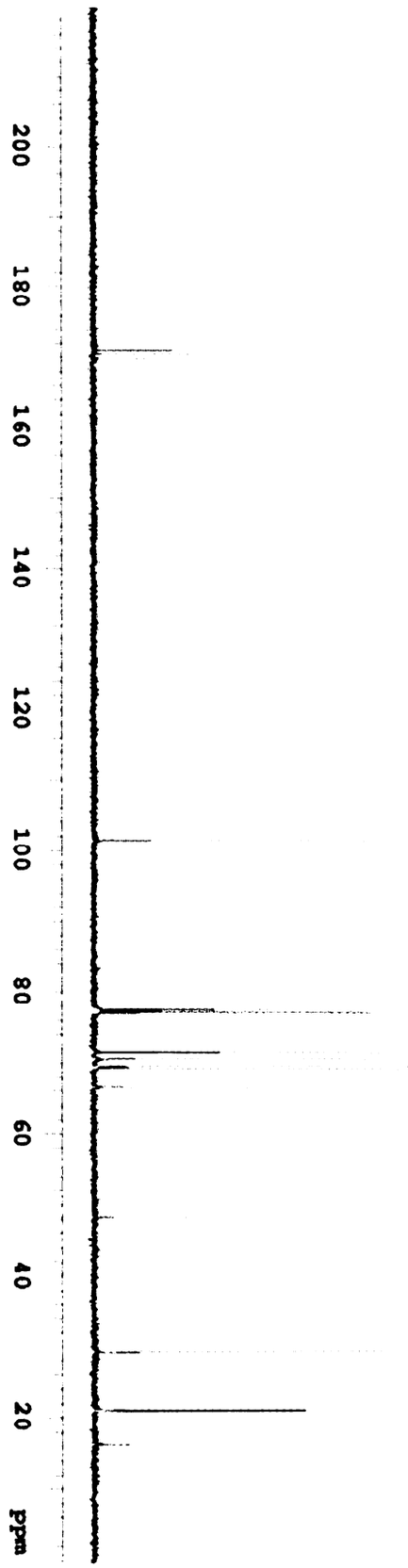
200
180
160
140
120
100
80
60
40
20
ppm

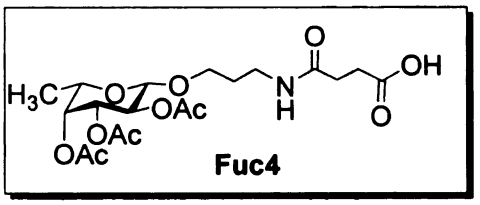

Fuc4

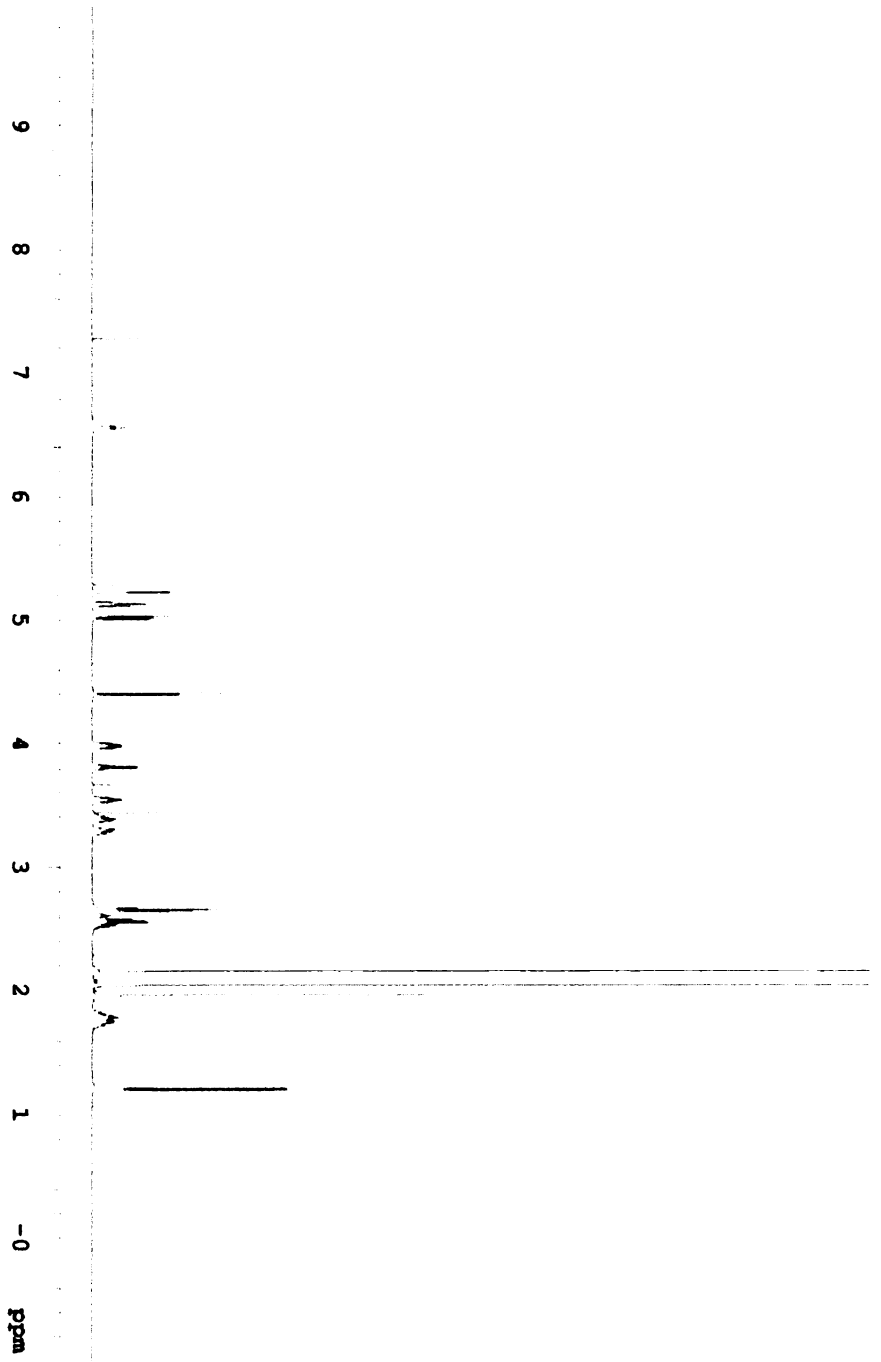

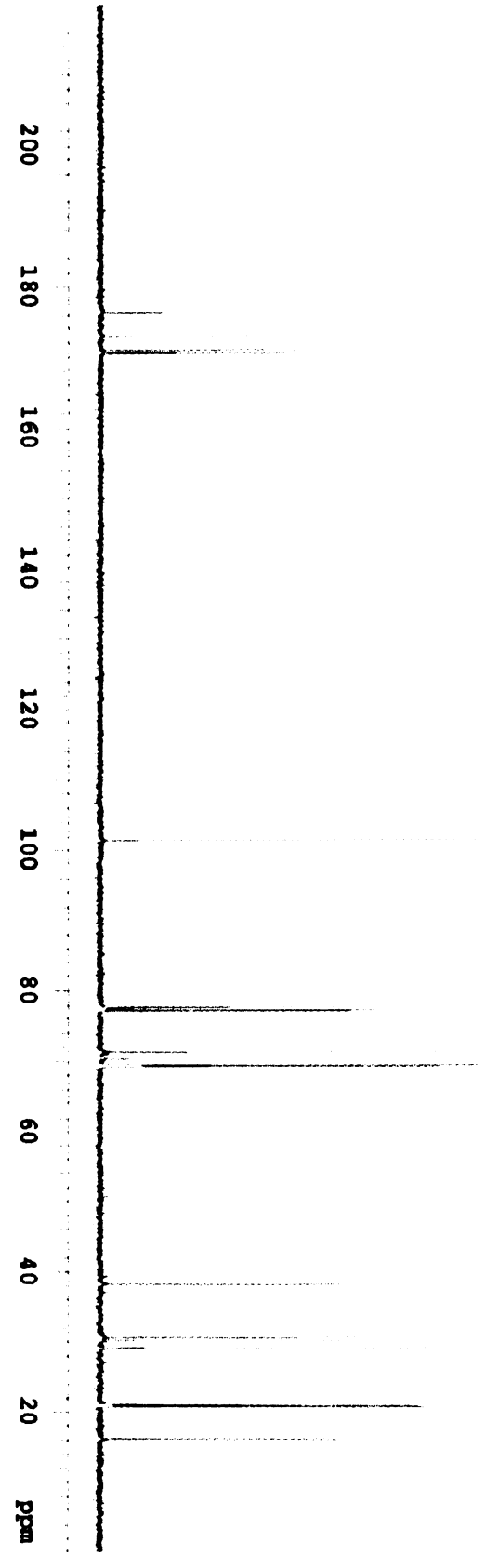
200
180
160
140
120
100
80
60
40
20
ppm

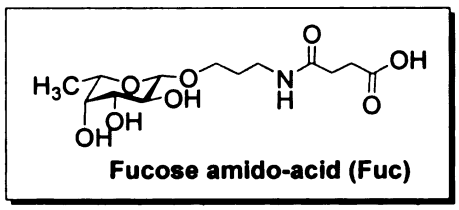

Fucose amido-acid (Fuc)

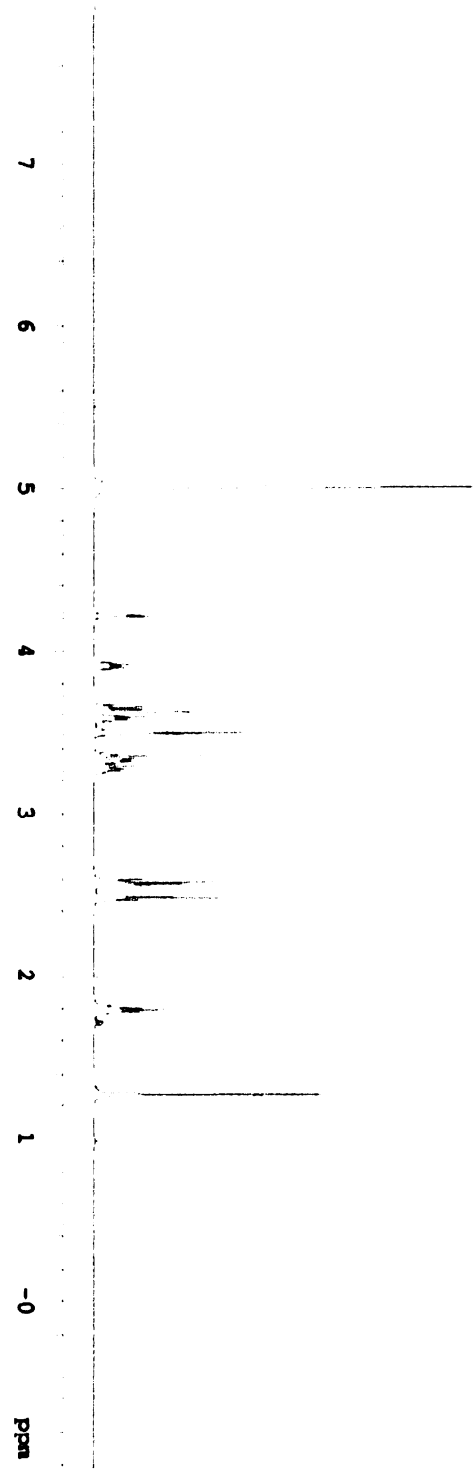

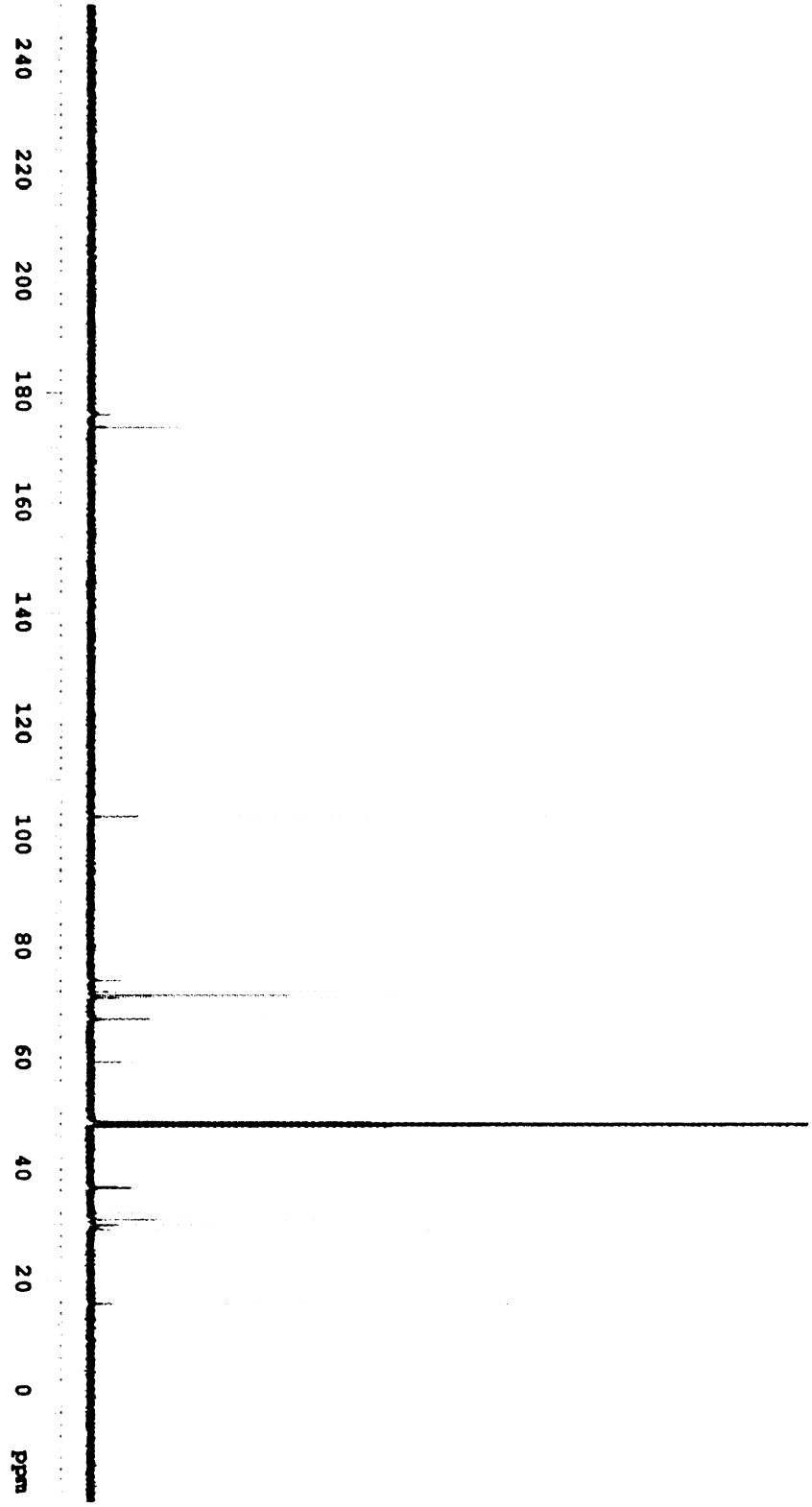
240
220
200
180
160
140
120
100
80
60
40
20
0
ppm

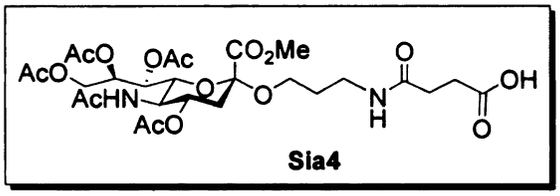

Sia4

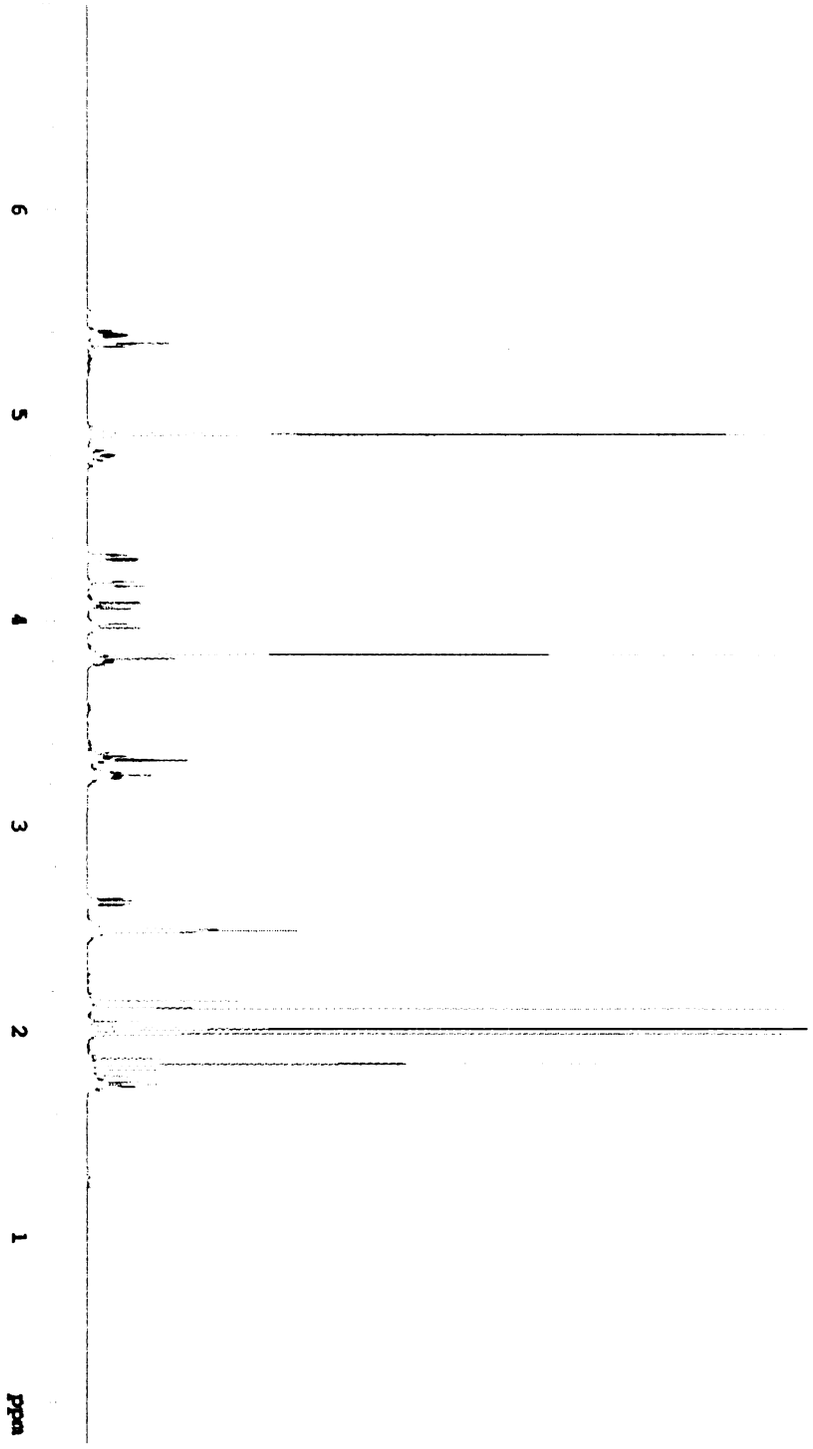

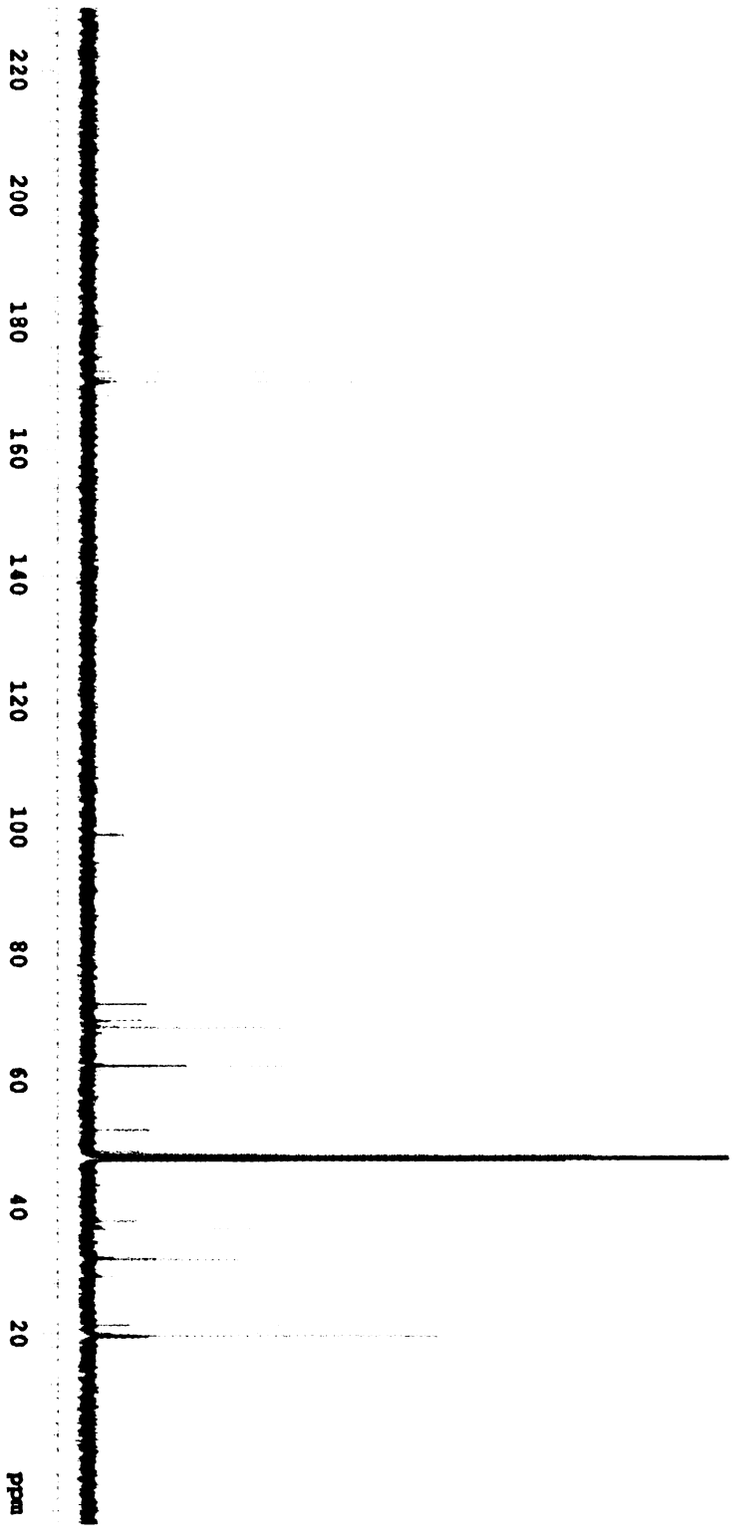
220
200
180
160
140
120
100
80
60
40
20
ppm

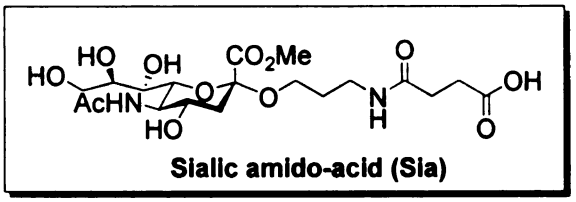

Sialic amido-acid (Sia)

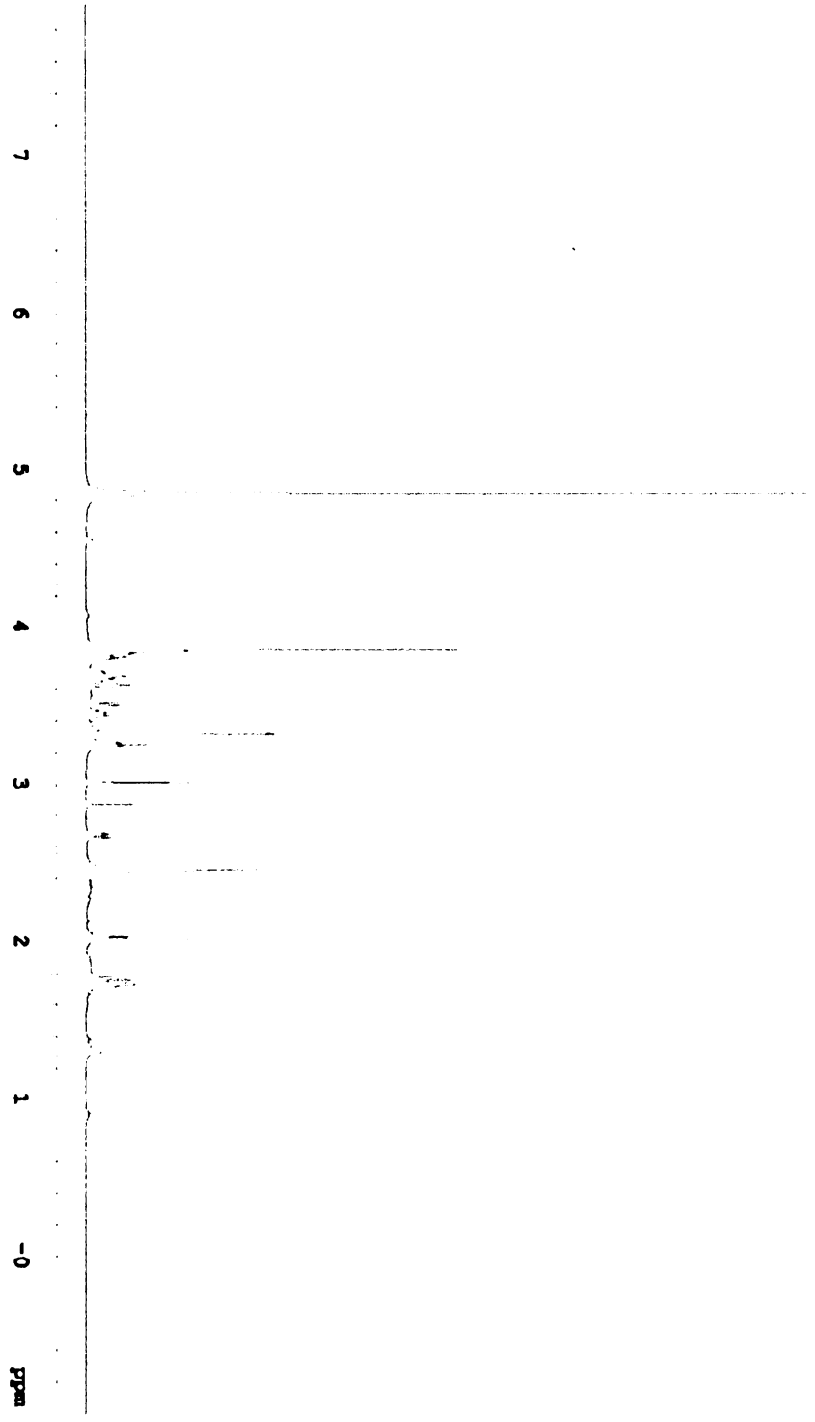

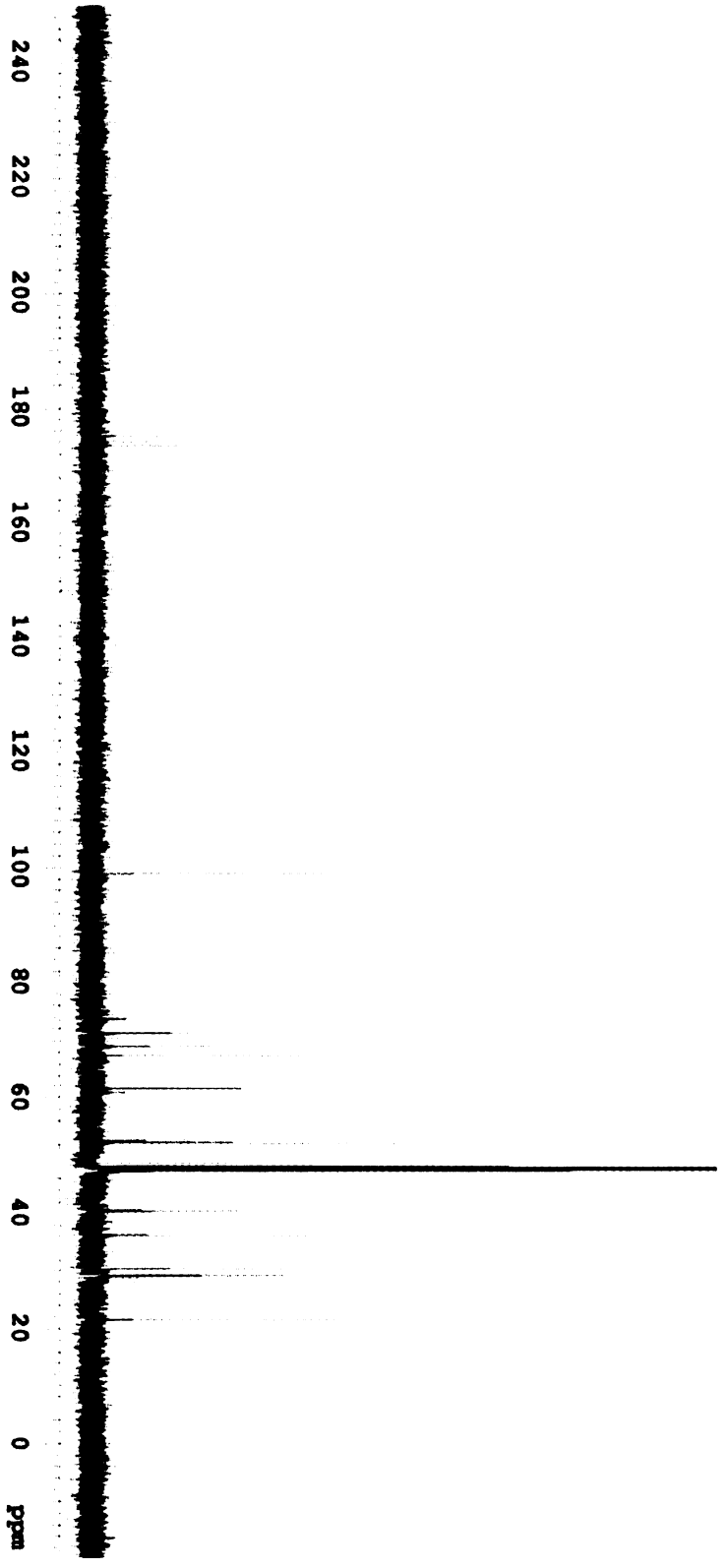
240
220
200
180
160
140
120
100
80
60
40
20
0
ppm

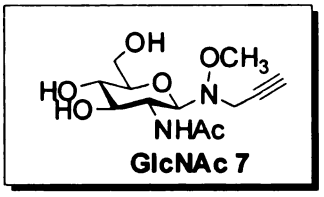

GlcNAc 7

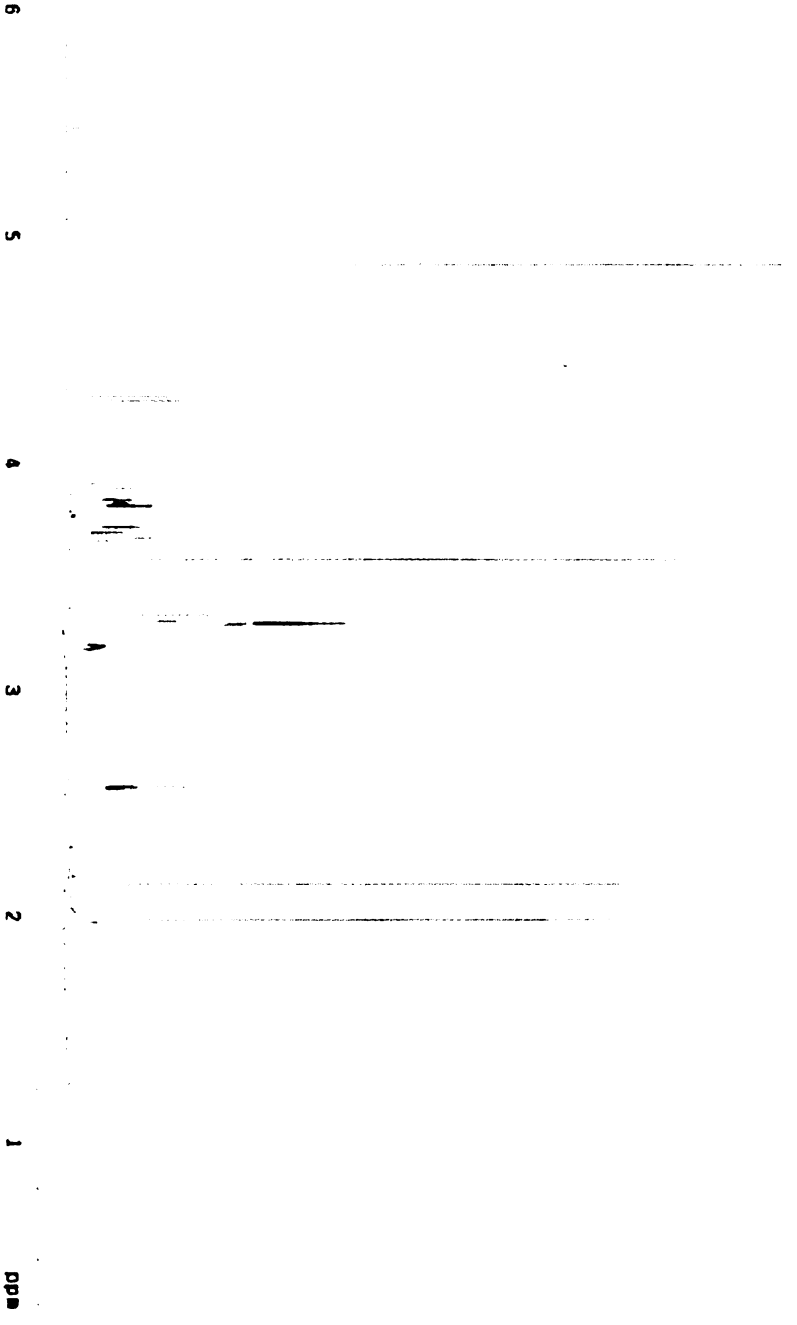

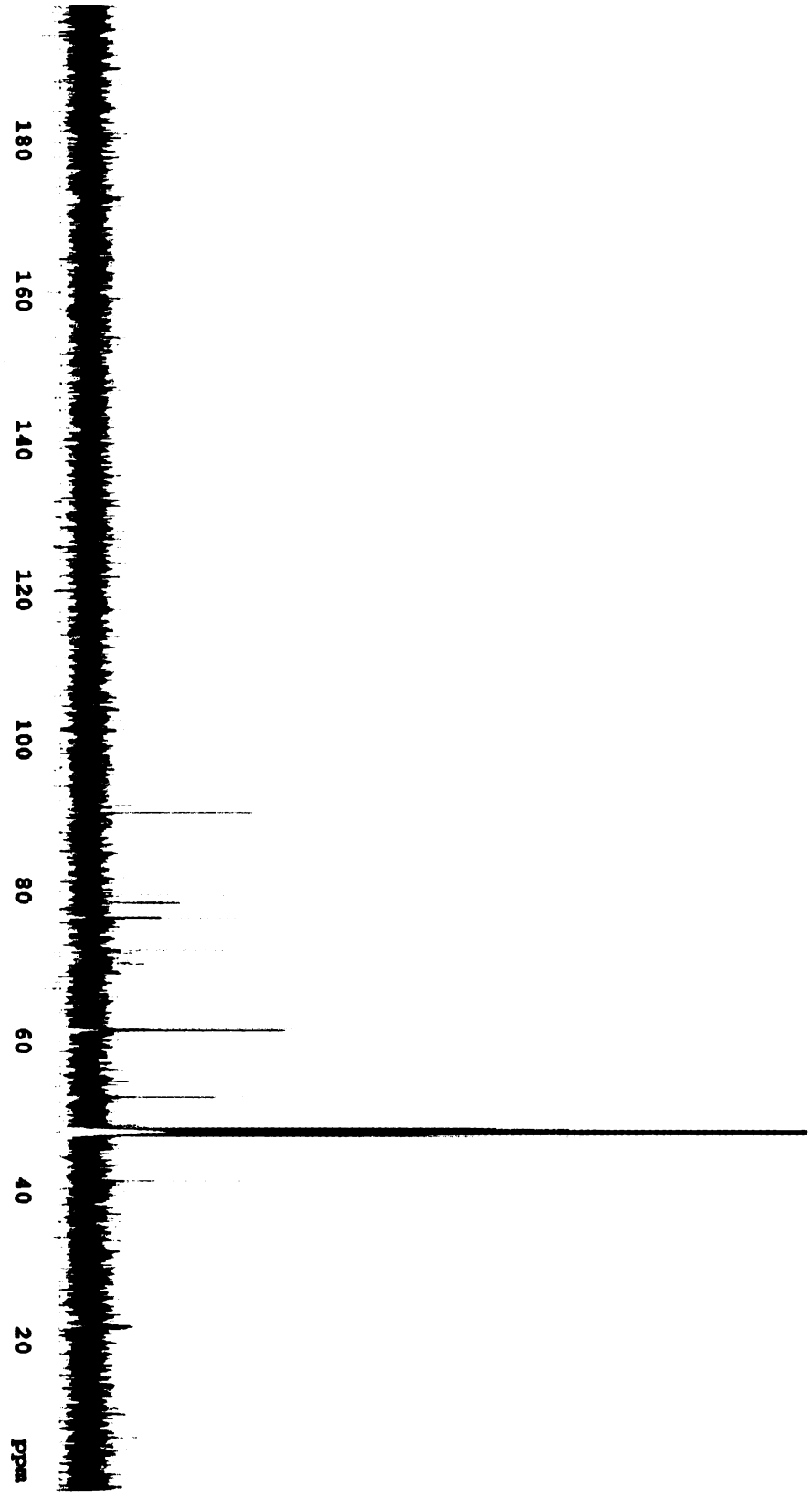
180
160
140
120
100
80
60
40
20
ppm

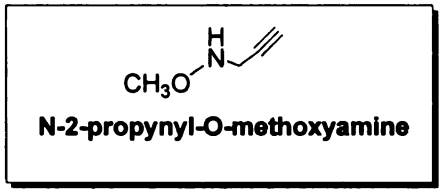

N-2-propynyl-O-methoxyamine

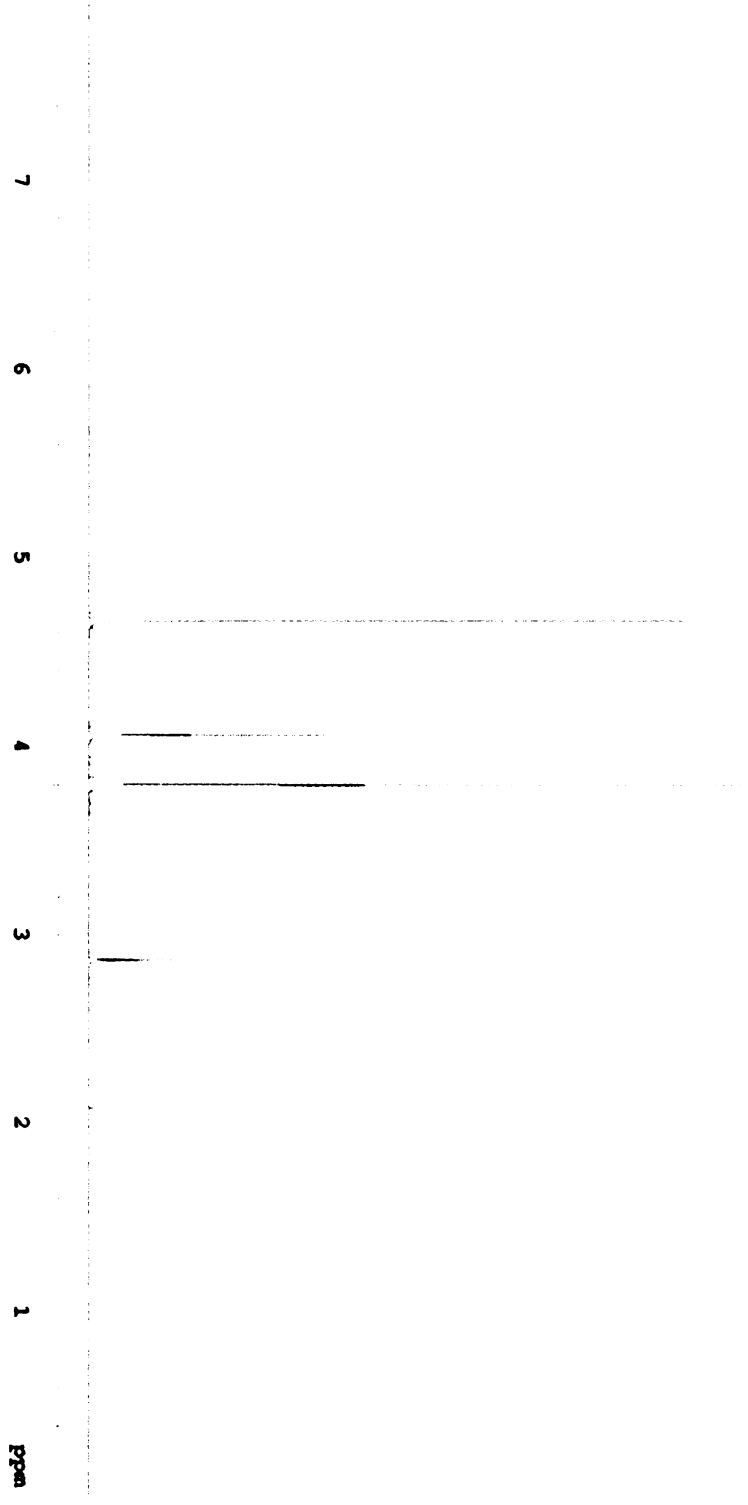

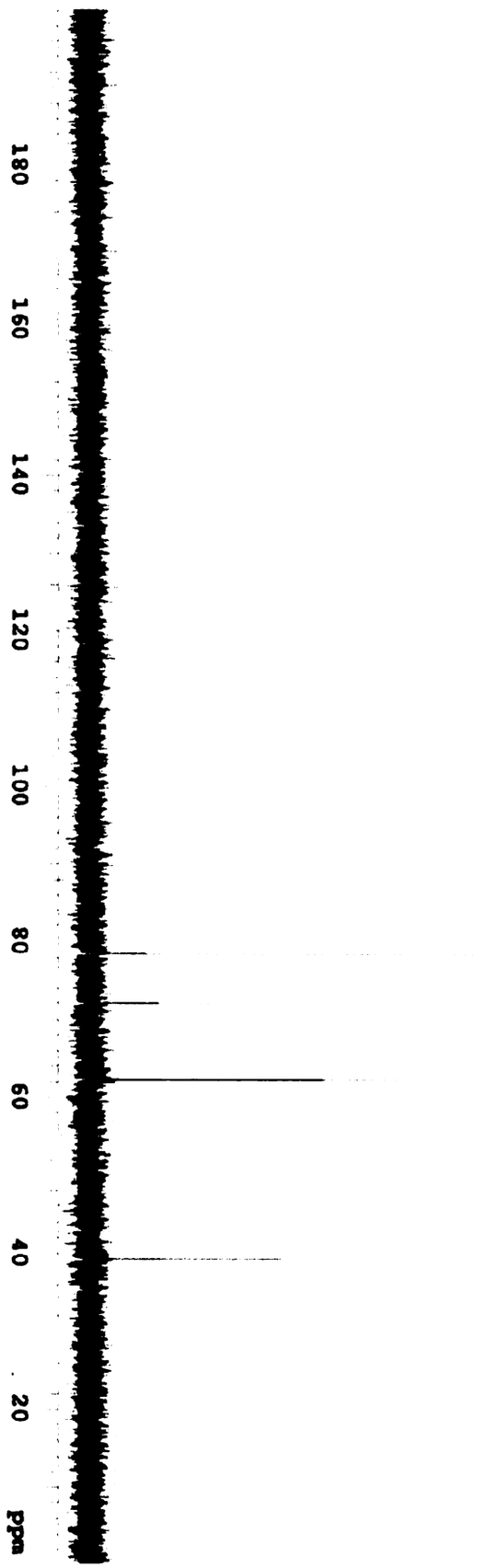
180
160
140
120
100
80
60
40
20
ppm

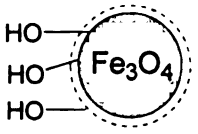

TEOS-NPs

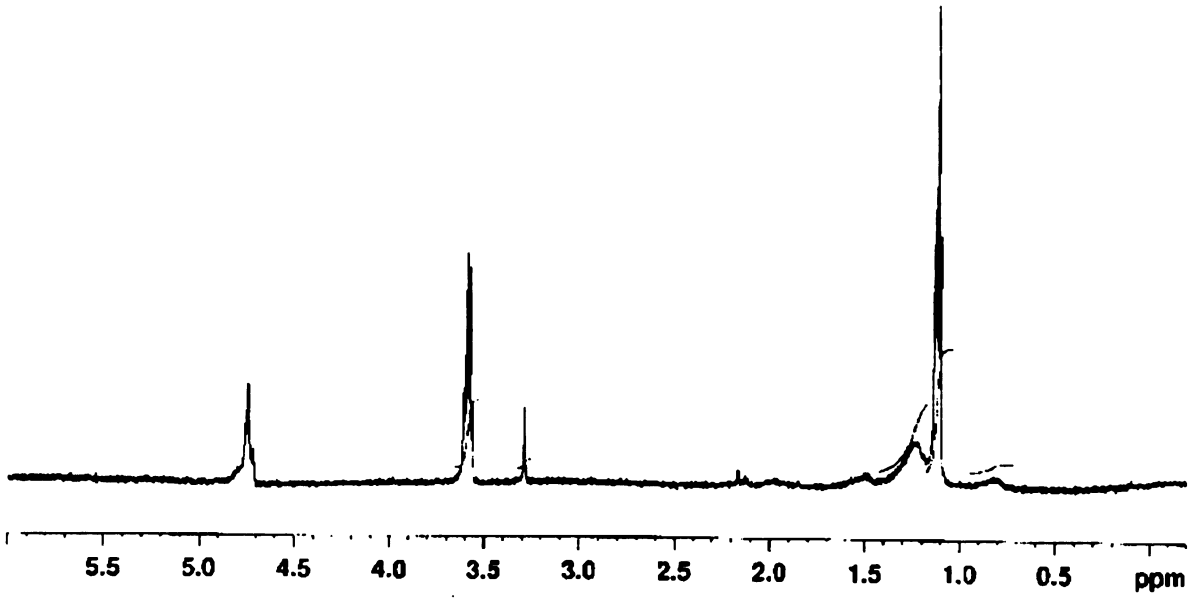

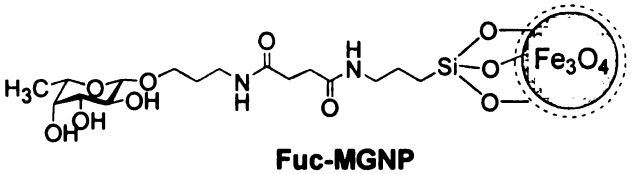

Fuc-MGNP

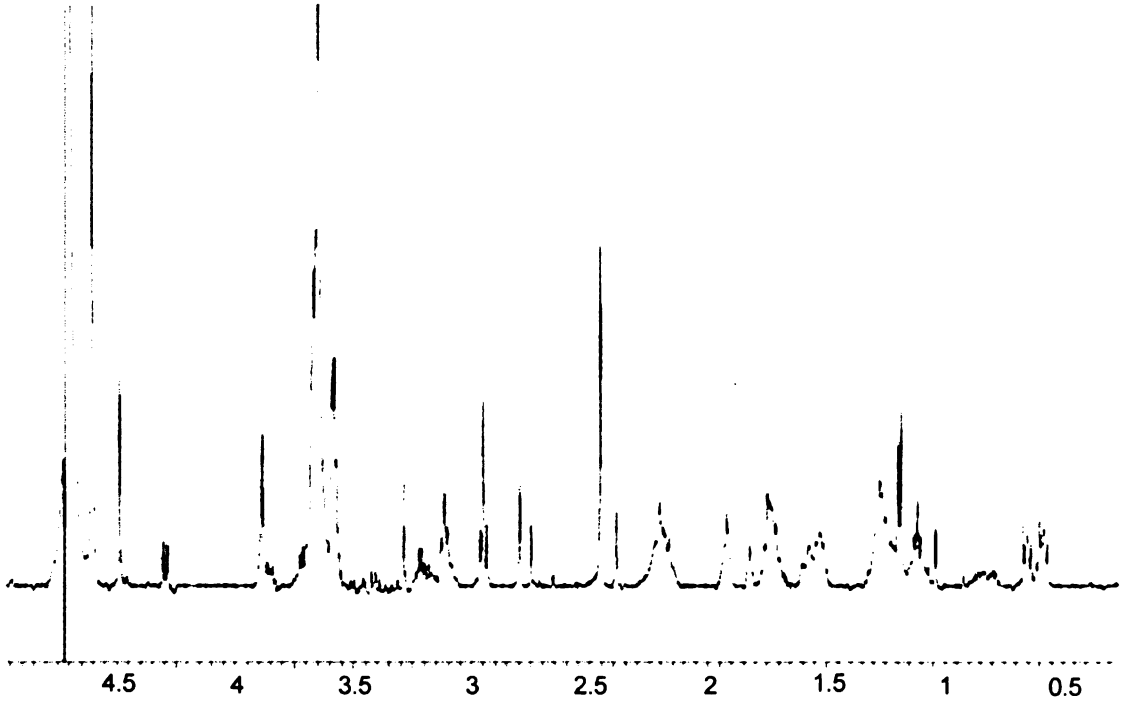

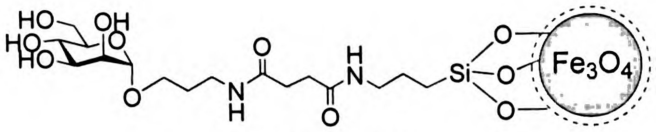
HO
OH
HO
O
HO
O
N
H
O
H
N
O
Si
O
O
O
Fe_3O_4

Man-MGNP

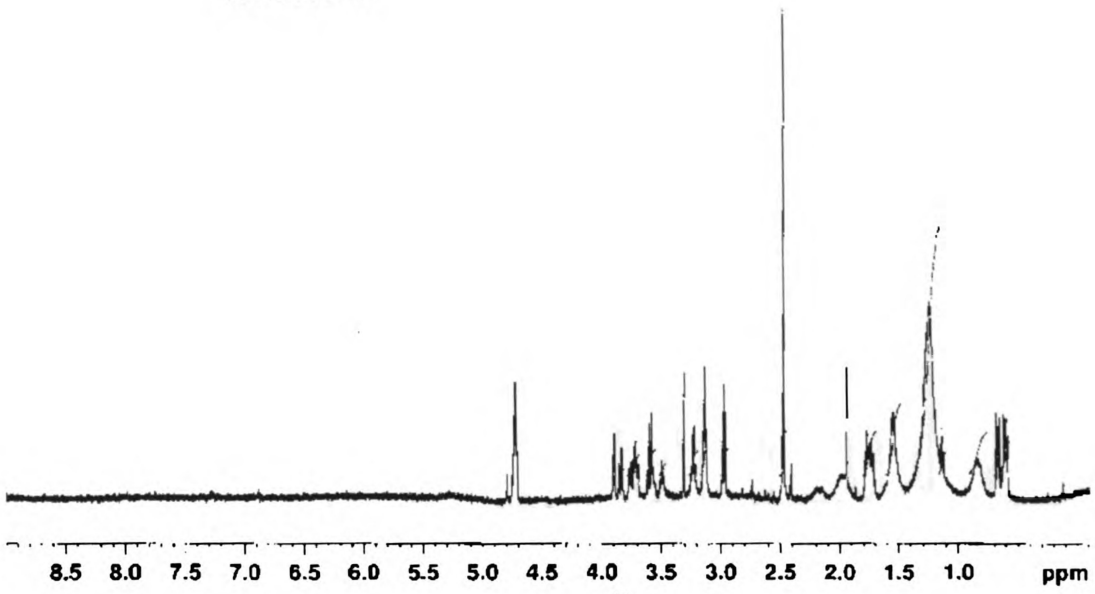
8.5
8.0
7.5
7.0
6.5
6.0
5.5
5.0
4.5
4.0
3.5
3.0
2.5
2.0
1.5
1.0
ppm

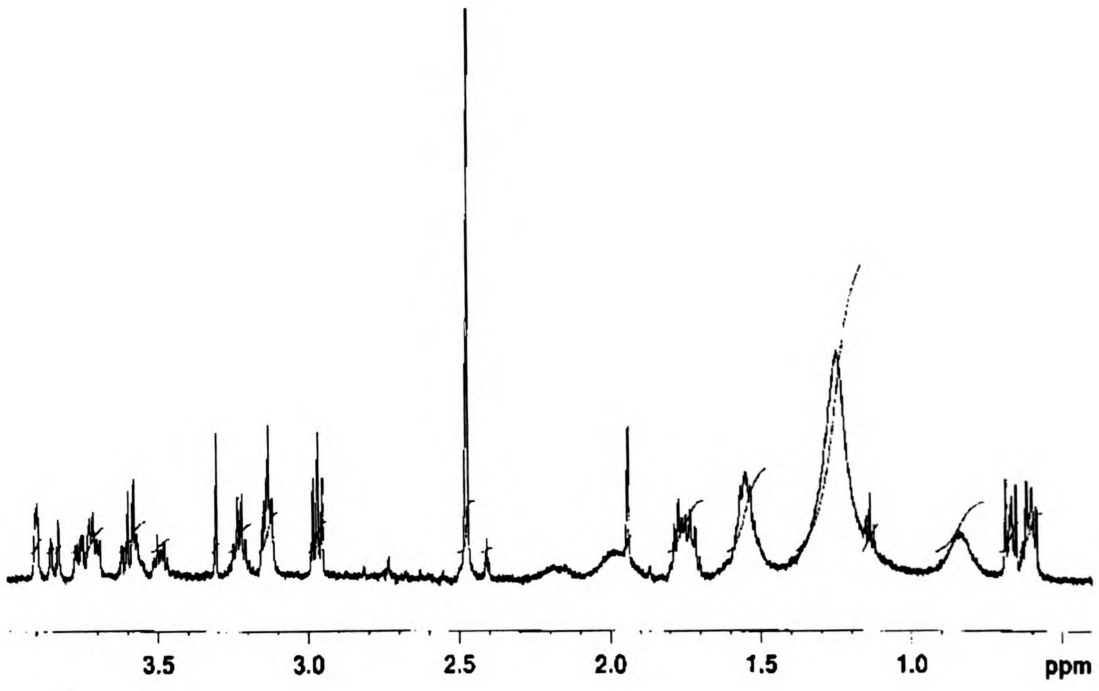
3.5
3.0
2.5
2.0
1.5
1.0
ppm

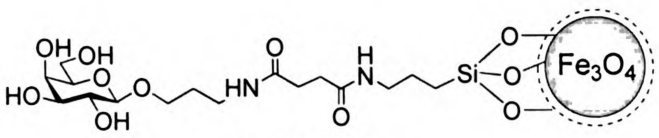
OH
OH
O
HO
O
OH
HN
O
H
N
O
Si
O
O
O
Fe_3O_4

Gal-MGNP

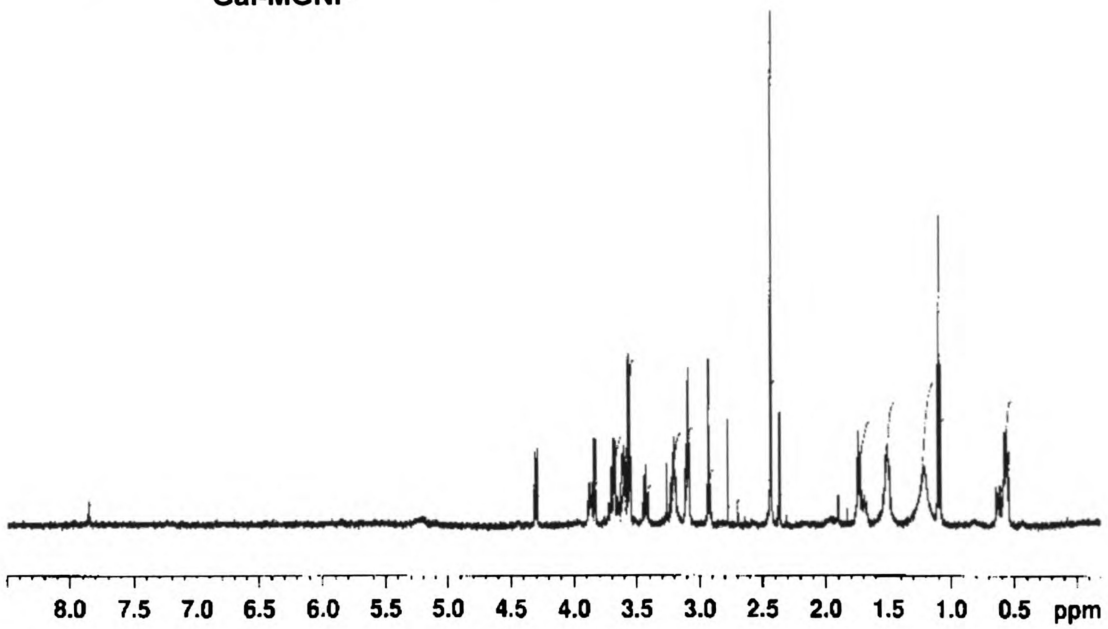
8.0
7.5
7.0
6.5
6.0
5.5
5.0
4.5
4.0
3.5
3.0
2.5
2.0
1.5
1.0
0.5
ppm

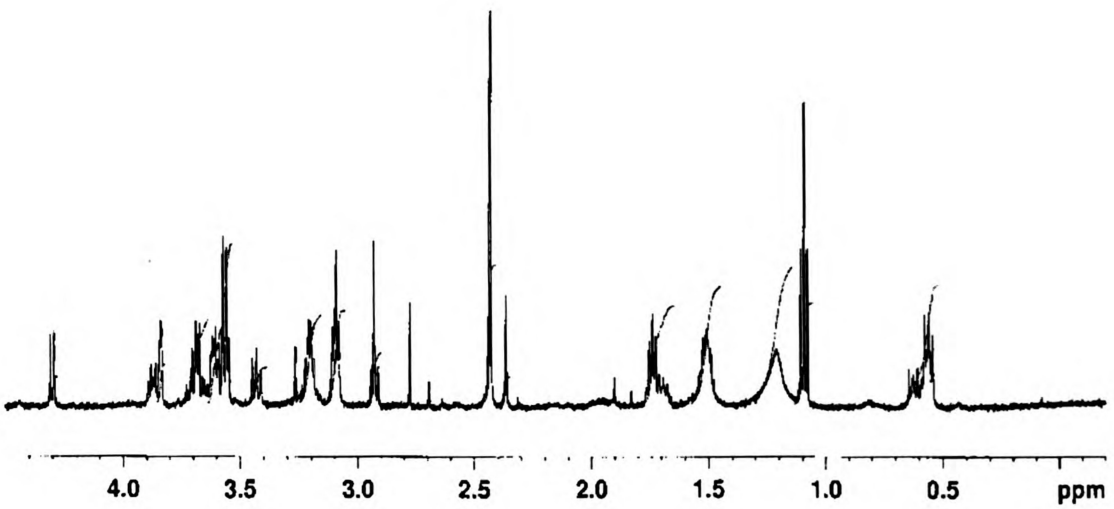
4.0
3.5
3.0
2.5
2.0
1.5
1.0
0.5
ppm